Regional Moment Tensors and the Structure of

the Crust in Central and Northern California

by

Michael Emmanuel Pasyanos

Sc.B. (Brown University) 1991

A dissertation submitted in partial satisfaction of the

requirements for the degree of

Doctor of Philosophy

in

Geophysics

in the

GRADUATE DIVISION

of the

UNIVERSITY of CALIFORNIA at BERKELEY

Committee in charge:

Professor Barbara Romanowicz, Chair
Professor Thomas McEvilly
Professor Jamie Rector

1996

The dissertation of Michael Emmanuel Pasyanos is approved:

_____

*Chair*                                                          *Date*

_____

*Date*

_____

*Date*

University of California at Berkeley

1996

Regional Moment Tensors and the Structure of

the Crust in Central and Northern California

Copyright © 1996

by

Michael Emmanuel Pasyanos

Abstract

Regional Moment Tensors and the Structure of
the Crust in Central and Northern California

by

Michael Emmanuel Pasyanos

Doctor of Philosophy in Geophysics

University of California at Berkeley

Professor Barbara Romanowicz, Chair


The upgrade of the Berkeley Digital Seismic Network (BDSN) has given seismol-
ogists an unprecedented tool to study earthquakes and structure in northern and
central California. Surface waves are particularly well-suited for this type of study.
Through the availability of this data and the application of several different tech-
niques, particularly the regional surface wave moment tensor inversion, valuable in-
formation can be learned about earthquake sequences, seismically-active areas, and
regional earth structure, leading to the development of a comprehensive picture of
the tectonic structure in California and the western United States.

The surficial geology of the region implies a complicated, laterally varying struc-
ture at depth. A geophysical inverse method with broad coverage and both crustal
and sub-crustal resolution which allows lateral variations, is required to image this
complex lithosphere. New, closely spaced broadband instruments recording moder-
ate to large regional earthquakes provide a suitable data set for this purpose. A
tomographic inversion method of surface wave phase velocities from these recordings
was chosen to perform this imaging. This method can be implemented with current
algorithms and computing power, and is described here.

The dissertation has been organized into three main sections. The first describes
the regional surface wave moment tensor method, along with examples and tests.
The second part shows applications of the technique, from the actual moment tensor

inversions to earthquake and regional studies. Finally, the third part of the work covers the results of the inversion for regional earth structure from the surface wave data, which is accomplished in two steps. A phase velocity tomography of both Love and Rayleigh waves is performed for a number of frequencies. In turn, the phase velocities are then inverted for a depth-dependent velocity profile. The results are compared to several other studies and are interpreted in light of the regional tectonics. In general, shallow and upper crustal features can be related to the tectonic environment. Deeper features, however, can be dissociated from near-surface features and may be strongly influenced by mantle processes.

*This work is dedicated to my father*

*Emmanuel Nicholas Pasyanos*

# Contents

# List of Figures

# List of Tables

# Acknowledgements

I would like to thank the members of my committee, Barbara Romanowicz, Tom McEvilly, and Jamie Rector, for all of their assistance in making this dissertation a much better end product. I am especially grateful to Barbara who as director of the Seismographic Station and my advisor provided me with opportunity, advice, and knowledge, as well as a stimulating environment to study seismology. She gave me the essential guidance that I needed early on, but provided me with the space that I needed afterwards.

There are many people to whom I am indebted. I would especially like to thank Doug Dreger, whose commitment and enthusiasm about earthquakes always had me searching for new things to discover. I would also like to thank Lind Gee who, particularly early in my graduate career, put in a lot of time and effort on my behalf. She is infinitely patient. Bob Uhrhammer, Doug Neuhauser, and Anthony Lomax, each in their own distinctive way, helped me through many of my difficulties with important conversations on seismic instrumentation, computers, and the philosophy of science.

Of course, there is the cast of characters who made working around the Seismographic Station a friendly, supportive, interesting and challenging environment: Suzanna Loper, Greg Anderson, Phoebe Southwood, Xiang-Dong Li, Charley Paffenbarger, Mike Antolik, Joe Durek, Steve Fulton, Mark Murray, Lane Johnson, Olivier Coutant, Nick Gregor, Ann Becker, Rick McKenzie, Dave Sharrock, Peggy Johnson, Ted Bohn, Charles Megnin, Ruben Amirbekian, Ludovic Breger, Rick McKenzie, Bill Karavas, and others.

I am also grateful to Lori Dengler, Bob McPherson, Jeroen Ritsema, Dave Oppenheimer, Karen Fischer, and many of my colleagues.

I would like to thank my family, as well, for teaching me the importance of learning, playing and discovering, and for supporting me in my efforts.

Most of all, I would like to thank my sweetie Juliann, who through the course of this work, went from girlfriend to fiancée to wife. She put up with, encouraged me, and loved me over the years. She even tried a hand at reading and editing my dissertation. Thank you for your love and support.

# Chapter 1

# Introduction

Two recent trends in seismology have been the availability and use of digital broadband data and the increasing emphasis on real-time seismology. Both of these phenomena are significant in changing the character and outlook of the field of seismology in both recent and coming years, the former in providing the field with increasing amounts of reliable data with which to study the earth, and the latter in concentrating the efforts of seismologists to provide the data as quickly and reliably as possible to the public and to each other. I have focussed on bringing these two trends to bear on my research. The other significant motivation of my research comes from the knowledge (or lack of knowledge) of California and the western United States, one of the most thoroughly studied areas of the globe. Many fundamental questions remain about the basic geology and tectonics of the region. It is hoped that this research can add some pieces to this complex puzzle.

## 1.1   Technical Motivation

The recent deployment of high quality digital broadband networks in several seismically active regions of the world provides unprecedented opportunities to design and implement robust moment tensor inversion techniques for rapid and reliable estimation of valuable earthquake parameters. Since January 1991, the Seismographic Station at UC Berkeley has been upgrading its digital broadband network, the Berkeley Digital Seismic Network (BDSN; Bolt, *et al.*, 1988; Romanowicz, *et al.*, 1992), which covers northern and central California and is linked to Berkeley by continuous digital telemetry (Romanowicz *et al.*, 1994). Several techniques are being developed

to complement the traditional reporting and cataloguing of local magnitude ($M_L$) by that of seismic moment, source mechanism, and eventually source rupture characteristics. In addition, the ability to study the structure of a region through the use of a small number of high quality, broadband instruments in lieu of a large network of short period seismometers is a very powerful tool which is just beginning to be utilized.

Currently, BDSN consists of fourteen stations (figure 1.1) recording broadband (DC to 10 Hz) ground velocity with Streckeisen (STS-1 or STS-2) or Guralp (CMG-T30) sensors (see Appendix A for a complete list of sites, locations, operation periods, and instruments). The stations span Northern and Central California from the Oregon border in the north to the Tehachapi Mountains in the south. Some additional sites are planned to densify and expand the network. The instruments are three-component, digital, high dynamic range, very broadband velocity transducers. They are co-located at each site with Kinemetrics FBA-23 strong motion accelerometers. Both data streams are digitized at various rates on 24-bit Quanterra data loggers. The wide range of frequencies that the broadband instruments record enable many studies which are impossible with narrow band instruments. The combined instrument package also has a remarkable breadth in amplitude: sensitive enough to record small earthquakes, but also allowing the largest earthquakes to remain on-scale. The combined systems give a nominal dynamic range of 200 dB, which is essential for being able to monitor the full range of earthquake sizes occurring in California.

Data from the remote stations are telemetered back to Berkeley in near-realtime via a variety of media such as digital ADN phone lines, microwave and radio circuits, and are available for retrieval within about 30 seconds after recording for VBB data, and within about 7 minutes for LP data. Currently, most BDSN station telemetry uses 56 kbit frame relay protocols on digital phone services. Frame relay provides one or more virtual circuits over a single digital phone circuit with 56 kbit/second to 1.5 MBit/second capacity. This allows a remote seismic site to send data to multiple receivers over a single digital phone circuit, and allows a central receiving site to receive data from multiple seismic stations over a single digital circuit. The data is then archived on an optical mass-storage "jukebox" in a compressed file format. The BDSN, together with broadband stations from other networks (TERRAscope, IRIS, USNSN), provides reasonable coverage of California and the western United States.

This dissertation represents an effort to utilize the broadband data in a number of different ways in an effort to try and understand earthquakes in particular and the earth in a broader sense.

The push for real-time seismology results from the rapid availability of high quality digital data. Efforts are being made to automate many of the procedures that scientists and investigators use regularly, to build in checks to make the system robust, and to avoid some of the problems that human operators would detect. The Rapid Earthquake Data Integration (REDI) Project at UC Berkeley (Romanowicz, *et al.*, 1994, Gee, *et al.*, 1996) and the Caltech USGS Broadcast of Earthquakes (CUBE) Project (Kanamori, *et al.*, 1991) at Caltech are two such projects that are engaged in this endeavor. Some of the procedures that are described have been developed with the idea of the real-time dissemination of this information in mind.

First and foremost is the development of techniques to determine the moment tensors of moderate-sized earthquakes. Because of the period range of the inversion, broadband data from a network are required. Moment tensors, perhaps the most fundamental parameters of an earthquake besides location, provide useful information about the size and mechanism of an event. Furthermore, moment tensors are often essential information to know before moving on to more complicated aspects of an earthquake, such as the source time function, directivity, or slip distribution-parameters useful in hazard assessment. Quickly calculating and disseminating this critical information has been a priority. Also, combining moment tensor information with various other techniques has yielded a surprising amount of information on a wide variety of subjects.

Finally, knowledge about the structure of the earth along source-receiver paths, which is available with a limited effort from the regional surface wave inversions, is used in order to model the regional velocity structure. Again, this is information which would be impossible without access to the broadband data. From the results of the surface wave tomography, a limited interpretation of geology and tectonics can be made. Keep in mind that this represents only one piece in a puzzle that involves many elements. A more in-depth analysis requires a more comprehensive treatment of the other parts of the problem and would include, among other things, geodetic data, gravity data, electromagnetic data, body wave data, reflection/refraction studies, surface geology, and tectonics. Surface waves, however, provide important

# BDSN Stations
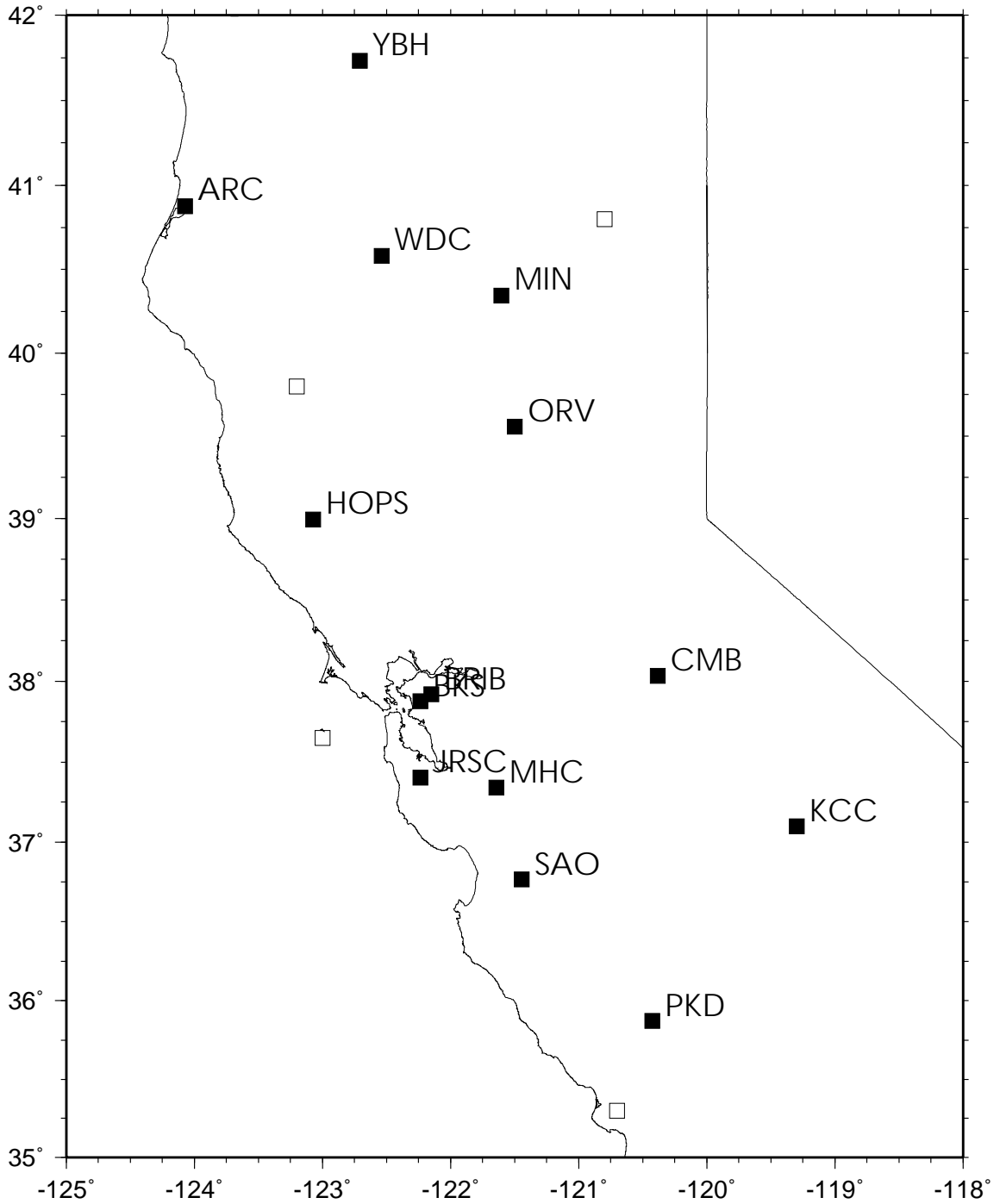


Figure 1.1: Broadband stations in the Berkeley Digital Seismic Network (BDSN). Stations operational as of May, 1996 are shown by filled squares. Planned stations are shown by empty squares.

information about the average velocity of the crust and upper mantle.

## 1.2 Geological Motivation

The other significant motivation has been the interesting and complicated geology of the region. In the classic view, known as the "California" model, the complex geology along the San Andreas Fault System is the result of a series of processes. Subduction and accretion occurring within a compressive regime was followed by primarily strike-slip motion occurring along major transform faults. Although this model has been considered to be everything ranging from too simplistic to completely wrong, it gives an estimate of the complexity of the geologic and crustal structure of the area.

Maps showing the structure and tectonics (from Fuis and Mooney, 1990) and geology (from Norris and Webb, 1990) of California (figures 1.2 and 1.3) illustrate the complexity of the system, as shown though the variability of geologic and tectonic units displayed over such a small area. There are huge granitic intrusions (Sierra Nevada and Peninsular Ranges), Cenozoic volcanism (Cascade Mountains and Modoc Plateau), metasedimentary and metavolcanic regions (Klamath Mountains and the Sierran Foothills), vast sedimentary basins (Great Valley, Santa Clara Valley, Salinas Valley), and some exotic metamorphic marine material (Franciscan Complex). In addition, the whole region is criss-crossed by faults, a large number of which have been active in the Holocene and historically. More broadly, the widely varying tectonics exist throughout the western United States (figure 1.4) as well, including active volcanism and mountain-building, hotspots, and broad areas of extension.

Questions remain as to how the western margin of the United States evolved into this level of complexity. Current theory, as summarized by Norton and Webb [1990], describes the processes which formed California and provides some understanding of its present state. During the Proterozoic and Paleozoic, much of California was a broad, shallow marine shelf. Marine conditions persisted into early Triassic time, until the onset of active subduction along the continental margin in the late Triassic. Active subduction continued during the Jurassic, allowing foreign marine debris to collide with the continent. This would explain the presence of accreted terranes along the west coast, including the Franciscan complex.
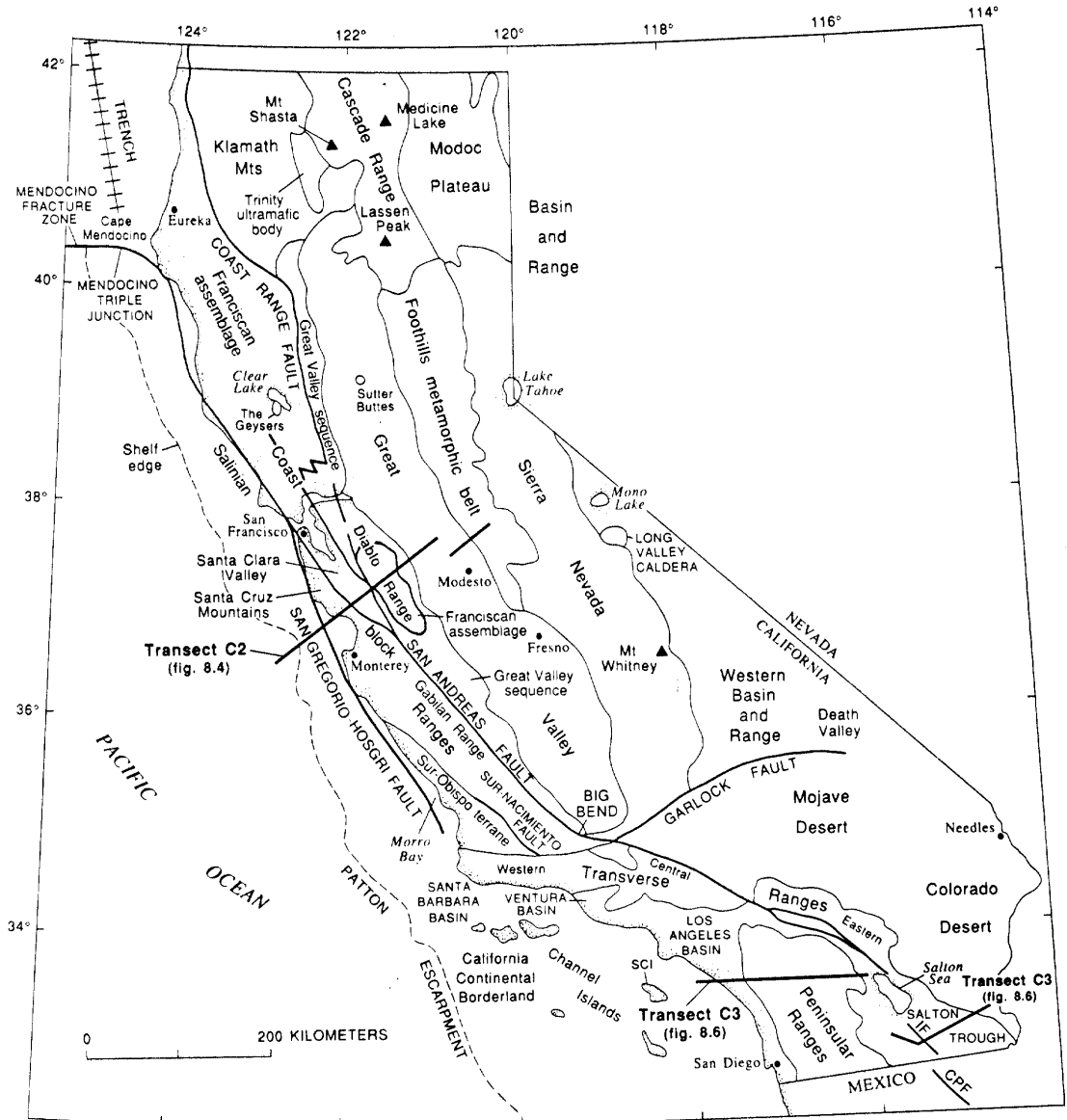
FIGURE 8.2. —California, showing place names, geologic provinces, selected geologic units, and locations of crustal transects shown in figures 8.4 and 8.6. The San Andreas fault extends from the Salton Trough to triple junction at Cape Mendocino. CPF, Cerro Prieto fault; IF, Imperial fault; SCI, Santa Catalina Island. Fault with crosslining is trench, offshore northern California.

Figure 1.2: Tectonic model of California (Fuis and Mooney, 1990).

6
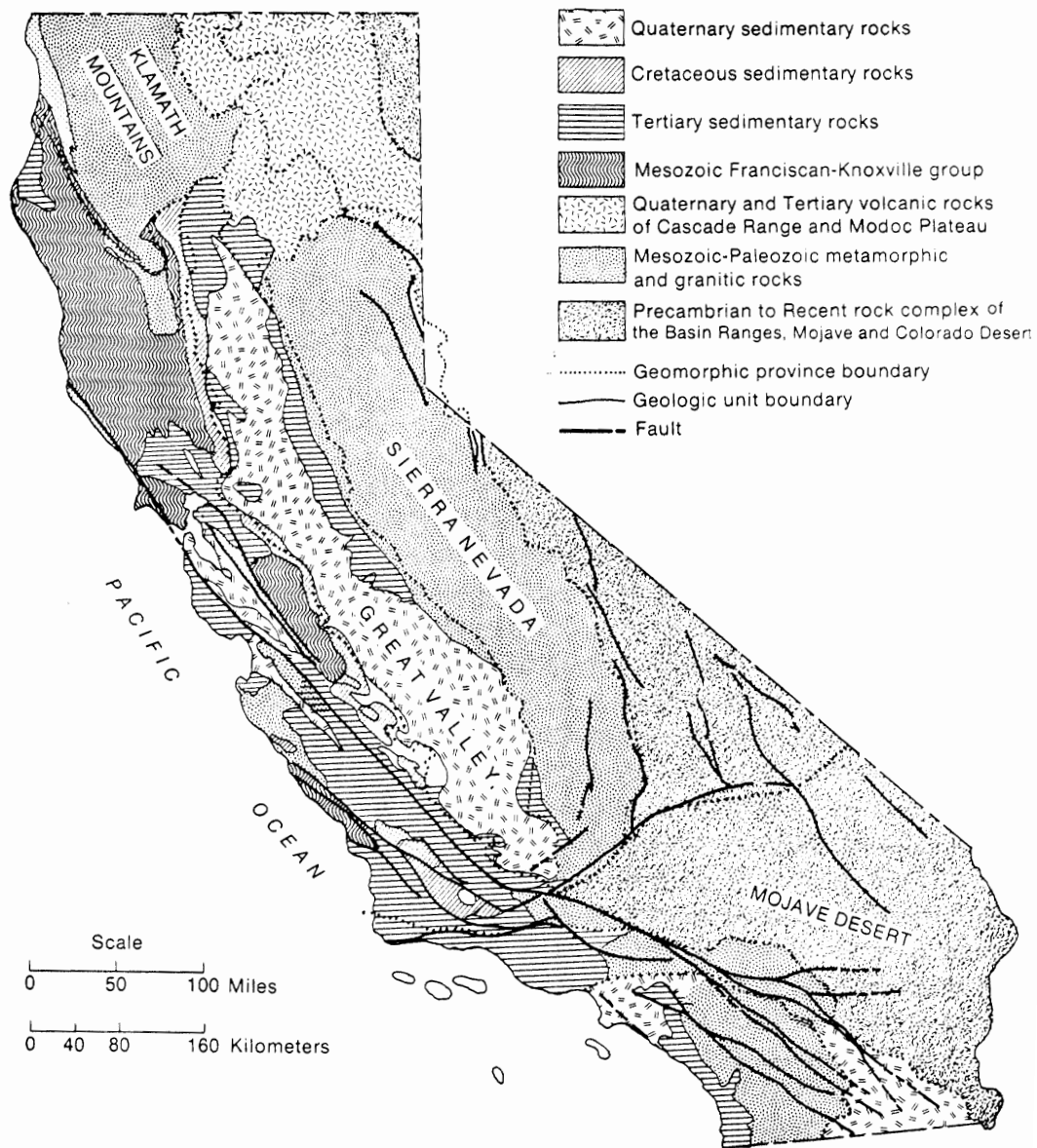
FIGURE 2-1 Geologic map of California, showing principal faults and generalized geologic units. (Source: California Division of Mines and Geology)

Figure 1.3: Generalized geologic map of California (Norris and Webb, 1990).

# Tectonic Provinces of the Western United States
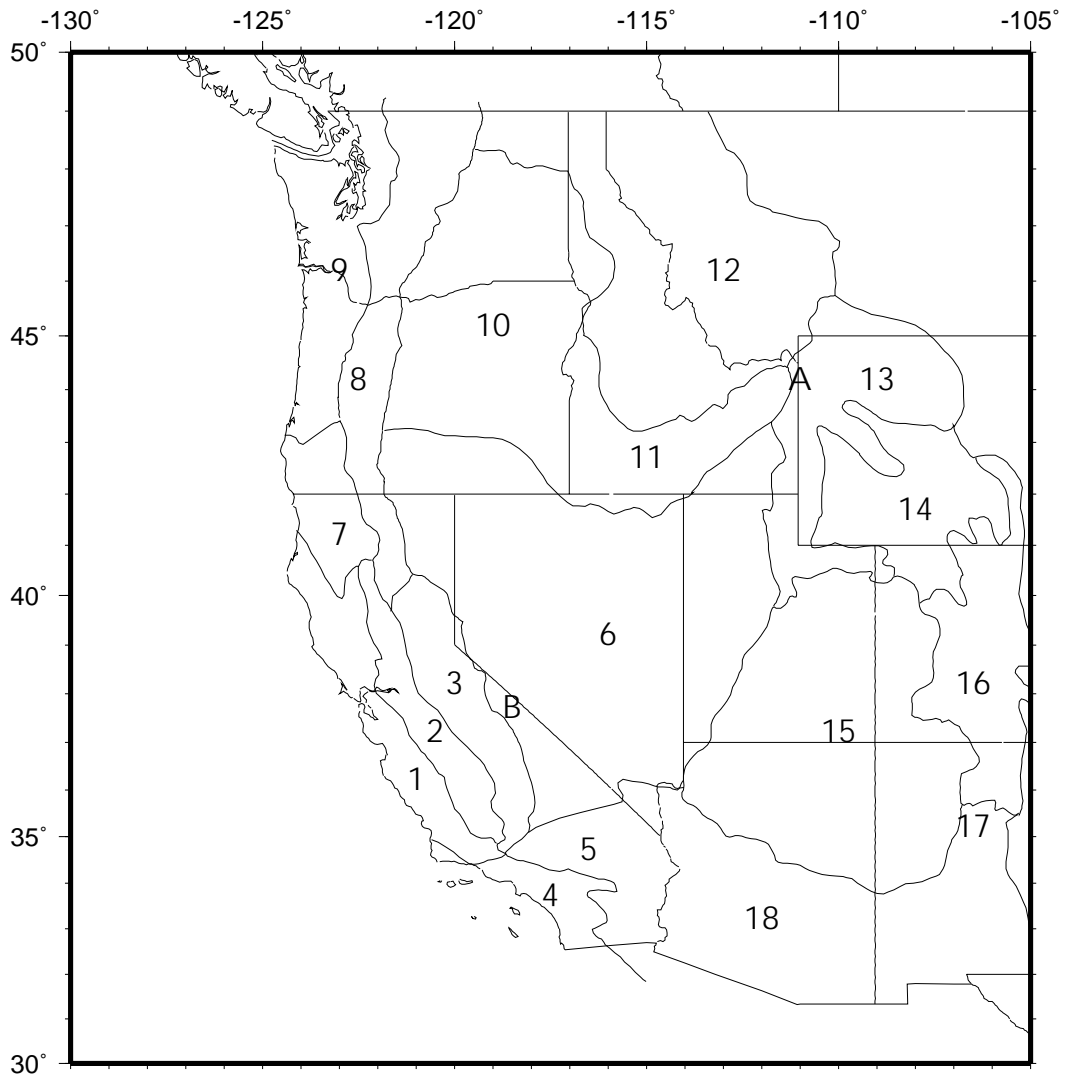


Key to provinces: 1) California Coast Ranges, 2) Great Valley, 3) Sierra Nevada, 4) Peninsular Ranges, 5) Mojave, 6) Northern Basin and Range, 7) Klamath Range, 8) Cascade Range, 9) Northwest Coast Ranges, 10) Columbia River Plateau, 11) Snake River Plain, 12) Northern Rockies, 13) Central Rockies, 14) Wyoming Basin, 15) Colorado Plateau, 16) Southern Rockies, 17) Rio Grande Rift, 18) Southern Basin and Range, A) Yellowstone, B) Mammoth Lakes

Figure 1.4: Tectonic provinces of the Western United States.

In the late Jurassic and Cretaceous periods, subduction continued and resulted in the Nevadan orogeny, during which time vast amounts of granitic magma were generated and extensive mountain building occurred (see figure 1.5). Large amounts of sediments were produced by the high Sierra Nevada Mountains and formed the thick beds of the Great Valley sequence. At the same time, subduction continued and Franciscan rocks were scraped off the sea floor and collided against the edge of the continent. For much of the time since then, the activation of right-lateral movement along the San Andreas fault has played a significant role in developing California's landscape. The Sacramento and San Joaquin River Valleys, collectively known as the Great or Central Valley, continue to amass sediments by draining the northern and southern portions of the Sierra Nevada Mountains, respectively. Active subduction and back-arc volcanism still continues north of the Mendocino Triple Junction and is expressed as the Cascade Range, which spans from Washington and Oregon down to Northern California, with terminating in the south at Sutter Buttes. There is also evidence for active transpression throughout the Coast Ranges (Jones, *et al.*, 1994a).

This scenario is further complicated by the divergent relative plate motions along the Gulf of California and Salton Trough at the southern end of the San Andreas System, and throughout the Basin and Range. Crustal extension, which began as subduction near the continental margin, was replaced by transform movement on the proto-San Andreas fault system. Microseismicity studies using the dense short period arrays (Hill, *et al.*, 1990; Eaton, 1989) show that the result of these different stress regimes is quite varied. For example, strike-slip motion in the Coast Ranges is mostly confined to a few major faults in the fault system (i.e. San Andreas, Hayward, Calaveras, etc.), whereas the primarily divergent motion in the Basin and Range is distributed over a wide area.

Evidence at the surface of the earth provides us with some information about the past, but earth scientists are still in the dark over what our geological history means for the present state of the crust and upper mantle in this region. Some of the answers lie in ascertaining the structure of the earth at depth. For example, is there any residual of a subducting slab at the present time? Is there a velocity contrast associated with the San Andreas Fault at depth? Does a "slab window" caused by the instability of the Mendocino Triple Junction exist? Is there any evidence of a Sierran root or a crustal detachment near the plate margin? What is the structure of the
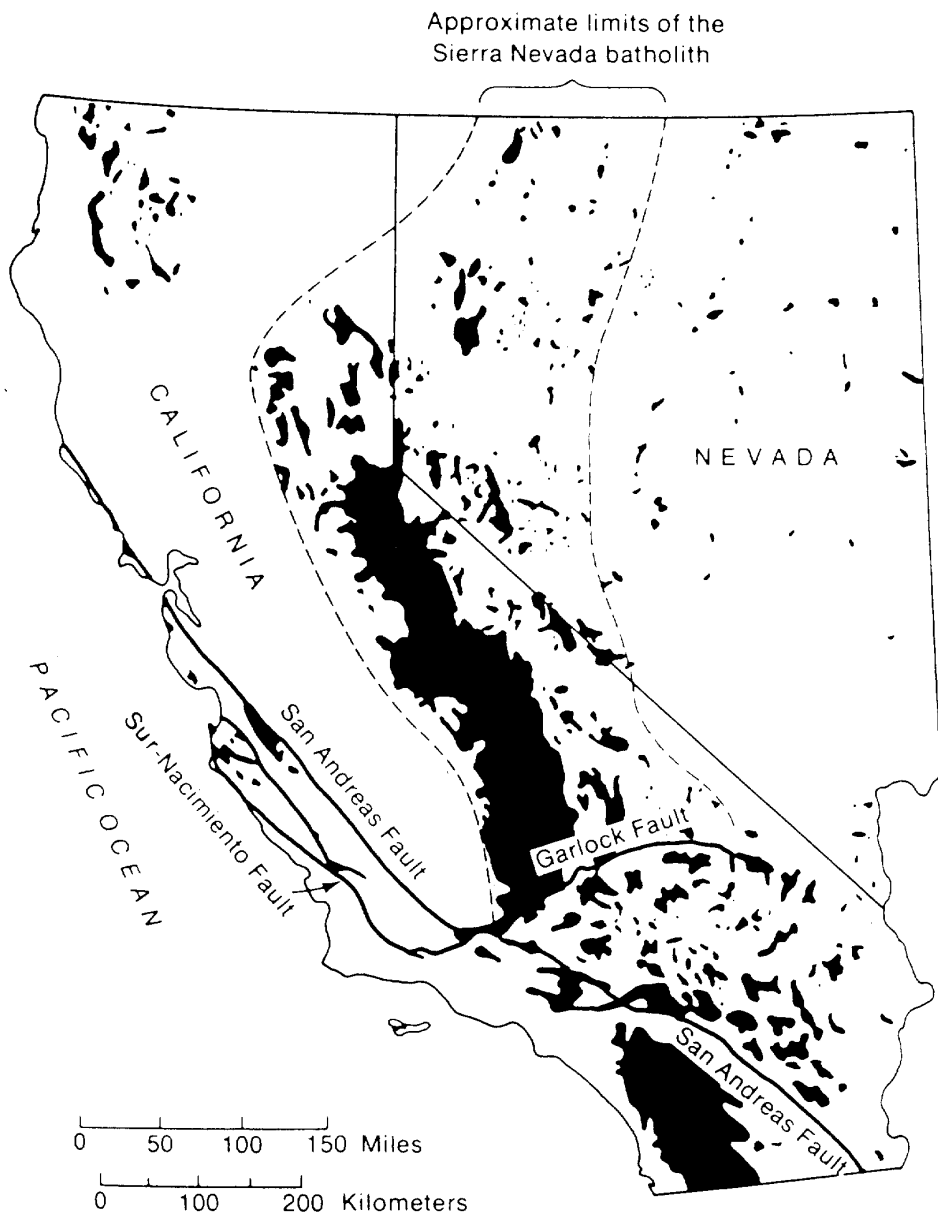
Figure 1.5: Granitic rocks in the Sierra Nevada batholith (Norris and Webb, 1990).

earth beneath volcanically active areas, such as the Cascades, Mammoth Lakes, and the Geysers/Clear Lake region? More generally, what do the current seismotectonics tell us about the tectonics of the past? It is hoped that by putting constraints on the structure of the crust and upper mantle, the seismic data can help to answer some of these questions.

## 1.3    Outline

Both the technical and geological motivations described above have driven and enabled the research of this dissertation. Chapter 2 covers the regional surface wave moment tensor method which has been successfully applied to regional earthquakes as the broadband network has gone on-line. The method is described, examples are given, and comparisons with other methods of obtaining focal mechanisms are made. Also covered are automation of the moment tensor procedures, velocity calibrations, and testing of the methodology.

Chapter 3 contains the compilation of moment tensor solutions obtained using the regional surface wave method. The systematic cataloguing of seismic moment tensors for northern and central California, which has been underway for over four years, can yield a valuable tool for understanding the tectonics of this active plate boundary zone. Additional sections describe particularly active or interesting regions in order to highlight some of the details. Next, the moment tensors are used to infer something about the stress regime in the crust. Finally, earthquake sequences, which have been studied in detail using moment tensors and other methods, are discussed.

Chapter 4 covers the efforts to investigate the structure of this region through the use of surface waves. Sections describe the phase velocity inversion method that is utilized, as well as show the inversion results and their interpretation. The phase velocities are, in turn, inverted in order to obtain layered velocity models for the region. The results are compiled to show maps and cross-sections of the substructure. Comparisons are made with other studies, detailing some similarities and differences, and attempts are made to answer some of the questions pertaining to California tectonics.

Finally, chapter 5 is a summary of the dissertation which reiterates the major conclusions, and presents a number of research directions that could be pursued in

the future.

# Chapter 2

# Regional Moment Tensors

Seismic moment tensors currently represent one of the most fundamental parameters to describe an earthquake source, on the same level as the origin time, location, and earthquake size. Moment tensors are the most general description of an earthquake point source, and provide a base level to study additional complexities, such as the source time function, non-uniform slip distribution, and directivity. Usually represented as "beachballs", moment tensors yield information about both the source strength and fault orientation of an earthquake.

A common approach to describing a seismic source is to approximate it by a model of equivalent forces, which produce identical displacements at the earth's surface. Furthermore, the approximation is often made that the seismic source has a small dimension compared to the wavelength of interest. This is known as the point source approximation. Moment tensors completely describe, in a first order approximation, the equivalent forces of general seismic point sources, which include slip on a fault surface, volume increases or decreases (due to explosions or phase transitions), and crack openings (Jost and Herrmann, 1989).

For three components of force and three possible arm directions, there are a total of nine (or 3×3) generalized couples needed to completely describe the moment tensor (Aki and Richards, 1980). In an isotropic medium the components of the moment tensor are given by

$$M_{kj} = \mu\, A \left( u_k \nu_j + u_j \nu_k \right) \tag{2.1}$$

where $\mu$ is the shear modulus, A is the area of the fault plane, $\mathbf{u}$ is the slip vector, and $\nu$ is the vector normal to the fault plane. Since M is symmetric and there are only 6

independent components to the tensor, the vectors **u** and · can be interchanged without affecting the displacement field, resulting in the inherent ambiguity of the fault plane. The seismic scalar moment is given by $M_o = \mu A \overline{u}$, and is usually expressed in units of dyne-cm or N-m.

Structure is characterized by Green's functions which are the displacement fields due to a unidirectional unit impulse. In other words, the Green's function describes at point x the displacement due to a unit force applied at point y. From symmetry, however, the same Green's function also describes displacement at point y due to a force at point x. In this form, the displacement at the free surface from a point source can be expressed as the combination of moment tensor elements (which describe the point source) and the Green's functions (which describe the structure). The representation theorem for seismic source simply becomes

$$d_n(\mathbf{x}, t) = M_{kj} \left[ G_{nk,j} * s(\overline{t}) \right] \tag{2.2}$$

where $d_n$ is the displacement in the n direction, $M_{kj}$ an element of the moment tensor, $G_{nk,j}$ is the partial derivative of the Green's function with respect to j, and $s(\overline{t})$ is the source time function for a synchronous source. More complicated source time functions than a delta function can be produced by convolving the time function with the Green's function.

## 2.1 Regional Surface Wave Moment Tensor Inversion

While the routine estimation of moment tensors for earthquakes worldwide has been underway for many years (CMT; Dziewonski, *et al.*, 1981), they have been limited for the most part to large global events (M > 5.5). Large earthquakes generate long period waves (~300 sec) which can be recorded at distant teleseismic stations and whose propagation is well-approximated by a spherically symmetric earth. Smaller earthquakes, however, only generate shorter period waves and are only recorded with good signal-to-noise ratio by closer local and regional stations. At these shorter periods, a three-dimensional velocity model is needed to account for complex smaller scale earth structure in the crust and uppermost mantle.

For the most part, then, information about faulting for smaller earthquakes has come from first motion mechanisms. Computer programs which determine fault plane solutions from first motions, such as the FPFIT program developed by researchers at the USGS Menlo Park (Reasenberg and Oppenheimer, 1985), have done a good job at making this a routine operation. Figure 2.1 shows an example for a well-covered event within the network. The fault plane and the auxiliary plane separate regions of dilatation and compression. As will be discussed later on, however, first motion mechanisms provide more limited information than moment tensor solutions. Only for a limited number of larger California earthquakes have moment tensors routinely been calculated from the global networks. For example, over the three year time period from January 1993 through December 1995, only fourteen Harvard CMT solutions were calculated in California and its vicinity.

It is clear that there has been a need for the routine estimation of moment tensor solutions for moderate size regional earthquakes. With the emergence of broadband networks in Northern California and other areas, it has been possible to pursue this. Moment tensor methods can utilize a number of particular parts of the waveform, depending on the type of Green's functions that are used. Since surface waves dominate the seismograms of regional earthquakes recorded at the broadband stations (figure 2.2), they are a natural choice to use for calculating moment tensors. In comparison, over the same time period there have been over 150 moment tensor solutions determined using this regional method. Although body waveform inversions might potentially yield more detailed information on the source process (Dreger and Helmberger, 1991), fundamental mode surface waves are particularly well suited for quasi-real time estimation of seismic moment, source mechanism, and centroid depth, given an initial epicentral location (e.g. Thio and Kanamori, 1991; Giardini, 1992).

This section describes the procedure that has been developed at UC Berkeley and illustrates its application to several recent sizeable events in Northern and Central California. The regional surface wave moment tensor inversion has been adapted from a two-step moment tensor inversion developed for teleseismic surface waves at intermediate periods (Romanowicz, 1982), and then extended to the case of mantle waves for the study of large global earthquakes (Romanowicz and Guillemant, 1984; Romanowicz and Monfret, 1986). Other studies (Patton and Zandt, 1991) have applied these techniques to estimate the source parameters for moderate size earthquakes in

950922 16:06 18.10
36–48.91 121–12.19
DEPTH = 7.44 KM
MAG = 4.10 C

RMS = 0.10 S
DMIN = 9 KM
AZM GAP = 37
# FM = 119

ERH = 0.2 KM
ERZ = 0.4 KM
MISFIT = 0.03 (+.03)
STDR = 0.67

STRIKE UNCERTAINTY = 5
DIP UNCERTAINTY = 18
RAKE UNCERTAINTY = 35
% MACHINE PICKS = 0

320,90,180

50,90,0

| DISCREPANT OBSERVATIONS | | | |
|---|---|---|---|
| STAT | DIST | AZM | AIN | PRMK |
| BEMM | 20 | 150 | 102 | EPU2 |
| HFEM | 26 | 317 | 97 | IPD0 |
| BBGM | 30 | 150 | 94 | IPU0 |
| BPCM | 46 | 235 | 88 | IPD1 |
| PHRM | 60 | 144 | 84 | IPU0 |
| CVLL | 106 | 329 | 57 | EPU2 |
| CGPM | 117 | 323 | 57 | EPU1 |
| JBGM | 117 | 301 | 57 | EPD2 |
| CBSM | 118 | 341 | 57 | EPU2 |
| CMOM | 123 | 335 | 55 | EPU2 |

Tue Feb 20 09:57:02 1996
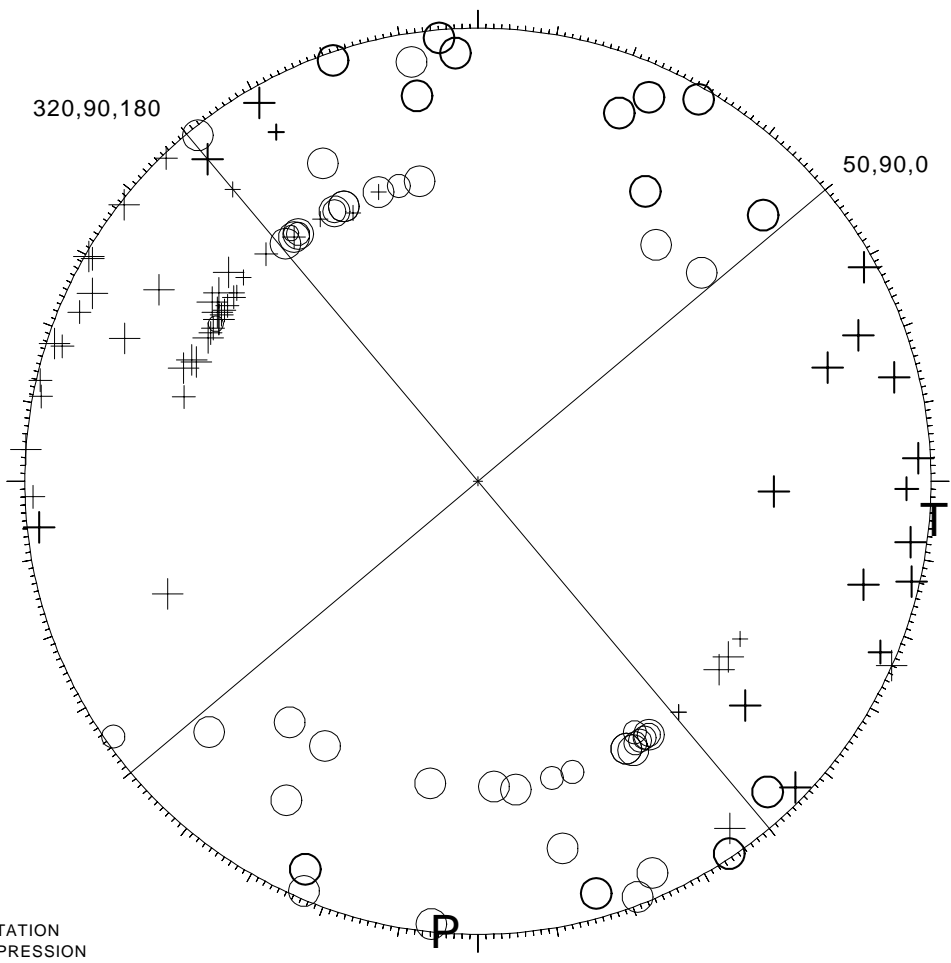
UP DWN
O  ○  DILATATION
+  +  COMPRESSION
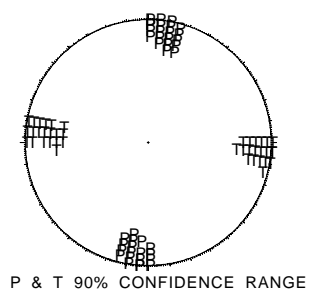
P & T 90% CONFIDENCE RANGE

m.arc

Figure 2.1: Example of a first motion mechanism for the M 4.1 09/22/95 event near Tres Pinos (Oppenheimer, personal communication).

17
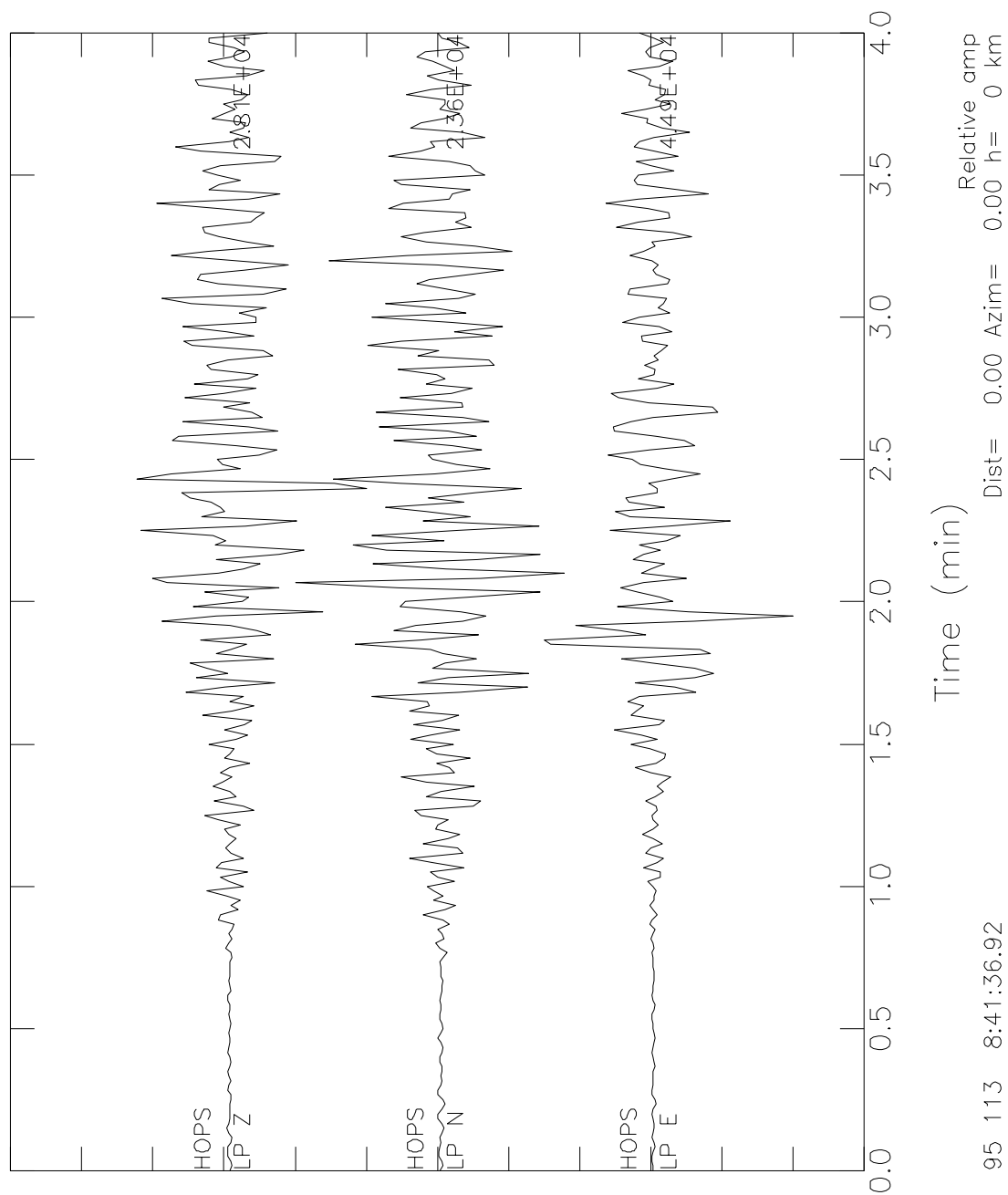
Figure 2.2: Surface waves recorded at a regional broadband station for a M5.0 event near The Pinnacles, CA. The waveforms are long-period, three-component data recorded at station HOPS (Hopland, CA). The traces are unfiltered.

the Western United States.

While the moment tensor inversion itself is a relatively straightforward procedure, its application to a particular region depends upon the accurate calibration of the local velocity structure to account for the lateral heterogeneity. Early on, considerable effort was made in comparing the dispersion curves of earthquakes with a source mechanism known from global methods (i.e. CMTs). The result was a regionalization of phase velocity corrections. A general description of the regional surface wave method is given here and more detailed discussion on path calibration will be given later on.

## 2.1.1  Background

The signal recorded at any particular station will be a function of several different operators, notably the source, propagation, and instrument. These operators are convolutions in the time-domain and, hence, are simply multiplications in the frequency-domain. Hence, the observed spectrum can be written as

$$U(r, \theta, \omega) = U_s(\theta, \omega) \, U_p(r, \theta, \omega) \, U_i(\omega) \qquad (2.3)$$

where $U_s$ is the source term, $U_p$ is the propagation term or Green's function, and $U_i$ is the instrument response term.

Since the goal is to determine the source term $U_s$, the other terms $U_p$ and $U_i$ must be accounted for in the process. $U_p$ is the Green's function and this term includes the wave propagation, geometrical spreading, and attenuation terms. In the case of surface waves, the propagation term is a function of the distance and phase velocity. As the name implies, this term keeps track of a wave being in or out of phase at a particular frequency. Geometrical spreading in the case of surface waves is simply the $1/\sqrt{r}$ loss of amplitude with increasing epicentral distance. Attenuation results from the loss of energy for waves travelling in anelastic media.

Finally, the ground motion is filtered by the instrument. The instrument term $U_i$, also referred to as the instrument transfer function, is known and must be removed. A short period instrument such as a Wood-Anderson seismometer would effectively only record the short period motion of the ground, whereas a long period instrument such as a Benioff seismometer would only allow long periods through. Fortunately,

as explained in section 1.1, broadband instruments record over a wide-range of frequencies, allowing an almost constant transformation from the digital units of the instrument to ground motion over the periods of interest.

The remaining source term is comprised of the source spectrum and a source phase delay term.

$$U_s(\theta, \omega) = S(\theta, \omega) \exp(-i\omega\tau/2) \tag{2.4}$$

where $S$ is the source spectrum and $\tau$ is the source duration. The source spectrum $S$ is a function of both the moment tensor and the corresponding excitation functions. The source term that is associated with the Rayleigh waves ($S_r$) will be observed on the vertical and radial components, while the source term associated with the Love waves ($S_l$) will be observed on the transverse component. The Rayleigh and Love source terms can be written as follows:

$$
\begin{aligned}
S_r(\theta, \omega) &= -P_r(\omega, h) M_{xy} \sin 2\theta + \frac{1}{2} P_r(\omega, h)(M_{yy} - M_{xx}) \cos 2\theta + \frac{1}{2} S_r(\omega, h) M_{zz} \\
&\quad + i\, Q_r(\omega, h) M_{xz} \sin\theta + i\, Q_r(\omega, h) M_{yz} \cos\theta \tag{2.5} \\
S_l(\theta, \omega) &= -\frac{1}{2} P_l(\omega, h)(M_{yy} - M_{xx}) \sin 2\theta - P_l(\omega, h) M_{xy} \cos 2\theta \\
&\quad - i\, Q_l(\omega, h) M_{xz} \sin\theta + i\, Q_l(\omega, h) M_{yz} \cos\theta \tag{2.6}
\end{aligned}
$$

The excitation functions for the Rayleigh waves $P_r$, $S_r$, and $Q_r$ and Love waves $P_l$ and $Q_l$ are described in Kanamori and Cipar [1974]. They are functions of both the frequency $\omega$ and source depth $h$. Notice that the Love waves, in and of themselves, do not contain enough information to solve for all the moment tensor components (since $M_{zz}$ is missing).

## 2.1.2  Method

The regional surface wave method (schematically represented in figure 2.3) consists of a number of steps (i.e. data extraction, data processing, etc.) which are described in detail in this section. First, three-component data from each station is extracted for the time-period of the event. The data is either extracted in miniSEED format or, if available only in another format, converted to miniSEED. MiniSEED is an international standard format for the exchange of digital seismological data (SEED Reference Manual, 1993). The data is next rotated from a station reference frame (Z,N,E) into an earthquake reference frame (Z,R,T) in order to separate the Love

20

and Rayleigh waves on the horizontal components on to the transverse and radial components, respectively (figure 2.4). The SAPLING program (see Appendix C), which was developed to read and process mini-SEED data, is used to update the instrument and event information in the headers, demean the data, rotate the data, and write out the data in AH, the format used by the moment tensor code.

The rest of the processing in performed with SMTINV (see Appendix C), the surface-wave moment tensor inversion program. Windows of group velocity, which travel with the velocity of waves of a particular frequency, are used to select the appropriate portion of the time sequence. Since the moment tensor inversion method uses fundamental mode surface waves, the windows are chosen in order to extract the fundamental mode for the periods of interest while trying to cut out body waves and higher modes. The Rayleigh wave group velocity window ranges from a wide 4.2–1.8 km/s window for the closest stations used in the inversion to a narrow 3.5–2.5 km/s window for the furthest stations. Larger windows are needed for closer distances in order to insure an adequate time window to capture a minimum number of cycles of data. Love wave windows are taken as 0.5 km/s faster for the starting time and 0.3 km/s faster for the ending time. A cosine taper is used to emphasize data in the center portion of the window and deemphasize data at the edges.

The data is then transformed to the spectral domain using a Fast Fourier Transform (figure 2.5). Depending on the size of the event, different periods are selected for the moment tensor inversion. In practice, for moderate-sized events (M < 5.5), a range of periods are chosen between 15 and 45 seconds, and larger events (M $\geq$ 5.5), from 25 to 75 seconds. The spectral data must now be corrected for propagation effects. This is accomplished by calculating the propagation term, which is a function of distance, average phase velocity, and average attenuation, and removing it in the frequency domain.

It follows from equation 2.4 that the source term can be corrected for the source phase delay in order to isolate the source spectrum, which is described in equations 2.5 and 2.6. In order to separate the $\theta$-dependent terms from these equations, it is useful to define azimuthal coefficients which are functions of $\omega$ for Rayleigh waves as:

$$A(\omega) = -P_r(\omega, h)M_{xy} \tag{2.7}$$

$$B(\omega) = \frac{1}{2}P_r(\omega, h)(M_{yy} - M_{xx}) \tag{2.8}$$

# Inversion Flowchart

- Extract Data
- Rotate

↓

- Take group velocity window
- Calculate spectra

↓

- Calculate and remove
  propagation term

↓

- Select station/components and
  periods
- Invert for moment tensor, source
  duration, and centroid depth

↓

- Assess solution
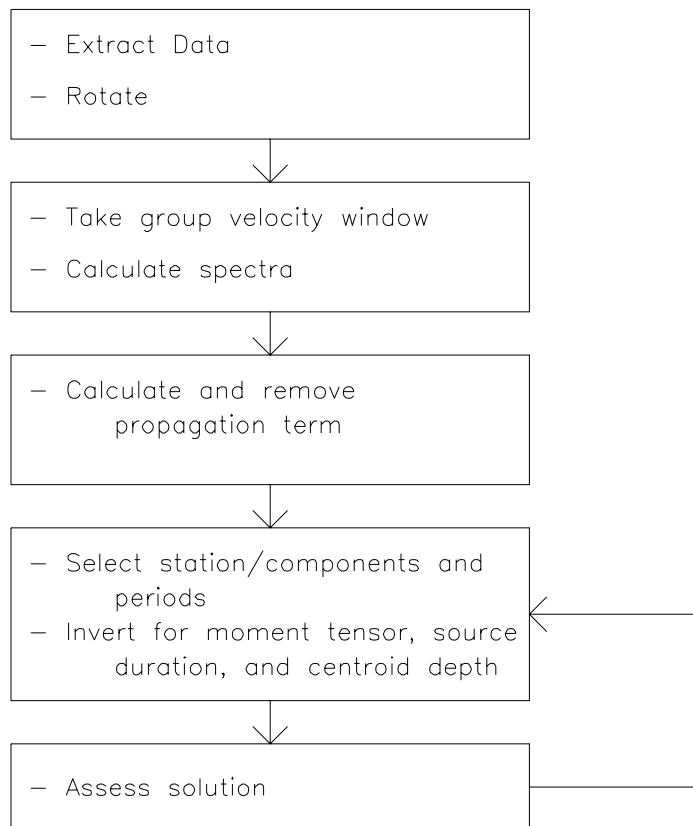
Figure 2.3: Schematic Representation of Regional Surface Wave Method.
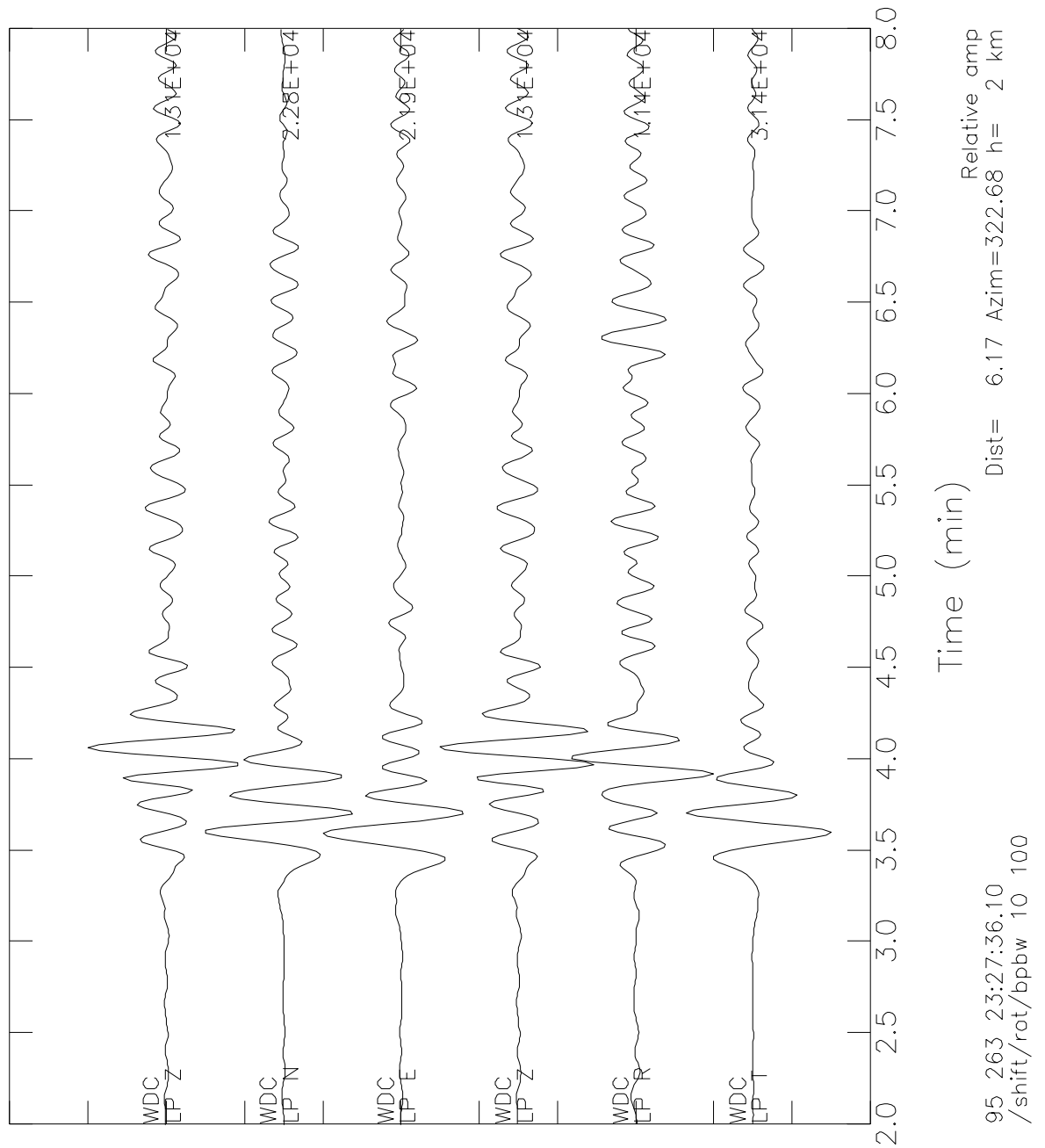
Figure 2.4: Three-component data for the 09/20/95 Ridgecrest earthquake at WDC (Whiskeytown) station before (upper triplet) and after (lower triplet) rotation. The waveform has been filtered between 10 and 100 seconds. Notice the isolation of the Love wave from the N and E components to the T component, and the retrograde motion of the Rayleigh wave on the Z and R components.
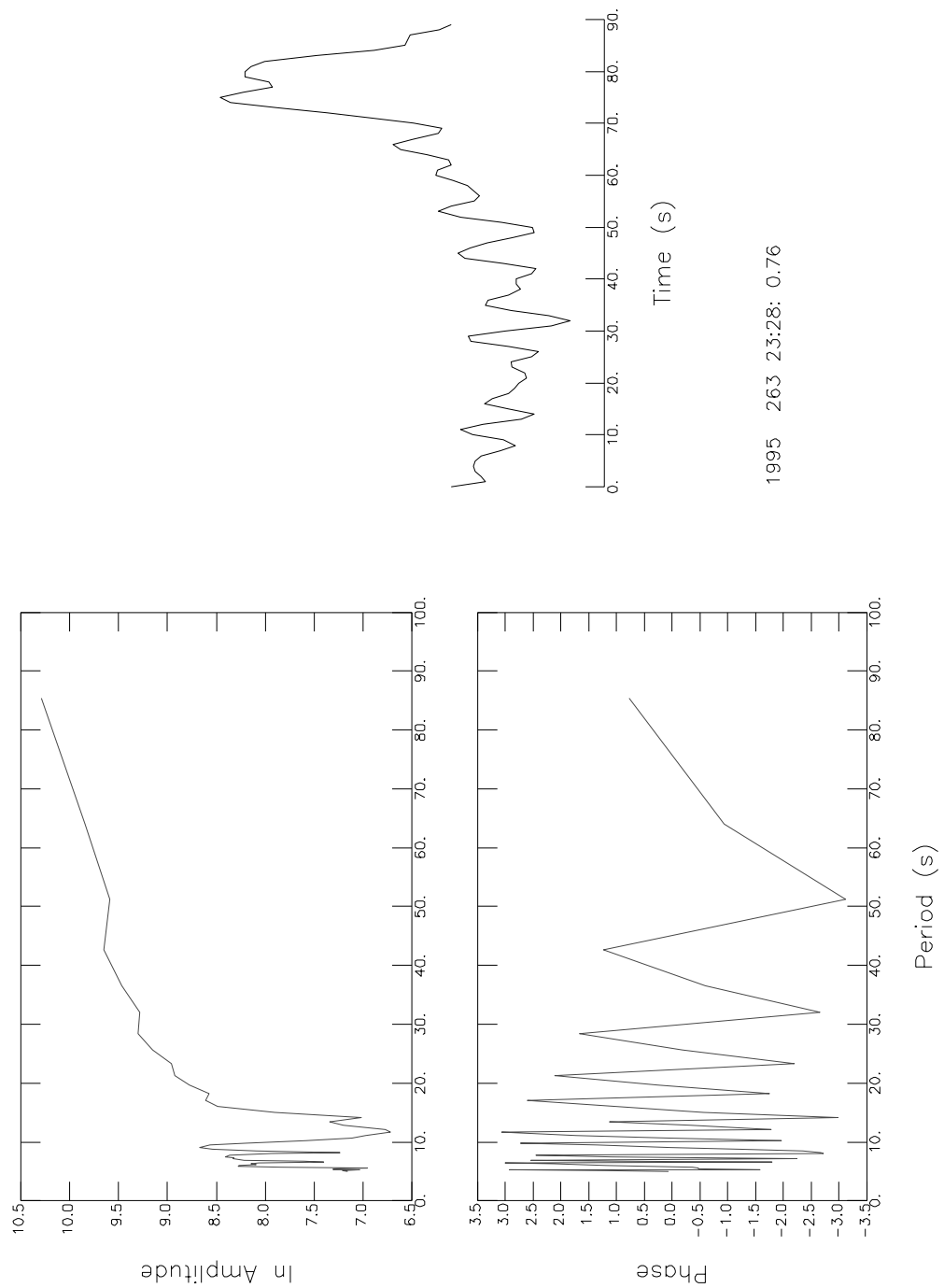
Figure 2.5: Displacement spectrum for the vertical component of the same event in the previous figure for a group velocity window of 3.8 to 2.2 km/s. The spectrum is relatively flat in amplitude over the 15 to 45 second period range. Holes in the Rayleigh wave spectra (as shown here) are sensitive to source depth. Displacement time series (unfiltered) for the group velocity window is shown to the right.

$$C(\omega) = \frac{1}{2}S_r(\omega, h)M_{zz} \tag{2.9}$$

$$D(\omega) = Q_r(\omega, h)M_{xz} \tag{2.10}$$

$$E(\omega) = Q_r(\omega, h)M_{yz} \tag{2.11}$$

and for Love waves as:

$$A'(\omega) = -\frac{1}{2}P_l(\omega, h)(M_{yy} - M_{xx}) \tag{2.12}$$

$$B'(\omega) = -P_l(\omega, h)M_{xy} \tag{2.13}$$

$$C'(\omega) = 0 \tag{2.14}$$

$$D'(\omega) = -Q_l(\omega, h)M_{xz} \tag{2.15}$$

$$E'(\omega) = Q_l(\omega, h)M_{yz} \tag{2.16}$$

where $P$, $Q$, and $S$ are the excitation functions calculated from a general velocity model appropriate for the region.

The source spectrum $S(\omega)$ can be decomposed into $\alpha$ and $\beta$, the real and imaginary parts of the source spectrum, respectively.

$$S(\theta, \omega) = U_s(\theta, \omega)\exp(i\omega\tau/2) = \alpha + i\beta \tag{2.17}$$

In turn, the real and imaginary terms can be expressed as functions of the azimuth from the source as follows:

$$\alpha(\theta, \omega) = A(\omega)\sin 2\theta + B(\omega)\cos 2\theta + C(\omega) \tag{2.18}$$

$$\beta(\theta, \omega) = D(\omega)\sin\theta + E(\omega)\cos\theta \tag{2.19}$$

where A, B, C, D, E are functions of $\omega$ and centroid depth $h$. It is assumed that all data outside of this functional form (constant, $\theta$, $2\theta$) is either station noise or unmodelled structure between the source and the receiver.

It is now possible to invert for the moment tensor using the two-step method described in Romanowicz and Monfret [1986]. In the first step of the inversion, one takes advantage of the simple azimuthal radiation pattern of earthquake sources to screen out unmodelled short wavelength variations of structure along source-station paths. Azimuthal coefficients are determined at a discrete set of frequencies by least square inversion of complex spectra, corrected for propagation using approximate elastic and anelastic models as described above. An estimate of half-duration of the

25

source is also computed in this step. Typically, the range of values for the source duration tau ($\tau$) is sampled every 0.5 seconds and runs from -2.0 to 3.0 seconds for small to moderate size events and from -2.0 to 5.0 seconds for the larger events. Negative source time durations are tested in order to account for any large errors in origin time.

In the second step, the azimuthal coefficients (A, B, C, etc.) are inverted at a series of trial depths to obtain estimates of the moment tensor $M$ and centroid depth $h$ using equations 2.7 and 2.12 (see Romanowicz and Monfret, 1986 for a detailed presentation). The advantage of this method over more conventional moment tensor inversions (e.g. Mendiguren, 1977; Patton, 1980; Kanamori and Given, 1981) is that individual propagation effects need not be known with as great a precision. However, source azimuthal coverage around the epicenter must be available to resolve the components of the radiation pattern. Typically, depth is sampled every 2 km from 4 km down to 20 km depth for events in California. If there is reason to believe that the event is deeper (i.e. centroid depth bottoming out at 20 km, very deep hypocentral depth), the trial depths are extended by sampling every 5 km.

Functions $P$, $Q$, and $S$ are the excitation functions calculated from a general velocity model which is appropriate for the region. The excitation functions of both Rayleigh and Love waves for a particular velocity model are shown in figure 2.6. Each line in the figures represent the excitation function at a particular depth sampled every 2 km from 4 km to 20 km. Notice the zero crossings for the Rayleigh wave functions $P$ and $S$ at short periods, which provide very effective ways of determining the source depth. In particular, the zero crossing for the $S_r$ excitation function spans a period range from 15 to 35 seconds, and therefore, the period of the null in the $C$ azimuthal function provides excellent depth resolution. Also note that at the surface both $Q_r$ and $Q_l$ start approaching zero for all periods. As the excitation functions near zero, division of the functions become unstable, and potential problems can exist in the determination of $M_{xz}$ and $M_{yz}$.

### 2.1.3   Discussion

The application to the regional case presents some important differences with the global case. In the global case, and for large earthquakes, the inversion relies on very
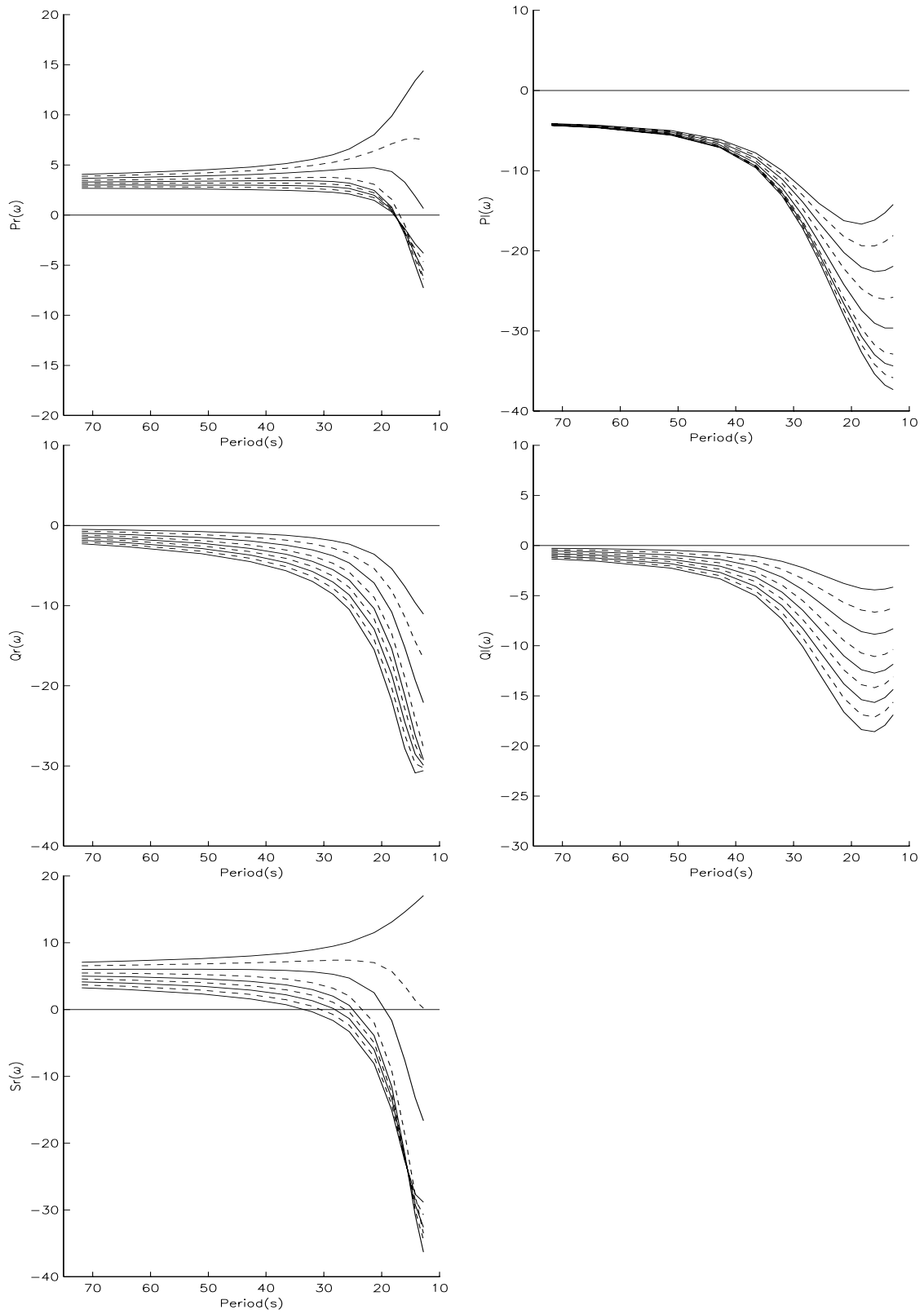
Figure 2.6: Excitation functions for the second step of the moment tensor inversion. First column shows those for Rayleigh waves; second column those for Love waves. Each line represents a different depth every 2 km between 4 and 20 km depth.

long period mantle waves ($\sim$200 sec) for which propagation effects are well approximated by using a spherically symmetric earth model since they sample the deeper part of the upper mantle which has relatively small lateral variations of structure. In the regional case, the inversion is limited to much shorter period waves (15–45 sec for most cases), first, because the most frequent moderate earthquakes of interest ($M_L \sim$ 3–5) do not excite much mantle wave energy, but also because of theoretical limitations due to the short distances ($\sim$50–400 km) travelled by the waves. Proper calibration of velocity variations is therefore essential.

One clear advantage of using shorter period data, which was alluded to earlier, is better depth resolution since the depth signature in the fundamental mode spectra of shallow earthquakes is largest in the period range 15–50 seconds (Tsai and Aki, 1971). The disadvantage, however, is somewhat greater sensitivity to the earth model used for propagation corrections. The shorter distance also implies that waves are not well dispersed and some caution has to be taken against contamination by body waves and higher modes; this limits the period range of study at the short period end and the distance range to distances greater than 50 km.

The global inversion yields reliable results using vertical component data only. In the regional case, both Love and Rayleigh wave (three component) data is used to compensate for a lack of azimuthal distribution that often exists in regional problems. Including Love waves also provides redundancy which can prevent cases where noisy data contaminate the source radiation pattern, a situation much more likely for smaller earthquakes. A laterally homogeneous medium for propagation corrections is initially used. The starting phase velocity model that has been developed is a modification of a Western U.S. crust and upper mantle model determined by Cara [1979] using higher mode surface waves [table 2.1]. The starting Q model is the PREM model (Dziewonski and Anderson, 1981). Both have been modified to better represent the California crustal structure. Comparisons of the phase velocity dispersion curves between the data and the starting model has allowed the progressive fine-tuning of models for a number of regions, each reflecting a particular tectonic regime (i.e. Coast Ranges, Great Valley, etc.). These regional path corrections have been incorporated as they have become available.

The preceding section illustrated a straightforward adaptation of a two-step moment tensor inversion to the regional case and its successful application to recent

Table 2.1: Western United States Velocity Model [Cara, 1979].

| WESTERN UNITED STATES | | |
|---|---|---|
| Depth | P-velocity | S-velocity |
| (km) | (km/s) | (km/s) |
| 2.50 | 4.00 | 2.00 |
| 23.50 | 6.15 | 3.60 |
| 42.50 | 6.70 | 3.79 |
| 0.00 | 7.80 | 4.40 |

The values are depth to bottom of layer, P-wave velocity, and S-wave velocity
respectively. Zero depth indicates upper mantle velocities.

earthquakes. Other sections in this chapter will discuss the advantages of the regional
moment tensor solutions over first motion mechanisms, and compare the moment
magnitude with other estimates of magnitude (including other moment magnitudes).

To further improve the results and allow the implementation of this method as
a routine quasi-real time procedure, the crustal models used for propagation correc-
tions must be fine tuned. This can be achieved as data from earthquakes accumulate,
through the comparison of solutions obtained using different methods. In the process,
detailed information about regional earth structure can be obtained. The develop-
ment of various velocity models is covered in the next section, while the inversion for
earth structure is developed later on in sections 4.1 and 4.2.

With accurate velocity models and robust moment tensor procedures, it should
be possible to develop a fully automated version of this method as part of the alarm
response at UC Berkeley, following the steps now proven successful in the global CMT
inversions (Ekström, 1992). This is covered in the section on automation and real-time
determination of moment tensors. Finally, a series of tests are performed to determine
the sensitivity of the moment tensor method to changes in various parameters used
in the inversion, including velocity and attenuation models.

## 2.1.4   Examples

Moment tensor solutions have been determined for hundreds of recent earthquakes
that have occurred in northern and central California. The following chapter has

maps of all of the events computed using this method and tables of the source parameters, as well as some interpretation of the seismicity and tectonics. A wide range of magnitudes and variety of mechanisms have been determined, although, as would be expected, the majority of events in northern and central California exhibit strike-slip mechanisms. However, in order to provide a sense of the inversion method, a few examples are shown for some of the earliest events calculated using this method and compared to solutions from other moment tensor methods.

The first example is for an event on 19 September 1992, located in the Geysers Geothermal Area. Figure 2.7 shows the fit to the Geysers data in amplitude and phase for a particular period (25.6 sec) and component (Z) compared to a preliminary solution obtained from a single station time domain body wave inversion (Dreger and Helmberger, 1993). Figure 2.7 also shows the mechanisms and the residual versus depth curve, indicating a shallow event ($\leq$ 4 km) consistent with the USGS depth of 3.4 km. The mechanisms obtained by the two methods are in agreement, although the moment obtained here gives a better fit to the amplitude data. Since there is no distinct residual minimum at shallow depths, a search performed at other reasonable depths (2–6 km) shows only a minimal change in the solution, varying by only about $5^o$ in strike and dip and 30% change in seismic moment.

Figure 2.8 shows the inversion results for a large earthquake on the Calaveras Fault in Gilroy on 16 January 1993. The inversion is performed using data from both the BDSN and TERRAscope (Kanamori and Hauksson, 1991) networks, in order to achieve good azimuthal coverage. In this case, the transverse component is shown to illustrate the Love waves. A depth of 8 km and a moment magnitude of 5.0 has been determined using this technique. The depth is consistent with a USGS depth of 7.9 km. The comparison solution is obtained using a near field waveform inversion (Uhrhammer, personal communication). The mechanism and seismic scalar moment obtained by both techniques are in good agreement with each other and the strike of the Calaveras Fault, with only a slight deviation in the rake of the fault plane.

The final example is shown for an event which occurred on 4 April 1993, near the town of Parkfield. Since the event is located at the southern end of the BDSN network, both BDSN and TERRAscope data is used in the inversion. Figure 2.9 shows the vertical component (at 25.6 seconds) in order to illustrate the difference between the Love and Rayleigh wave radiation patterns for earthquakes with similar

30
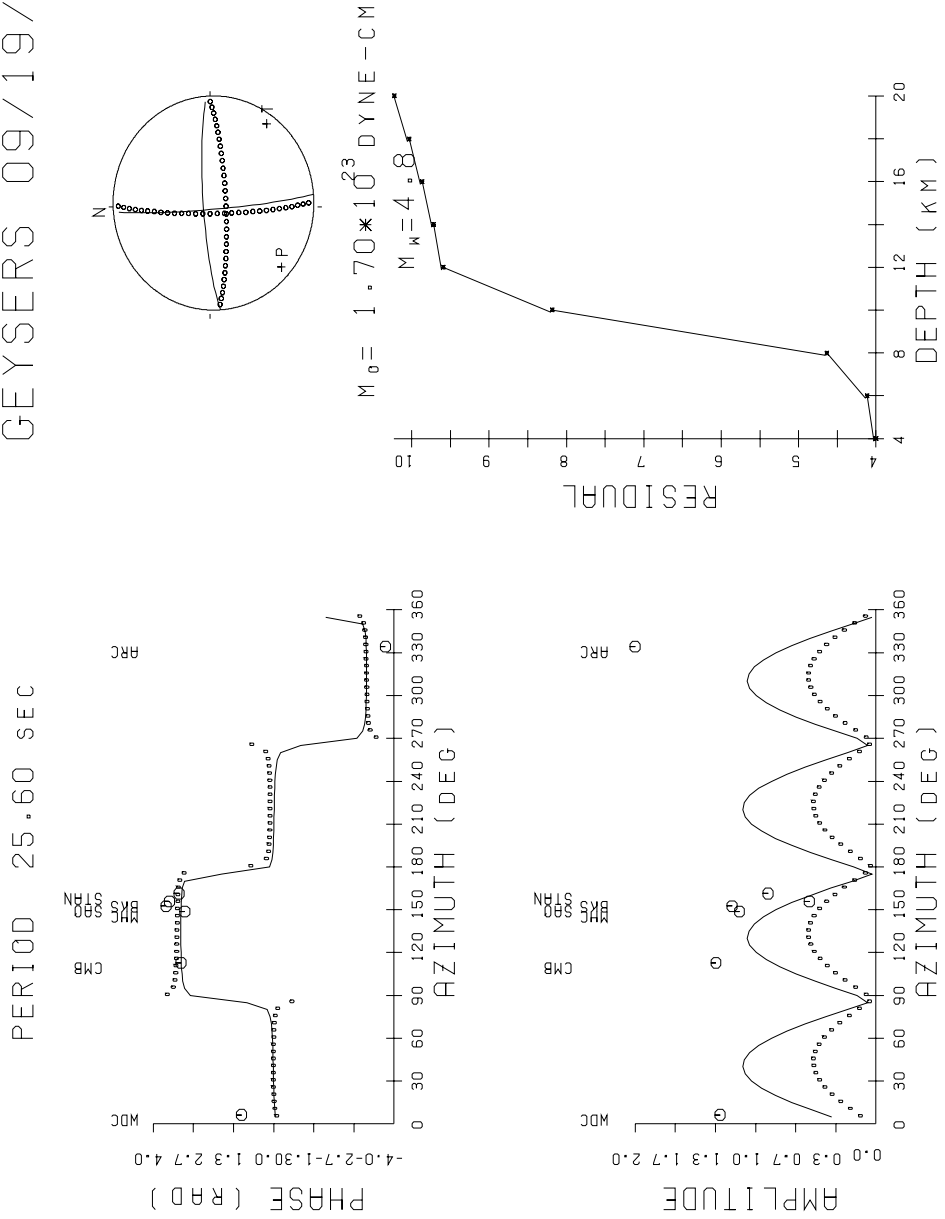
Figure 2.7: Source amplitude and phase as a function of azimuth for the Geysers event of September 19, 1992 for a particular component (Z) and frequency (25.6 sec). Data are shown by the large circles. Station name is given above each data point. The solid line indicates the solution obtained using regional surface waves. The small circles indicate the comparison solution. Also shown, the residual versus depth curve for the inversion along with the focal mechanisms for the various solutions.
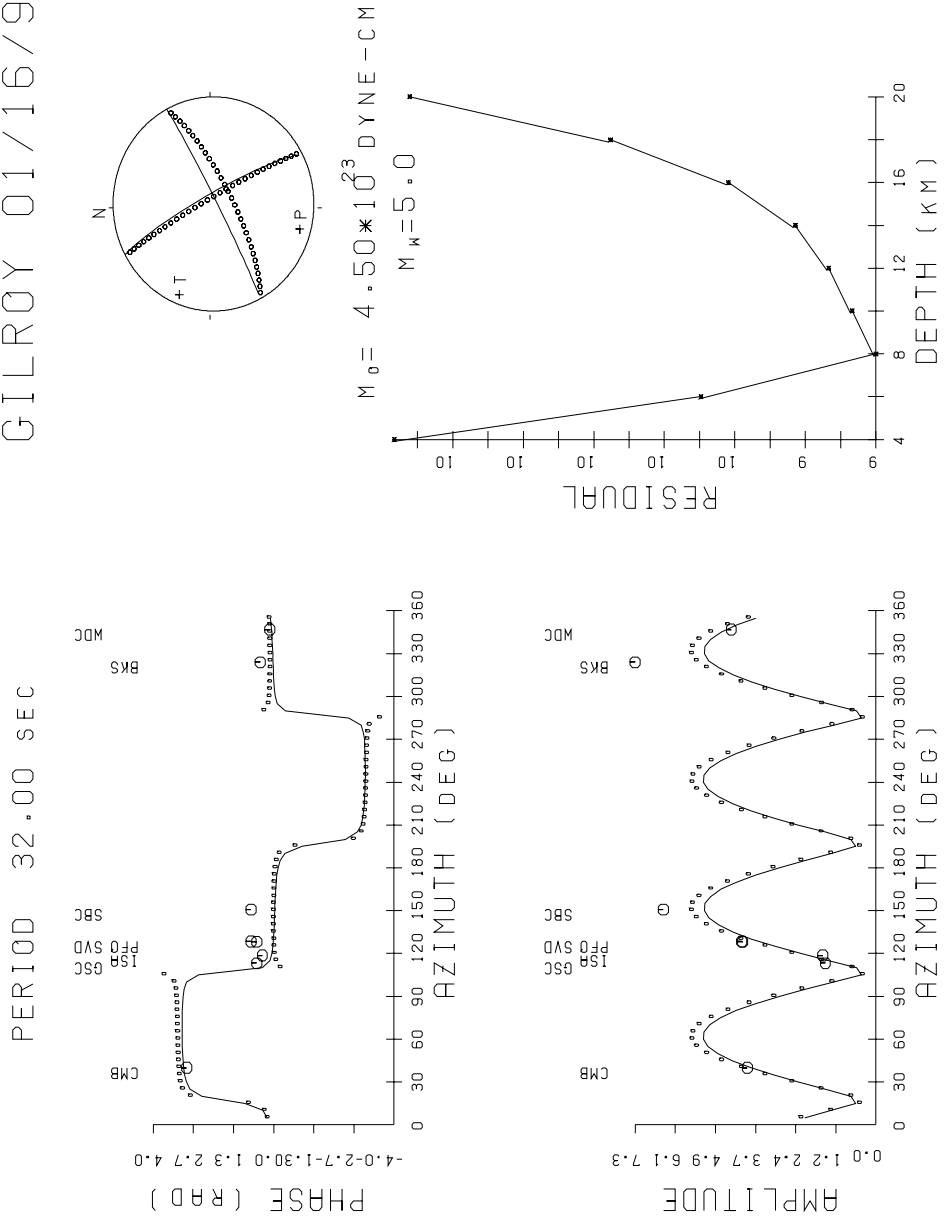
Figure 2.8: Same as figure 2.7 for the Gilroy event of January 16, 1993 (transverse component - 32.0 sec). The solid line indicates the solution obtained using regional surface waves.

32

focal mechanisms. In this case, nodes occur where there are maxima for the other wavetype, and vice versa. The phase behaves differently as well. For example, at the azimuth of the strike ($\sim 330$ degrees), the Rayleigh waves have a minimum and a phase shift, while the Love waves have a maximum and a constant phase. The comparison solution is that obtained using a near field waveform inversion (Uhrhammer, personal communication).

### 2.1.5 Comparison with First Motion Mechanisms

Calculating moment tensor solutions have several advantages over simply using focal mechanisms as determined from first motions. First, because moment tensors utilize the long period motion of the earthquake, they more accurately describe the complete motion of the earthquake than the first motions. First motions mechanisms are only looking at the initial slip of the source, which can be different than the overall motion of the earthquake. Secondly, moment tensors describe both the fault orientation and source strength of an earthquake. Unlike focal mechanisms, moment tensors provide an estimation of the size of the earthquake, through the calculation of moment magnitude $M_w$ from the seismic scalar moment $M_o$ (Hanks and Kanamori, 1979). In many respects, the moment magnitude is a more robust estimator of size than the traditional methods of estimating magnitude that are used along with the focal mechanisms (i.e. $M_L$, $M_d$, etc.). For one, $M_w$ is an estimator that accounts for the amplitude radiation patterns of source mechanisms. By taking into account the radiation pattern of the earthquake, the magnitude is not biased by the distribution of stations recording the earthquake, and hence provides a more accurate measure of the overall size of the event. Also, moment magnitude is an estimator of size that does not saturate for large earthquakes. Figure 2.10 shows the amplitude of various size earthquakes over a broad period range for two different source models. At the longest periods, where $M_o$ is measured, there is no decrease in the amplitude levels which represent saturation.

Additionally, first motion solutions are basically limited to double couple mechanisms for the source. Moment tensors completely describe, to first order, the equivalent forces of general seismic point sources (Jost and Herrmann, 1989). The general moment tensor can be decomposed into a double couple (representing a simple shear),
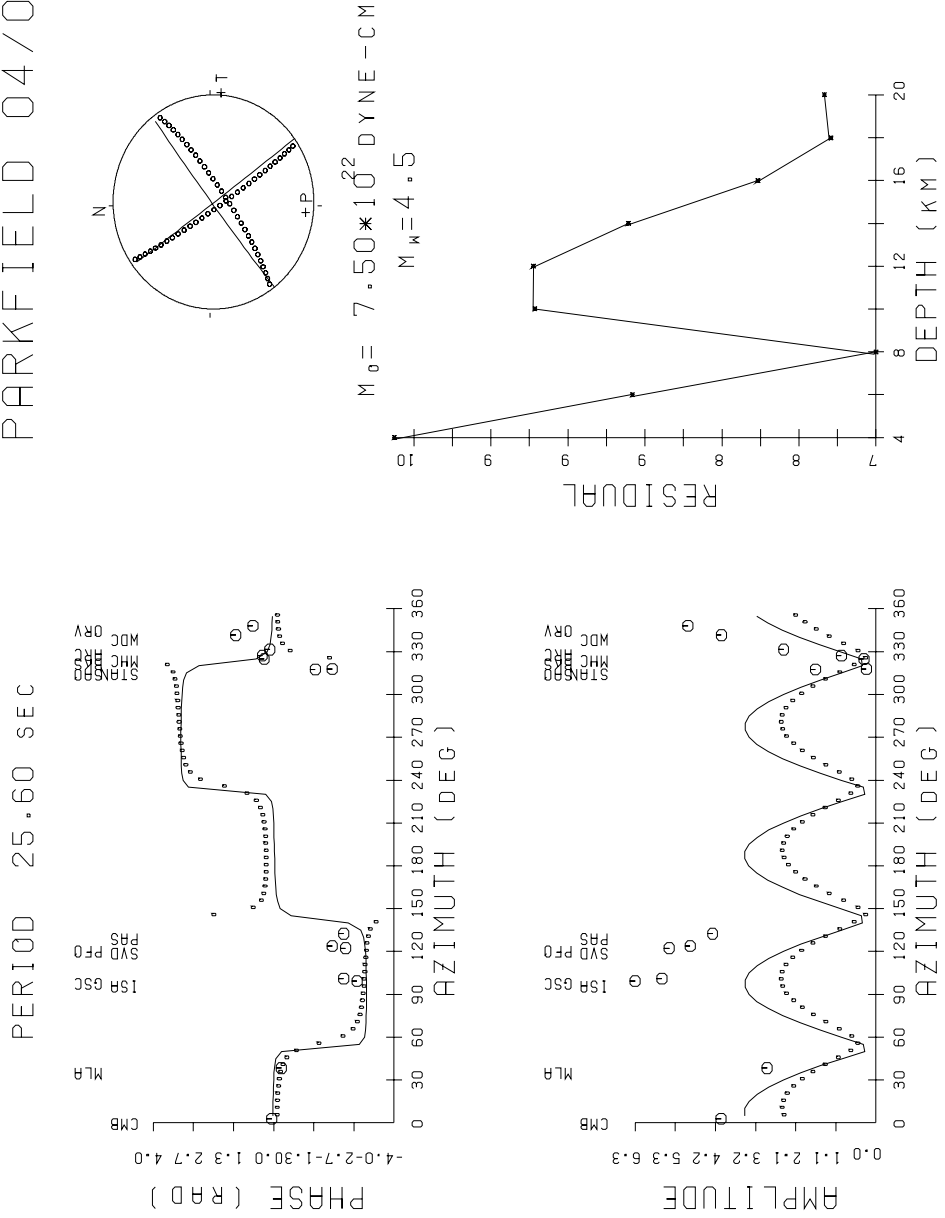
Figure 2.9: Same as figure 2.7 for the Parkfield event of April 4, 1993 (vertical component - 25.6 sec). The solid line indicates the solution obtained using regional surface waves.
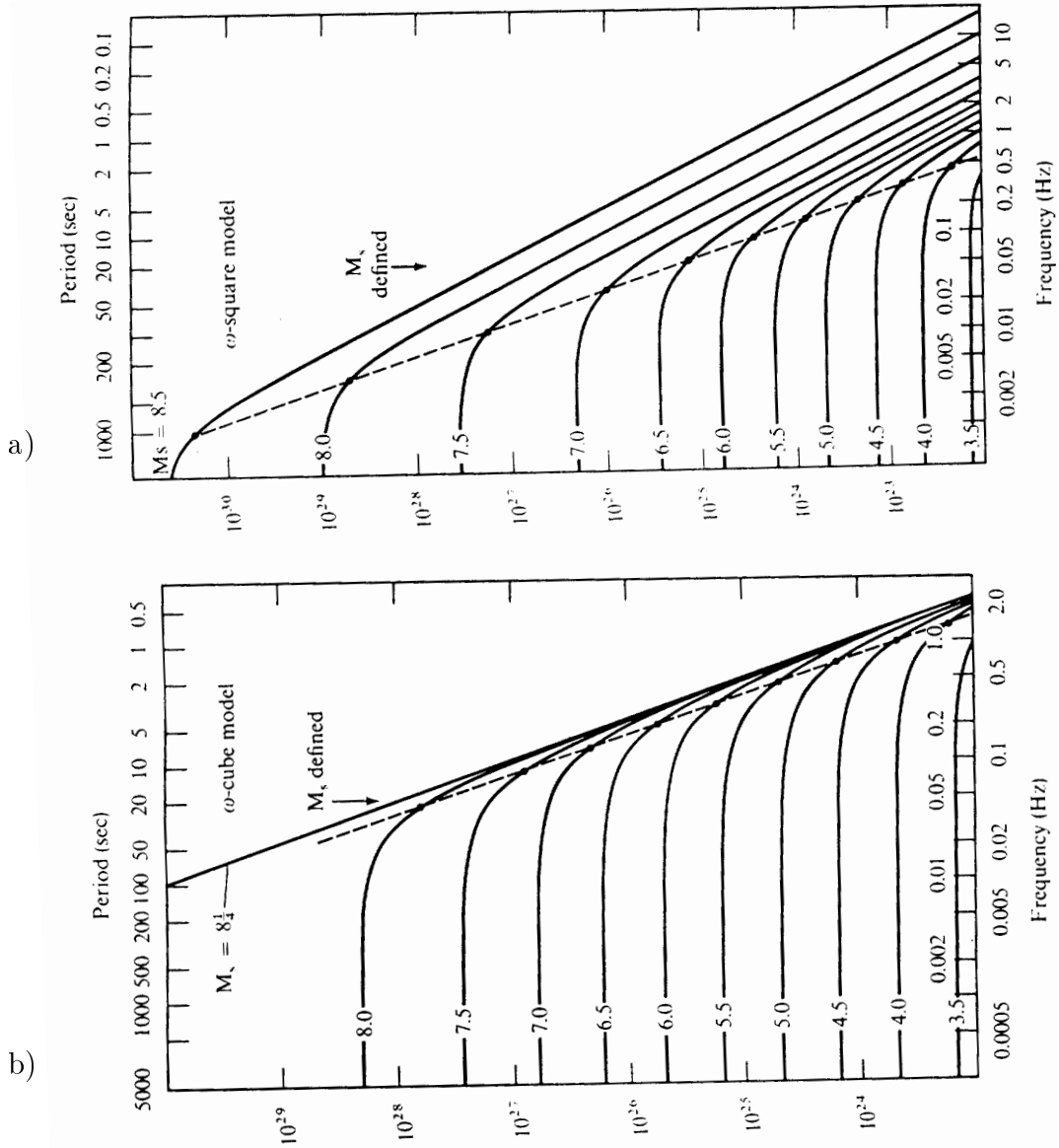
Figure 2.10: Spectra of far-field body wave displacements from earthquakes with different magnitudes for $\omega$-square (a) and $\omega$-cube models (b). Notice the saturation of $M_s$ for large earthquakes. From Aki & Richards [1980].

an isotropic component (representing a volume change), and a compensated linear vector dipole or CLVD (representing a dipole that is corrected for the effect of volume change). First motion solutions must assume a simple double couple source. In this general form, moment tensors allow for the possibility of crack openings and explosive or implosive sources. The former is of interest to those monitoring for fluid injection in volcanic areas or near faults; the latter is of interest in the nuclear discrimination problem. Since the $M_{xx}$ and $M_{yy}$ components cannot be separated in the equations for surface waves (see equations 2.7 and 2.12), in practice the constraint of no volume change is assumed in order to solve for these moment tensor elements individually. The presence of a large CLVD component would indicate a seismic source that is not a simple shear dislocation of a pure double couple source, although deviations from a pure double couple can also be due to the presence of noise in the data. Jost and Herrmann [1989] performed a series of moment tensor tests on synthetic data by adding noise. In the first four cases, pseudo-random noise of 0%, 14%, 28%, and 56% were added to the synthetics. In another case, the polarity of one of the stations was reversed. In the pseudo-noise case, the inversions performed admirably, with nearly the same double couple solution recovered in all cases. The percentage of non-double couple solution, however, went from 92% with no noise, to only 69% in the case of 56% noise. As velocity models improve, it is hoped that the existence of seismic sources that cannot be described by simple shear motion can be resolved.

The uncertainty estimates of moment tensor solutions also appear to be significantly lower than the uncertainties of focal mechanisms, which can often suffer from several nonunique solutions (Oppenheimer, 1986). It has been estimated that, without *a priori* knowing the mechanism of an earthquake, it would take about 60 optimally located short period stations to match the level of uncertainty of a moment tensor solution (Uhrhammer, personal communication). For the moment tensor solutions, estimates of uncertainties for each of the resolved elements of the inversion are available from the least squares calculation. The uncertainties in each of the moment tensor components can be propagated to determine the uncertainties of the angles of the focal mechanism and moment magnitude. In general, uncertainties are on the order of 10 degrees for the angles and around 0.3–0.5 of a magnitude unit. Of course, these only represent the formal uncertainties and do not reflect the additional uncertainties of the velocity model, for instance. These uncertainties are comparable to the

differences that we see between various methods of moment tensor determination. In general, however, they are much better than the estimates of uncertainty from first motion mechanisms.

Finally, the seismic scalar moment $M_o$ is a quantity easily related to other source parameters of interest (Kanamori and Anderson, 1975). For example, if a circular fault is assumed, then the moment is related to stress drop $\Delta\sigma$ and source radius a by $M_o = \frac{16}{7}\Delta\sigma a^3$. By estimating the source radius from the aftershock distribution, one can determine the stress drop from the seismic scalar moment. In this manner, the seismic scalar moment can be related to parameters such as slip, stress drop, source dimension, seismic energy, etc.

### 2.1.6    Comparison with Other Magnitudes

One advantage of moment tensor determination is that it provides a more robust estimate of earthquake size than other magnitude determinations (i.e. $M_L$, $M_S$, $m_b$, $M_d$) since the moment magnitude scale ($M_w$) is based directly on the radiated energy (Hanks and Kanamori, 1979). $M_w$ is related to the seismic moment $M_o$ (measured in dyne-cm) by the following equation:

$$M_w = \frac{2}{3}\,logM_o - 10.67 \qquad (2.20)$$

where $M_o = \mu Au$, $\mu$ is the shear modulus in dyne/cm$^2$, A is the area of the fault surface in cm$^2$, and u is the average fault slip in cm. Consequently, the values of $M_o$ are compared to those of local magnitude $M_L$ and coda duration magnitude $M_d$.

Local magnitude, of course, is the original magnitude scale that Richter developed in order to determine the size of earthquakes in southern California (Richter, 1935). The Richter scale was designed for the standard short-period torsion seismometer widely available at the time, the Wood-Anderson seismometer. Although these instruments are generally not in operation, the same procedure is used to compute the local magnitude today using synthetic Wood-Anderson responses calculated from broadband instruments. Duration magnitude has a more complicated history. Tsumara [1967] applied the concept of relating magnitude to duration for shallow events in Japan, and Lee, *et al.* [1972] to earthquakes in central California. Real and Teng [1973], in a study of duration and local magnitude in southern California, found that a quadratic function (instead of a linear one) was needed in order to relate

magnitude and duration for larger earthquakes. Herrmann [1975] implemented the same basic relation to earthquakes in the central United States. The current method for determining duration magnitudes in northern California are made using the procedure of Eaton [1992]. Site corrections were made for all of the stations in the NCSN and compared to UC Berkeley $M_L$.

Figures showing the regressions between moment and local magnitude $M_L$ is shown in figure 2.11, and between moment and coda duration magnitude $M_d$ in figure 2.12. Although the scatter that is seen in the two figures is about the same, the values that are obtained by fitting a least squares line of the form $log(M_o) = a + bM$ is much more consistent for the $M_o/M_d$ comparison. The best fitting lines are $log(M_o) = 16.59 + 1.37M_L$ and $log(M_o) = 16.26 + 1.51M_d$ for the local magnitude and coda magnitude measurements, respectively. Since moment magnitude has been defined where a = 16.1 and b=1.5 (Thatcher and Hanks, 1972; Hanks and Kanamori, 1979), the comparison to duration magnitude is particularly good, with slightly lower estimates of magnitude than the moment magnitudes, but stable over a wide period range. The comparison to local magnitude, however, shows that the local magnitude is consistently higher, with particularly large discrepancies at higher magnitude levels. These results indicate that the relationship between $M_o$ and magnitude originally determined, and more recently tested for regional moment tensors in Southern California (Thio and Kanamori, 1995), also holds for earthquakes in Northern California.

Other measurements have been made in the past between seismic moment and local magnitude using various methods of estimating the seismic moment. For example, when seismic moment was calculated using P and S displacement spectra, Bakun and Lindt [1973] found that the log seismic moment-local magnitude relation was $log(M_o) = 17.02 + 1.21M_L$. Bolt and Herraiz [1983] estimated the seismic moment of regional and local earthquakes based on measures of amplitude and duration made directly on the Wood-Anderson seismogram. They found the corresponding relation of $log(M_o) = 17.92 + 1.11M_L$, although the uncertainties of these measurements were rather high. In both of these results and, to a lesser extent, using $M_o$ calculated from regional moment tensors, the high constant and shallow slope in the regression produce flatter curves than Thatcher and Hanks [1972]. This illustrates the problems of $M_L$ for low magnitude levels, where noise can increase the magnitude estimate, and for high magnitude levels, where saturation can decrease the magnitude estimate.

The regressions for coda duration magnitude do not indicate this effect.

Another regional moment tensor inversion method has also been in use at UC Berkeley. A time-domain complete waveform method (Dreger and Helmberger, 1993) has also worked successfully at calculating regional moment tensors, and the two methods have allowed the comparison of the results. Only the discrepancies in the estimation of moment magnitude are shown here for the comparisons of magnitudes (figure 2.13), but the mechanisms produced by the two methods will be presented later on. The comparison, in this case, is excellent and the uncertainties in the measurements are very small. The data is fit by $M_w(CWF) = 0.98 \; M_w(SurfaceWaves)$ - 0.02.

Finally, the same comparison is made between the regionally determined $M_w$ and those determined teleseismically using the Harvard CMT technique (Dziewonski, *et al.*, 1981). Figure 2.14 illustrates the results, although it is based on fewer measurements than the other comparisons. As in the case of the two regional moment tensor methods, the comparison is excellent, and there is practically no difference between the least square regression and a straight one-to-one ratio, except for a slight difference over the extrapolated low magnitude region. The best fitting function is $M_w(HarvardCMT) = 1.02 \; M_w(SurfaceWaves)$ - 0.14. This is very encouraging in demonstrating that there is continuity between the global and regional moment tensor inversions.

A statistical comparison for all of the events considered, irrespective of magnitude, is shown in table 2.2. The overall difference between $M_w$ and $M_L$ is -0.053 ± 0.096, between $M_w$ and $M_d$ is +0.161 ± 0.048, between $M_w$ and complete waveform regional $M_w$ is -0.075 ± 0.011, and between $M_w$ and Harvard $M_w$ is -0.016 ± 0.009. The mean discrepancy is lower for local magnitude because the two lines intersect instead of having a constant offset. The variance of the difference for local magnitude, however, is twice that of the variance for the difference with coda magnitude, meaning that there is much more scatter in this measurement. In either case, the discrepancy is generally less (and the scatter is much less) for comparisons of $M_w$ with each other, than to local estimates of magnitude, which are in turn less than the large 0.213 ± 0.057 difference between $M_L$ and $M_d$. This seems to confirm that moment magnitude, even regionally determined, is the most robust determination of magnitude.
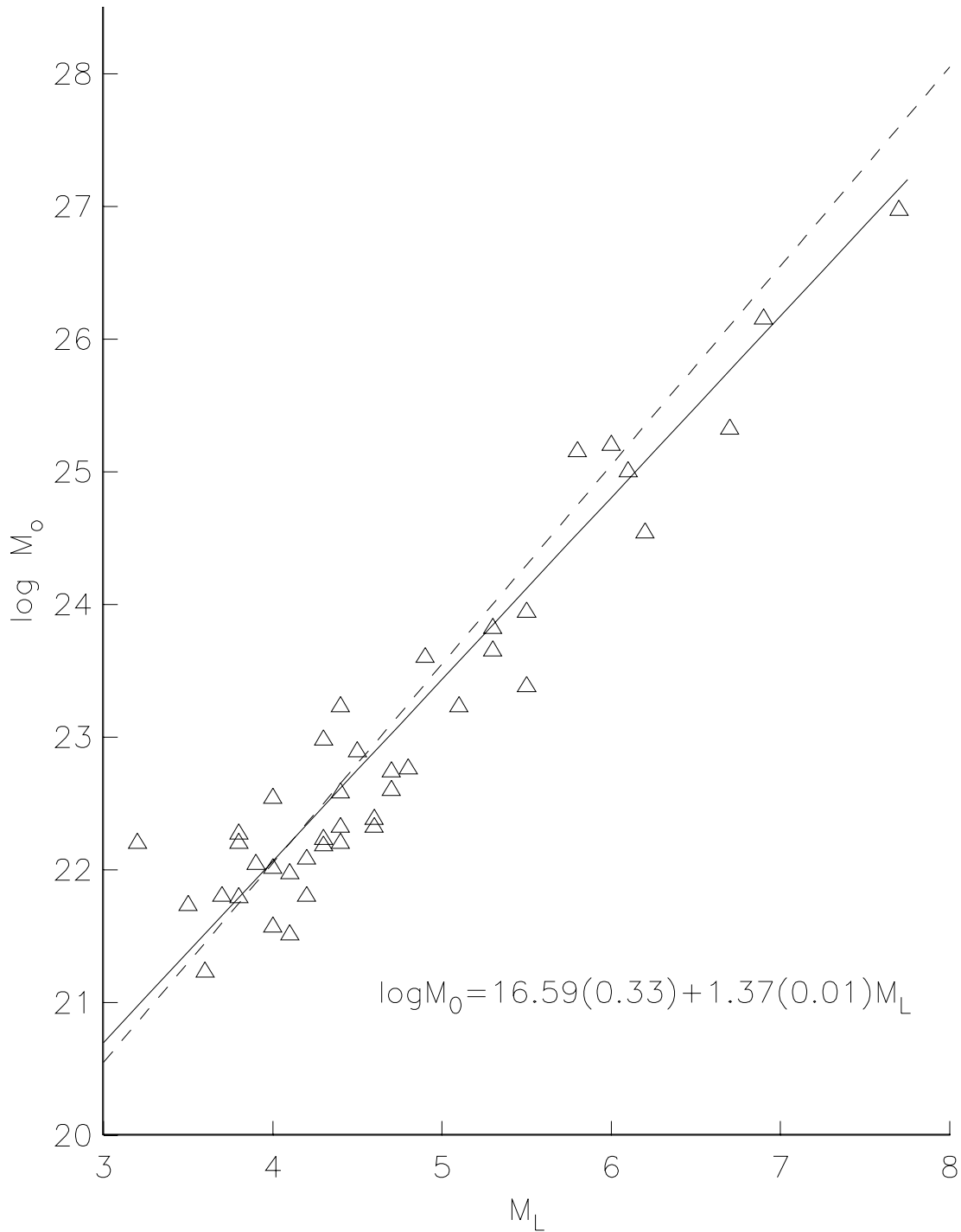
Figure 2.11: A comparison of $M_o$ and $M_L$ for all events in the catalog. The solid line shows the least squares fit to the data, while the dashed line represents the fit predicted by Thatcher and Hanks.
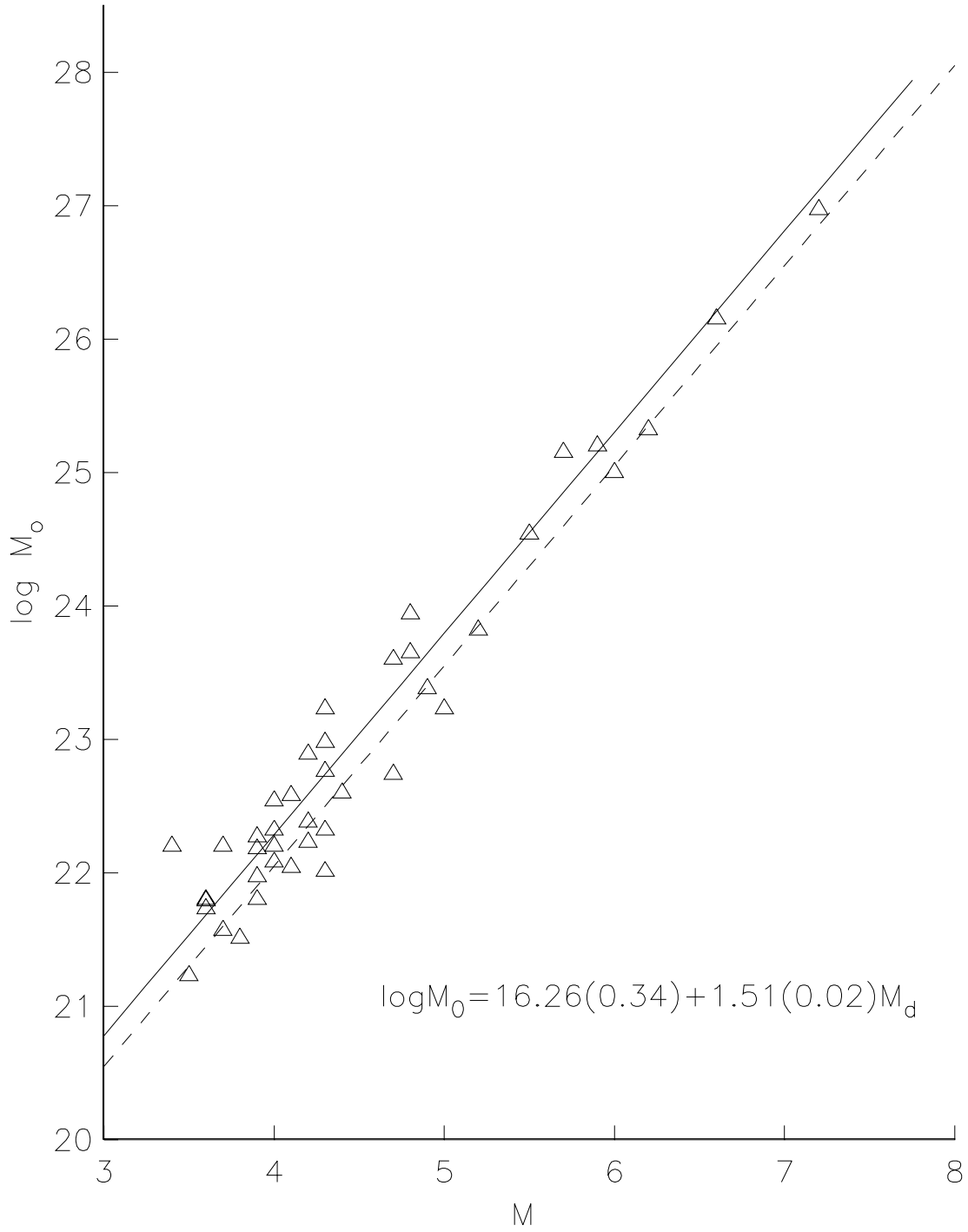
Figure 2.12: A comparison of $M_o$ and $M_d$ for all events in the catalog. Otherwise, same as figure 2.11.
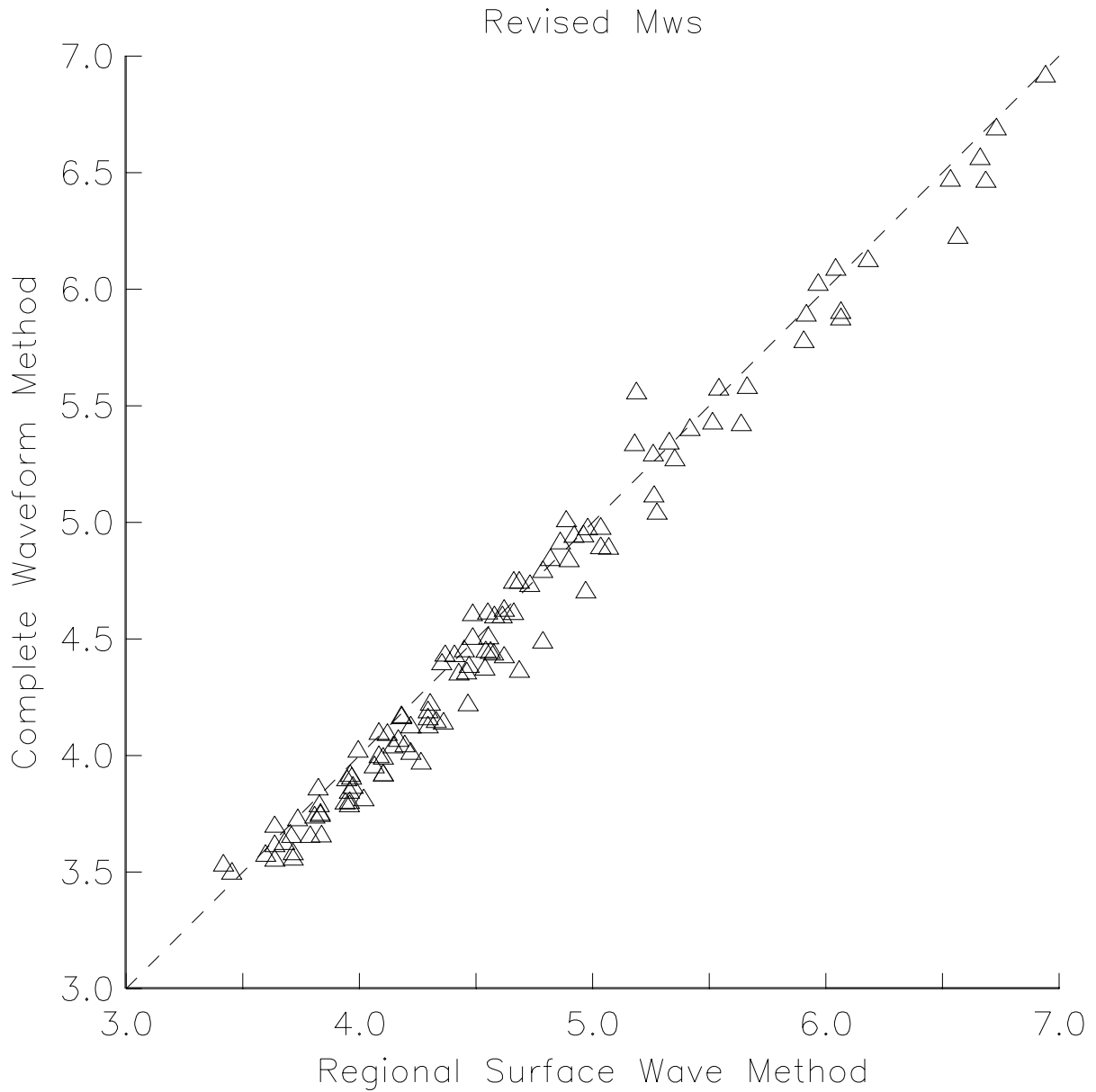
Figure 2.13: A comparison of the $M'_w s$ from the regional surface wave and complete waveform methods for all events in the catalog.
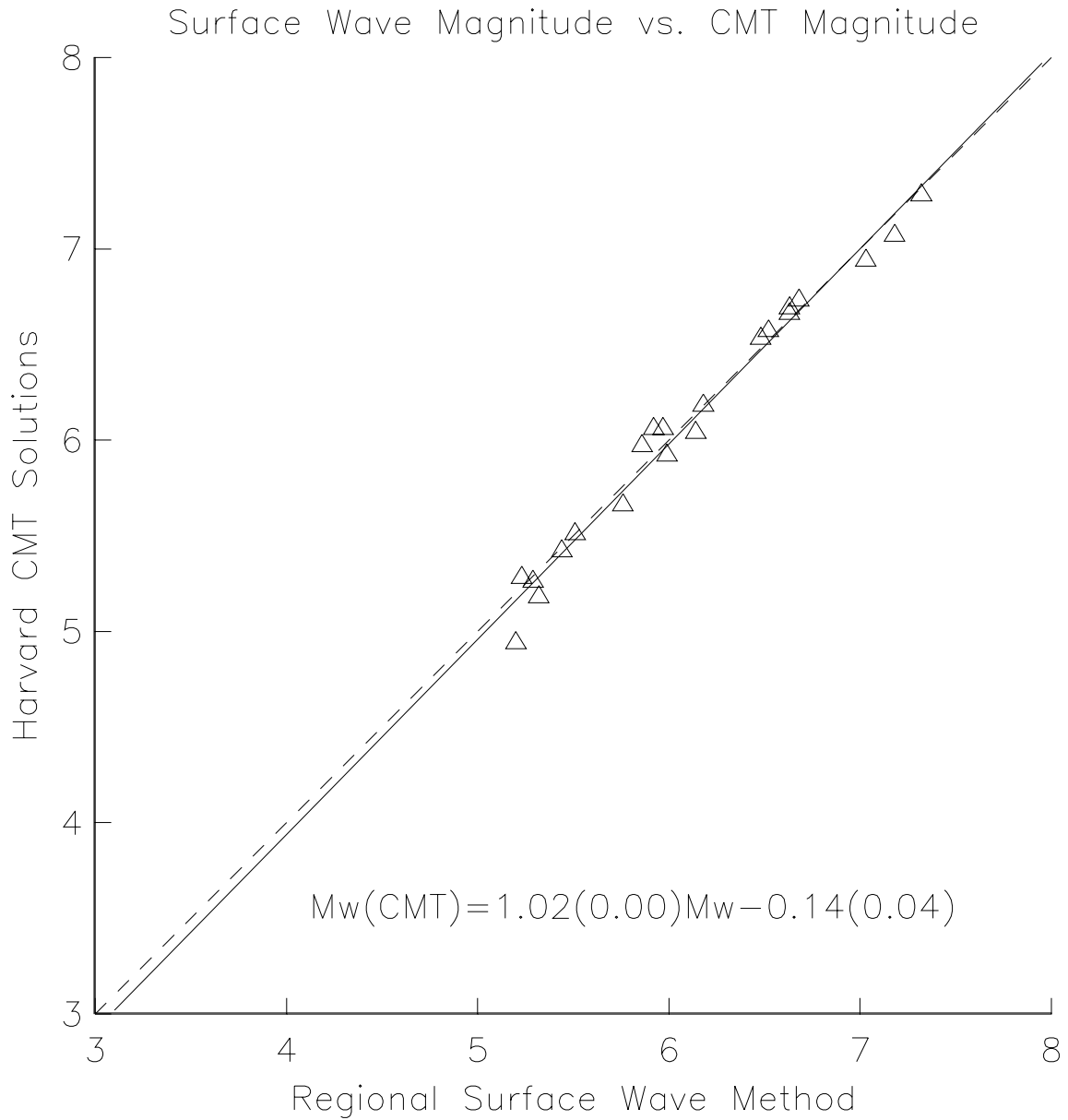
Figure 2.14: A comparison of two $M'_w s$, one from the regionally determined moment tensor method; the other from Harvard CMT.

Table 2.2: Statistical differences in magnitude determinations.

| | $M_w$ (CMT) | $M_w$ (CWF) | $M_L$ (BDSN) | $M_d$ (NCSN) |
|---|---|---|---|---|
| $M_w$ (RSW) | -0.016 ± 0.009 | -0.075 ± 0.011 | +0.053 ± 0.096 | -0.161 ± 0.048 |

Numbers shown are the mean and standard deviation of the difference of the column magnitude from regional surface wave magnitude. $M_L$ and $M_d$ values are obtained from the Northern California Earthquake Data Center. CMT refers to Harvard CMT method. CWF refers to the complete waveform method.

## 2.2 Velocity

As mentioned in the previous section, the accurate calibration of regional structure, in this case represented by phase velocities, is essential in order to obtain accurate regional moment tensors. Because both Love and Rayleigh waves are dispersive, so that their velocities depend on frequency, phase velocities must be estimated over a wide range of frequencies. This section discusses some velocity observations in California, the methods used to extract the phase velocities along a given source-receiver path, phase velocity models of specific regions and their corresponding structural models. The regionalization scheme has been developed in order to account for the variations in structure over the area of interest for the purposes of retrieving surface wave moment tensors. Later on in the text, the development of a more accurate phase velocity model is presented.

### 2.2.1 Velocity Observations

If the earth were completely laterally homogeneous, the problem would be simple. Surface waves would travel along the great circle path from the source to the receiver. Complexities such as waves coming from non-great circle paths, multipathing, and conversions between modes would not exist. When viewed globally at very long periods (T > 120 seconds), these conditions essentially exist for the earth, and hence laterally homogeneous earth models can be used as a good first approximation for the purposes of teleseismic moment tensor inversions. In addition, over the distances of teleseismic inversions, higher modes are well-separated from the fundamental mode surface waves. Unfortunately, for the higher frequencies utilized in the regional moment tensor inversion, these simplifications break down, and multipathing, mode interactions, and mode conversions at boundaries are seen.

Multipathing, of course, is a well observed phenomenon where waves arriving at a particular place have traveled two or more paths to their destination. Richter [1958] describes long period Rayleigh waves as follows: "Identification is sometimes difficult because the wave fronts may approach from a direction appreciably different from that of the epicenter. This is interpreted as due to horizontal refraction where the waves cross an important structural boundary; it is very noticeable on the North American west coast, where the large surface waves of many teleseisms arrive after

crossing the boundary between the Pacific basin and the continental area. On rare occasions, when the waves are travelling nearly along such a boundary, two successive G waves and two successive R waves are recorded because of passage along different paths with different velocities." The effect is particularly noticeable for shorter period waves.

Figure 2.15 shows an example of regionally recorded multipathed waves. In the figure, an event in Berkeley is recorded by the horizontal components of WDC, a station in Whiskeytown, 400 km away and approaching the station at a great circle azimuth of 165 degrees. The initial particle motion is oriented transverse to the great circle path, primarily in the east-west direction, which is the motion that would be expected for an incoming Love wave. Later in the record, however, the direction of the particle motion slowly starts to shift counterclockwise. Instead of coming in directly from the south, the Love waves are approaching from the SE direction, or from the direction of the Great Valley. The slower waves have been trapped in the sedimentary basin of the Great Valley and the orientation of the waves has changed to reflect this. The reverberation of this large basin is frequently observed at Whiskeytown station, which lies at the NW corner of the valley.

Clearly, there are large velocity contrasts between different tectonic regimes which must be calibrated. The approach taken was to develop a regionalization scheme in which the area of interest was divided into several tectonic regimes. In turn, a distinct regional velocity model was provided for each tectonic regime. The regional velocity structure is a first order approximation of the surface wave propagation and although there will be different velocities along different paths, it will not make use of off-great circle propagation and multipathing.

## 2.2.2   Regional Velocity Models

Preliminary velocity models were constructed for California and vicinity by analyzing some of the larger local events for which well-constrained source mechanisms were available. Because of the large lateral inhomogeneities in California, only source-receiver paths which had pure-paths within distinct tectonic regions were used. The source phase for these events was calculated and subtracted from the phase of the
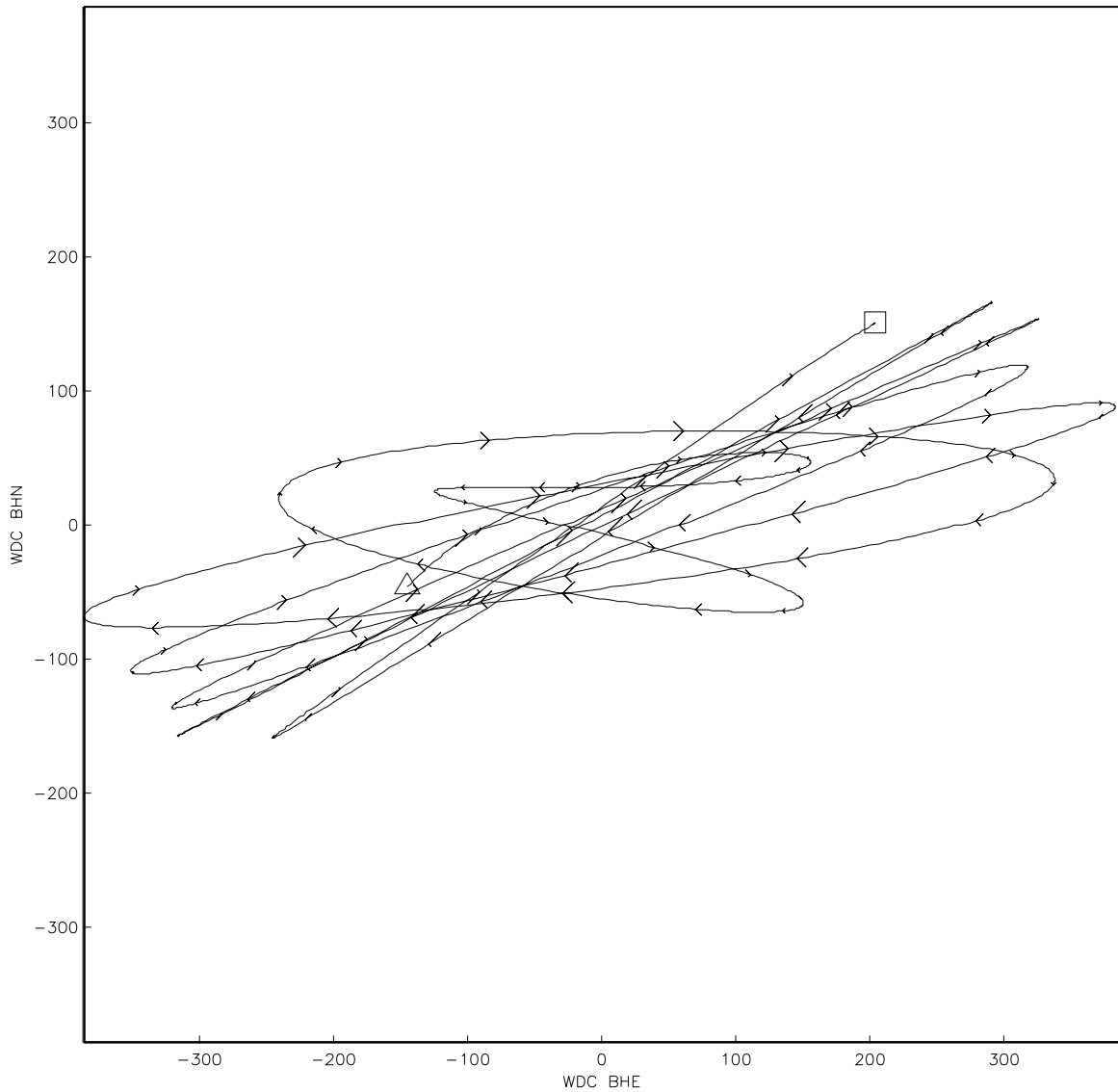
Figure 2.15: Particle motions observed at Whiskeytown, CA. The x and y axes are the east and north components. The waveform begins at the triangle and ends at the square, with arrows showing time evolution. The data has been bandpass filtered between 10 and 100 seconds.

47

surface waves at the stations. The phase velocity $c$ was then determined using:

$$c(T) = \frac{\Delta}{(\phi - \phi_o + 2\pi \times n) \times T} \qquad (2.21)$$

where $\Delta$ is the source-receiver distance, $T$ is the period, $\phi$ is the phase of the data, $\phi_o$ is the source phase, and $n$ is an integer arising from the $2\pi$-indeterminacy in phase measurements. The value for $n$ was chosen at longer periods assuming that the phase velocities determined here are close to the phase velocities for the Western United States (WUS) model. The curves for different $n$'s are sufficiently separated at long period to allow this determination unambiguously.

An example of this procedure for one source-receiver path is illustrated in figure 2.16. In this particular case, the dispersion curve is the phase velocity for Love waves for the 3 February 1994 Idaho-Wyoming border earthquake recorded at SAO. Velocity in km/s is plotted against period from 10 seconds to 100 seconds. The solid line represents the recorded data for various values of the integer $n$. The dotted lines represent the WUS reference model. The solid line near the reference curve represents the dispersion curve that was ultimately selected for this source-receiver path. The other solid lines are the rejected phase velocity curves for different integer values of $n$. In general, the phase velocity along this path is in pretty good agreement with the reference model. For this particular path, the phase velocity is slightly faster than the reference model, except at shorter periods where it is slightly slower.

California and Western Nevada were divided up into regions with distinct dispersion curves. These regionalized models are used to correct the phase of the data for the propagation delay. Initially, five regions were used to account for the lateral variations: Coast Ranges, Great Valley, Sierra Nevada, Southern California, and Basin & Range. Outside the area of the velocity regions, appropriate dispersion curves were selected. Initially, the models used were the generic Western United States model for source-receiver paths to the North and to the East, and the PREM model (Dziewonski and Anderson, 1981) for paths offshore to the West. Regions were added or replaced as more information became available. A "Pacific" velocity model replaced the PREM model for events off the coast. In addition, a model covering Oregon and the northern portion of California was added after the Klamath Falls earthquake sequence provided enough data to create a new model. Also, the Southern California model was replaced with the results of Thio and Kanamori [1995] who, in a similar
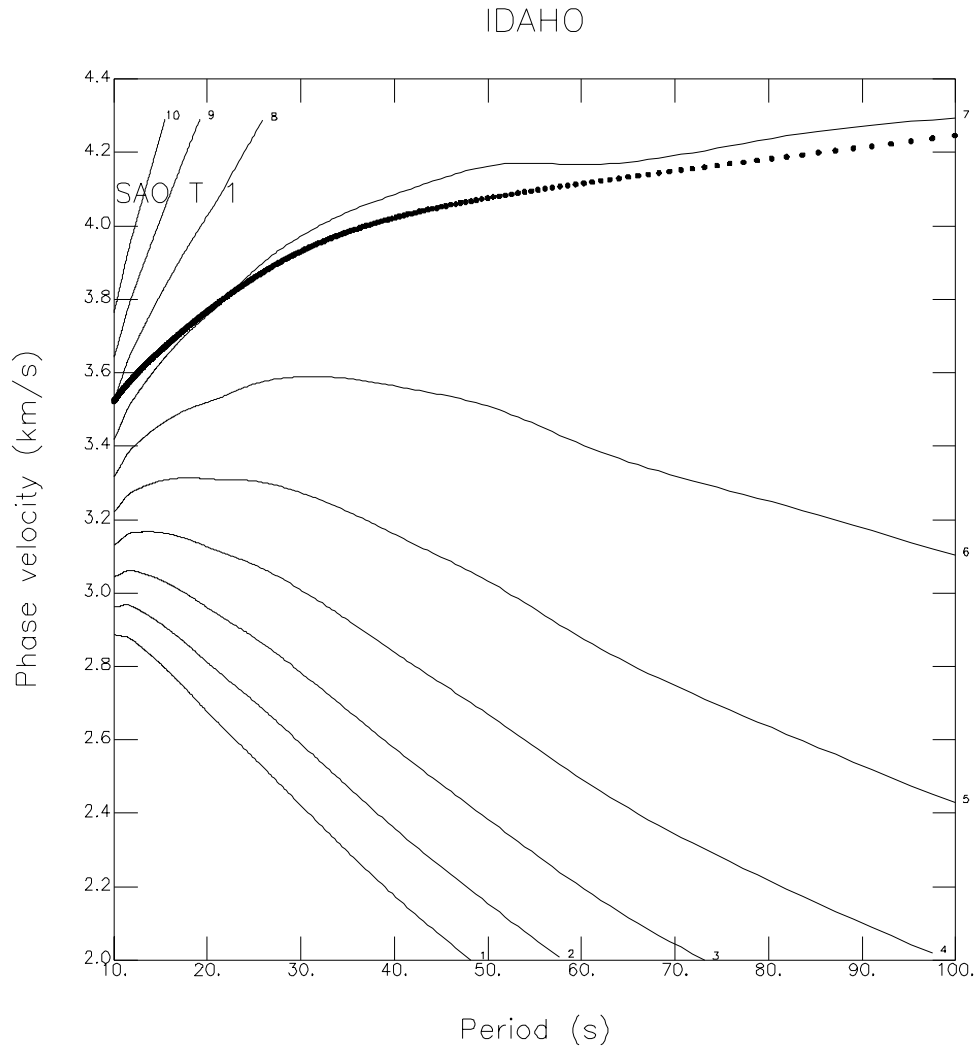
Figure 2.16: Example of a typical dispersion curve, shown for the 2/3/94 Idaho/Wyoming border event recorded at SAO. The solid lines are possible dispersion curves for this path, while the dotted line is the reference dispersion curve.

study, estimated phase velocities for five regions in this portion of the state: Central, Mojave, Peninsular, Transverse, and Western.

The dispersion curves for the various models are shown for Love and Rayleigh waves in figure 2.17a and b, respectively. There are several particular things to note. One is that the largest variation is for the shortest periods (about 0.4 km/s at 10–15 seconds). This is expected from the highly heterogeneous upper layers. Also, notice that there is still a variation of 0.05 km/s at long periods. This is due to the differences in crustal thickness and upper mantle velocities between the models. Notice the high upper crust velocities in the Sierra Nevada and Basin & Range models compared to the other models. There are still considerable variations in the model over the phase velocities typical inversion period range of 15–45 seconds.

## 2.2.3   Estimation of Structure

An estimation of structure can be made from the inversion of the regional phase velocity dispersion curves. For each region, a layered velocity model is calculated using the SURF program (Herrmann, 1991). The surface wave theory of the code is based in part on the work of Russell [1986] and for the inversion theory, SURF makes use of the subroutines given by Lawson and Hanson [1974]. A linear inverse problem can be formulated as $\mathbf{Gm} = \mathbf{d}$, where $\mathbf{d}$ is the data vector, $\mathbf{m}$ is the model vector, and $\mathbf{G}$ is the data kernel. The model parameters estimated using the least squares solution is $\mathbf{m}_{est} = \mathbf{G}^{-g}\mathbf{d}$. The generalized inverse $\mathbf{G}^{-g}$ for a damped least squares solutions is as follows:

$$\mathbf{G}^{-g} = [\mathbf{G^T G} + \epsilon^2 \mathbf{I}]^{-1} \mathbf{G^T} \qquad (2.22)$$

where $\epsilon$ is the damping parameter. As the damping parameter is increased, the solution moves farther away from the standard least squares solution.

Using the SURF program, one can either invert for the shear wave velocity $\beta$ with the density $\rho$ fixed, or alternatively, one can invert for $\beta$ with Poisson's ratio $\nu$ fixed. The second option was selected because the inversion seemed to behave better, producing fewer low-velocity zones. The dispersion curves are inverted for a 1-D velocity of the crust and upper mantle using the following equation:

$$\delta c = \int_0^{z0} p(z)\, \delta\beta\, dz \qquad (2.23)$$
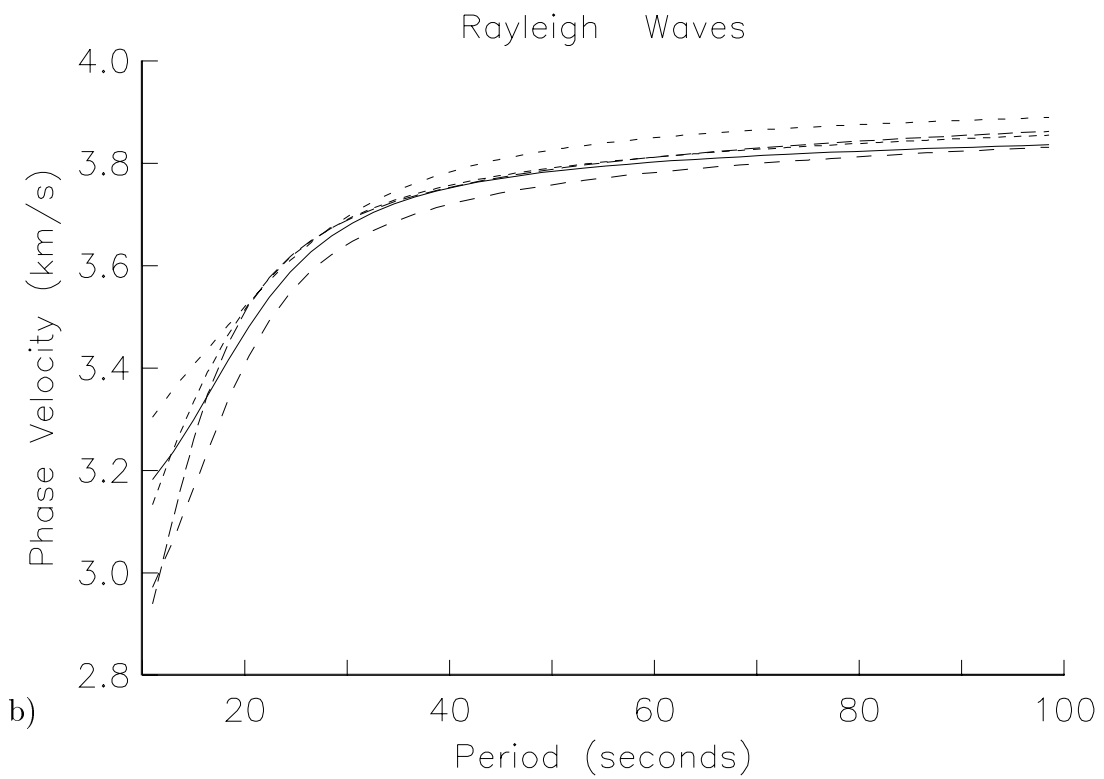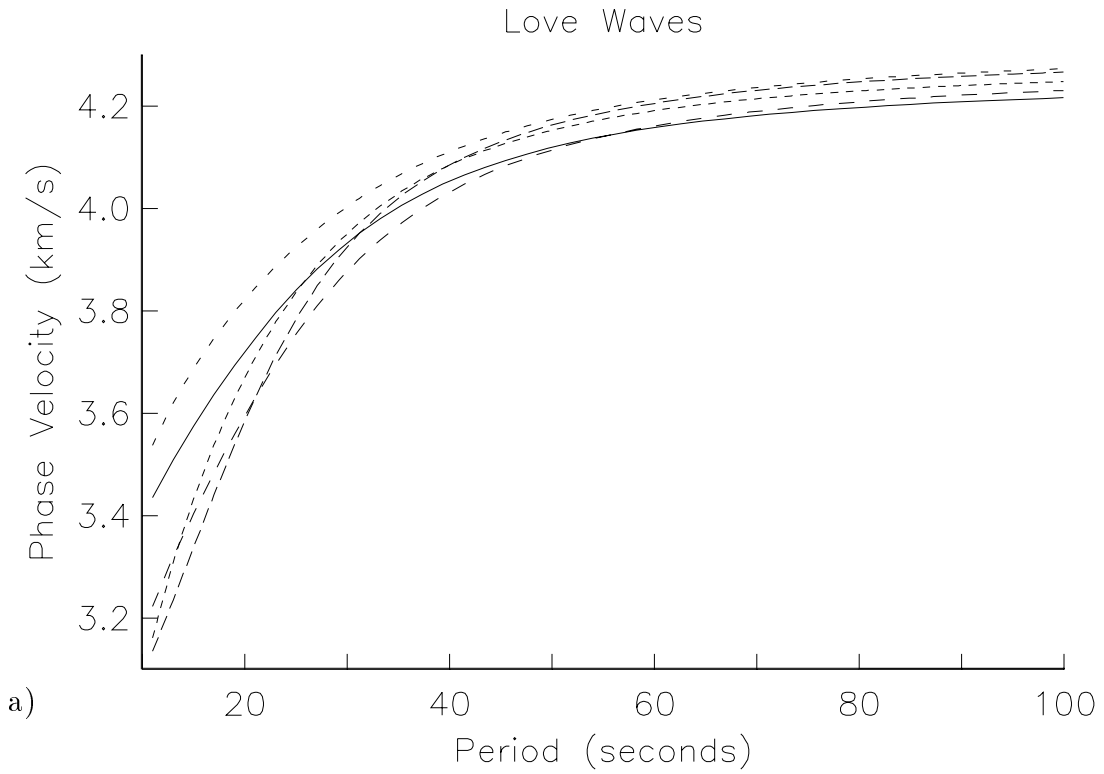
Figure 2.17: Regional dispersion curves shown for the regional models. a) Love waves, b) Rayleigh waves.

where $\delta c$ is the perturbation in phase velocity from the phase velocity of the previous model, p(z) is the sensitivity function ("partial derivatives") at that frequency, $\delta\beta$ is the perturbation in the shear wave velocity from the previous model, and z is the depth which ranges from the surface to the maximum depth of integration z0. The inversion tries to fit both Love and Rayleigh wave data with an isotropic model.

Equation 2.23 shows that the inversion to determine the velocity model depends on the partial derivatives of the same model, which results in a non-linear inversion. Consequently, the inversion is accomplished by taking a number of linear inversions where, at each step, the partial derivatives are calculated using the previously determined model. SURF allows either a velocity inversion where the layer thicknesses are fixed and the layer velocities are changing, or a depth inversion where the layer velocities are fixed and the layer thicknesses are changing. In order to allow for the most general velocity structure in the layered velocity inversion, both depth inversions and velocity inversions are performed and the layer thickness and the layer velocity are alternately allowed to vary. Several iterations are then performed, with the damping parameter increased with each iteration. Changes in the damping parameter allow large changes in the model initially in order to sample the model space, but shift to small changes in order to sample the area around the local (and hopefully global) minimum more precisely. Also, efforts are made to disallow some non-physical models, such as large low-velocity layers.

The sensitivity of the phase velocities from different periods is useful for assessing what part of the dispersion curves are controlling the velocities at which depths. The "partial derivative" curves for both the Rayleigh and Love waves are shown in figure 2.18 and 2.19. In general, the Rayleigh wave kernels are much sharper at a particular frequency. They do a good job of controlling the velocities at depth. The Love wave kernels are more smoothed out with depth and their sensitivity to shallow structure persists at long periods. They control the shallow velocity structure, as well as constraining the overall crustal velocity. The starting model selected for the inversion is the velocity model used by the USGS to compute Calnet locations for the appropriate region in the Hypoinverse program (Klein, 1989). In the inversion, both the velocity and thickness of the layer is allowed to vary. The results are given in table 2.3.

Overall, the results are reasonable models for each region, as suggested by other
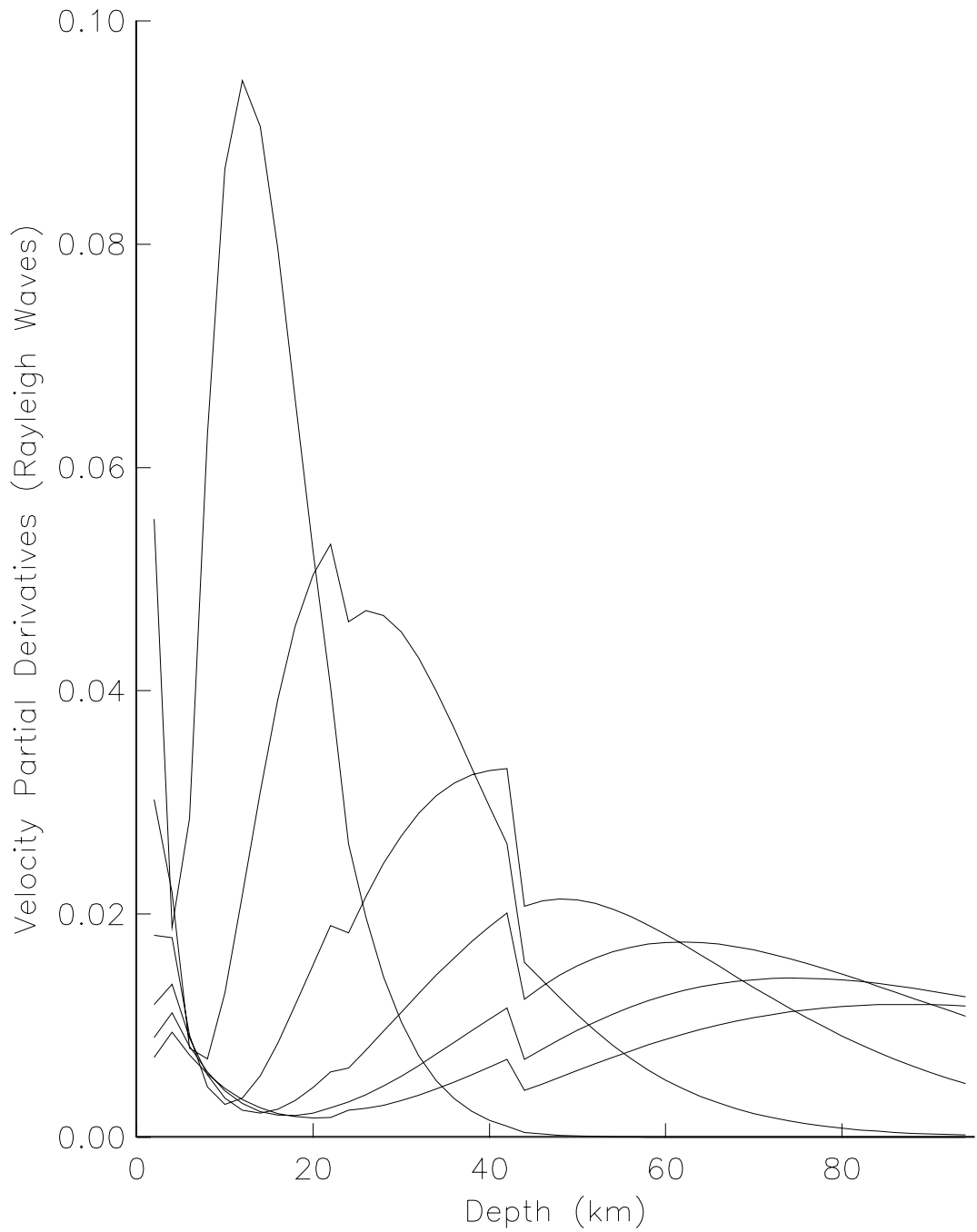
Figure 2.18: Velocity partial derivatives for Rayleigh waves shown for 10 sec (peak at 15 km), 20 sec, 30 sec, 40 sec, 50 sec, and 60 sec waves.
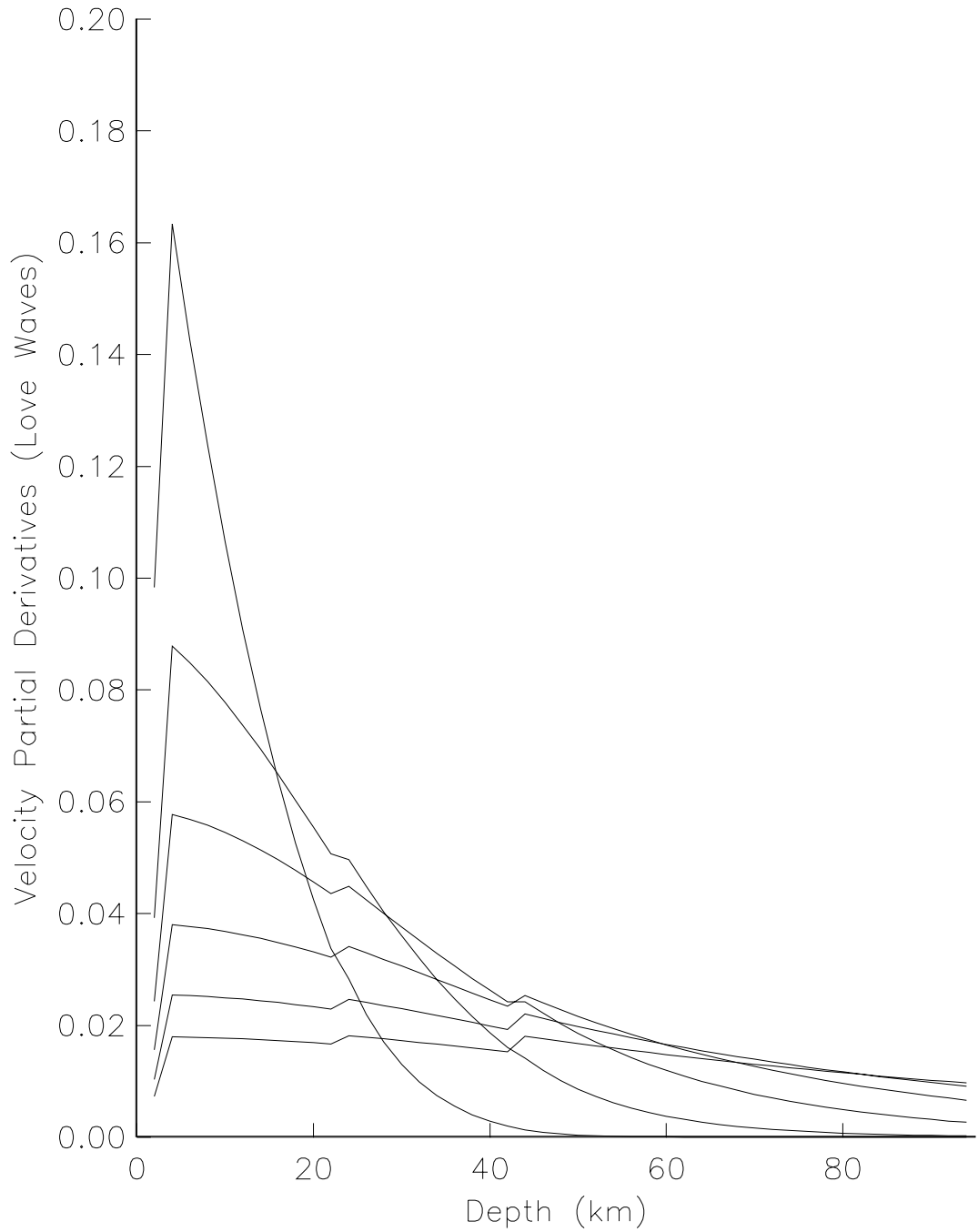
Figure 2.19: Velocity partial derivatives for Love waves shown for 10 sec (sharp-peak curve), 20 sec, 30 sec, 40 sec, 50 sec, and 60 sec waves.

Table 2.3: Velocity models determined for various regions.

| BASIN & RANGE | | | CASCADE | | | COAST RANGES | | | GREAT VALLEY | | |
|---|---|---|---|---|---|---|---|---|---|---|---|
| 3.9 | 5.10 | 2.55 | 5.2 | 3.10 | 1.77 | 2.6 | 3.77 | 1.89 | 0.8 | 2.53 | 1.27 |
| 26.8 | 6.32 | 3.57 | 30.6 | 6.15 | 3.50 | 15.3 | 5.92 | 3.34 | 5.9 | 5.03 | 2.51 |
| 30.5 | 6.67 | 3.77 | 33.6 | 6.76 | 3.86 | 25.2 | 6.01 | 3.40 | 15.3 | 6.24 | 3.53 |
| 0.0 | 7.72 | 4.35 | 0.0 | 7.93 | 4.61 | 0.0 | 7.75 | 4.37 | 29.4 | 6.80 | 3.84 |
| | | | | | | | | | 0.0 | 7.77 | 4.38 |
| PACIFIC | | | S. CALIFORNIA | | | SIERRA NEVADA | | | WESTERN U.S. | | |
| 0.6 | 2.28 | 1.30 | 4.5 | 4.85 | 2.74 | 5.6 | 4.95 | 2.80 | 2.5 | 4.00 | 2.00 |
| 6.4 | 4.57 | 2.61 | 14.1 | 5.13 | 2.90 | 13.3 | 6.60 | 3.72 | 23.5 | 6.15 | 3.60 |
| 10.6 | 6.45 | 3.68 | 26.9 | 6.98 | 3.95 | 38.2 | 6.79 | 3.84 | 42.5 | 6.70 | 3.79 |
| 16.8 | 6.97 | 3.97 | 0.0 | 7.81 | 4.40 | 0.0 | 7.83 | 4.41 | 0.0 | 7.80 | 4.40 |
| 0.0 | 7.96 | 4.51 | | | | | | | | | |

The values are depth to bottom of layer (in km), P-wave velocity (in km/s), and S-wave velocity (in km/s), respectively. A zero depth indicates the velocities in the upper mantle halfspace.

geological and geophysical data. For example, the depth to the Moho varies from 17 km in the Pacific Ocean to 25 km in the Coast Ranges to 38 km in the Sierra Nevada Mountains, which is fairly consistent with other observations. Similarly, P-wave velocities at the surface vary from 2.28 km/s in the Great Valley to 5.10 km/s in the Basin and Range. Inversely, the dispersion curves can be computed from the velocity model. These recomputed dispersion curves are the regional phase velocities that are applied as structural corrections for the moment tensor solution.

## 2.3 Automation and Real-Time Determination

As discussed in earlier sections, the installation of continuously telemetered, digital, high-dynamic range broadband instruments of the Berkeley Digital Seismic Network (BDSN) has allowed the opportunity to perform regional moment tensor calculations for moderate sized earthquakes in and around the network area. At the same time, the Rapid Earthquake Data Integration (REDI) system was developed to rapidly respond to earthquakes (Gee, *et al.*, 1996). This system automatically locates, determines the magnitude, and issues notifications of earthquakes in California.

Recently, efforts have been made to produce reliable focal mechanisms in as timely a manner as possible. This is to rapidly determine the faulting style of the events and to estimate the seismic moment. Characterization of the fault orientation is important for rapid hazard analysis because aftershock production differs among fault types (Uhrhammer, 1986). Fault orientation is also important for preliminary estimates of directivity. In addition, King *et al.* [1994] have recently shown that regional static stress changes induced by mainshocks can lead to identification of likely areas of increased aftershock activity. To accomplish the goal of rapid fault plane determination, the moment tensor methods were streamlined, the velocity models were accurately calibrated, and the procedures began to make use of the rapid locations determined by the already existing REDI system. Pasyanos, *et al.* [1996] discuss the techniques employed for automating the two regional methods employed at Berkeley (regional surface wave and complete waveform). The particular procedures used for the automation of the regional surface wave method are outlined here.

### 2.3.1 Automation Procedure

Since June 1994, the procedures for determining regional moment tensors for northern and central California have been fully automated. As a result, a preliminary computer-determined solution is available within 9 - 15 minutes after the occurrence of an event. The solutions are currently reviewed by an analyst and the information is disseminated to the outside community via email messages (see Appendix B). In this section, I evaluate the possibility of releasing the moment tensor solutions automatically. In the near future, these automatic moment tensor procedures will be fully integrated into the REDI processing. The moment tensor procedure is activated

using the UNIX *cron* command, which causes the system to check every few minutes for new events.

Generally, the procedures are robust and work well if the following conditions are met: 1) there is a reasonably good hypocentral location, 2) the source-receiver structure is accurately calibrated, and 3) noisy stations are removed. Since this isn't always the case, I discuss the biases that might be caused by non-ideal conditions. If the preliminary information indicates that the event is large enough to process using the regional surface wave method, then a working directory is created for the event. Even though the current minimum magnitude for earthquakes that can be processed using this method is about M3.6, processing starts for events with $M \geq 3.4$ in order to account for variations in magnitude determination.

Data are extracted from the Northern California Earthquake Data Center (NCEDC) and rotated from a station reference frame (Z,N,E) into an earthquake reference frame (Z,R,T). The computer-determined epicentral locations are assumed as the centroid location. Small errors in the epicenter will not be significant, but large errors can affect the rotation into the earthquake reference frame, as well as the assumed station-receiver distance. Small errors in the origin time are effectively absorbed by changes in the estimated source duration. Because this procedure is a frequency domain method, the data is then transformed to the spectral domain using a Fast Fourier Transform. Depending on the size of the event, different periods are selected for the moment tensor inversion. In practice, for moderate-sized events (M < 5.5), a range of periods are chosen between 15 and 45 seconds, and for larger events ($M \geq 5.5$), from 25 to 70 seconds.

At this point, an appropriate model is selected for each source-receiver path, in order to account for lateral heterogeneity. This is accomplished by applying a phase velocity correction appropriate for one of calibrated regional models. The existing regional models are Coast Ranges, Great Valley, Sierra Nevada, Southern California, Basin & Range, Cascade, and Pacific. Not properly accounting for the structure at this point can introduce noise into the procedure. Improvements in the future include dropping the regionalization scheme and dynamically determining the appropriate structure along each source-receiver path from a three-dimensional model of phase velocity.

Finally, the stations are selected and the inversion is performed. For the auto-

mated procedures, it is important to be able to choose only those stations that will have a high signal-to-noise ratio. This is accomplished in the surface wave procedures by assigning to each station and component a parameter based on the long-term noise characterization of each station. An effective way of characterizing the overall noise level is to calculate the power spectral density of noise windows for each station and component. Taken daily over a long time period, such as a year, the typical levels of the microseismic noise at that station can be determined. For example, over a one year period from July 1994 – July 1995, the low frequency (32 – 128 sec period) power spectral density at station YBH was -172 ± 2 dB and -169 ± 2 dB for the vertical and horizontal components, respectively, classifying them as both as quiet components. In general, hard-rock sites located away from the coastline are the quietest stations. Stations located on less competent rock or close to shore tend to be noisier. Unsurprisingly for the surface-installed instruments, the noise is higher on the horizontal components than on the vertical components.

The long-term noise is used to determine a station's noise parameter, specified as a number between one and four. Noise level one is reserved for the quietest stations that are available, while noise level four designates the noisiest stations that are still used in the moment tensor inversions. This noise parameter, along with the preliminary magnitude and source-receiver distance, determines whether or not this particular component is used in the inversion. This ad hoc method is illustrated in figure 2.20 for four different noise levels. In each case, a higher magnitude level is required for longer source-receiver distances. However, there is also an increase in the magnitude from increasingly noisier stations. For example, at a distance of 500 km from the event a station with noise level, one needs a preliminary magnitude of 3.2 to be chosen, whereas a noise level 4 station must have a magnitude of 4.7 before the station is selected.

## 2.3.2 Moment Tensor Comparisons and Quality Control

It has already been successfully demonstrated that the two regional moment tensor methods produce similar results for earthquakes over a large magnitude range (Romanowicz, *et al.*, 1993). Based on comparing the mechanisms, Ritsema, *et al.* [1994] find that differences in the angles of the focal mechanism of about 10° and difference
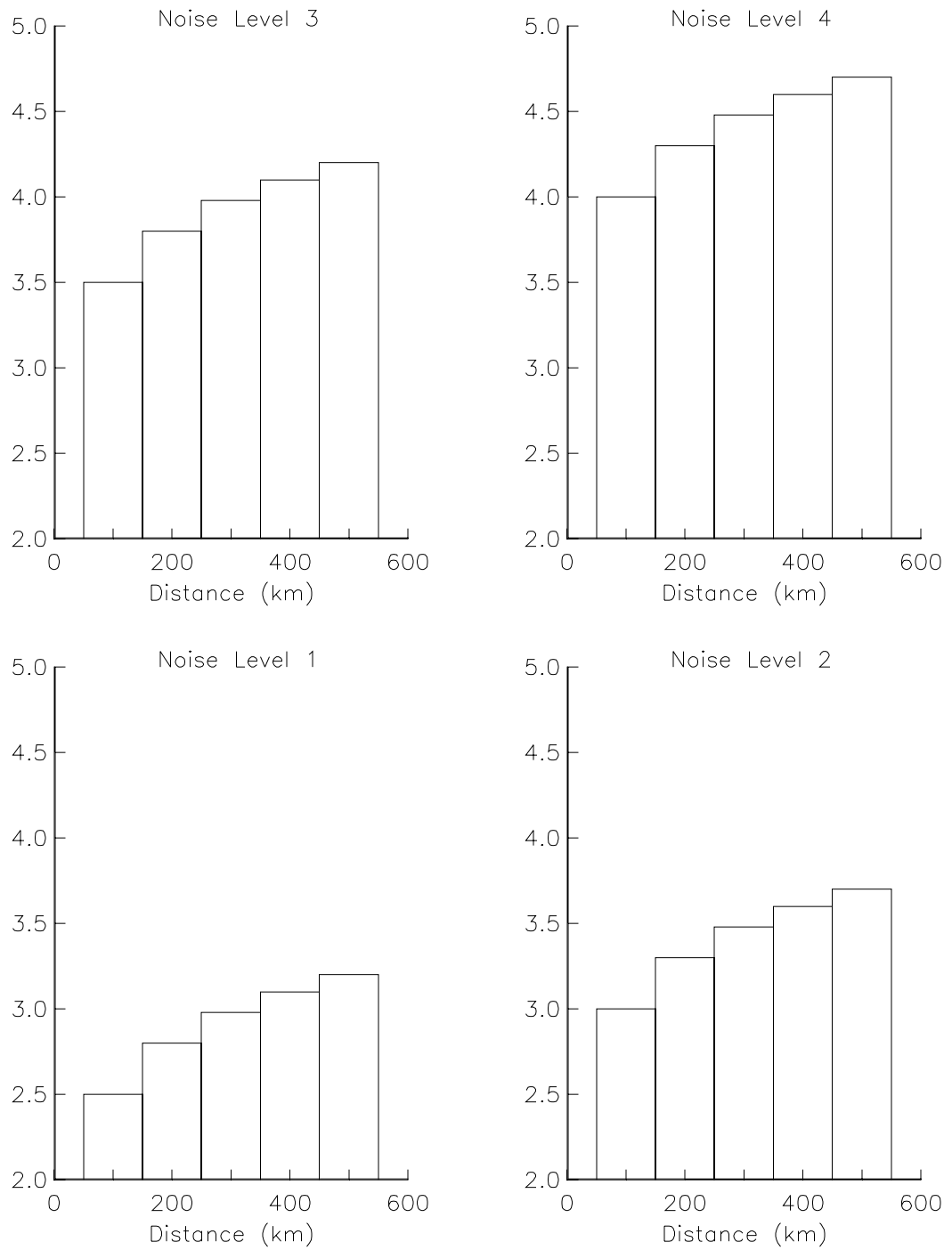
Figure 2.20: The minimum magnitude required to use the station in the inversion. Four noise levels are shown, each which demonstrates the minimum magnitude as a function of distance from 100 to 500 km.

in the seismic scalar moment of about 50% can be expected. Sources of noise include ambient noise levels, source complexity for large events and over-simplification of crustal structure models. The latter is likely to be the most important and therefore comparisons of the two regional methods are used to help ascertain the implications of the necessary oversimplification of crustal models. Studying the remaining differences is important in quantifying changes that might be needed to the existing methods, such as calibrating structure. At this point, one needs an objective function to measure the differences between any two given moment tensors. This function is useful in comparisons between moment tensor solutions obtained from using different methods, and comparisons between automatic and revised solutions. This function is also required to be dependent strictly on mechanism and not on the seismic scalar moment, which can be compared separately.

The moment tensor difference function $\mu$ is defined as the root mean square of the differences of the nine moment tensor elements normalized by their respective seismic scalar moment $M_o$.

$$\mu = \sqrt{\frac{\sum_{i=1}^{3} \sum_{j=1}^{3} (M_{ij}^{(1)\prime} - M_{ij}^{(2)\prime})^2}{8}} = \sqrt{\frac{\sum_{i=1}^{3} \sum_{j=1}^{3} (\delta M_{ij}')^2}{8}} \qquad (2.24)$$

where $M_{ij}' = M_{ij}/M_o$. The $\sqrt{8}$ normalization factor causes $\mu$ to range from a value of 0 (for a perfect fit) to a value of 1 (for double-couple mechanisms of exactly the opposite sense of motion). In this manner, one is able to objectively measure the difference in the estimated source mechanisms. Figure 2.21 illustrates $\mu$ as a function of mechanism change. The first and second columns show the change due to a rotation in strike and dip on a strike-slip mechanism. The third column shows the effect of a change in rake for a reverse mechanism and the last column shows the change of a rotation in strike on a normal mechanism. For values of $\mu < 0.25$, the source mechanisms are essentially the same, but start to diverge for $0.25 < \mu < 0.50$. For $\mu > 0.50$, the mechanisms are significantly different from one another.

One can now proceed to assess the quality of the moment tensor solutions by first comparing the magnitudes and then the mechanisms of the two regional solutions. In each case, the comparisons consider all events determined by the two methods for the four year time period from January 1991 to December 1995. The assessment of the two methods for moment magnitude $M_w$ was considered earlier in the comparison of

# Changing Mechanisms
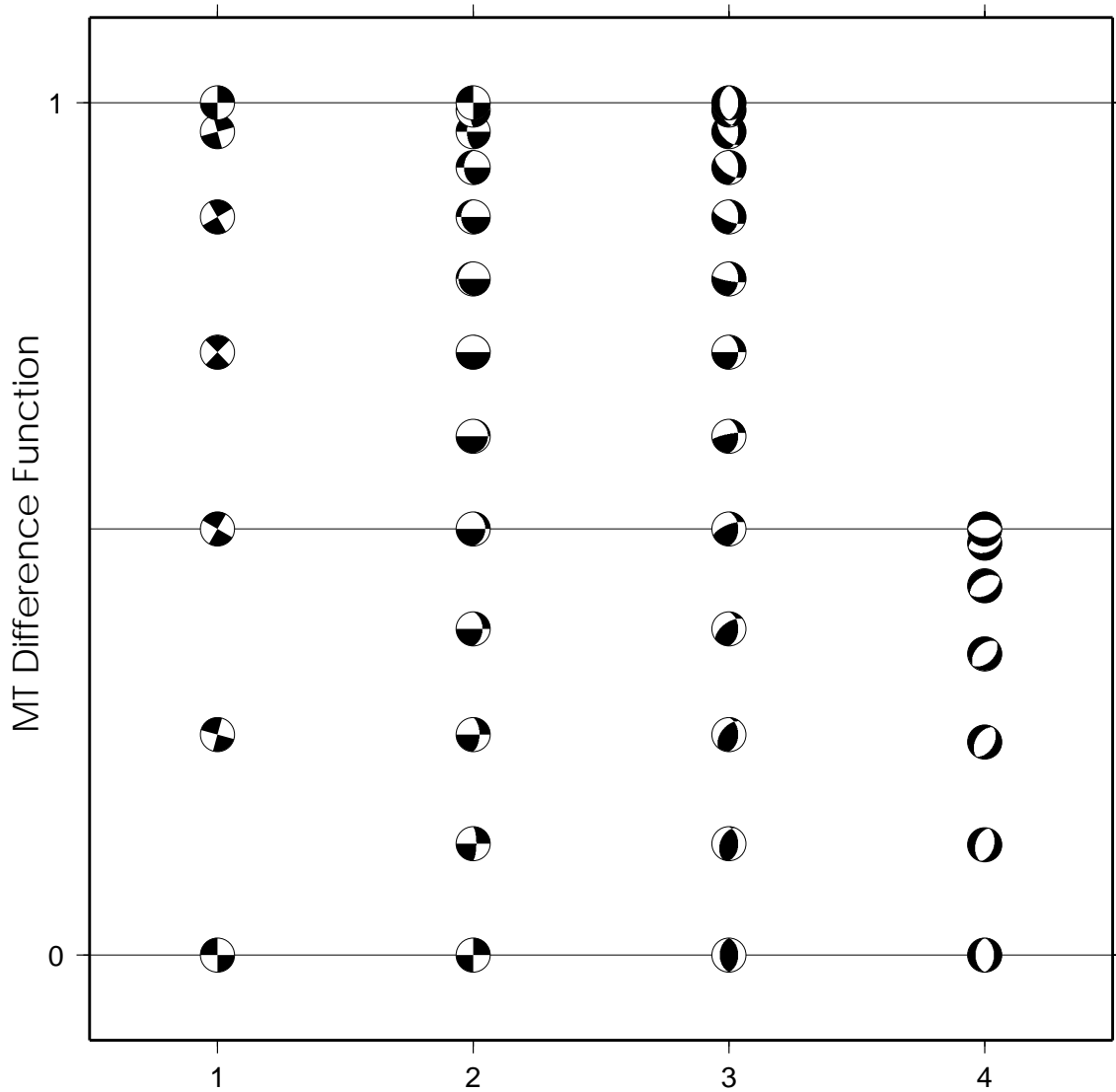


Figure 2.21: Variations in the moment tensor difference function $\mu$ for changes in strike, rake, and dip angles. The first column shows a change in strike, the second column shows a change in dip, the third column shows a change in rake, and the last column shows a change in rotation for a normal mechanism. Mechanism #1 is fixed as shown on the bottom line; mechanism #2 is perturbed as shown in each column.

magnitudes. Figure 2.13 shows $M_w$ obtained from the regional surface wave method plotted against those obtained from the regional waveform method for 63 events. In general, they compared very well. The least squares fit to the data indicates that there is a slight bias towards a higher magnitude for the surface wave method as compared to the waveform method.

In a few rare Geysers cases (8/23/93 and 8/29/94), the moment magnitude determinations are between a half to a full magnitude unit higher than the other determinations ($M_L$ and $M_d$) but consistent with each other, indicating a larger earthquake source whose high frequency energy is being attenuated significantly near the source.

Even so, there seems to exist a slight bias between the two moment determinations that is significant in light of the typical variations. One possible explanation is that differences in the models used by the individual inversion methods, particularly the attenuation quality factor Q, are causing the discrepancy. Unfortunately, this simple explanation does not seem to bear out. Tests of the moment tensor inversion using a wide range of Q values show that attenuation is a highly insensitive parameter. Changes in the $Q_s$ ranging from 200 to 950 have little or no effect on either the mechanism or the seismic scalar moment. The reason is that the periods used in the moment tensor inversion ($> 15$ seconds) have such large wavelengths that the number of cycles over the typical distance ranges (in this case 100-600 km) used are small.

Other tests using synthetic data show that both solutions recover the same mechanisms and scalar moments. This rules out the possibility that there are inherent differences in the two different regional methodologies. A more likely explanation is that the differences are caused by the imperfect estimation of the velocity structure of the earth. Dreger and Helmberger [1993] have compared various models and have found that changes in velocity model parameters, such as the average crustal velocity, can have large effects on the inversion. The calibration of the velocity structure of the earth is an ongoing effort; by continuing to compare earthquake solutions from the two regional methods, the velocity models should be improved.

Next, the function $\mu$ is used to compare the mechanisms to each other. Figure 2.22 shows the "beachballs" of the mechanisms plotted at the location of $\mu$ and the individual $M_w's$. Lines connect the solutions determined using the two techniques and the dot is plotted at the $M_w$ calculated using the mean $M_o$ from the two methods. Most of the events plot below the $\mu = 0.5$ cutoff which, as mentioned earlier, indicates

that the solutions are similar. There are a few exceptions, most of which are either close to the $M3.5$ cutoff for the regional methods, or were determined early in the development of the codes. It should be noted that the moment tensor methods have evolved with time. In addition to the continued refinement of the velocity models, early on the broadband station coverage was sparse and distant and noisier stations more strongly depended upon. The evolution of the moment tensors methods with time, along with the number of broadband stations in BDSN, is illustrated in figure 2.23. Over time, the number of events calculated has increased dramatically. Although the largest discrepancies in moment magnitude do not appear to change much with time, there are very consistent moment magnitudes for the largest events, and the largest discrepancies occur for the smaller events that are approaching the noise floor.

Since the goal is to determine moment tensors automatically and to distribute this preliminary information to outside sources without human intervention, the automatic mechanisms are compared to the revised, human-reviewed mechanisms. Figure 2.24 shows a plot similar to figure 2.13 comparing the $M_w$ of the automatic solutions to the revised solutions. Again, $M_w$ appears to be a relatively robust parameter and, even for solutions with incorrect determinations of mechanism and/or depth, $M_w$ does not usually vary by more than 0.2. The corresponding plot for mechanisms is shown in figure 2.25. Obviously, there are more significantly different mechanisms in this comparison that in the comparison of the two revised solutions. In 78% (38/49 cases) of the surface wave moment tensors and 61% (19/31 cases) of the complete waveform moment tensors, the mechanisms plot below the $\mu = 0.5$ cutoff, indicating a reasonable solution. In a substantial number of cases, the automatic solution was very good, and little or no further revisions were made. Event 13859, an event off the coast of Mendocino, is an obvious outlier in both cases. Generally, however, it appears that the automated solutions are behaving relatively well.

Can a procedure be devised to check the preliminary solutions for accuracy? One possible method is by comparing the two automatic mechanisms. In cases where the automatic mechanisms agree, there is in general a robust estimator of the source mechanism. Figures 2.26 and 2.27 show a comparison between the automatic moment tensor methods. Because the automatic events would include all cases where the automatic moment tensors have been initiated, including microwave glitches, "splits"
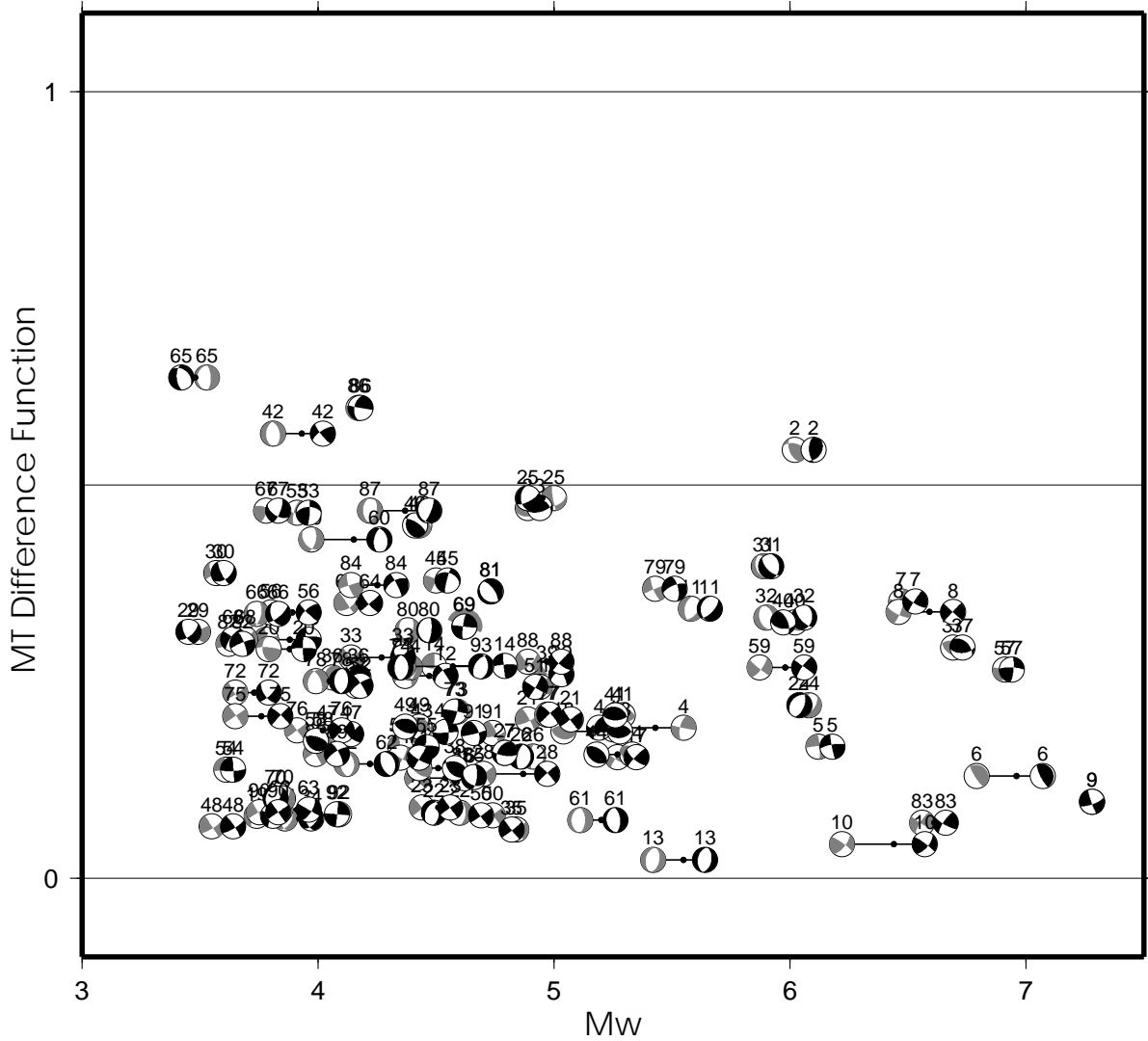
Figure 2.22: A comparison of the revised regional surface wave (black) and complete waveform (grey) moment tensor solutions for all events from January 1991 to July 1995. Numbers above the focal mechanisms are listed in chronological order. The x-axis is moment magnitude $M_o$, the y-axis is the moment tensor difference function $\mu$.
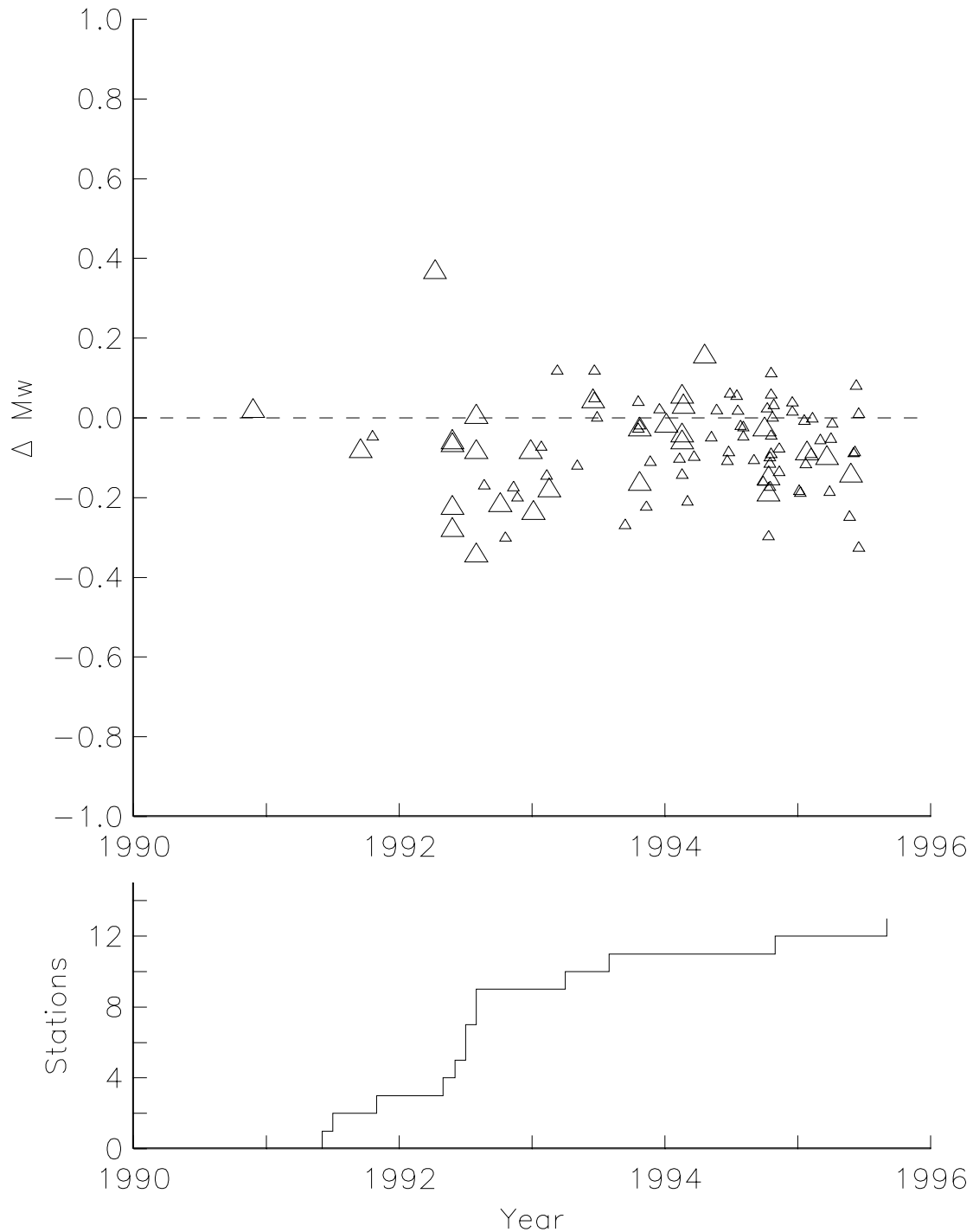
Figure 2.23: Moment tensors versus time. Top figure shows differences in $M_w$ between the two methods as a function of time; bottom figure illustrates the number of broadband stations in operation as a function of time. Events greater than magnitude 5.0 are shown by larger symbols.

65
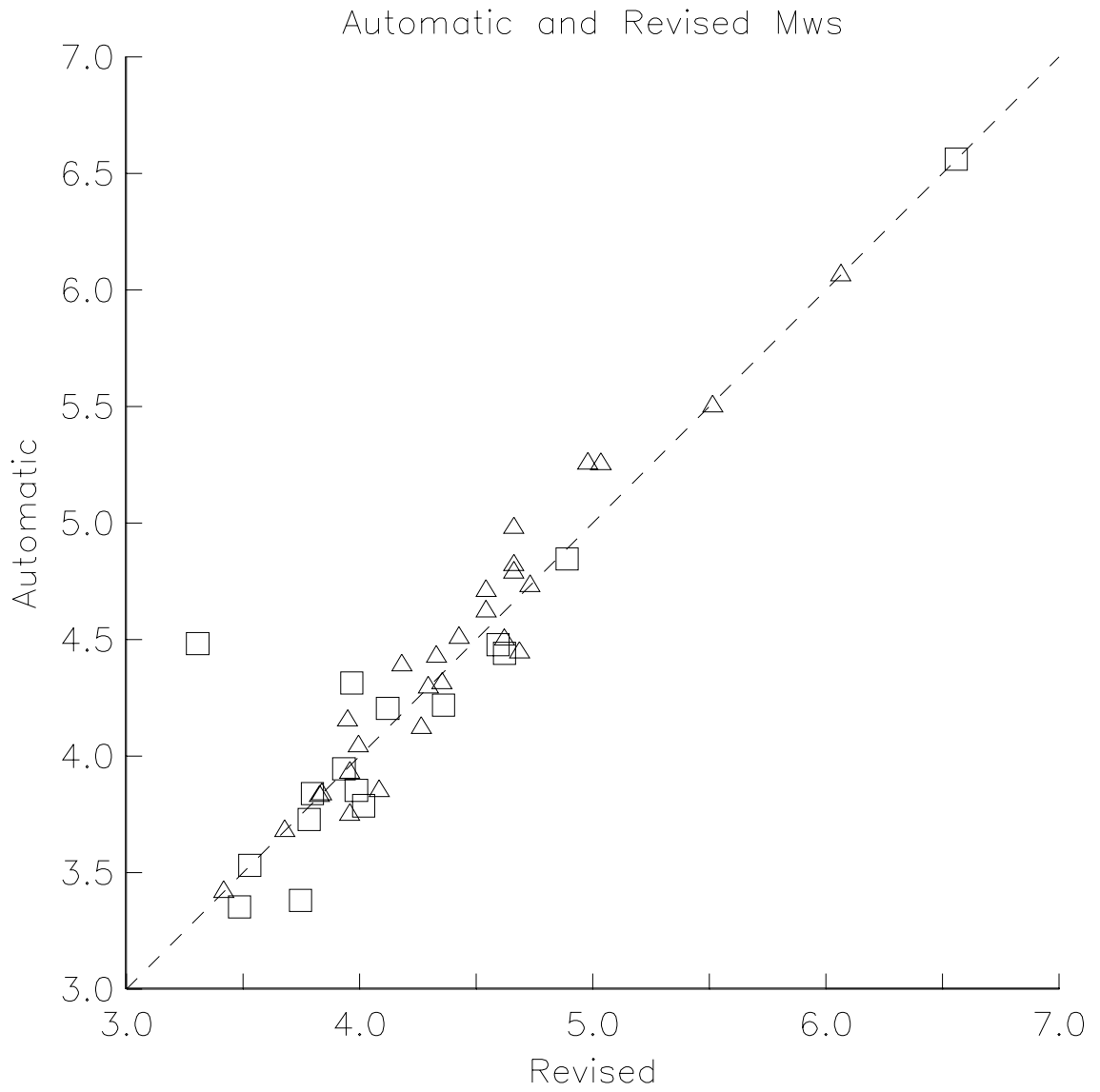
Figure 2.24: A comparison of the automatic and revised $M'_w s$ for all events in the catalog. Triangles are values from regional surface wave method. Squares are those from the complete waveform method.
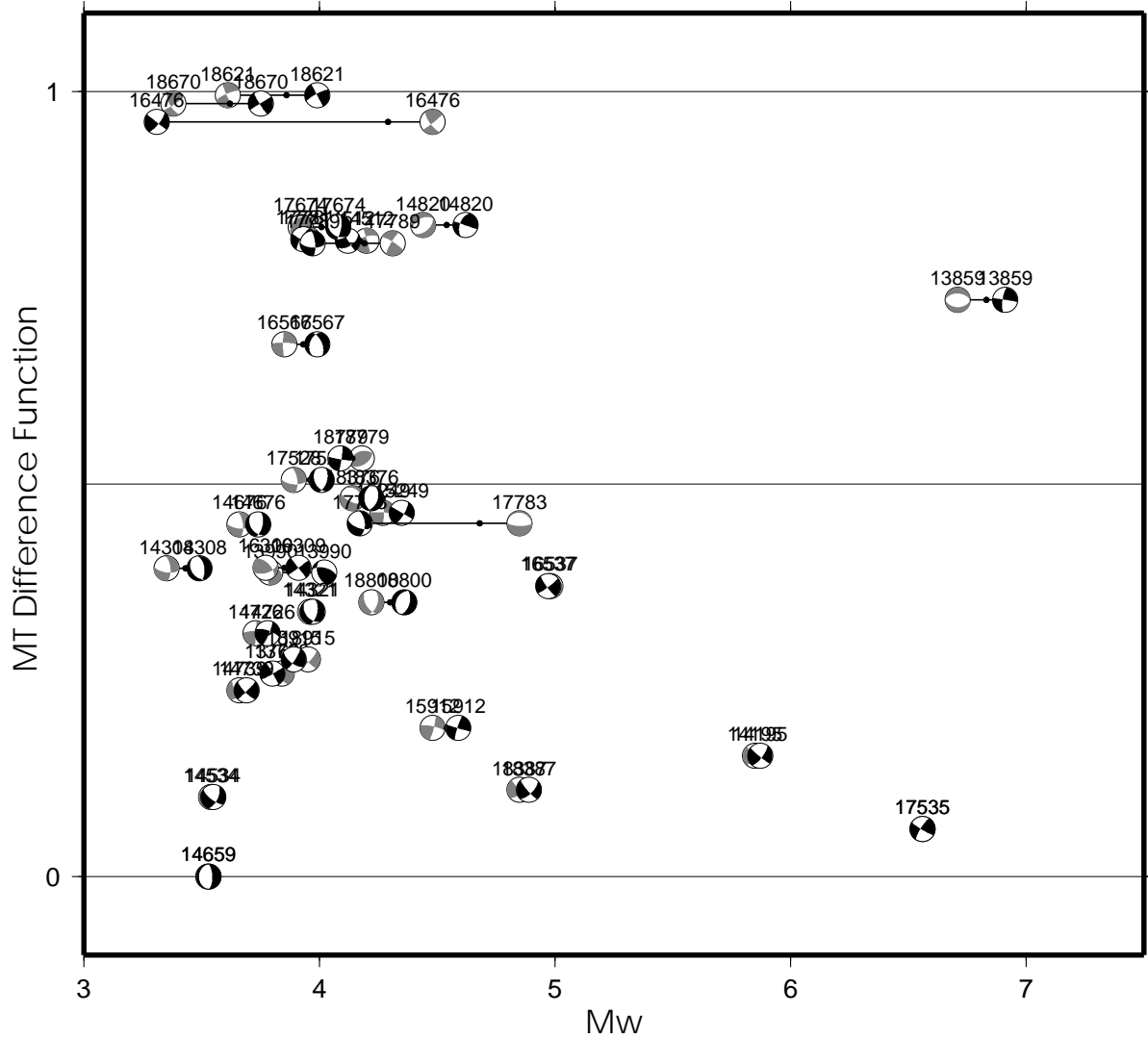
Figure 2.25: A comparison of the automatic (grey) and revised (black) moment tensor solutions for regional surface wave method. Axes are the same as those in figure 2.21. Numbers above the focal mechanisms are REDI event numbers.

of real events, events at the moment tensor threshold, or anything that is initially determined by the real-time system to be an event, the figures have been culled to only include those events which eventually were human-reviewed and processed completely. In this case, only 31% (11/35 cases) of the events plotted below the $\mu$ = 0.5 cutoff. The three largest events show very good agreement. Unfortunately, one of the events (13859) had poor mechanisms which were similar between the two methods. For the other two $M_w$ 5 events (16537 and 18387), the automatic solutions were dissimilar, but the mechanism of one of the methods was good.

### 2.3.3 Quality Control of Automation Procedures

Of course, no automated system is completely foolproof. Noisy stations, imperfect models, and relying on computer locations can all contribute to produce incorrect moment tensor solutions. As a result, procedures have been developed to try and prevent incorrect solutions from being broadcast. Parameters such as variance reduction, percent double couple, azimuthal aperture, number of stations, number of components, and depth resolution are all factors in determining the quality of the moment tensor solution. By comparing the automatic moment tensor solutions to the revised moment tensor solutions in light of these parameters, one can optimize the quality function to determine whether or not there is a reliable solution. The current decision process mainly involves accepting or rejecting an automatic solution. In the future, this process will incorporate more and more of the decisions of the analyst and in trying to improve on the solution by taking a corrective course of action, such as adding or removing a given station from the data set.

Parameters of the moment tensor solution are generated by an average of the parameters of the individual methods, weighted by the solution quality of the individual methods. For example, a very robust determination of $M_w$ is computed as:

$$M_w = \frac{(M_w^{(1)} * QUAL^{(1)} + M_w^{(2)} * QUAL^{(2)})}{QUAL^{(1)} + QUAL^{(2)}} \qquad (2.25)$$

where $QUAL$ is the solution quality. Similar estimations can be made of other parameters, such as source depth.

In addition, the moment tensor solutions can be compared to see if there are significant differences between the two mechanisms. Given that the methods often use different stations, different models, and different parts of the waveform, it is unlikely
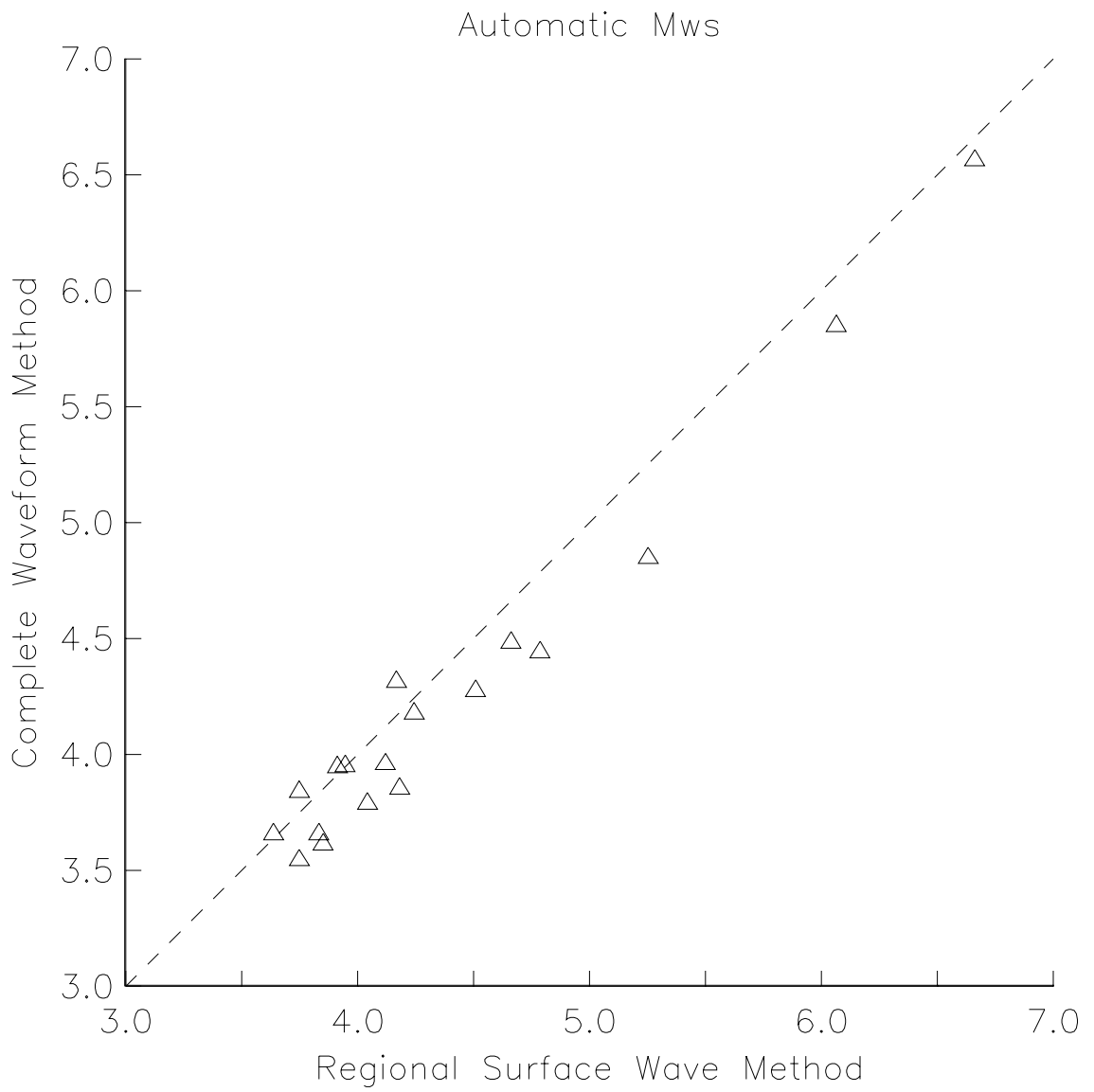
Figure 2.26: A comparison of the automatic $M'_w s$ for all true events in the catalog. Splits and microwave glitches have been removed.
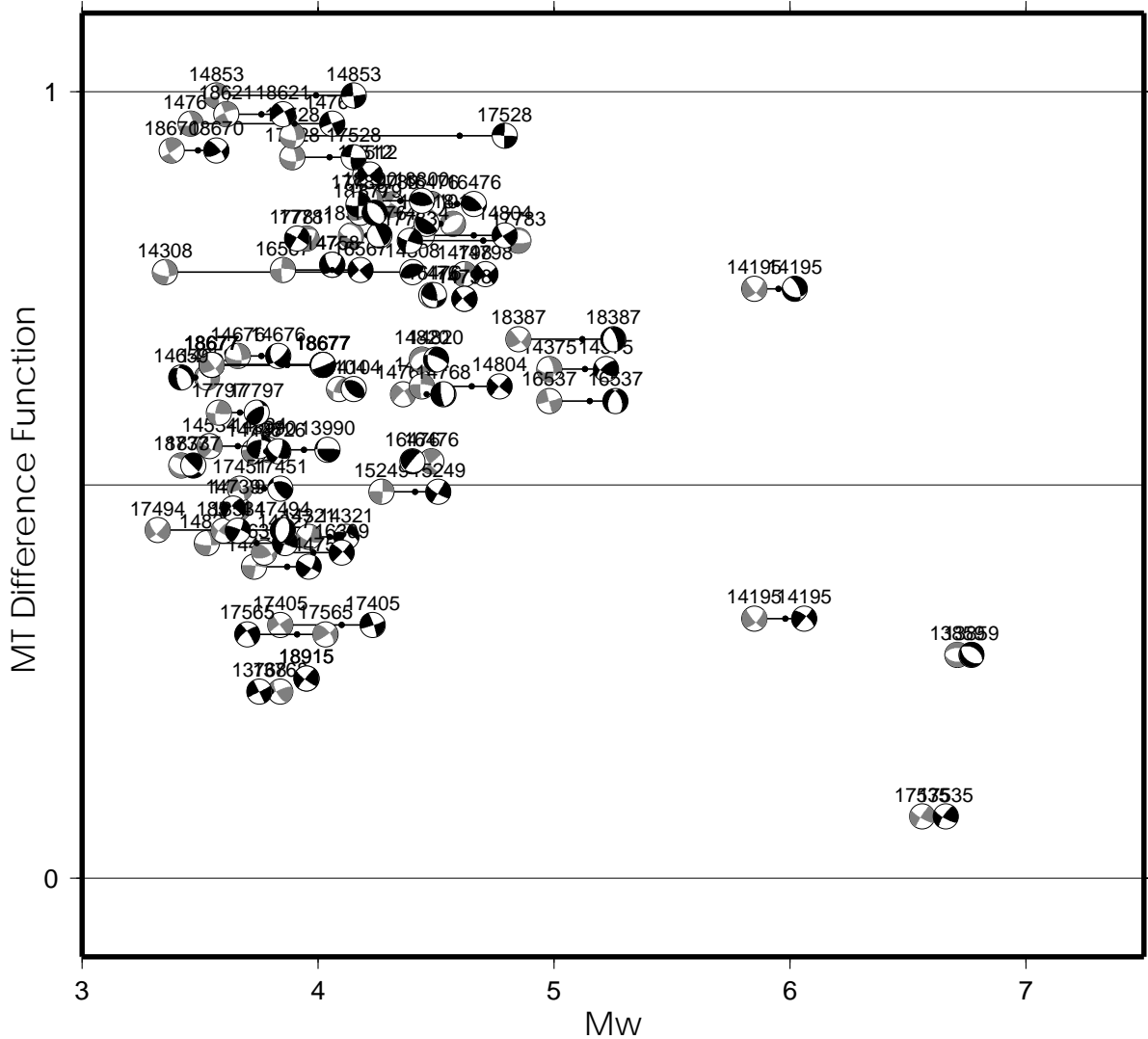
Figure 2.27: A comparison of the automatic regional surface wave (grey) and complete waveform (black) moment tensor solutions. Axes are the same as those in figure 2.21. Numbers above the focal mechanisms are the REDI event numbers.

that both methods would generate the same incorrect solution. The similarity of the two solutions can be used as a factor to assess the dependability of the moment tensor solutions. Because of the procedures to filter out bad data, the quality assessment of each method, and the comparison of the two methods, automatic moment tensor solutions can be reliably generated in a timely manner.

In the current configuration of the system each moment tensor procedure runs independently. If the automatic solutions were immediately released, the automated procedures would generate reasonable solutions about 60-80% of the time, and produce $M_w$ within 0.1 magnitude units of the revised solutions about 50-70% of the time and within 0.2 magnitude units about 80-90% of the time. These numbers are based purely on the previous performance of the system. Additionally, the quality of the moment tensor solutions increases with $M_w$ due to a higher signal-to-noise ratio and reliance on data from a larger numbers of stations; this bodes well for its incorporation into automated systems such as REDI. By improving each of the independent methods and using their solutions, the mechanism and magnitude can be generated reliably enough to immediately release, first the moment magnitude, and then complete moment tensor solutions to the community.

## 2.4   Inversion Tests

In order to determine the robustness of the regional surface wave moment tensor technique, it is useful to conduct a few tests to see how sensitive the method is to changes in various parameters. For example, the models that are used in the inversion are one-dimensional approximations of the structure that lies along the source-receiver path. Knowing that these are just empirical approximations to the real earth structure and knowing that these models have a certain degree of inaccuracy, it is of interest to gauge what effect the uncertainties in the model have on the moment tensor solution. Tests have been performed on location and origin time, velocity model, depth, station coverage, inversion period, and attenuation.

### 2.4.1   Location Test

This section addresses the problem of imperfect hypocentral locations. This would be important for events located off-shore, particularly near Cape Mendocino, where location and origin time and velocity model trade off. This would also be relevant in the case of events along major faults. For example, along the San Andreas Fault near San Juan Bautista there is a very large velocity contrast across the fault from the granitic rocks of the Salinian block and the adjacent rocks of the Franciscan. The velocity contrast can cause mislocations which could have very direct effects on the strike and dip of the resulting mechanism, although the general strike-slip motion of the events do not change. Finally, this test is particularly relevant to the automation of moment tensors, where the initial computer-determined locations may not be as good as human-reviewed ones. Even considering only human-determined solutions, there can be considerable differences in locations depending on the stations selected, the way the phases are picked by the analyst, the weighting method used, and the model or models employed in the inversion.

For this particular case, I selected the 1/16/93 Gilroy earthquake. This event was located near the center of both the BDSN and NCSN networks, so the final location should be as good as possible. The location was then perturbed by 10 km in both latitude and longitude in both directions at 2 km intervals. The results are shown in table 2.4. The moment tensor inversion appears to be relatively insensitive to changes in origin time, changing by only a few degrees in the angles of the fault

planes. Small errors in origin time can be accommodated by comparable changes in the source phase, which are determined by solving for the duration of the source in the inversion. Another curious observation is that, in this particular case, the inversion is relatively insensitive to changes in longitude, while it is highly sensitive to changes in latitude. In this particular case, most of the stations are located to the north, with only one to the east. This suggests that some large scale changes in the location and origin time may not be significant but, depending on the geometry of the problem, errors on the order of 2 km can affect the solution.

## 2.4.2   Model Test

Next, the inversion was tested by varying the model used in the inversion. This case could arise in poorly calibrated areas where a single reference model might be used for a particular area, instead of one specifically calibrated for the region. For example, in the western states outside of California and Nevada, the regional surface wave method uses a generic Western United States model instead of calibrating many individual regions over this large area. Alternatively, the region could be improperly calibrated.

The 8/11/93 San Felipe event was chosen because of the abundance of models which exist for this region. In addition to the normal regionalization used in the moment tensor inversion (in this case, mostly Coast Range or CR model but some Great Valley or GV paths to stations in the Sierra Nevada Mts.) , the inversion was performed with all Coast Range paths, the GIL7 model that is used for this area by the time-domain waveform fitting inversion (Dreger, 1994), and the Southern California (SOCAL) (also from Dreger, 1994) and Western United States (WUS) models. Table 2.5 shows the test results. All of the models basically yield right-lateral strike-slip mechanisms. As the models used become less representative of the region, however, changes in both depth and seismic scalar moment estimates occur. Where the velocity models are the most similar (as between NORM and CR), there are few changes. This demonstrates that the model should probably be close approximation of the structure along the propagation path because large differences can significantly affect the solution. The largest changes are more likely to occur where there are substantial differences between the model and earth structure in crustal thickness or

Table 2.4: Values for origin time, latitude, and longitude are deviations from origin time and epicentral location. Origin time is in seconds; latitude, longitude, and depth are in kilometers; $M_o$ is in dyne-cm.

| $\Delta$ O.T. | $\Delta$ Lat. | $\Delta$ Lon. | Strike/Dip/Rake | $M_o$ | $M_w$ | Depth |
|---|---|---|---|---|---|---|
| 0.0 | 0.0 | 0.0 | 224./85./-7. | 3.2e23 | 5.0 | 8. |
| 0.5 | 0.0 | 0.0 | 223./84./-15. | 2.9e23 | 4.9 | 10. |
| 1.0 | 0.0 | 0.0 | 222./84./-14. | 2.9e23 | 4.9 | 10. |
| 2.0 | 0.0 | 0.0 | 221./83./-3. | 2.7e23 | 4.9 | 10. |
| 0.0 | -10.0 | 0.0 | 266./87./-62. | 3.7e23 | 5.0 | 24. |
| 0.0 | -8.0 | 0.0 | 266./87./-62. | 3.7e23 | 5.0 | 24. |
| 0.0 | -6.0 | 0.0 | 266./87./-62. | 3.7e23 | 5.0 | 24. |
| 0.0 | -4.0 | 0.0 | 266./87./-62. | 3.7e23 | 5.0 | 24. |
| 0.0 | -2.0 | 0.0 | 266./87./-62. | 3.7e23 | 5.0 | 24. |
| 0.0 | 2.0 | 0.0 | 224./80./-17. | 3.3e23 | 5.0 | 10. |
| 0.0 | 4.0 | 0.0 | 225./73./-25. | 5.2e23 | 5.1 | 24. |
| 0.0 | 6.0 | 0.0 | 234./82./-40. | 5.0e23 | 5.1 | 24. |
| 0.0 | 8.0 | 0.0 | 76./88./64. | 4.7e23 | 5.1 | 24. |
| 0.0 | 10.0 | 0.0 | 266./87./-62. | 3.7e23 | 5.0 | 24. |
| 0.0 | 0.0 | -10.0 | 227./86./-13. | 3.3e23 | 5.0 | 14. |
| 0.0 | 0.0 | -8.0 | 227./86./-13. | 3.3e23 | 5.0 | 14. |
| 0.0 | 0.0 | -6.0 | 227./86./-13. | 3.3e23 | 5.0 | 14. |
| 0.0 | 0.0 | -4.0 | 227./86./-13. | 3.3e23 | 5.0 | 14. |
| 0.0 | 0.0 | -2.0 | 227./86./-13. | 3.3e23 | 5.0 | 14. |
| 0.0 | 0.0 | 2.0 | 227./86./-13. | 3.3e23 | 5.0 | 14. |
| 0.0 | 0.0 | 4.0 | 50./89./.20. | 3.4e23 | 5.0 | 16. |
| 0.0 | 0.0 | 6.0 | 50./83./20. | 3.7e23 | 5.0 | 18. |
| 0.0 | 0.0 | 8.0 | 51./81./22. | 3.7e23 | 5.0 | 18. |
| 0.0 | 0.0 | 10.0 | 51./82./17. | 3.9e23 | 5.0 | 18. |

Table 2.5: Test of model estimation for 8/11/93 San Felipe event. Mo in dyne-cm, depth in kilometers.

| Model | Str/Dip/Rake | Str/Dip/Rake | Mo | Mw | Depth |
|-------|-------------|-------------|------|------|-------|
| NORM | 227/86/-7 | 317/83/-176 | 2.7e23 | 4.92 | 8 |
| CR | 227/84/-4 | 317/86/-174 | 2.7e23 | 4.92 | 8 |
| GIL7 | 229/86/-9 | 320/81/-176 | 2.5e23 | 4.90 | 8 |
| SOCAL | 229/83/-10 | 320/80/-173 | 3.2e23 | 4.97 | 10 |
| WUS | 228/86/-9 | 319/81/-176 | 3.2e23 | 4.97 | 10 |

average crustal velocity.

### 2.4.3 Depth Test

In some instances, changes in the estimated centroid depth can produce large changes in the moment tensor. Precise depth determination can sometimes be difficult for events located outside the network region. For this reason, the depth test was conducted for the 2/3/94 Idaho event, well outside of the BDSN network. In this case, the moment tensor solution is shown at each trial depth, along with the percent double couple. Table 2.6 illustrates the results.

The best centroid depth determined by the moment tensor solution is 8 km. This is exactly the same as the NEIC depth of 8 km for the event. As the depth is modified, several changes occur. First, seismic scalar moment changes drastically with depth, producing a 0.23 moment magnitude difference between the shallowest and deepest depths tested. Secondly, the mechanism varies only slightly at first from trial depths between 6 and 16 km, but becomes significant at 4 km and 18 km, and produces a completely different mechanism altogether at 20 km. Hence, we see the seismic scalar moment varies significantly with depth, but the mechanism is fairly robust over a wide depth range.

One can get an estimate of how well resolved a particular centroid depth is by looking at the residual vs. depth curve for the event. In general, the sharper the curve, the more reliable the depth estimate. Broad curves indicate large uncertainties. A convenient way of describing this quantity is the percentage above the minimum residual value. An examination of these curves for figures 2.7 – 2.9 show a variety of

Table 2.6: Test of depth determination for 2/3/94 Idaho event. Mo in dyne-cm, depth in kilometers. Asterisk denotes minimum variance.

| Depth | Mo | Mw | Str/Dip/Rake | Perc DC |
|---|---|---|---|---|
| 4 | 9.93e24 | 5.96 | 6/8/-97 | 91 |
| 6 | 8.67e24 | 5.93 | 11/20/-92 | 73 |
| 8 | 8.10e24 | 5.91 | 5/29/-90 | 96 * |
| 10 | 5.23e24 | 5.78 | 14/22/-89 | 100 |
| 12 | 4.73e24 | 5.75 | 17/20/-86 | 69 |
| 14 | 4.56e24 | 5.74 | 19/20/-83 | 50 |
| 16 | 4.45e24 | 5.73 | 25/21/-76 | 29 |
| 18 | 4.41e24 | 5.73 | 50/27/-42 | 9 |
| 20 | 4.46e24 | 5.73 | 330/80/154 | 9 |

results. The Geysers event (figure 2.7) has a sharp residual-depth curve. Only the residuals at depths of 4 km and 6 km satisfy this requirement at levels of 5%, and event 10% above the minimum residual. In the case of the Gilroy event (figure 2.8), this is a rather broad minimum. At the 5% level reasonable depths can be seen down to 16 km, and at the 10% level, a significant portion of the depth range (6 − 18 km) falls in this category. The final example, shown for Parkfield (figure 2.9), is interesting because of the dual minima. The residual values at 18 and 20 km depth are nearly coincident with the 5% level. At the 10% level, the acceptable centroid depths still include only the 8 km value in the upper crust, but also values from 16 - 20 km in the lower crust. In summary, minima that are sharper than the 5% criteria are well constrained, and the 10% criteria might be too strong.

### 2.4.4 Station Coverage Test

Another concern is how well the inversion performs when the station coverage is poor. A test was performed for the 4/25/93 and 4/29/93 Cataract Creek, Arizona earthquakes, using two station sets to perform the inversion. One station set include only BDSN stations, the other set included two stations from the National Seismic Network (NSN). These stations ANMO and TUC, located in Alburqueque, New Mex-

Table 2.7: Test of station coverage for 4/25/93 and 4/29/93 Cataract Creek events. Mo in dyne-cm, depth in kilometers.

| Event | Stations | Mo | Mw | depth |
|-------|----------|------|------|-------|
| 4/25/93 | BDSN only | 2.5e23 | 4.90 | 8 |
| 4/25/93 | BDSN,ANMO,TUC | 1.2e23 | 4.70 | 16 |
| 4/29/93 | BDSN only | 1.6e24 | 5.44 | 8 |
| 4/29/93 | BDSN,ANMO,TUC | 6.8e23 | 5.19 | 16 |

ico and Tucson, Arizona, respectively, greatly improve the azimuthal coverage for the event, expanding the maximum azimuthal spread from only 30 degrees to 210 degrees.

Table 2.7 shows the results of this test. For the two events, the moment tensor solutions change in a similar manner. When the azimuthal coverage is increased, the seismic scalar moment drops considerably, along with a shift in depth from 8 to 16 km. The first change is most likely a function of the second. The increased azimuthal coverage allows the inversion to obtain a better depth, forcing down the moment estimate in the process. In both cases, the mechanism does not change. Other estimates of the moment tensor for this event using other methods indicate basically the same mechanism, as well. Complete waveform modelling obtains $M_o$ estimates of 1.0e23 dyne-cm ($M_w4.6$) and 6.1e23 dyne-cm ($M_w5.2$) for the 4/25 and 4/29 events, respectively (Romanowicz, *et al.*, 1993). These values for the seismic moment are much more in line with those obtained using the better station coverage. In general, better station coverage is always preferred because very small azimuthal coverage can cause problems with the inversion.

### 2.4.5 Inversion Period Test

Certain periods are selected in order to optimize the moment tensor inversion. For example, the periods should be significantly longer than the source duration so that the earthquake is well-approximated as a point source. The earthquake must still have a good signal-to-noise ratio at the selected periods, so care must be taken to avoid using longer periods for smaller events. This is the reason why earthquakes with M > 5.5 are inverted using 25 to 75 second surface waves, while 15 to 45 second

Table 2.8: Test of inversion period for 12/18/95 Double Spring Valley event. Mo in dyne-cm, depth in kilometers. Asterisk denotes normal period range used for an event this size.

| Period | Str/Dip/Rake | Str/Dip/Rake | depth | Mo | Mw |
|--------|--------------|--------------|-------|--------|--------|
| 15 - 25 | 128/59/141 | 240/58/38 | 14. | 1.96e23 | 4.83 |
| 15 - 45 | 130/66/147 | 235/60/28 | 14. | 2.10e23 | 4.85 * |
| 25 - 45 | 319/81/-157 | 225/67/-10 | 14. | 2.78e23 | 4.93 |
| 25 - 75 | 315/85/205 | 223/64/-5 | 14. | 3.00e23 | 4.95 |
| 45 - 75 | 114/42/191 | 16/83/-49 | 14. | 5.97e23 | 5.15 |

waves are used for smaller earthquakes. This test shows the result of using a variety of period ranges for an event.

Table 2.8 shows the case of a M4.8 aftershock of the Double Spring Valley earthquake sequence (12/18/95). This particular event was chosen because it was a mid-level event which should have some small signal in the longest inversion periods that are tested, but at a much higher signal-to-noise ratio. The solutions determined using the shortest period ranges, including the period range normally used for an event this size, basically give the same normal solution. As longer period data is included, the solutions evolve into a strike-slip event, which does not agree with the mechanism as determined using other methods (Dreger, personal communication). In this case, at the longest periods, the farthest stations are contributing significant noise which results in changing the mechanism as well as increasing the seismic scalar moment significantly.

### 2.4.6 Attenuation Test

Synthetic tests were performed to determine the effect of changes in the quality factor Q (in all of these cases $Q_p$ is approximated by 9*$Q_s$/4). Table 2.9 shows the changes, or rather lack of changes, in the moment tensor solution corresponding to changes in the attenuation parameter. The results show that attenuation is a highly insensitive parameter. Changes in the $Q_s$ ranging from 200 to 950 have little or no effect on either the mechanism or the seismic scalar moment. The reason is probably that the periods used in the moment tensor inversion (greater than 15 seconds) have

Table 2.9: Test of attenuation factor for 7/12/95 San Benito (top) and 6/18/95 Quincy (bottom) events. Mo in dyne-cm, depth in kilometers.

| Qs (Q) | Str/Dip/Rake | Str/Dip/Rake | depth | Mo | Mw |
|---|---|---|---|---|---|
| 200 | 314/80/-147 | 218/58/-12 | 8. | 1.4e22 | 4.06 |
| 350 | 314/83/-146 | 219/56/-8 | 8. | 1.3e22 | 4.04 |
| 500 | 314/83/-146 | 219/56/-8 | 8. | 1.3e22 | 4.04 |
| 650 | 314/83/-146 | 219/56/-8 | 8. | 1.3e22 | 4.04 |
| 800 | 314/83/-146 | 219/56/-8 | 8. | 1.3e22 | 4.04 |
| 950 | 314/82/-147 | 219/57/-9 | 8. | 1.3e22 | 4.04 |
| 200 | 207/74/-15 | 301/76/-164 | 8. | 1.5e22 | 4.08 |
| 350 | 207/76/-16 | 301/75/-165 | 8. | 1.5e22 | 4.08 |
| 500 | 207/76/-17 | 301/74/-165 | 8. | 1.5e22 | 4.08 |
| 650 | 208/76/-17 | 302/74/-165 | 8. | 1.5e22 | 4.08 |
| 800 | 208/77/-17 | 302/73/-166 | 8. | 1.5e22 | 4.08 |
| 950 | 208/77/-17 | 302/73/-166 | 8. | 1.5e22 | 4.08 |

such large wavelengths that the number of cycles over the typical distance ranges that are used (in this case 100–600 km) is small.

Dreger and Helmberger [1993] have compared various models and have found that changes in velocity model parameters, such as the average crustal velocity, can have large effects on the inversion. The effect in attenuation, therefore, is believed to be secondary to the much larger effects of the velocity models (i.e. average crustal velocity) and inversion methods.

## 2.4.7   Test Conclusions

In general, the inversion method is not extremely sensitive to conditions that may exist when generating a near-real time moment tensor solution. The inversion gives fairly reasonable results for locations that are not too far from the refined location. Very poor locations, however, do pose problems for the solution. The inversion must have enough depth resolution to constrain the proper solution. Small discrepancies in source depth do not, in general, result in large changes in the solution. Depth

resolution is not good enough to warrant the grid search at finer intervals than 2 km.

The particular periods used in the inversion are not very important, as long as the signal-to-noise ratio is high in that period range. This is relatively easy to determine empirically for earthquakes in a particular area. One parameter that does seem to be critical in the estimation of moment using the regional surface wave moment tensor method is a reasonable azimuthal coverage of stations. Poor azimuthal coverage is equivalent to a sparse station inversion. Large variations in seismic scalar moment are a consequence of poor azimuthal coverage, although the mechanism still seems stable.

Using models that are appropriate for a particular region are essential for the inversion. Inappropriate models can result in large shifts in the phase over several periods and will affect the mechanism of the solutions as well as the selection of depth. It is critical to estimate the crustal thickness and average crustal velocities of a region, although the inversion is generally not very dependent on parameters such as the velocity of the uppermost crust and the values of Q used in the model. One reason that the relatively few regional models have been effective is that, by modelling at a tectonic level, they successfully approximate the variations in crustal thickness and average crustal velocity of California's complicated structure. A finer regionalization, although desirable, would represent fine tuning of the largest significant model variations.

# Chapter 3

# Results and Applications of Regional Moment Tensors

In this chapter, results and applications of the regional moment tensors are presented, starting with tables and maps of the moment tensors, which are organized first by time and then by area for the most active regions in Northern and Central California. In addition, moment tensor solutions are used to study the state of stress in the crust. Finally, studies of particular earthquake sequences are made using the moment tensor solutions as a basis for further investigations.

## 3.1   Moment Tensors for Events

This section lists and plots all of the events whose moment tensor solution was calculated using the regional surface wave method over a 4 year period from 1992 to 1995. There are a total of 186 events computed in this manner. Earthquakes are grouped by year. As paths became better calibrated and more broadband stations became available, the effective threshold for moment tensor determination was lowered. In addition, studying particular earthquake sequences was a motivation for performing large numbers of moment tensor inversions. Subsequently, a greater number of solutions were calculated in later years. Earthquake size ranged from a seismic scalar moment of 9.3 x $10^{26}$ dyne-cm ($M_w$ 7.3) for the Landers earthquake to 9.7 x $10^{20}$ dyne-cm ($M_w$ 3.3) for a small Mammoth Lakes event, spanning about six orders of magnitude in moment.

### 3.1.1   1992 Events

Figure 3.1 and table 3.1 show the 20 events calculated in 1992. Major earthquakes occurring that year included three events near the Mendocino Triple Junction, and the Landers and Big Bear sequences. The Mendocino events included a M 7.1 normal event on April 25 and two strike-slip events (M 6.5, M 6.7) on April 26. In southern California, the Landers (M 7.3) and Big Bear sequences of June 28 were both strike-slip events on nearly perpendicular fault systems. The Landers earthquake was the largest event to occur in the contiguous United States since the 18 August, 1959 Hebgen Lake, Montana, event (M 7.7), and the largest event in California since the 21 July, 1952 Kern County event (M 7.8). The Central Coast Ranges and Walker Lane were relatively quiet during this time period.

### 3.1.2   1993 Events

The 44 events calculated in 1993 are shown in figure 3.2 and table 3.2. A normal event in Eureka Valley (M 6.0) on May 17 (see section 3.4.1) and two normal events near Klamath Falls, Oregon (M 5.9, M 6.0) on September 21 (see section 3.4.2) register as the most significant events of the year. In addition, the seismicity around the Central Coast Ranges increased, with a string of strike-slip earthquakes from Santa Rosa down to Parkfield, including two strike-slip events: a M 5.1 event near Gilroy (January 16) and a M 5.0 event near San Felipe (August 11), both on the Calaveras fault. Walker Lane had a dramatic increase in seismicity, but it was a relatively quiet year near the Mendocino Triple Junction and in Southern California.

### 3.1.3   1994 Events

Figure 3.3 and table 3.3 show the 79 moment tensors calculated for events in 1994. Significant earthquakes occurred near Northridge, along the Mendocino Fault, and near Double Spring Flat, Nevada. The reverse event at Northridge (M 6.7) on January 17 killed 57 people and caused about $20 billion in damage (see section 3.4.3). A M 6.9 strike-slip event occurred on September 1 along the Mendocino Fault separating the Pacific and Gorda Plates (see section 3.4.4). Finally, on September 12, a M 6

Table 3.1: Source parameters for 1992 events.

| Location | Date | O.T. (UTC) | Lat. ($^o$N) | Lon. ($^o$W) | Depth (km) | $M_L$ | $M_w$ | $M_o$ (N-m) | Str/Dip/Rake |
|---|---|---|---|---|---|---|---|---|---|
| Mendocino | 030892 | 22:17 | 40.26 | 124.23 | 12 | 5.3 | 5.2 | $6.8 * 10^{23}$ | 102/74/145 |
| JoshuaTree | 042392 | 04:50 | 33.96 | 116.32 | 10 | 6.7 | 6.2 | $2.1 * 10^{25}$ | 169/86/166 |
| Mendocino | 042592 | 18:06 | 40.33 | 124.23 | 10 | 6.4 | 7.1 | $4.5 * 10^{26}$ | 349/13/106 |
| Mendocino | 042692 | 07:41 | 40.44 | 124.57 | 10 | 6.5 | 6.5 | $7.1 * 10^{25}$ | 213/85/14 |
| Mendocino | 042692 | 11:18 | 40.39 | 124.57 | 10 | 6.5 | 6.7 | $1.2 * 10^{26}$ | 222/88/0 |
| Mendocino | 050592 | 10:46 | 40.28 | 124.34 | 12 | 4.5 | 4.4 | $4.1 * 10^{22}$ | -6/73/-17 |
| Mendocino | 060592 | 21:46 | 40.29 | 124.55 | 10 | 4.9 | 4.9 | $2.9 * 10^{23}$ | -50/27/-93 |
| Landers | 062892 | 11:57 | 34.20 | 116.44 | 10 | 7.7 | 7.3 | $9.3 * 10^{26}$ | 161/85/-164 |
| BigBear | 062892 | 15:05 | 34.20 | 116.83 | 10 | 6.9 | 6.6 | $7.9 * 10^{25}$ | 307/84/155 |
| SkullMt,NV | 062992 | 10:14 | 36.72 | 116.29 | 8 | 6.1 | 5.6 | $3.5 * 10^{24}$ | 43/66/287 |
| Fallon,NV | 072092 | 20:09 | 39.34 | 119.11 | 8 | 4.5 | 4.5 | $7.2 * 10^{22}$ | 328/86/-141 |
| Coalinga | 091692 | 06:14 | 35.97 | 119.87 | 8 | 4.3 | 4.1 | $1.4 * 10^{22}$ | -50/48/111 |
| Geysers | 091992 | 23:04 | 38.86 | 122.79 | 4 | 4.9 | 4.8 | $1.7 * 10^{23}$ | 175/85/172 |
| MonoLake | 101092 | 17:54 | 37.99 | 118.58 | 6 | 4.1 | 3.9 | $9.7 * 10^{21}$ | 167/75/160 |
| Parkfield | 102092 | 05:28 | 35.93 | 120.48 | 10 | 4.3 | 4.6 | $9.6 * 10^{22}$ | 234/89/353 |
| Quincy | 102092 | 13:02 | 39.98 | 120.76 | 10 | 3.9 | 3.6 | $3.1 * 10^{21}$ | 133/80/150 |
| BigBear | 112792 | 22:17 | 34.34 | 116.89 | 7 | 5.3 | 5.4 | $1.2 * 10^{24}$ | 130/70/171 |
| BigBear | 120492 | 02:08 | 34.37 | 116.90 | 6 | 5.9 | 5.3 | $9.2 * 10^{23}$ | -77/46/106 |
| SanLeandro | 122092 | 21:05 | 37.85 | 122.14 | 12 | 3.7 | 3.9 | $7.0 * 10^{21}$ | -20/71/103 |
| Quincy | 122592 | 04:25 | 39.95 | 120.84 | 14 | 4.2 | 3.8 | $5.8 * 10^{21}$ | 295/88/191 |

Epicentral and local magnitude information from the UCB/USGS Northern California Earthquake Data Center (NCEDC). Source parameters, centroid depth, seismic scalar moment ($M_o$), and moment magnitude ($M_w$) as computed from regional surface wave moment tensor method.

Figure 3.1: Moment tensors for 1992 events.

Table 3.2: Source parameters for 1993 events.

| Location | Date | O.T. (UTC) | Lat. ($^o$N) | Lon. ($^o$W) | Depth (km) | $M_L$ | $M_w$ | $M_o$ (N-m) | Str/Dip/Rake |
|---|---|---|---|---|---|---|---|---|---|
| MonoLake | 011193 | 13:32 | 38.02 | 118.74 | 6 | 3.8 | 3.9 | $9.1 * 10^{21}$ | 270/82/7 |
| MonoLake | 011193 | 18:19 | 38.05 | 118.73 | 8 | 4.0 | 3.9 | $8.2 * 10^{21}$ | 168/83/163 |
| Kensington | 011593 | 11:13 | 37.92 | 122.29 | 5 | 3.3 | 3.4 | $1.6 * 10^{21}$ | 296/80/347 |
| Gilroy | 011693 | 06:29 | 37.03 | 121.46 | 8 | 5.1 | 5.1 | $4.5 * 10^{23}$ | 144/86/-179 |
| Geysers | 011893 | 23:27 | 38.84 | 122.83 | 6 | 3.9 | 4.1 | $1.6 * 10^{22}$ | 4/42/-93 |
| Geysers | 011993 | 00:24 | 38.84 | 122.78 | 6 | 3.6 | 3.9 | $8.2 * 10^{21}$ | 2/51/-102 |
| PyramidLake,NV | 021093 | 21:48 | 40.40 | 119.58 | 12 | 4.8 | 4.5 | $6.0 * 10^{22}$ | 213/39/-66 |
| Geysers | 021593 | 18:04 | 38.79 | 122.76 | 6 | 3.5 | 4.2 | $2.2 * 10^{22}$ | 325/86/-121 |
| Geysers | 031693 | 03:59 | 38.79 | 122.77 | 10 | 3.5 | 4.0 | $1.2 * 10^{22}$ | 203/72/-69 |
| Parkfield | 040493 | 05:21 | 35.95 | 120.51 | 8 | 4.4 | 4.6 | $7.8 * 10^{22}$ | 143/89/179 |
| EurekaValley | 051793 | 23:20 | 37.17 | 117.77 | 10 | 6.2 | 6.0 | $1.3 * 10^{25}$ | 20/59/-103 |
| EurekaValley | 051893 | 01:03 | 37.15 | 117.76 | 10 | 5.3 | 5.1 | $4.6 * 10^{23}$ | 199/55/-101 |
| EurekaValley | 051893 | 23:48 | 37.06 | 117.78 | 10 | 5.3 | 4.9 | $2.4 * 10^{23}$ | 175/42/-149 |
| EurekaValley | 051993 | 03:14 | 37.15 | 117.79 | 6 | 4.9 | 4.5 | $6.5 * 10^{22}$ | 179/61/-109 |
| EurekaValley | 051993 | 14:13 | 37.14 | 117.77 | 6 | 5.2 | 4.9 | $2.2 * 10^{23}$ | 191/65/-88 |
| EurekaValley | 052093 | 01:17 | 37.19 | 117.76 | 6 | 4.2 | 4.3 | $3.6 * 10^{22}$ | 166/56/-118 |
| Coso | 052093 | 20:14 | 36.10 | 117.69 | 6 | 4.6 | 4.6 | $9.0 * 10^{22}$ | 320/61/-134 |
| Bakersfield | 052893 | 04:47 | 35.15 | 119.10 | 24 | 5.1 | 4.8 | $1.7 * 10^{23}$ | 99/71/132 |
| Petrolia | 072793 | 21:17 | 40.29 | 124.61 | 6 | 3.9 | 4.4 | $4.1 * 10^{22}$ | 97/65/-132 |
| MammothLakes | 081193 | 05:48 | 37.53 | 118.88 | 4 | 4.5 | 4.2 | $2.4 * 10^{22}$ | 165/39/-77 |
| SanFelipe | 081193 | 22:33 | 37.31 | 121.67 | 8 | 4.6 | 5.0 | $3.2 * 10^{23}$ | 227/86/-7 |
| BigBear | 082193 | 01:46 | 34.03 | 116.32 | 8 | 4.8 | 4.6 | $8.1 * 10^{22}$ | 11/54/-119 |
| Geysers | 082393 | 15:03 | 38.81 | 122.83 | 6 | 3.5 | 4.2 | $2.4 * 10^{22}$ | 189/56/-88 |
| LakeIsabella | 090693 | 10:32 | 36.00 | 118.37 | 4 | 3.5 | 3.7 | $3.7 * 10^{21}$ | 333/79/-114 |
| RogersCreek | 091993 | 20:49 | 38.12 | 122.45 | 4 | 3.3 | 3.5 | $1.7 * 10^{21}$ | 156/62/-148 |
| RogersCreek | 091993 | 21:10 | 38.12 | 122.45 | 4 | 3.4 | 3.6 | $2.8 * 10^{21}$ | 153/76/-139 |
| KlamathFalls,OR | 092193 | 03:28 | 42.14 | 122.10 | 12 | 6.1 | 5.9 | $8.4 * 10^{24}$ | 353/37/-59 |
| KlamathFalls,OR | 092193 | 04:16 | 42.27 | 122.01 | 4 | 4.3 | 4.6 | $10.0 * 10^{22}$ | 3/23/-68 |
| KlamathFalls,OR | 092193 | 05:45 | 42.22 | 122.17 | 12 | 5.8 | 6.0 | $1.4 * 10^{25}$ | 9/37/-46 |
| KlamathFalls,OR | 092193 | 06:14 | 42.39 | 122.09 | 8 | 4.8 | 4.8 | $1.7 * 10^{23}$ | 7/42/-89 |
| KlamathFalls,OR | 092393 | 06:21 | 42.30 | 122.04 | 8 | 4.8 | 4.6 | $9.3 * 10^{22}$ | 6/47/-62 |

Same as Table 3.1.

# 1993 Events
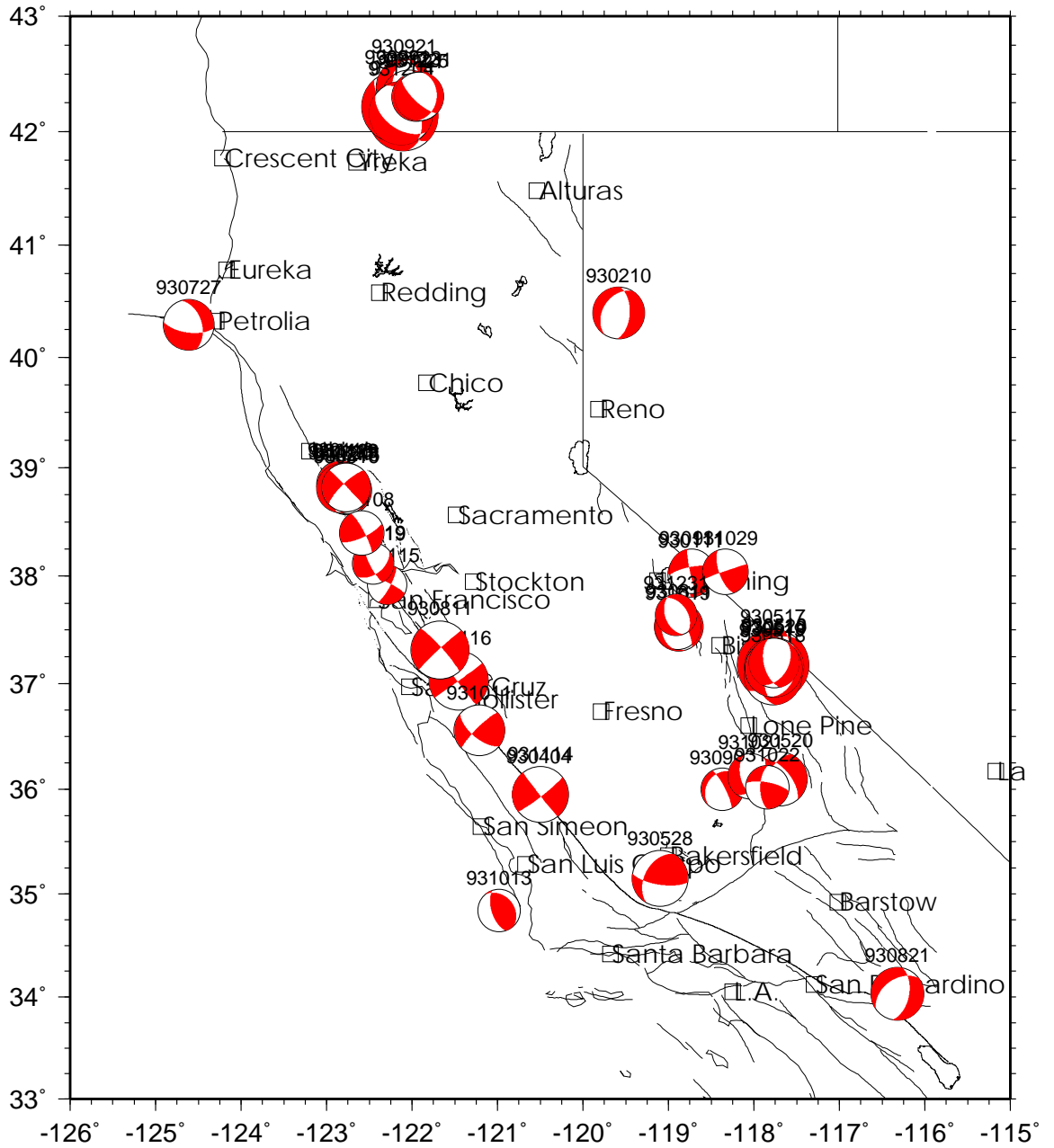


Figure 3.2: Moment tensors for 1993 events.

Figure 3.3: Moment tensors for 1994 events.

Table 3.2: (continued) Source parameters for 1993 events.

| | | | | | | | | | |
|---|---|---|---|---|---|---|---|---|---|
| Pinnacles | 101193 | 07:19 | 36.56 | 121.21 | 6 | 4.2 | 4.3 | $3.9 * 10^{22}$ | 130/64/169 |
| SantaMaria | 101393 | 09:54 | 34.84 | 120.98 | 6 | 3.6 | 3.7 | $4.6 * 10^{21}$ | 162/61/102 |
| Mammoth | 101993 | 04:47 | 37.53 | 118.89 | 6 | 3.7 | 4.0 | $1.1 * 10^{22}$ | 323/67/-111 |
| OwensValley | 102193 | 14:37 | 36.12 | 118.04 | 6 | 3.9 | 4.0 | $1.0 * 10^{22}$ | 164/53/-127 |
| Coso | 102293 | 16:30 | 36.02 | 117.84 | 4 | 3.8 | 3.8 | $5.2 * 10^{21}$ | 181/62/158 |
| MonoBasin | 102993 | 11:53 | 38.04 | 118.33 | 4 | 4.0 | 3.9 | $9.6 * 10^{21}$ | 251/88/23 |
| SantaRosa | 110893 | 20:20 | 38.40 | 122.59 | 22 | 3.3 | 3.8 | $6.5 * 10^{21}$ | 332/80/163 |
| Parkfield | 111493 | 12:25 | 35.95 | 120.50 | 8 | 4.8 | 4.8 | $1.9 * 10^{23}$ | 142/88/-174 |
| Geysers | 112993 | 10:47 | 38.82 | 122.77 | 20 | 3.8 | 4.2 | $2.2 * 10^{22}$ | 316/88/-166 |
| KlamathFalls,OR | 120493 | 22:15 | 42.16 | 122.13 | 10 | 5.4 | 5.4 | $1.5 * 10^{24}$ | 330/42/-72 |
| KlamathFalls,OR | 122593 | 12:33 | 42.30 | 121.95 | 4 | 3.5 | 4.2 | $2.3 * 10^{22}$ | 147/65/-108 |
| KlamathFalls,OR | 123193 | 18:08 | 42.31 | 121.92 | 4 | 3.6 | 4.3 | $2.7 * 10^{22}$ | 134/71/-112 |
| MammothLakes | 123193 | 21:29 | 37.62 | 118.92 | 8 | 3.7 | 3.6 | $3.1 * 10^{21}$ | 159/46/-81 |

Same as Table 3.1.

strike-slip event occurred at Double Spring Flat, along the California-Nevada border
(see section 3.4.5). The Central Coast Ranges continued their high seismic activity.

### 3.1.4   1995 Events

Moment tensors determined in 1995 are shown in figure 3.4 and table 3.4 for
44 events. The only major event that occurred this year was a M 6.7 strike-slip
earthquake, on February 2, located well offshore in the Gorda plate. However, there
were several other events of interest. On April 23 the Bay Area experienced a M 5.0
strike-slip event on the San Andreas Fault near the Pinnacles, and on September 4
a M 4.9 strike-slip event near Healdsburg. A pair of large events (M 5.3 and M 5.5)
occurred near the town of Ridgecrest in the southern portion of the Walker Lane Belt.
The rest of Southern California has been relatively quiet, with aftershock sequences
of Northridge and Landers still continuing. One curious observation is the occurrence
of 3 events with centroid depths in the $30 - 50$ km depth range, all of them strike-slip
events.

Table 3.3: Source parameters for 1994 events.

| Location | Date | O.T. (UTC) | Lat. ($^o$N) | Lon. ($^o$W) | Depth (km) | $M_L$ | $M_w$ | $M_o$ (N-m) | Str/Dip/Rake |
|---|---|---|---|---|---|---|---|---|---|
| SantaMonica | 010994 | 23:00 | 34.00 | 118.50 | 18 | 3.7 | 3.9 | $7.0*10^{21}$ | 304/83/-169 |
| Watsonville | 011194 | 10:53 | 36.99 | 121.72 | 8 | 4.2 | 4.1 | $2.0*10^{22}$ | 157/27/336 |
| Northridge | 011794 | 12:30 | 34.24 | 118.56 | 14 | 6.7 | 6.7 | $1.4*10^{26}$ | 87/53/59 |
| Northridge | 011794 | 13:26 | 34.31 | 118.45 | 10 | 4.7 | 4.9 | $2.3*10^{23}$ | 80/58/95 |
| Northridge | 011794 | 17:56 | 34.23 | 118.57 | 10 | 4.6 | 4.6 | $8.2*10^{22}$ | 137/48/113 |
| Northridge | 011794 | 20:46 | 34.32 | 118.56 | 10 | 5.3 | 5.0 | $4.0*10^{23}$ | 333/78/-153 |
| Northridge | 011794 | 23:33 | 34.33 | 118.69 | 4 | 6.1 | 5.9 | $10.0*10^{24}$ | 98/49/43 |
| Northridge | 011894 | 00:43 | 34.38 | 118.69 | 10 | 5.4 | 5.2 | $6.4*10^{23}$ | 89/53/98 |
| Northridge | 011894 | 04:01 | 34.34 | 118.63 | 4 | 4.6 | 4.4 | $4.4*10^{22}$ | 121/35/69 |
| Northridge | 011894 | 13:24 | 34.28 | 118.57 | 4 | 4.2 | 4.3 | $3.2*10^{22}$ | 244/58/343 |
| Northridge | 011894 | 15:23 | 34.30 | 118.59 | 8 | 5.0 | 4.8 | $1.6*10^{23}$ | 126/59/106 |
| Northridge | 011994 | 04:40 | 34.37 | 118.55 | 6 | 4.5 | 4.3 | $3.2*10^{22}$ | 148/44/112 |
| Northridge | 011994 | 09:13 | 34.31 | 118.75 | 8 | 4.0 | 3.9 | $7.9*10^{21}$ | 108/46/82 |
| Northridge | 011994 | 14:09 | 34.23 | 118.50 | 10 | 4.4 | 4.5 | $6.2*10^{22}$ | 86/67/99 |
| Northridge | 011994 | 21:09 | 34.36 | 118.71 | 10 | 5.5 | 5.2 | $8.7*10^{23}$ | 90/58/79 |
| Northridge | 011994 | 21:11 | 34.37 | 118.70 | 10 | 4.9 | 4.8 | $1.8*10^{23}$ | 300/33/130 |
| Northridge | 012194 | 18:39 | 34.30 | 118.46 | 10 | 4.7 | 4.5 | $6.4*10^{22}$ | 359/59/130 |
| Northridge | 012494 | 04:15 | 34.34 | 118.55 | 8 | 4.7 | 4.4 | $4.5*10^{22}$ | 115/63/110 |
| Northridge | 012494 | 05:50 | 34.36 | 118.63 | 10 | 4.3 | 4.2 | $2.0*10^{22}$ | 328/44/137 |
| Northridge | 012494 | 05:54 | 34.37 | 118.63 | 10 | 4.4 | 4.1 | $1.9*10^{22}$ | 317/46/134 |
| Northridge | 012994 | 11:20 | 34.38 | 118.68 | 8 | 5.3 | 5.2 | $7.5*10^{23}$ | 244/87/7 |
| Bishop | 020194 | 08:01 | 37.28 | 118.35 | 12 | 4.2 | 4.0 | $1.2*10^{22}$ | 142/79/160 |
| DeathValley | 020494 | 00:10 | 36.37 | 117.08 | 16 | 4.1 | 3.9 | $7.1*10^{21}$ | 229/82/27 |
| Mendocino | 022194 | 13:40 | 40.42 | 125.61 | 24 | 4.1 | 4.5 | $7.3*10^{22}$ | 88/87/-159 |
| Coalinga | 022394 | 06:58 | 36.29 | 120.35 | 8 | 3.5 | 3.7 | $4.0*10^{21}$ | 322/46/87 |
| StoneCanyon | 030194 | 02:45 | 36.64 | 121.25 | 6 | 3.4 | 3.9 | $8.3*10^{21}$ | 45/79/-32 |
| Petrolia | 030294 | 10:21 | 40.66 | 125.41 | 20 | 3.8 | 4.0 | $10.0*10^{21}$ | 312/81/166 |
| Markleeville | 030794 | 16:49 | 38.84 | 119.76 | 6 | 3.9 | 3.7 | $4.1*10^{21}$ | 339/61/-126 |
| Mendocino | 031394 | 16:59 | 40.37 | 125.29 | 22 | 4.3 | 4.7 | $1.4*10^{23}$ | 191/71/51 |
| Northridge | 032094 | 21:20 | 34.28 | 118.47 | 8 | 5.4 | 5.2 | $6.6*10^{23}$ | 305/49/87 |
| Coalinga | 033194 | 19:59 | 36.18 | 120.31 | 6 | 4.2 | 4.4 | $4.3*10^{22}$ | 308/77/104 |
| Coalinga | 033194 | 20:02 | 36.16 | 120.30 | 6 | 4.1 | 4.4 | $4.0*10^{22}$ | 305/76/100 |

Same as Table 3.1.

Table 3.3: (continued) Source parameters for 1994 events.

| | | | | | | | | | |
|---|---|---|---|---|---|---|---|---|---|
| SanBernadino | 040694 | 19:01 | 34.19 | 117.10 | 6 | 5.0 | 4.6 | $7.6 * 10^{22}$ | 194/83/-51 |
| Coalinga | 042194 | 16:37 | 36.29 | 120.43 | 8 | 4.4 | 4.4 | $4.6 * 10^{22}$ | 302/68/69 |
| Pinnacles | 051994 | 16:45 | 36.53 | 121.27 | 8 | 3.9 | 4.1 | $1.9 * 10^{22}$ | 224/87/21 |
| Mendocino | 052494 | 20:11 | 40.94 | 124.92 | 20 | 3.4 | 3.6 | $3.2 * 10^{21}$ | 327/82/167 |
| Northridge | 052594 | 12:56 | 34.31 | 118.39 | 8 | 4.7 | 4.4 | $4.0 * 10^{22}$ | 114/56/100 |
| Mammoth | 060894 | 09:02 | 37.57 | 118.87 | 6 | 3.4 | 3.3 | $9.7 * 10^{20}$ | 1/73/-43 |
| Landers | 061694 | 16:24 | 34.27 | 116.41 | 6 | 4.7 | 4.7 | $1.2 * 10^{23}$ | 54/86/-6 |
| Petrolia | 061994 | 10:39 | 40.36 | 124.57 | 18 | 4.7 | 4.9 | $2.7 * 10^{23}$ | 30/87/-4 |
| Berkeley | 062694 | 08:42 | 37.90 | 122.32 | 8 | 4.1 | 4.2 | $2.1 * 10^{22}$ | 327/81/-163 |
| Mendocino | 070294 | 13:43 | 40.25 | 124.67 | 12 | 3.4 | 4.0 | $9.8 * 10^{21}$ | 4/83/39 |
| Bishop | 070394 | 23:42 | 37.85 | 118.31 | 8 | 3.6 | 3.6 | $3.2 * 10^{21}$ | 356/88/170 |
| Landers | 080194 | 21:34 | 34.63 | 116.52 | 20 | 4.6 | 4.5 | $5.5 * 10^{22}$ | 179/84/170 |
| TresPinos | 082894 | 01:22 | 36.81 | 121.22 | 10 | 3.9 | 4.0 | $9.7 * 10^{21}$ | 134/83/156 |
| Geysers | 082994 | 05:09 | 38.81 | 122.82 | 6 | 3.1 | 4.1 | $1.6 * 10^{22}$ | 202/50/-75 |
| Mendocino | 090194 | 15:15 | 40.44 | 125.90 | 8 | 6.7 | 6.9 | $2.9 * 10^{26}$ | 5/79/13 |
| Modesto | 090794 | 19:09 | 37.54 | 121.27 | 8 | 4.1 | 4.0 | $1.1 * 10^{22}$ | 285/62/73 |
| MendocinoFZ | 090994 | 16:18 | 40.37 | 125.95 | 14 | 3.8 | 4.0 | $1.2 * 10^{22}$ | 271/86/175 |
| DoubleSpringFlat | 091294 | 12:23 | 38.86 | 119.77 | 12 | 6.0 | 6.1 | $1.4 * 10^{25}$ | 306/88/-167 |
| DoubleSpringFlat | 091294 | 17:14 | 38.90 | 119.82 | 8 | 4.2 | 4.3 | $2.8 * 10^{22}$ | 191/55/-73 |
| DoubleSpringFlat | 091294 | 23:57 | 38.76 | 119.72 | 6 | 5.3 | 5.3 | $8.8 * 10^{23}$ | 356/59/-87 |
| DoubleSpringFlat | 091394 | 06:15 | 38.71 | 120.08 | 6 | 4.4 | 4.3 | $3.1 * 10^{22}$ | 158/57/-94 |
| DoubleSpringFlat | 091394 | 07:33 | 38.77 | 119.66 | 8 | 3.7 | 3.7 | $3.7 * 10^{21}$ | 146/81/-170 |
| DoubleSpringFlat | 091394 | 11:50 | 38.65 | 119.71 | 20 | 4.2 | 4.0 | $9.7 * 10^{21}$ | 121/89/-159 |
| DoubleSpringFlat | 091394 | 21:22 | 38.91 | 119.89 | 20 | 4.4 | 4.2 | $2.4 * 10^{22}$ | 49/88/-12 |
| DoubleSpringFlat | 091794 | 02:59 | 38.84 | 119.32 | 12 | 4.1 | 3.4 | $1.5 * 10^{21}$ | 176/61/-65 |
| DoubleSpringFlat | 091794 | 12:36 | 38.72 | 119.65 | 4 | 4.2 | 3.8 | $6.3 * 10^{21}$ | 49/72/-49 |
| DoubleSpringFlat | 091994 | 07:25 | 38.74 | 119.62 | 8 | 4.0 | 3.8 | $6.2 * 10^{21}$ | 21/74/-37 |
| DoubleSpringFlat | 091994 | 14:06 | 38.82 | 119.84 | 12 | 4.0 | 3.6 | $3.2 * 10^{21}$ | 308/82/-162 |
| DoubleSpringFlat | 092094 | 15:38 | 38.74 | 119.64 | 8 | 4.9 | 4.5 | $7.3 * 10^{22}$ | 139/83/171 |
| DoubleSpringFlat | 092094 | 15:40 | 38.74 | 119.70 | 8 | 4.9 | 4.6 | $10.0 * 10^{22}$ | 221/87/4 |
| DoubleSpringFlat | 092194 | 06:51 | 38.80 | 119.67 | 12 | 3.8 | 3.7 | $4.0 * 10^{21}$ | 28/70/38 |
| DoubleSpringFlat | 092194 | 18:47 | 38.70 | 119.66 | 6 | 3.9 | 3.9 | $9.4 * 10^{21}$ | 18/64/-94 |

Same as Table 3.1.
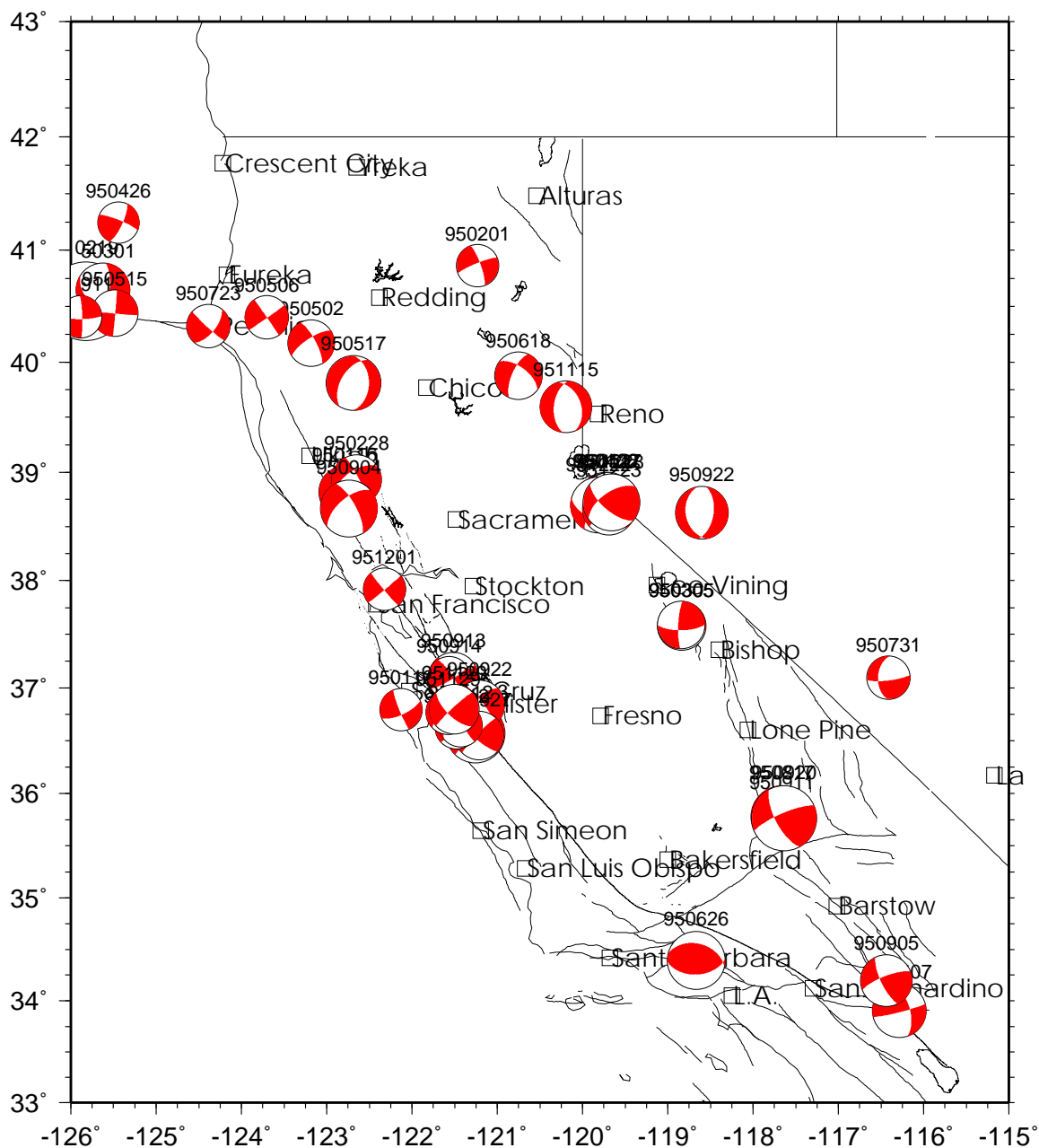
Figure 3.4: Moment tensors for 1995 events.

Table 3.3: (continued) Source parameters for 1994 events.

| | | | | | | | | | |
|---|---|---|---|---|---|---|---|---|---|
| MendocinoFZ | 092194 | 02:09 | 40.42 | 124.69 | 20 | 4.3 | 4.6 | $9.6 * 10^{22}$ | 97/88/171 |
| Eureka | 092794 | 11:25 | 40.65 | 124.07 | 24 | 3.6 | 3.8 | $6.1 * 10^{21}$ | 30/68/-82 |
| DoubleSpringFlat | 101094 | 03:07 | 38.74 | 119.63 | 12 | 4.8 | 4.4 | $4.9 * 10^{22}$ | 31/88/-12 |
| SanJuanBautista | 101194 | 23:13 | 36.86 | 121.62 | 8 | 3.6 | 3.8 | $5.4 * 10^{21}$ | 45/72/-30 |
| MendocinoFZ | 101494 | 00:57 | 40.32 | 124.62 | 20 | 4.2 | 4.5 | $5.8 * 10^{22}$ | 274/86/175 |
| Ridgecrest | 101994 | 00:49 | 35.51 | 117.49 | 8 | 4.1 | 3.9 | $6.9 * 10^{21}$ | 235/82/14 |
| MendocinoFZ | 111394 | 07:53 | 40.39 | 125.34 | 16 | 3.7 | 4.0 | $1.2 * 10^{22}$ | 192/87/6 |
| Mendocino | 111494 | 01:28 | 40.35 | 124.48 | 20 | 4.3 | 4.6 | $8.3 * 10^{22}$ | 281/87/166 |
| Klamath | 111794 | 20:29 | 42.26 | 122.26 | 8 | 4.4 | 4.4 | $3.8 * 10^{22}$ | 182/50/-89 |
| DoubleSpringFlat | 111894 | 20:50 | 39.13 | 119.79 | 14 | 4.4 | 4.1 | $1.4 * 10^{22}$ | 224/78/26 |
| AlumRock | 120494 | 10:35 | 37.35 | 121.71 | 10 | 3.7 | 3.8 | $6.4 * 10^{21}$ | 223/87/-7 |
| AlumRock | 120794 | 03:21 | 37.35 | 121.73 | 10 | 3.8 | 4.1 | $1.6 * 10^{22}$ | 43/88/9 |
| Parkfield | 122094 | 10:27 | 35.90 | 120.49 | 6 | 5.0 | 5.0 | $3.3 * 10^{23}$ | 227/87/-10 |
| DoubleSpringFlat | 122194 | 05:50 | 38.71 | 119.73 | 6 | 4.2 | 4.1 | $1.6 * 10^{22}$ | 6/49/-86 |
| Eureka | 122694 | 14:10 | 40.81 | 124.44 | 20 | 5.1 | 5.5 | $2.1 * 10^{24}$ | 247/67/-27 |

Same as Table 3.1.

Table 3.4: Source parameters for 1995 events.

| Location | Date | O.T. (UTC) | Lat. ($^o$N) | Lon. ($^o$W) | Depth (km) | $M_L$ | $M_w$ | $M_o$ (N-m) | Str/Dip/Rake |
|---|---|---|---|---|---|---|---|---|---|
| DoubleSpringFlat | 010695 | 00:12 | 38.76 | 119.73 | 6 | 4.7 | 4.5 | $5.7*10^{22}$ | 6/74/-85 |
| MontereyBay | 011295 | 23:42 | 36.80 | 122.13 | 10 | 3.6 | 3.7 | $4.2*10^{21}$ | 158/83/-160 |
| Geysers | 011695 | 01:34 | 38.82 | 122.79 | 4 | 3.8 | 4.4 | $5.1*10^{22}$ | 215/59/-72 |
| Burney | 020195 | 22:04 | 40.87 | 121.23 | 20 | 3.8 | 3.7 | $3.7*10^{21}$ | 248/81/-12 |
| GordaPlate | 021995 | 04:03 | 40.55 | 125.83 | 20 | 6.3 | 6.7 | $1.1*10^{26}$ | 120/76/165 |
| ClearLake | 022895 | 23:09 | 38.93 | 122.65 | 8 | 4.0 | 4.3 | $3.5*10^{22}$ | 333/82/-148 |
| OffshorePetrolia | 030195 | 10:55 | 40.65 | 125.62 | 4 | 4.2 | 4.7 | $1.1*10^{23}$ | 6/70/-57 |
| Mammoth | 030595 | 00:07 | 37.58 | 118.89 | 10 | 4.9 | 4.2 | $2.1*10^{22}$ | 101/90/139 |
| Mammoth | 030595 | 02:48 | 37.59 | 118.84 | 16 | 4.1 | 4.1 | $1.6*10^{22}$ | 183/79/19 |
| DoubleSpringFlat | 042295 | 14:31 | 38.76 | 119.72 | 6 | 4.5 | 4.5 | $5.6*10^{22}$ | 22/77/-77 |
| Pinnacles | 042395 | 08:41 | 36.57 | 121.26 | 10 | 4.9 | 5.0 | $4.0*10^{23}$ | 223/86/19 |
| GordaPlate | 042695 | 15:22 | 41.24 | 125.44 | 20 | 3.6 | 3.7 | $3.5*10^{21}$ | 292/80/165 |
| Covelo | 050295 | 12:56 | 40.17 | 123.18 | 35 | 3.8 | 4.1 | $1.5*10^{22}$ | 332/74/-161 |
| Petrolia | 050695 | 12:46 | 40.40 | 123.70 | 45 | 3.6 | 3.8 | $6.3*10^{21}$ | 325/89/178 |
| Indio | 050795 | 11:03 | 33.90 | 116.29 | 8 | 5.0 | 4.7 | $1.1*10^{23}$ | 76/85/32 |
| MendocinoFZ | 051595 | 21:57 | 40.44 | 125.49 | 12 | 4.2 | 4.1 | $1.5*10^{22}$ | 95/89/-178 |
| Covelo | 051795 | 02:29 | 39.81 | 122.68 | 6 | 4.3 | 4.7 | $1.2*10^{23}$ | 211/51/-70 |
| DoubleSpringFlat | 052795 | 05:49 | 38.79 | 119.69 | 20 | 4.1 | 3.9 | $9.3*10^{21}$ | 219/85/10 |
| Hollister | 061695 | 04:20 | 36.75 | 121.46 | 8 | 3.9 | 4.0 | $10.0*10^{21}$ | 58/89/6 |
| Quincy | 061895 | 22:23 | 39.88 | 120.75 | 8 | 4.4 | 4.1 | $1.7*10^{22}$ | 204/67/-32 |
| Castaic | 062695 | 08:40 | 34.40 | 118.67 | 10 | 4.9 | 5.0 | $3.1*10^{23}$ | 87/49/79 |
| SanBenito | 071295 | 21:58 | 36.56 | 121.24 | 8 | 4.0 | 4.1 | $1.4*10^{22}$ | 130/89/151 |
| Petrolia | 072395 | 21:21 | 40.33 | 124.39 | 36 | 3.4 | 3.8 | $5.4*10^{21}$ | 132/84/-153 |
| Ridgecrest | 081795 | 22:39 | 35.78 | 117.66 | 8 | 5.2 | 5.3 | $1.1*10^{24}$ | 189/52/-102 |
| Healdsburg | 090495 | 14:16 | 38.67 | 122.74 | 10 | 4.7 | 4.9 | $2.5*10^{23}$ | 331/71/-148 |
| BigBear | 090595 | 20:27 | 34.20 | 116.43 | 4 | 4.7 | 4.4 | $5.3*10^{22}$ | 249/75/18 |
| Petrolia | 091195 | 14:18 | 40.41 | 125.89 | 4 | 3.7 | 3.7 | $4.1*10^{21}$ | 358/83/-10 |
| Ridgecrest | 091195 | 18:37 | 35.78 | 117.66 | 16 | 4.2 | 4.0 | $1.2*10^{22}$ | 242/85/25 |
| Gilroy | 091395 | 20:36 | 37.10 | 121.51 | 8 | 4.3 | 4.3 | $3.2*10^{22}$ | 59/72/23 |
| Gilroy | 091495 | 08:22 | 37.09 | 121.56 | 6 | 3.8 | 3.7 | $4.5*10^{21}$ | 59/80/14 |
| Ridgecrest | 092095 | 23:27 | 35.76 | 117.63 | 8 | 5.5 | 5.5 | $2.3*10^{24}$ | 247/77/23 |
| Hawthorne,NV | 092295 | 14:47 | 38.63 | 118.60 | 8 | 4.6 | 4.6 | $7.5*10^{22}$ | 9/54/-78 |

Same as Table 3.1.

Table 3.4: (continued) Source parameters for 1995 events.

| | | | | | | | | | |
|---|---|---|---|---|---|---|---|---|---|
| TresPinos | 092295 | 16:06 | 36.84 | 121.21 | 8 | 4.1 | 4.3 | $3.1 * 10^{22}$ | 323/77/-155 |
| Pinnacles | 092795 | 16:44 | 36.55 | 121.21 | 10 | 4.2 | 4.2 | $2.2 * 10^{22}$ | 224/83/15 |
| Salinas | 111295 | 16:30 | 36.62 | 121.48 | 8 | 3.6 | 3.7 | $4.2 * 10^{21}$ | 47/85/-49 |
| TresPinos | 111295 | 20:58 | 36.65 | 121.43 | 6 | 3.8 | 3.8 | $6.0 * 10^{21}$ | 321/88/-136 |
| Truckee | 111595 | 20:34 | 39.60 | 120.20 | 8 | 4.8 | 4.5 | $6.0 * 10^{22}$ | 186/52/-73 |
| SanJuanBautista | 112995 | 18:47 | 36.77 | 121.57 | 10 | 4.0 | 3.9 | $8.4 * 10^{21}$ | 128/73/156 |
| SanJuanBautista | 112995 | 23:12 | 36.80 | 121.51 | 8 | 4.4 | 4.3 | $3.1 * 10^{22}$ | 227/84/24 |
| Richmond | 120195 | 23:11 | 37.92 | 122.32 | 10 | 3.6 | 3.7 | $4.2 * 10^{21}$ | 50/88/-3 |
| DoubleSpringFlat | 122295 | 09:00 | 38.70 | 119.82 | 16 | 5.1 | 4.8 | $1.9 * 10^{23}$ | 210/75/44 |
| DoubleSpringFlat | 122395 | 05:39 | 38.66 | 119.69 | 10 | 4.7 | 4.6 | $8.6 * 10^{22}$ | 228/84/38 |
| DoubleSpringFlat | 122895 | 18:28 | 38.72 | 119.66 | 14 | 4.8 | 4.8 | $2.1 * 10^{23}$ | 130/66/147 |

Same as Table 3.1.

## 3.2 Active Regions in Northern and Central California

Our understanding of tectonics in California and the western United States comes from studying the seismic deformation of the crust, primarily through earthquake seismology. Geodesy studies, such as those using the Global Positioning System (GPS), can also provide information on deformation that occurs both seismically and aseismically. To the best of our knowledge, however, most significant deformation occurs during the faulting of large earthquakes, so seismic investigation still provides an essential means of studying active tectonic structures. The source mechanism of the earthquake reveals the motion associated with these structures. Of course, the seismic source only reveals the sense and orientation of motion at depth. When combined with surface observations, this provides a method of reconstructing the geometry of fault motion that may not been revealed from the geology. In this way, the active geomorphological features in an area may become clear.

It is important to study both earthquake sequences and particular active regions by utilizing the capabilities of moment tensor analysis for moderate-sized earthquakes. New advances or techniques in source studies often lead to insights about the mechanisms of active faulting, and the information from large numbers of moment tensor solutions can provide an understanding of the complexity of a region which cannot be seen from studying only the large events. It is for this purpose that active areas such as Mammoth Lakes and Long Valley, Parkfield and Coalinga, the Central Coast region, The Geysers Geothermal Area, and the Mendocino Triple Junction are examined.

### 3.2.1 Mammoth Lakes and Long Valley

Long Valley, an area between Bishop and Mammoth Lakes, overlies the Long Valley Caldera. The caldera is a 17 km (north to south) by 32 km (east to west) elliptical depression formed by an eruption 700,000 years ago (Bailey *et al.*, 1976). Long Valley is bounded on the west and southwest by the Sierra Nevada, on the north by Glass Mountain, on the east by the Benton Range, on the south and southeast by the Bishop tableland, and is centered on the resurgent dome. Earthquakes at

Mammoth Lakes in May, 1980 were accompanied by a rise in elevation of the resurgent dome, and a continuation of earthquakes in the region.

While one of the most active regions in California, the seismicity is often limited to earthquakes which are too small to determine regional moment tensors. Another complication is the tendency of events in the Long Valley region to occur in earthquake "swarms". As a result, often two or more nearly equal-size earthquakes occur within a minute or two of each other, making it difficult to perform moment tensors on either of the individual earthquakes. In "typical" earthquake sequences, early aftershocks are often several magnitudes smaller than the mainshock and therefore do not interfere as much as a similar-timed swarm earthquake.

With these caveats, figure 3.5 shows seismicity ($M \geq 3$) over the five year period from 1992 − 1996 and moment tensors determined over this time period. Long Valley is shown in the center portion of the map. Outer and inner rings delimit the caldera and the resurgent dome, respectively. Mono Lake and the Mono Lake Fault are located to the north, and the White Mountain Fault is the large fault shown in the eastern portion of the map. Outside of the Long Valley area, in the Mono Basin, the earthquakes have strike-slip mechanisms, most likely with right-lateral slip on north-south striking faults. These are very typical mechanisms for this portion of the Walker Lane Belt. Most seismicity, however, is concentrated near Long Valley Caldera. The majority of earthquakes occurring during this time were located either within the caldera southwest of Mammoth Lakes or south of the caldera and west of the Hilton Creek Fault. Most of the events located in the area were too small to perform moment tensor inversions. First motion mechanisms exist for many of these earthquakes. Events running from the resurgent dome and the south moat of the caldera and continuing southward have a wide variety of mechanisms ranging from strike-slip to oblique normal to normal, but consistently having extension in the same ENE direction. Moment tensors calculated for events in this region are compatible with this. The centroid depths of the events span a range from 4 km to 12 km which is also consistent with the high frequency depths.

Focal mechanisms indicate that on the west side of the caldera, near Mammoth Mountain, mechanisms for events change from extension in an ENE-WSW direction to extension in a NW-SE direction. Unfortunately, there are no moment tensor solutions at Mammoth Mountain and in the western caldera to confirm this phenomenon. Moos

and Zoback [1993] attribute the rotation of the extensional stress field at Mammoth Mountain and in this area to a relatively localized anomaly, and speculate that it may be caused by near-lithostatic pore pressure at depth.

## 3.2.2   Parkfield

Parkfield is located on the San Andreas Fault about halfway between San Francisco and Los Angeles. This area has produced five similar M6 events at about 22 year intervals since 1881 (1881, 1901, 1922, 1934, 1966), as well as being at the north end of the M 8 1857 break (Bakun and McEvilly, 1984). It is probably most famous for the Parkfield experiment, an intensive monitoring effort which hopes to capture the next predicted event (Bakun and Lindh, 1985). Most of the seismicity in the region occurs right along the San Andreas Fault. While the predicted M6 earthquake has not occurred, a number of smaller M 4 – 5 earthquakes have occurred near the 1966 nucleation zone at Middle Mountain zone. Events in October 1992, April 1993, November 1993, and December 1994 registered as magnitude 4.6, 4.2, 4.7, and 5.0 earthquakes, respectively, and moment tensors were performed for all of them. Figure 3.6 is a plot of seismicity (earthquakes M $\geq$ 3.0) and moment tensors from 1992 – 1996. The long fault segment running from the northwest to the southeast corners of the map is the San Andreas Fault, and the fault running parallel to the San Andreas to the southwest is the Rinconada Fault.

Because of the Parkfield experiment and the installation of a high density borehole array in the vicinity, the accuracy of the centroid depths can be assessed. All of the Parkfield events show intermediate centroid depths (6 – 10 km), which occur just above and below the nucleation zone (9 – 10 km). Information about the locations in the Parkfield region are from Johnson (personal communication). The October 1992 earthquake occurred 3 km SE of the nucleation zone, had a hypocentral depth of 9 km, and ruptured NW along strike. For comparison, the centroid depth of the event calculated from the moment tensor was 10 km. The April 1993 event had a high frequency location about 1.5 km SE of the nucleation zone and at 6 km depth. It also ruptured NW along strike and had a centroid depth of 8 km. The November 1993 event was centered just below the nucleation zone at a depth of about 10 km. It ruptured to the NW and had a centroid depth of 8 km. Finally, the December
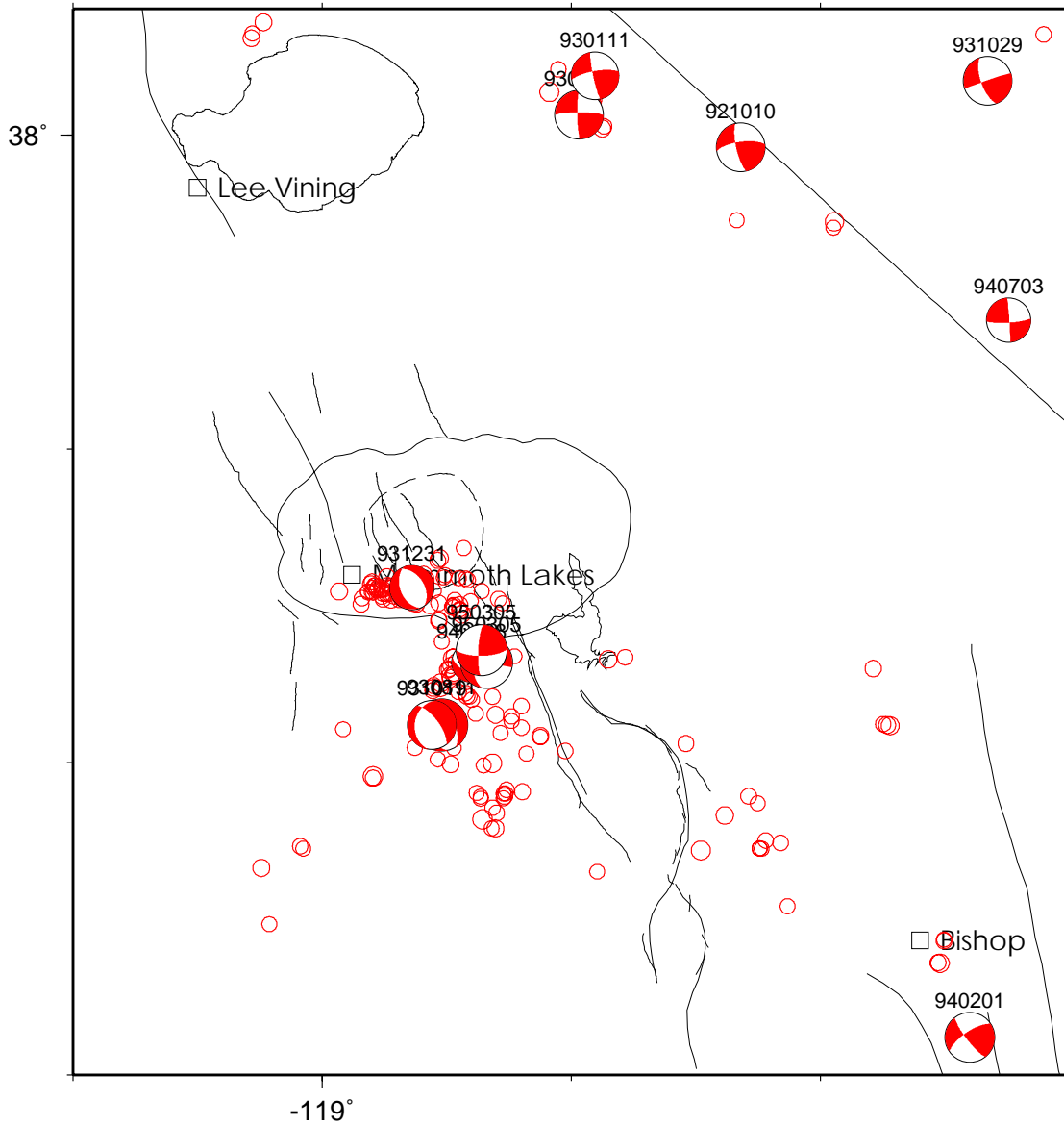
Figure 3.5: Map of the Mammoth Lakes and Long Valley caldera region. Outer and inner rings delimit the caldera and the resurgent dome, respectively.

Figure 3.6: Map of the Parkfield and Coalinga region.

1994 event was located about 5 km SE of the nucleation zone at a depth of 7 km. It ruptured updip to the NW and the centroid depth was 6 km. In each of these cases, the centroid depth (which is only sampled every 2 km) was very close to the hypocentral depth, especially in light of the rupture pattern of the earthquake (Johnson, personal communication).

The San Andreas Fault serves as a major boundary between the Salinian block to the southwest and the Franciscan, Coast Range Ophiolite assemblages, and Great Valley Sequence to the northeast. The Salinian block consists of mostly Late Cretaceous granitic rocks, metamorphic rocks and Tertiary sedimentary rocks. To the northeast, the Franciscan assemblage is overlain by Late Jurassic Coast Range ophiolite and Upper Cretaceous Great Valley sequence. The Franciscan assemblage is composed of oceanic sedimentary rocks which were accreted to the North American continent. Parkfield is situated at the southern end of the creeping segment of the San Andreas, which is located between the large breaks of 1857 and 1906.

To the northeast, near the town of Coalinga, lies another seismically active fault buried deep beneath the Cenozoic sediments of the Central Valley and hidden from surface expression. On May 2, 1983, the town was jolted by a M 6.5 earthquake on a low-angle thrust fault. This event highlighted the importance of "blind thrust" faults in assessing fault hazards in California, a lesson reinforced in the Northridge earthquake. Mechanisms, low dip angle (between 45 degrees and subhorizontal), and centroid depths (6 – 8 km) determined from the moment tensors for this region are compatible with low-angle thrusts. In addition, the mechanisms strike counterclockwise from the strike of the San Andreas Fault, consistent with the anticline. Although many of these blind thrusts are relatively quiet between large events, smaller earthquakes recorded along these faults should serve as warnings of the seismic potential along the Coast Range and other thrust faults.

Figure 3.6 shows another interesting phenomena that is seen more or less throughout the San Andreas Fault System: the partitioning of slip along the fault. Earthquakes exhibiting strike-slip motion, such as those in the Parkfield region, primarily occur directly on the San Andreas Fault, while earthquakes having compressive motion, such as those near Coalinga, occur in the off-fault region. The partitioning, as well as the large rotation in the regional stress suggested by the two different mechanisms, has important implications for the strength of the San Andreas Fault (see

section 3.3.5).

### 3.2.3   Central Coast Ranges

The Central Coast Ranges are comprised of the region on the west side of the Central Valley just south of San Francisco Bay. The region is interesting from a tectonic perspective because of the nature of faulting changes from a single fault in the southern portion to a multi-strand region around the Bay Area to the north. This splaying of faults produces an interesting fault geometry. In the north, the Santa Cruz Mountains are on the west side of the San Andreas Fault and the Santa Clara Valley on the east side, with the Calaveras Fault serving as the eastern boundary of the valley, separating it from the Diablo Range. South of the splay, the San Andreas runs through the Coast Ranges, with the granitic rocks of the Gabilan Range rising to the west. On October 17, 1989 the M 6.9 Loma Prieta earthquake struck the southern Santa Cruz Mountains, producing extensive damage throughout the Bay Area. In addition, the M 5.9 Coyote Lake earthquake (08/06/79) and the M 6.2 Morgan Hill earthquake (04/24/84) ruptured 20 km long segments of the Calaveras Fault.

Figure 3.7 plots M $\geq$ 3 seismicity and moment tensor solutions from 1992–1996. The large throughgoing fault running from northwest to southeast is the San Andreas. The Calaveras Fault locates east of San Jose and Gilroy, and its southern end terminates at the San Andreas Fault. In the north, it moves inland from the Hayward Fault, which runs on the east side of the San Francisco Bay. The Sargent Fault is the small fault which runs between the San Andreas and Calaveras Faults. To the west are the San Gregorio Fault in the Monterey Bay and the Rinconada Fault near the Salinas Valley. To the east, near the San Luis Reservoir, is the Quien Sabe Fault, and to the northeast is the Livermore fault. The creeping segment of the San Andreas fault runs from San Juan Bautista down to Cholame.

Quite a few large strike-slip earthquakes have occurred during the time period including, at the magnitude five level, 16 January 1993 M 5.1 Gilroy, 11 August 1993 M 5.0 San Felipe (east of San Jose), 23 April 1995 M 5.0 Bear Valley (near the Pinnacles), as well as dozens of magnitude four events. The few non-strike-slip events are noteworthy. The 11 January 1994 M 4.1 event near Watsonville is interesting because of its unusual oblique mechanism and its proximity to the Loma Prieta earthquake, which also had an oblique mechanism. The 7 September 1994 M

Figure 3.7: Map of the Central Coast Range region.

4.0 thrust event near Modesto has an unusual "off-fault" location which most likely was situated on the Coast Range Thrust, hidden beneath the Central Valley. Centroid depths for these earthquakes are at intermediate depths for the San Andreas System, most occurring between 6 and 12 km.

### 3.2.4   The Geysers and Clear Lake

The Clear Lake volcanics are a belt of young volcanic rocks that stretch from the north end of Lake Berryessa to Clear Lake. The Geysers are an unusual area of hot springs and steam vents located in the Mayacmas Mountains south of Clear Lake. Steam wells at the Geysers Geothermal field make it one of the largest geothermal power operations in the world, and seismicity levels in the area make it one of the most active regions in California. It is located in an area dominated by right-lateral strike-slip motion on NNE striking faults (Maacama, Rodgers Creek, etc.). The Maacama Fault is seen at the western edge of figure 3.8, and the Healdsburg-Rodgers Creek system at the southern edge. The geothermal area is bounded by the Mercuryville and Collayomi faults to the southeast and northwest, respectively.

Studies of earthquakes in the geothermal area show a variety of mechanisms for The Geysers region, despite the preponderance of right-lateral strike-slip faults. Moment tensor solutions for the largest earthquakes in the region show that most have normal mechanisms (figure 3.8), although there are several strike-slip events as well. The largest earthquake recorded during the time period (09/19/92) is strike-slip, but not in keeping with either the other strike-slip events or the lateral motion of the nearby faults. It is clear from the presence of normal events that the local stress field at The Geysers differs considerably from the regional transpressive stress field in the Coast Ranges. The centroid depths for all the moment tensors are shallow ($<$ 5 km), consistent with stress changes that would result from fluid injection into the region near the surface. Oppenheimer [1986] found that focal mechanisms at The Geysers are a function of depth, with shallow earthquakes dominantly strike-slip and reverse, while the relatively deeper earthquakes have normal faulting. Outside of the geothermal area, along the strike-slip faults, the centroid depths are intermediate.

The ability to perform moment tensor inversions for many earthquakes in the Geysers has been aided by a significant increase in the number of earthquakes, and
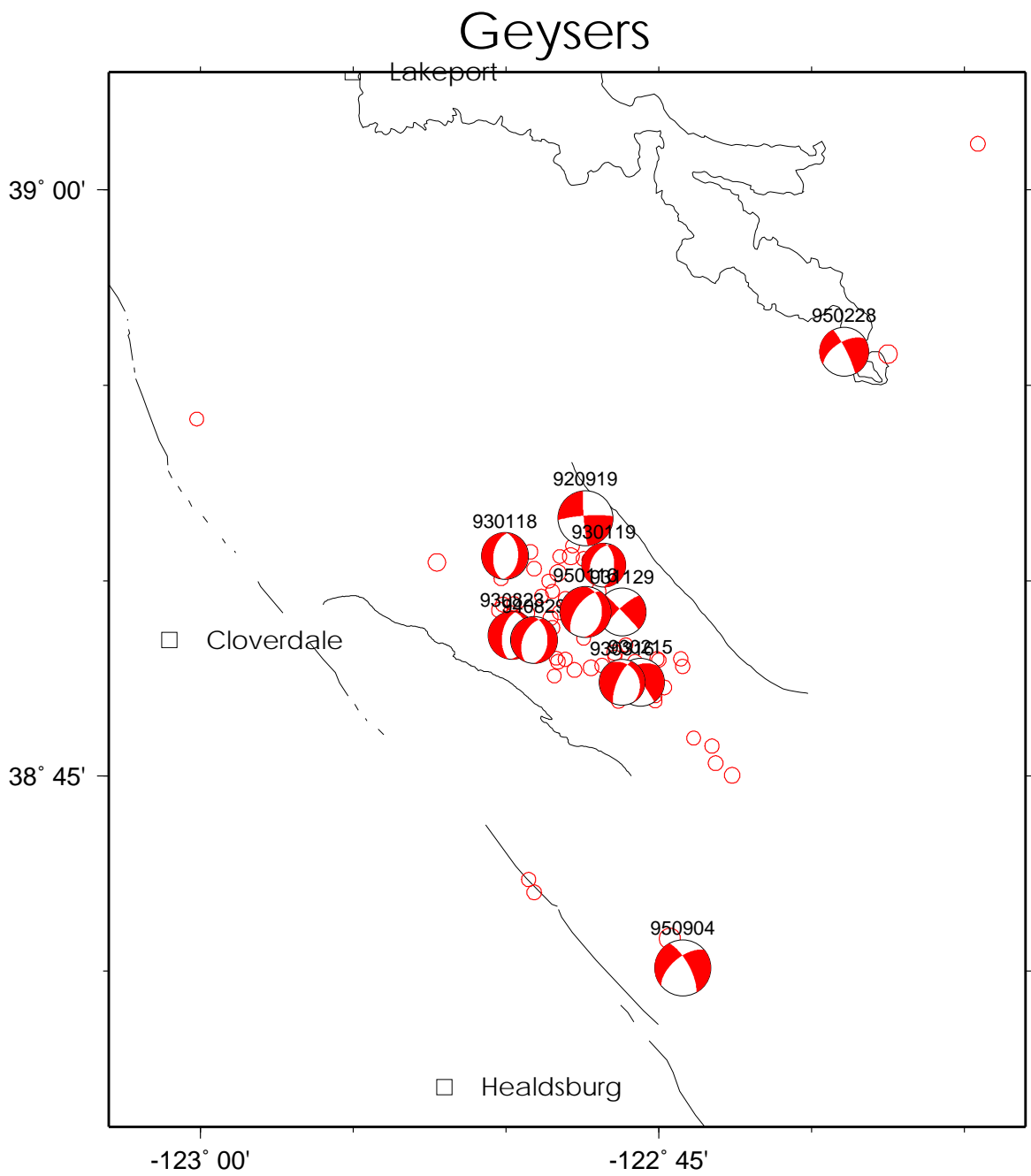
Figure 3.8: Map of The Geysers and Clear Lake region.

Table 3.5: Recent seismicity at The Geysers. Number of earthquakes each year at various magnitude levels.

| Year | M ≥ 2.0 | M ≥ 2.5 | M ≥ 3.0 | M ≥ 3.5 | M ≥ 4.0 |
|------|---------|---------|---------|---------|---------|
| 1980 | 58  | 21 | 3  | 0 | 0 |
| 1981 | 69  | 22 | 5  | 0 | 0 |
| 1982 | 70  | 23 | 7  | 0 | 0 |
| 1983 | 91  | 28 | 5  | 0 | 0 |
| 1984 | 115 | 32 | 5  | 1 | 0 |
| 1985 | 131 | 36 | 9  | 3 | 1 |
| 1986 | 167 | 50 | 10 | 0 | 0 |
| 1987 | 159 | 46 | 16 | 0 | 0 |
| 1988 | 127 | 42 | 14 | 4 | 0 |
| 1989 | 118 | 33 | 13 | 5 | 0 |
| 1990 | 118 | 38 | 8  | 6 | 1 |
| 1991 | 111 | 33 | 14 | 3 | 0 |
| 1992 | 136 | 44 | 11 | 2 | 1 |
| 1993 | 123 | 45 | 15 | 4 | 0 |
| 1994 | 166 | 45 | 12 | 1 | 1 |
| 1995 | 137 | 38 | 8  | 1 | 0 |

large earthquakes in particular, that have occurred in the area (see figure 3.9 and table 3.5). In the early 1980's, there was an average of less than one event per year occurring at the current lowest magnitude level (M 3.5) for computing regional surface wave moment tensors – a significant increase from the 1970's (Eberhart-Phillips and Oppenheimer, 1984). By the 1990's, an average of 4 events per year were occurring at the same magnitude level.

One notable observation at the Geysers is that in a few cases (i.e. 8/23/93 and 8/29/94) the moment magnitude determinations are between a half to a full magnitude unit higher than the other determinations ($M_L$ and $M_d$) but consistent with other moment tensor solutions. This size discrepancy is not observed in any other region where moment tensor inversions were performed. The simplest explanation is that the events are larger earthquake sources whose high frequency energy is being
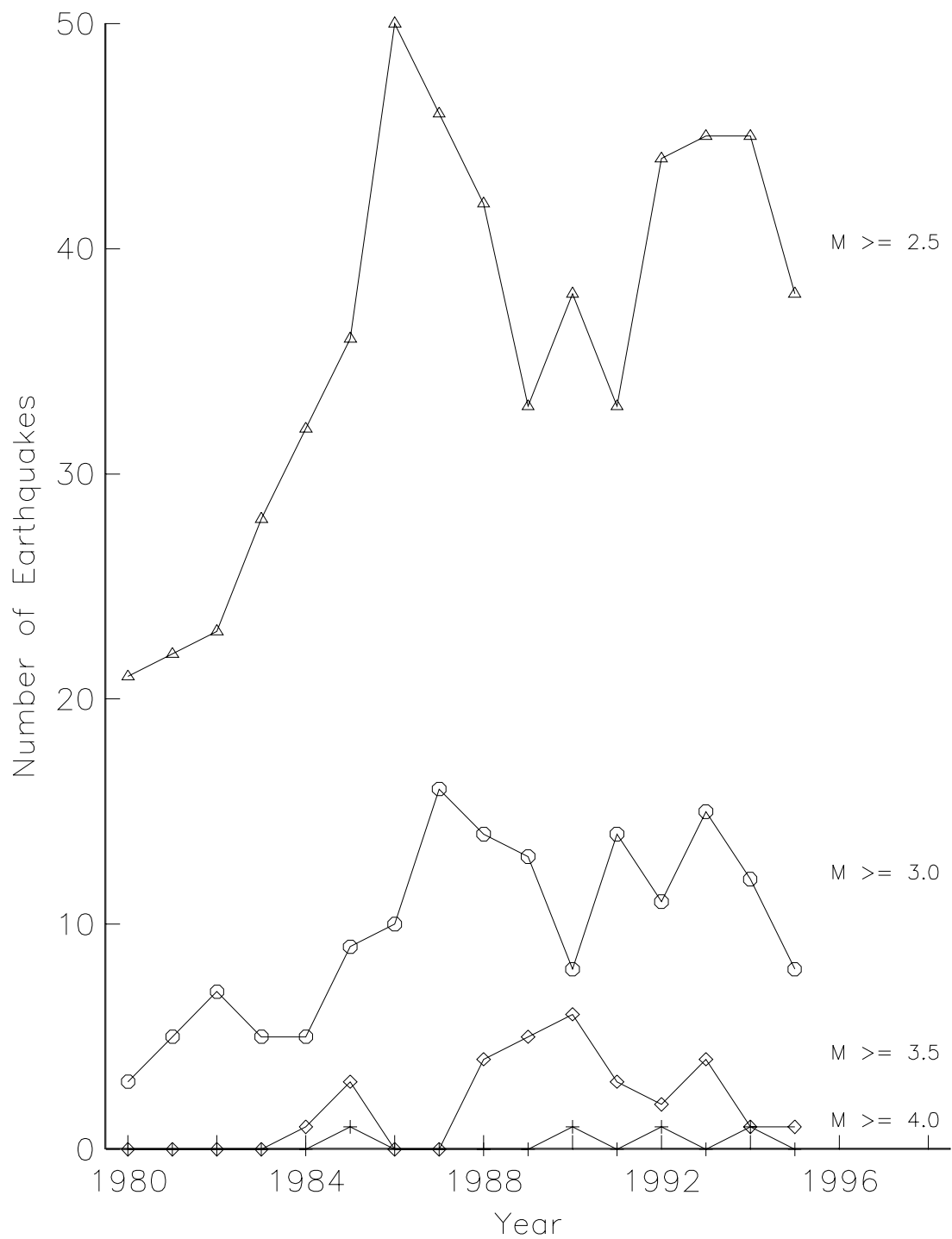
Figure 3.9: Increasing seismicity at The Geysers. Number of earthquakes per year as a function of time for several magnitude levels.

attenuated significantly near the source, presumably in the produced region, where there is a lot of fracturing and the presence of fluids.

### 3.2.5 Mendocino Triple Junction

The Mendocino Triple Junction (MTJ) occurs at the intersection of the Pacific plate, North American plate, and the southern portion of the Juan de Fuca plate, called the Gorda plate. North of the junction, the Gorda plate subducts below the North American plate; south of the junction, the Pacific plate moves north relative to the North American plate along the San Andreas Fault System; and west of the junction, the Mendocino Fault separates the Gorda and Pacific plates. The MTJ is an unstable triple junction that has migrated northward over the last 30 m.y. since the Pacific and North American plates first bordered one another. Seismicity occurs most notably along the Mendocino Fault, particularly close to the MTJ but within the Gorda Plate as well.

Relative plate motions (Atwater, 1970) indicate that the relative motion between the Gorda plate and the Pacific plate is about 5.8 cm/yr, roughly perpendicular to the Gorda Ridge. The plate motion can be resolved into 5.1 cm/yr right-lateral displacement along the Mendocino Fault and about 2.7 cm/yr convergence across it. The relative motion between the Pacific and North American plates in this region is about 5.8 cm/yr, mostly right-lateral slip across the San Andreas Fault system, with a minor component of compression. The Gorda Plate subducts obliquely beneath the North American plate at a rate of about 2.5 cm/yr in the N52°E direction (Eaton, 1989).

Figure 3.10, showing seismicity and moment tensors over the 1992 – 1996 time period, demonstrates that this region has intense seismic activity, particularly close to the Triple Junction. The fault running east-west is the Mendocino Fault, and the one curving up along the coast from the southeast is the San Andreas Fault. The continuation of the San Andreas Fault along the Mendocino Fault out to sea, as shown by the fault map, is not very well resolved. The subduction zone separating the Gorda and North American plates, also not well determined, is not shown. Active slip is occurring as extension at the Gorda Ridge, compression between the Gorda and North American Plates (04/25/92), and right-lateral strike-slip motion along the plate boundary at the Mendocino Fault (09/01/95; see section 3.4.4). In addition,

the compressional deformation is causing the fragmentation of the southeast corner of the Gorda Plate resulting in strike-slip earthquakes in this region (04/25/92 a & b; 11/08/80 Eureka). There is also some minor deformation in the overriding North American Plate. Considering the relative plate motions and active seismicity, underthrusting earthquakes have been historically rare. Additionally, beyond the 04/25/92 earthquake sequence, there were no thrust events calculated in the region over a four year time period. This might indicate that compression deformation occurs only in major events that rupture large segments.

Most of the centroid depths for events in the Mendocino region (at the Gorda Ridge, within the Gorda Plate, and on the Mendocino Fault) are at moderate (8 − 12 km) depths. One might expect that the large compressional events such as the 04/25/92 Petrolia event have a deeper source. For the most part, this has not been observed, except for some deep events ($\sim$ 30 km) east of the Mendocino Triple Junction, presumably within the subducting Gorda plate.
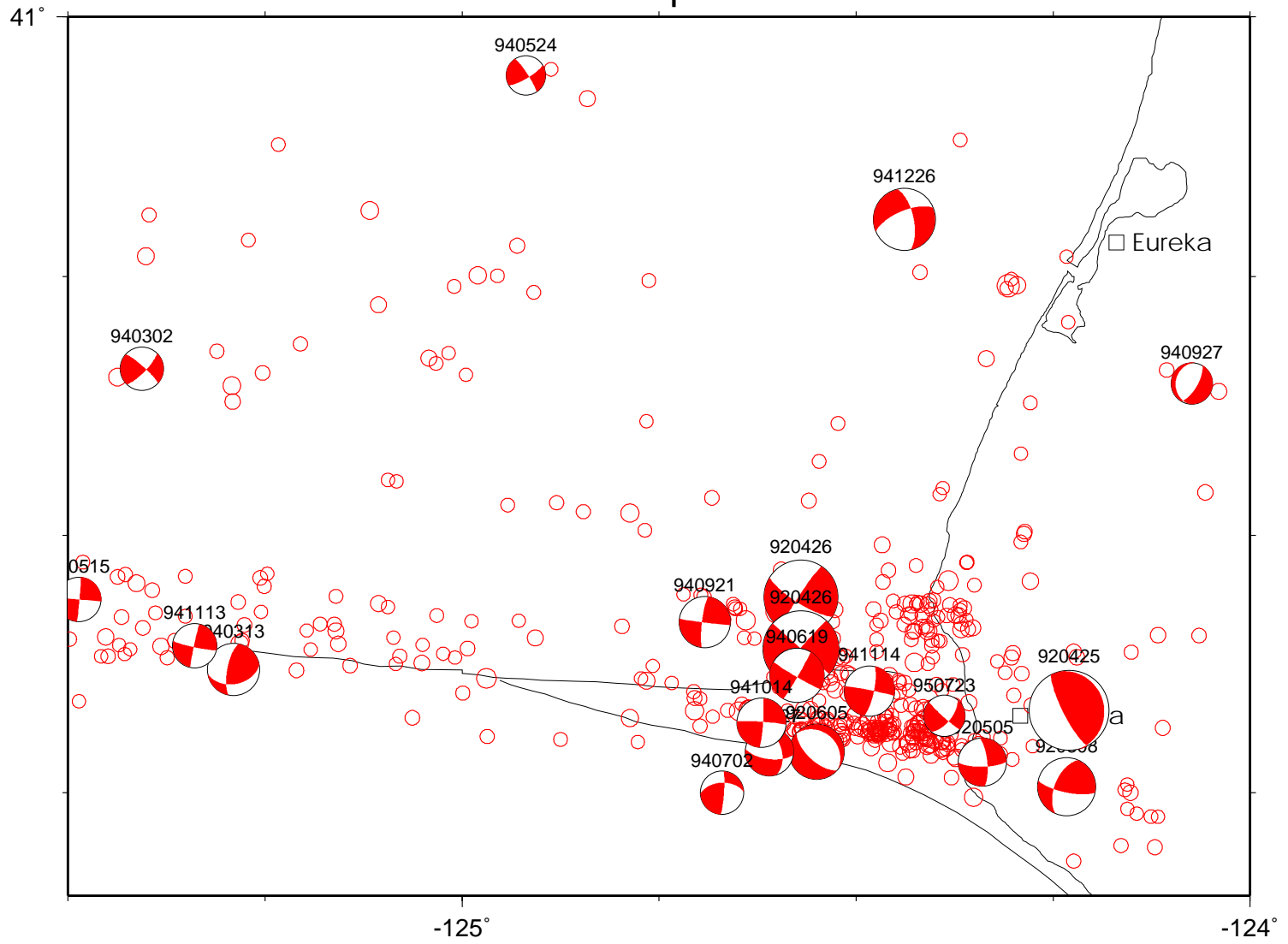
Figure 3.10: Map of the Mendocino Triple Junction region.

## 3.3    State of Stress in the Crust

Since Anderson developed his theories on the dynamics of faulting (Anderson, 1951; first edition in 1942), geophysicists have recognized the intimate role between stresses and earthquakes. On one hand, stress orientations (regional and local) determine the nature of earthquake faulting, both in a broad tectonic sense of favored faulting styles but also in the sense of faulting for a specific earthquake. On the other hand, earthquakes can be used to provide some insight into the state of stress in the crust and the nature of the faulting, allowing us to study neotectonics through seismology. Anderson theory, which is based on the Coulomb failure criterion, simplifies the relationship between the two, and allows the determination of aspects of one from the other.

One way of measuring the orientations of principal tectonic stresses in a region is through earthquake focal mechanisms. Zoback, *et al.* [1987] noted that, except in the case of earthquakes along major faults which are thought to be very weak (such as the Hayward and San Andreas faults), there is a good correlation between the stress measured in this manner and other types of stress data (i.e. borehole elongation and hydraulic fracturing). Therefore, the moment tensor of an earthquake can be used to provide information about the stress regime that caused the earthquake to occur. Circumstances which can complicate or destroy the assumptions of Anderson theory can be remedied by resorting back to Coulomb theory. In addition, a number of studies have shown that the Coulomb stress criterion is an effective way of quantifying the static stress offsets caused by earthquakes.

### 3.3.1    Anderson's Theory of Faulting

The Anderson Theory of Faulting is a mechanical theory which has proven very successful at predicting most of the various types of observed earthquake faulting. It is based on the principle of Coulomb fracturing, which states that a material shortens in the direction of maximum principal compression (represented by $\sigma_1$) and expands in the direction of least principal compression ($\sigma_3$). The intersection of the two possible fault orientations is parallel to the intermediate principal stress ($\sigma_2$). As a result, the orientation and sense of slip of the faults can be predicted given the orientation of the principal stresses and shape of the Mohr envelope (Suppe, 1985). Similarly,

the orientation of the principal stresses can be predicted from the orientations of the faults and their slips.

The rest of the theory follows from the assumption that, in the case of shallow faulting, one of the principal stresses must be perpendicular to the surface of the earth. Anderson theory predicts three possible classes of near-surface faults. If $\sigma_1$ is vertical then normal faulting occurs, if $\sigma_2$ is vertical then strike-slip faulting occurs, and if $\sigma_3$ is vertical then thrust faulting occurs. The orientation of the fault planes and sense of motion on them depends upon the other two principal stresses. The P and T axes from earthquakes, which represent the maximum and minimum principal stress directions, respectively, can be used to determine the stress orientation in a region. By convention, compressive stress is defined as positive. Hence, the compressional axis is the maximum or greatest stress and the tensional axis is the least or minimum stress.

Figures 3.11 and 3.12 are a compilation of the horizontal P and T axes from all of the earthquake moment tensors. Several general trends in the data from these figures are clear, and these trends are indicative of broad changes in the stress field. The P-axes are primarily oriented north-south with some small variations moving from west to east. Large changes occur going from south to north, particularly when crossing the Mendocino Triple Junction. Also, in several instances the P-axes become very small, indicating the (maximum) stress orientation is vertical (Klamath Falls, OR; Eureka Valley, etc.) The T-axes are generally oriented in the east-west direction, again with only a little variation across the region, except where crossing the Mendocino Triple Junction. The amplitude, however, changes radically in southern California, indicating the compressive regime of the area near the Transverse Ranges.

Several caveats should be made about Anderson's theory of faulting. The theory is based upon the Coulomb fracture criterion in a homogeneous near-surface stress field. Deviations from these assumptions complicate the theory. First of all, Coulomb theory may not be completely valid in describing the failure of materials and may, for example, depend upon the level of the intermediate principal stress direction. Secondly, rock in the earth is not homogeneous; it is layered, highly variable, and anisotropic. The near-surface stress field, particularly near magma chambers, can be highly variable as well. In addition, pre-existing fractures of both small and large scale, in the form of faults, are found in nature. This can have a particularly large

# Greatest Principle Horizontal Stress
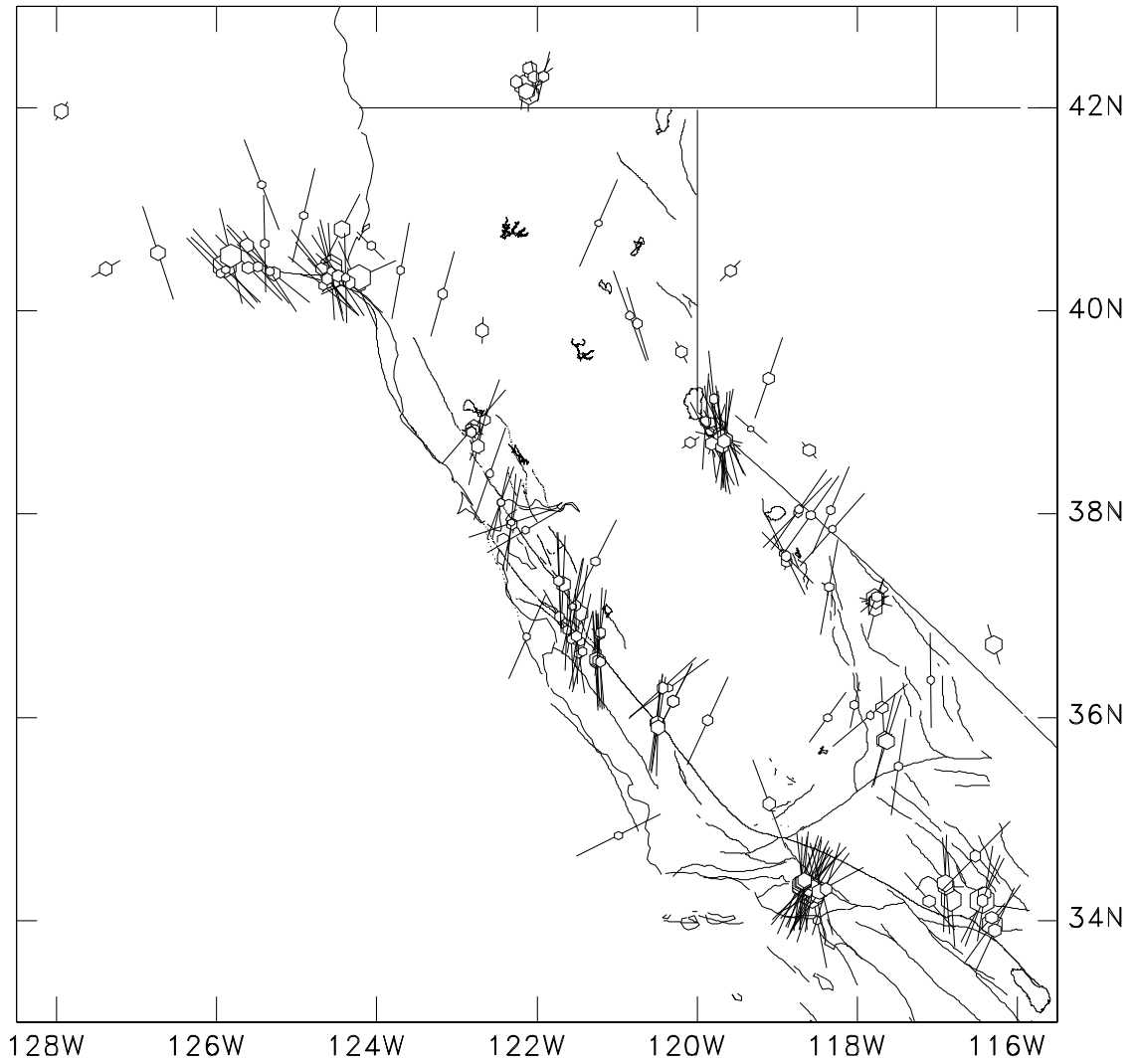


Figure 3.11: Horizontal P axes as determined from moment tensors.

# Least Principle Horizontal Stress
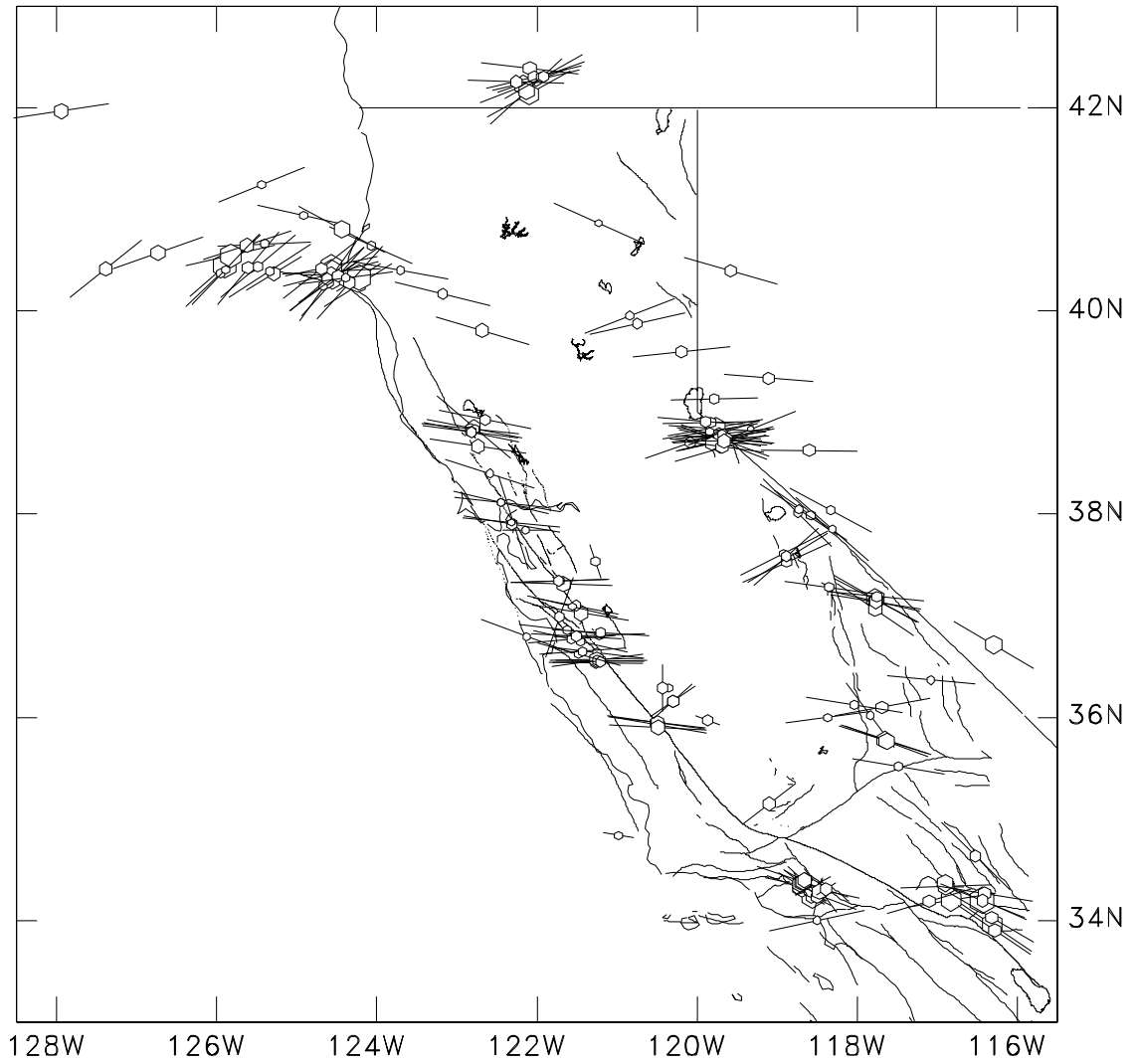


Figure 3.12: Horizontal T axes as determined from moment tensors.

effect on the estimated stress field, which will be discussed in the next section.

### 3.3.2   Stress Regime of the San Andreas Fault System

One advantage of determining reliable moment tensor estimates of moderate size events is the ability to get a more complete look at the stress of the total system by not limiting oneself to only the larger events. When looking at the results for California and vicinity in this light, some interesting patterns seem to emerge. In events located along the San Andreas Fault System, the maximum horizontal compressive directions are consistently rotated ~45 degrees east of the local strike of the fault system (events in the Central Coast Range from Clear Lake down to Parkfield). This would seem to indicate that the direction of maximum horizontal stress in the region is north-south and that the regional stresses are given by:

$$\sigma_1(N-S) > \sigma_2(V) > \sigma_3(E-W) \tag{3.1}$$

where $\sigma_{1,2,3}$ are the principal stresses.

Events located off of the San Andreas Fault System are consistent with the maximum horizontal compressive directions demonstrated by Zoback, *et al.* [1987] for non-San Andreas events, which indicate a northeast-southwest direction of compression. Prime examples of this are thrust events on the west side of the Great Valley near Coalinga and Modesto, as well as the large strike-slip event near the Geysers. In addition, off-Calaveras events at Mt. Hamilton also show this phenomenon. This would indicate that the regional stresses near the San Andreas are:

$$\sigma_1(NE-SW) > \sigma_2(V) \sim \sigma_3(NW-SE) \tag{3.2}$$

where $\sigma_V$ and $\sigma_{NW-SE}$ are nearly the same magnitude since $\sigma_V$ is the least principal stress when reverse faulting occurs. This is consistent with other types of stress measurements in the area (Mount and Suppe, 1987) including borehole breakouts, trends of recent (Pliocene to Holocene) fold axes, and the fault plane solutions of large recent earthquakes (i.e. 1983 Coalinga and 1985 Avenal).

Across the Great Valley, the direction of compression in the Sierra Nevada and Walker Lane changes slightly. The greatest principal horizontal stress direction is

about 30 degrees west of north, and here both strike-slip and normal faulting occur. Examples are shown for events in the Northern Sierra near Quincy and Susanville, Double Spring Flat, and the Mammoth Lakes region. Since normal faulting indicates that the vertical principal stress is the greatest principal stress, the regional stresses in this area are:

$$\sigma_1(NNW - SSE) \sim \sigma_2(V) >> \sigma_3(WSW - ENE) \tag{3.3}$$

where $\sigma_{NNW-SSE}$ and $\sigma_V$ are about the same amplitude and readily interchange as the maximum principal stress.

Moving further inland, faulting in the Basin and Range region is primarily limited to normal faulting and there is a rerotation of the direction of maximum horizontal compression. Examples of this stress orientation are the Little Skull Mt. , Eureka Valley, and Ridgecrest events. Regional stresses in the area can be characterized as:

$$\sigma_1(V) > \sigma_2(NE - SW) >> \sigma_3(NW - SE) \tag{3.4}$$

where $\sigma_V$ is now greater than $\sigma_{NE-SW}$.

In Southern California, there is a counterclockwise rotation of both the on-fault and off-fault stress axes. Similar to Northern and Central California, the reverse faulting indicates that the magnitudes of $\sigma_V$ and $\sigma_{ESE-WNW}$ are of the same order. Hence:

$$\sigma_1(NNE - SSW) > \sigma_2(V) \sim \sigma_3(ESE - WNW) \tag{3.5}$$

The Northridge and Landers earthquakes are examples of this stress system.

The differences between the on- and off-fault stress regimes can be explained by a weak San Andreas Fault. The focal mechanisms along the San Andreas system are controlled by the orientation of the fault and do not reveal the principal stress directions. Mount and Suppe [1987] have observed this phenomenon and used the data to explore the tectonic faulting style of the San Andreas system. The lack of distributed slip across the deformation zone argues against the high-drag distributed shear features that would be predicted by wrench tectonics. The observations are consistent with a tectonic process with low-drag decoupled transcurrent and thrust deformation. Such a model would have little or no distributed shear.

### 3.3.3  Stress Regime of The Geysers Geothermal Area

The Geysers Geothermal Area is a special case in studying the stress regime along the San Andreas System. Both the elevated pore pressure and local stress field of the "magma chamber" affect the stress field. The fluid injection that is utilized for steam production has a great effect on the principal stresses. Fluid injection lowers the effective stress on all of the stress components by the pore pressure (see equation 3.13). On a Mohr diagram, this has the effect of moving the Mohr down the positive x-axis closer to the origin. Since the circle lies closer to the Mohr envelope, failure becomes more likely to occur.

In addition to changing the amplitudes of the stress field, the stress directions are affected as well. A large local stress field created by the geothermal region can have a great effect on the total stress field near the anomaly. Figure 3.13 shows the effect of the superposition of the local stress field on the regional stress field. The local stress field at the Geysers is undoubtedly more complicated than the simple local stress field illustrated in the figure.

For this reason, different portions of the Geysers area may have quite different stresses from neighboring regions, both inside and outside of the geothermal field. In any case, most of the region that could be studied with earthquakes yields a stress orientation of

$$\sigma_1(N-S) \sim \sigma_2(V) > \sigma_3(E-W) \tag{3.6}$$

This stress orientation is different from the orientation in the surrounding region (equation 3.2) in both the direction and relative strengths of the principal stresses. However, this stress orientation, particularly that of the greatest principal stress, is quite variable.

Oppenheimer [1986] sees much of the same thing using first motion solutions from earthquakes in the region. In this study, fault plane solutions are used to discern between two possible mechanisms for the induced earthquakes. The first model hypothesizes that the stress perturbations are related to the contraction of the reservoir, whereby in the second model entails the conversion of aseismic deformation to stick-slip deformation. The first model is rejected because it would be expected to have a radial component, whereas the second model would have a stress field
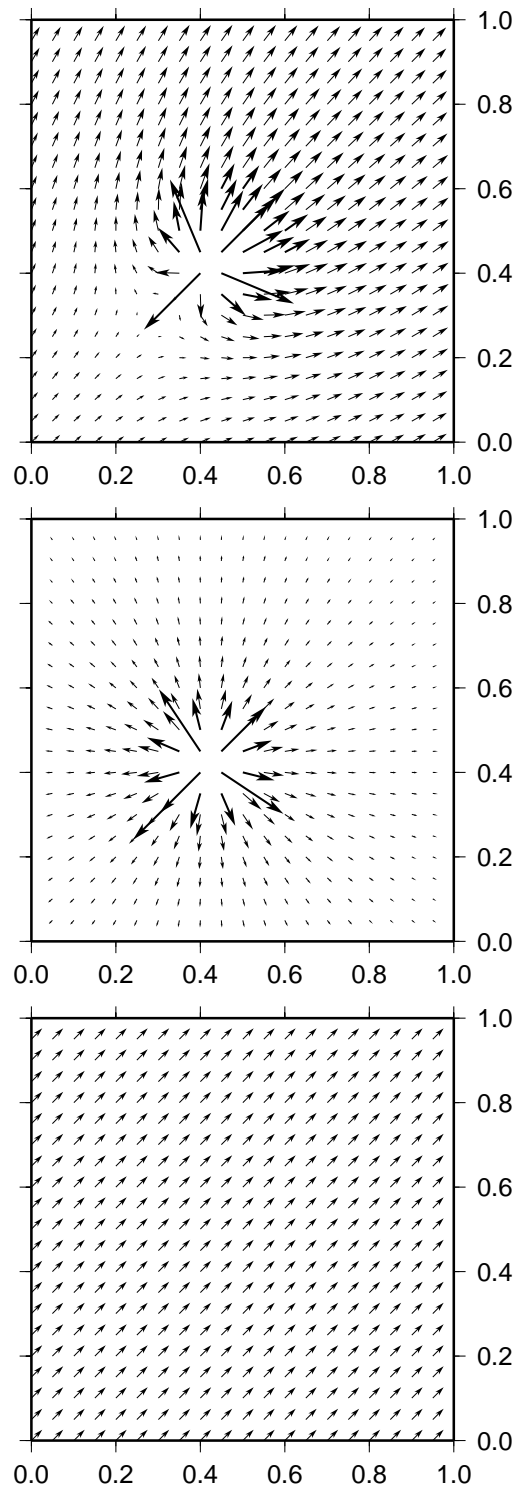
Figure 3.13: An example of the regional and local stress field and the superposition of the two fields shown on top.

consistent with the regional stress field. The stresses determined from moment tensor solutions are consistent with this observation as well.

### 3.3.4   Stress Regime of the Gorda Plate

Along the Mendocino Fracture Zone and at the Mendocino Triple Junction, the stress directions are also compatible with a weak fault at the plate boundary. Along the fault, the stress directions give a consistent rotation in the direction of both the P and T axes by about 45 degrees:

$$\sigma_1(NW - SE) > \sigma_2(V) > \sigma_3(NE - SW) \tag{3.7}$$

where the vertical stress is the intermediate principle stress. Away from the plate boundary and within the Gorda Plate, however, there is a stress distribution that slowly varies from west to east. In the western portion of the Gorda Plate, the stress distribution can be described by:

$$\sigma_1(NNW - SSE) \sim \sigma_2(V) > \sigma_3(WSW - ENE) \tag{3.8}$$

where the vertical stress is comparable in amplitude to the greatest principal horizontal stress and allows the occurrence of normal events along the Gorda Ridge. In the eastern portion of the Gorda Plate, the vertical stress decreases to the point where its amplitude is around that of the least principal horizontal stress. This is accompanied by a rotation in the stress field by about 30 degrees, illustrated very well by the rotation of the least principal horizontal stress (figure 3.12). The total stress field is given by:

$$\sigma_1(NNE - SSW) > \sigma_2(V) \sim \sigma_3(ESE - WNW) \tag{3.9}$$

indicating that when $\sigma_3$ is vertical, compression in the northeast direction, and hence Cascadia subduction zone earthquakes, can occur.

This is consistent with the observations of McPherson [1989], who described a change from a region of strike-slip faulting to a region of normal faulting and downslab tension at a longitude of 124.15 degrees west. This has been attributed to the removal of the north-south compression caused by the Juan de Fuca and Pacific Plates in the western portion of the slab.

Figure 3.14 is a summary plot of the stress regimes in California. The principle stress directions in the regions discussed are shown along with the preferred faulting style or styles. Notice the progression of faulting styles from normal at the Gorda Plate to thrust along the coast both north and south of the Mendocino Triple Junction and back to normal inland within the Basin and Range. Of course, strike-slip faulting is present throughout the region and dominant at the plate boundaries of the San Andreas Fault and Mendocino Fault. For comparison, Zoback and Zoback [1980] characterize the San Andreas province as $\sigma_1(\sim N-S) > \sigma_2(V) > \sigma_3(\sim E-W)$, the Sierra Nevada as $\sigma_1(NNE) \sim \sigma_2(V) >> \sigma_3(WNW)$, and the Basin and Range - Rio Grande Rift as $\sigma_1(V) > \sigma_2(NNE) >> \sigma_3(WNW)$. These observations are similar to the stresses derived from the regional moment tensors, with the exception of the Sierra Nevada province, where there is the same sense of motion, but a rotation in the direction of the principal axes.

### 3.3.5 Near Fault Tectonics

These observations have important implications on both the orientation and magnitude of stress around the San Andreas Fault System. If only events which occur off the main transform faults in the system are considered, then the focal mechanisms give us an orientation of about 45° degrees for the maximum horizontal stress. This is consistent with other estimates of principal stress orientation (43.9° from Mount and Suppe, 1987) and results in a stress orientation which is at a high angle (84°) to the strike of the San Andreas Fault.

In addition, one can determine the magnitude of horizontal deviatoric stress by estimating the shear stress on the San Andreas and the angle of maximum stress, through the equation:

$$\sigma_T = \left[\frac{\sigma_1 - \sigma_2}{2}\right] \sin 2\theta \qquad (3.10)$$

where $\sigma_T$ is the shear stress on a fault plane and $\theta$ is the angle between $\sigma_1$ and the normal to the fault. This relationship is illustrated in figure 3.15. Since $\theta$ is about 6 degrees and the shear stress on the fault is estimated to be around 200 bars, then the maximum horizontal deviatoric stress is about 1000 bars.

The low frictional stress of the San Andreas Fault System decouples the plate motion into two distinct components, one strike-slip component parallel to the fault

120
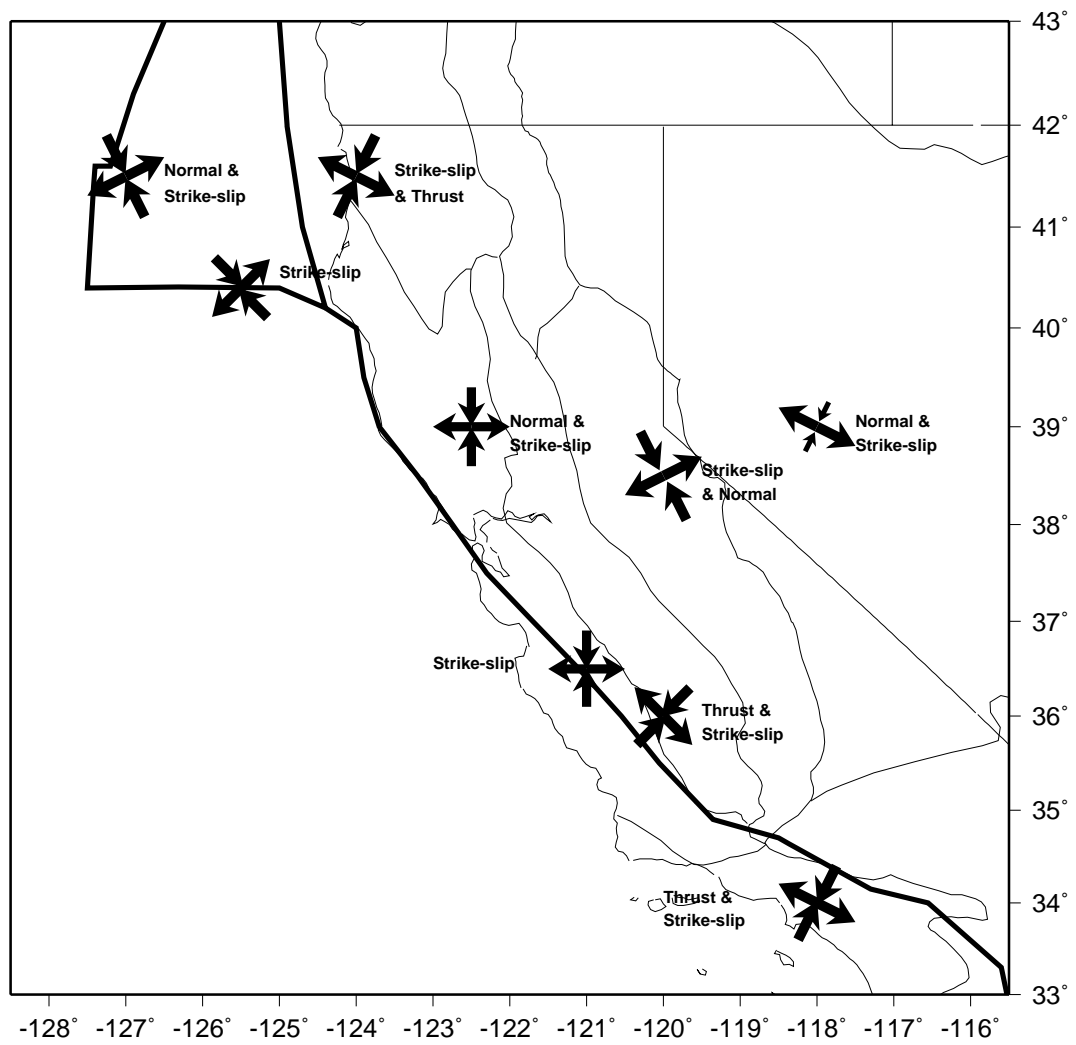
Figure 3.14: Summary plot of stress regimes in California. Thin lines are coast, state boundaries, and tectonic provinces. Thicker lines represent the plate boundaries.

121
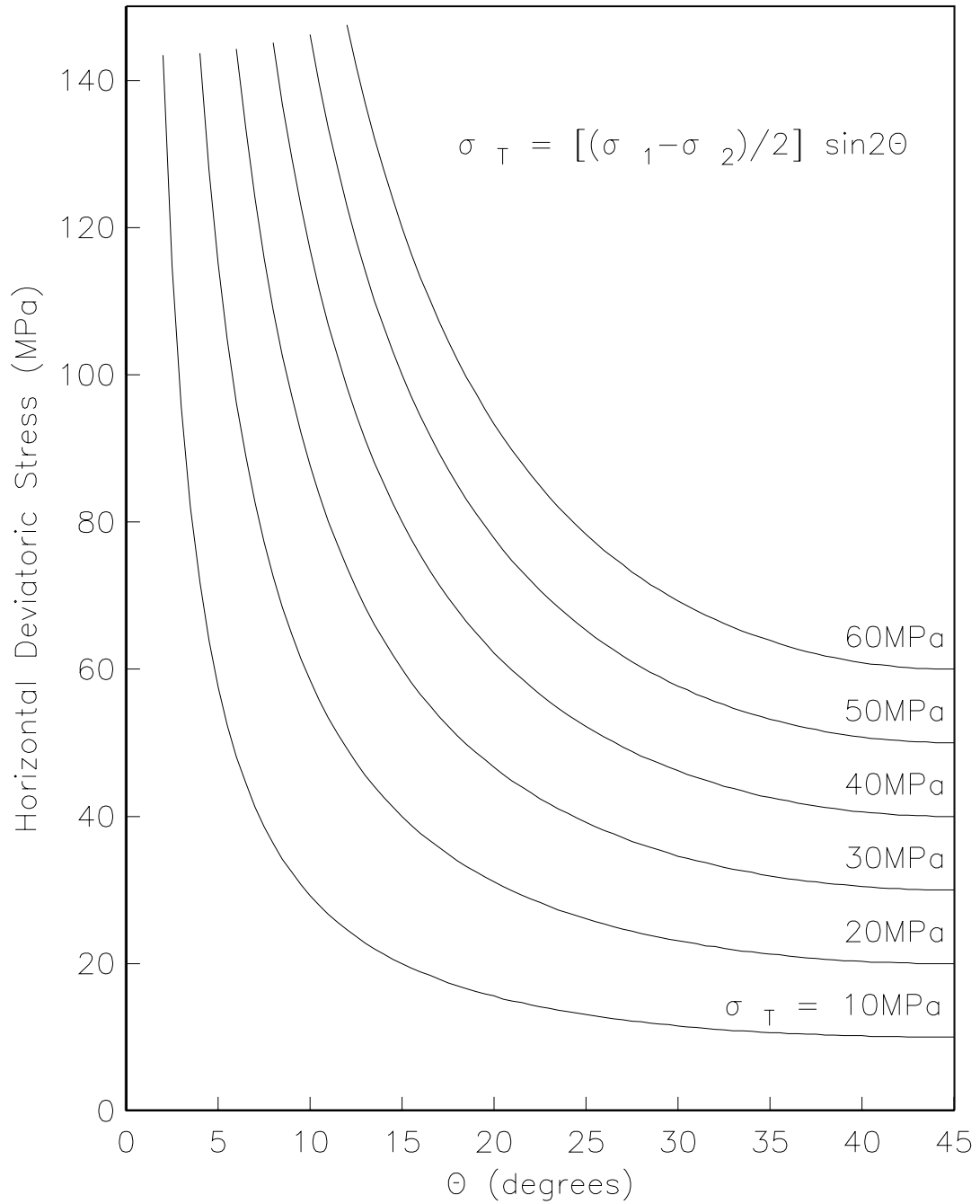
Figure 3.15: Stress orientation as a function of deviatoric stress.

122

and the other a compressive component nearly perpendicular to the fault (Mount and Suppe, 1987).

### 3.3.6 Coulomb Failure Criterion

Shear failure under compressive stress states is commonly described with the Coulomb criterion (Scholtz, 1990)

$$\tau = \tau_o + \mu \sigma_n \tag{3.11}$$

where $\tau$ and $\sigma_n$ are the shear and normal stresses resolved on any plane within the material, $\tau_o$ is the cohesion of the material, and the parameter $\mu$ is called the coefficient of internal friction. With pore pressure added to the equation, the effective stress is replaced by the normal stress minus the pore pressure, and the relative equations become:

$$\tau = \tau_o + \mu(\sigma_{eff}) \tag{3.12}$$

$$\tau = \tau_o + \mu(\sigma_n - p) \tag{3.13}$$

where p is the pore pressure.

Anderson Theory of Faulting is based on the Coulomb failure criterion, but in more complicated areas, where there are large changes in material properties or the pore pressures are widely variable, it is useful to consider another failure criterion. The Coulomb failure function (CFF) is derived from the Coulomb criterion as follows:

$$CFF = \tau - \tau_o - \mu(\sigma_n - p) \tag{3.14}$$

If the CFF is positive, then failure occurs. In practice, the absolute levels of the stresses in the earth usually cannot be measured and are not known. The analogous situation in Anderson Theory is knowing the relative levels of the principal stresses but not their absolute values. Instead of the absolute CFF then, only changes in the CFF are considered; these are given by:

$$\Delta CFF = \delta\tau - \delta\tau_o - \mu(\delta\sigma_{eff}) \tag{3.15}$$

$$\Delta CFF = \delta\tau - \delta\tau_o - \mu(\delta\sigma_n - \delta p) \tag{3.16}$$

If $\Delta CFF$ is positive, either by increasing the shear stress or the pore pressure or by decreasing the cohesion or the normal stress, then the fault has moved closer to failure. Conversely, if $\Delta CFF$ is negative, then the fault has moved further from failure.

The CFF provides a measure of the proximity of a fault to failure and has been used to explore earthquake-induced stress changes on faults in the vicinity (Reasenberg and Simpson, 1992). This is used in the next section for the Double Spring Flat earthquakes to investigate the favored faulting of aftershocks. Another area of application for the CFF might be to use the stress changes in the Geysers to model changes in pore pressure both laterally and vertically in and around the geothermal area.

## 3.4    Application to Earthquake Sequence Studies

In the course of this research, detailed studies were performed on several earthquakes of note. The basis of all of these investigations were the regional moment tensor inversions. The source parameters and scalar moment of the mainshock and aftershocks provided fundamental information on the sense of slip, possible fault orientations, and the extent of the earthquake rupture. More detailed studies were able to provide some insight into fault dynamics, stress redistribution, and the tectonic implications. In the following sections are overviews of the investigations for the 5/17/93 Eureka Valley, CA; 9/21/93 Klamath Falls, OR; 1/16/94 Northridge, CA; 9/1/94 Mendocino, CA; and 9/12/94 Double Spring Flat, NV sequences. The results from the moment tensors illustrated here have contributed to other in-depth studies on these earthquakes, which include directivity, slip distributions, structural performance, tsunami hazards, and intensity studies, and can be found in Loper, *et al.*, [1993] (Eureka Valley), Dreger, *et al.*, [1995] (Klamath Falls), Moehle, [1994] (Northridge), Dengler, *et al.*, [1995] (Mendocino Fault), and Pasyanos, *et al.* [1995] (Double Spring Flat). Moment tensor solutions for the earthquakes recounted in these sequences are not recorded here again but are contained in the catalogs of section 3.1.

### 3.4.1    Eureka Valley

The 17 May, 1993 Eureka Valley, CA sequence represents the earliest attempt to fully apply the regional moment tensor results in order to study an earthquake sequence. The sequence represented a challenge in several senses. Although it was the earliest significant event since the upgrade of a large part of the network in the previous year, at the time the network was much smaller than the current configuration (see Appendix A). In addition, the earthquake's remote location truly made this a regional study. The mainshock in this sequence, which occurred at 23:20 UTC (16:20 pm Pacific Daylight Time), had a moment magnitude of 6.0 and was followed by a particularly active aftershock sequence, which is typical for events east of the Sierra Nevada Mts.

Eureka Valley is a basin comprised of Quaternary alluvium located in the Walker Lane Belt of eastern California. It is a NNW trending valley located between the Saline and Last Chance Ranges. Because the earthquake was located in a remote

125

area, there was only minor damage in Independence and Lone Pine, although it was felt over an area from San Francisco and Los Angeles, CA to Carson City, Ely, and Las Vegas, NV. The event was also remote with respect to the seismometers (over 110 km from the nearest broadband station MLA), and on the border of three short period networks (Northern California Seismic Network, Southern California Seismic Network, and the University of Nevada, Reno network). As a result, the locations are not well constrained and the depths are poorly determined. Aftershock studies, therefore, are not the best method for learning about the whole sequence.

Six events, including the mainshock, were large enough to be suitable for a regional surface wave moment tensor inversion. The moment tensors for these events are shown in figure 3.16. The centroid depth of the mainshock was 10 km. Normal and oblique normal events are determined for the mainshock and the largest aftershocks. Normal faults are not unexpected in this region and are associated with the large basins in the region including Owens Valley, Panamint Valley, and Death Valley. Unlike the locations, which show very large scatter and do not indicate the activation of any particular fault, the fault plane solutions of the larger events indicate that the event activated an unnamed fault in the Eureka Valley which strikes about 10 degrees east of north and dips to the west.

If it is assumed that the locations of the larger events are better determined than the smaller ones and that the locations which have depths shallower than 1 km are poorly located, then one can begin to make some sense of the earthquake sequence. Figures 3.17 shows two cross-sections of the region. The map view of these cross-sections are shown in figure 3.16. Moment tensors have been plotted at the high frequency location of the event. Cross-section A - A′ shows that the larger events are located on a structure which is dipping at angle of about 65° from the surface. This is consistent with the fault plane solution dips determined by moment tensor solutions. From the seismicity, there is also the possibility of a shallowing of dip at depth which is indicative of listric faulting. This is confirmed by the dip of the moment tensor solutions. The mainshock, the deepest large event in the sequence, has a dip of about 35°, while those close to the surface have dips that steepen towards about 80°. Cross-section B - B′ shows that the bottom of seismicity shallows to the south.

A west-dipping normal fault would imply that the eastern block is the upthrown

126
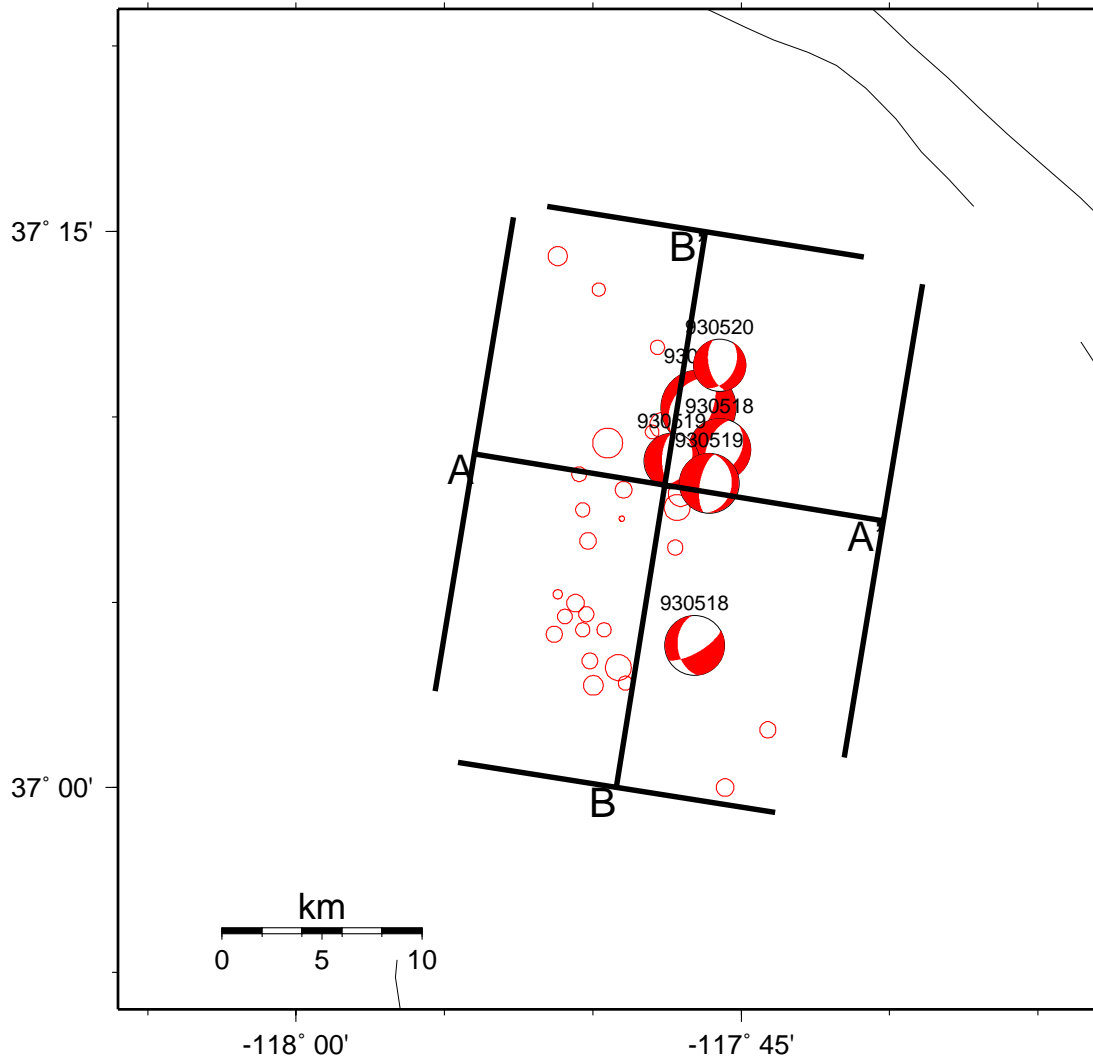
Figure 3.16: Map of Eureka Valley moment tensors with seismicity (M ≥ 3.0) and moment tensor solutions from 05/17/93 − 05/17/94. Lines show the California-Oregon border, and major faults. Areas viewed in cross-sections are designated in bold.
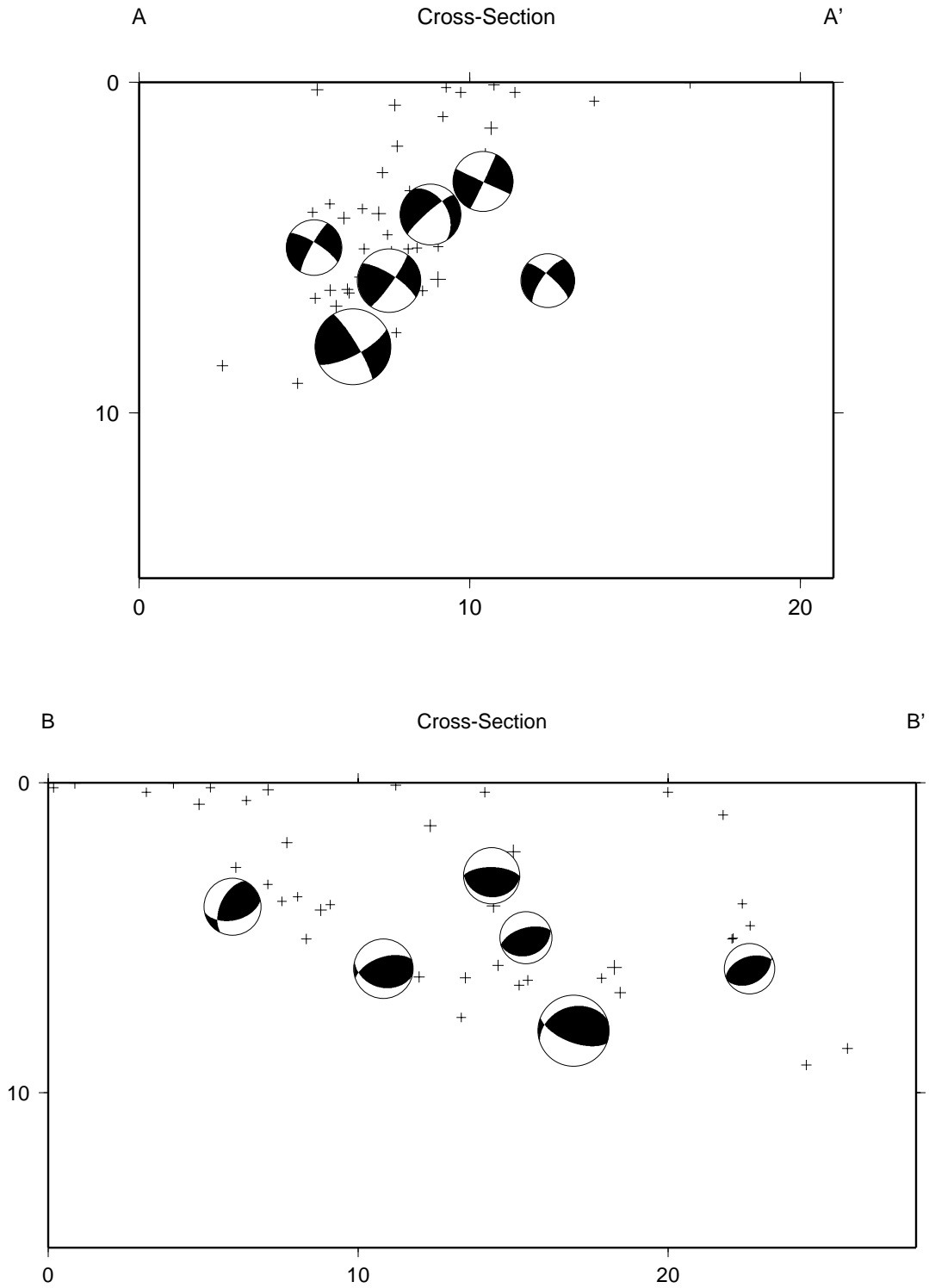
Figure 3.17: Cross-sections for the Eureka Valley earthquake perpendicular and parallel to the fault across the aftershock region. Aftershock locations are from the Northern California Earthquake Data Center. Moment tensors from regional surface waves.

block. A reconnaissance of ground cracking shortly after the event confirmed this observation (Suzanne Hecker, personal communication). Vertical displacements of 5-20 mm were observed along limited portions of two surface cracks. The motion along these cracks was down to the west and up to the east. The two zones of cracking suggest secondary faulting on surface splay faults. A closer look at the tectonics of the region shows that each of the faults within the Saline Range are characterized by an upthrown eastern block, similar to the earthquake fault. This would seem to suggest imbricate faulting in the region. All of these elements (normal faulting dipping to the west, upthrown block to the east, and a basin structure to the east) combined with the shallowing of the fault at depth, would imply that continental extension along the lines of various models with these features (see figure 3.18 from Lister, *et al.*, 1980) is plausible. These include symmetric pure-shear models (e.g. Miller, *et al.*, 1983), low-angle detachment fault models (Wernicke, 1981, Wernicke and Burchfiel, 1982), and delamination models.

### 3.4.2   Klamath Falls

The 21 September, 1993 Klamath Falls sequence provided another opportunity to test the ability of broadband stations for studies of earthquake sequences. A M 4.1 foreshock occurred at 3:16 UTC (8:16 pm on September 20th Pacific Daylight Time). The mainshocks in the sequence were two $M_w$ 6.0 events occurring at 3:28 UTC and 5:45 UTC (8:28 pm and 10:45 am PDT), just over two hours apart. The earthquakes were located in a normally seismically inactive region of Oregon, 16 km northwest of the city of Klamath Falls, Oregon. This region sits in the northwestern portion of the Basin and Range Province. The earthquakes caused two deaths and damaged more than 1,000 buildings. Total damage has been estimated at \$7.5 million (Wiley, *et al.*, 1993). The events were felt as far north as Eugene, OR and as far south as Redding, CA.

The Klamath Basin is a north-trending alluvium filled fault-block basin situated between the Cascade Range to the west and Miocene to Recent flows to the east (Baldwin, 1981). Although there have been no other significant earthquakes previously recorded in the area, the normal faulting seen in this earthquake sequence is typical for this tectonic province, and is responsible for the basin generation in the
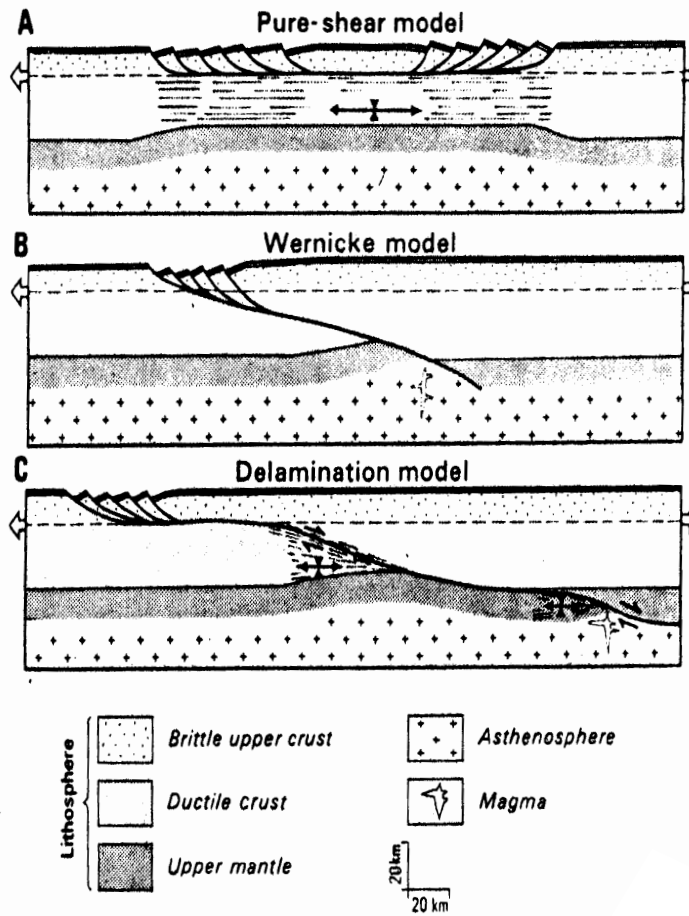
Figure 3.18: Various models for continental extension (from Lister). The dip direction of the models shown in B and C are opposite from that appropriate for the Eureka Valley sequence.

region, and in the Klamath Basin in particular. Due to the quiet nature of the region, this area is not as heavily instrumented as areas in California, and therefore the regional studies were essential to the analysis.

Figure 3.19 illustrates the source parameters for events in the sequence determined using the regional surface wave moment tensor inversion. Most of the events in the sequence were normal mechanisms. There was a pronounced 10° to 20° rotation in strike between the northern and southern portions of the fault and the two mainshocks. For example, the strike of the second mainshock rotates 16° from an azimuth of 353° to 9°. The foreshock mechanism is also consistent with strike of the first mainshock. Both of the mainshocks have a centroid depth of 12 km. Cross-sections both approximately east-west and north-south across the region (figures 3.20a and b, respectively) show the distribution of events with depth across and along the fault. The depths of the aftershocks are poorly constrained and produce a shotgun pattern in the cross-sections. The earthquakes are probably no deeper than 15 km.

One question is whether the earthquake ruptured the east-dipping or west-dipping fault plane. The former would likely make the Lake-of-the-Woods fault zone the causative structure. A knee in the fault zone makes this structure appealing. A number of faults on the east-side of Klamath Lake are also consistent with the earthquake rupture. Since the west-dipping plane is shallower than the east-dipping plane, the surface expression of the fault can be farther away. The cross-sections (figure 3.20) indicate that the west-dipping fault is the causative structure and that aftershocks occurred updip and to the north from the mainshocks although, as mentioned earlier, the earthquake locations are poor. Even using portable stations and a master event relocation, Braunmiller, *et al.* [1995] find that the aftershock distribution does not reveal a fault plane, although deeper events generally occur east of the shallower events.

A more complete broadband analysis, using empirical Green's function to determine slip parameters, illustrated that both events in the sequence ruptured towards the north and the rotation in strike acted as a barrier that most likely prevented a single $M_w 6.2$ rupture (Dreger, *et al.*, 1993). This has been previously observed in other sequences as well, including the 1966 Parkfield, 1979 Coyote Lake, and 1984 Morgan Hill events in California (King and Nábělek, 1985). Because of the geometry of the station coverage, however, the empirical Green's function method was unable

Figure 3.19: Map of Klamath Falls moment tensors with seismicity (M $\geq$ 3.0) and moment tensor solutions from 09/21/93 – 09/21/94. Lines show the Klamath Lake, California-Oregon border, and major faults. Areas viewed in cross-sections are designated.
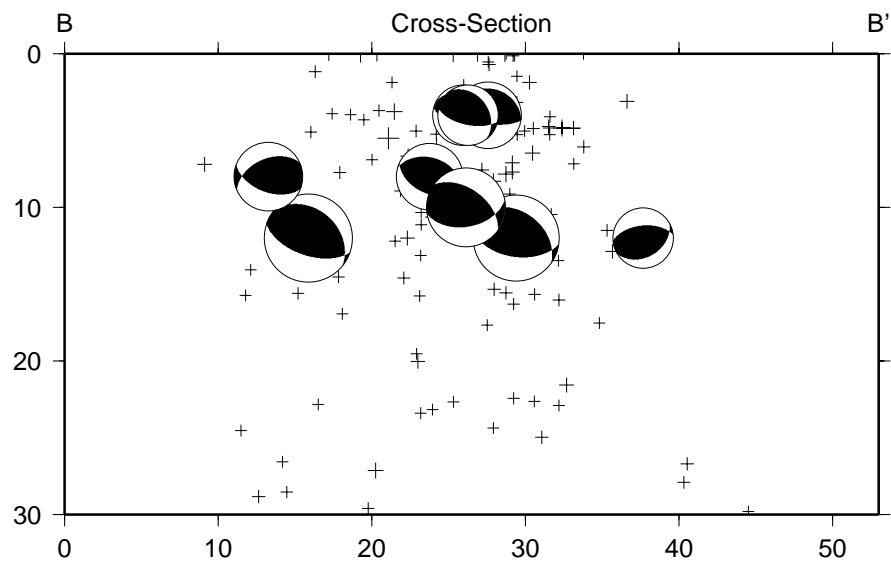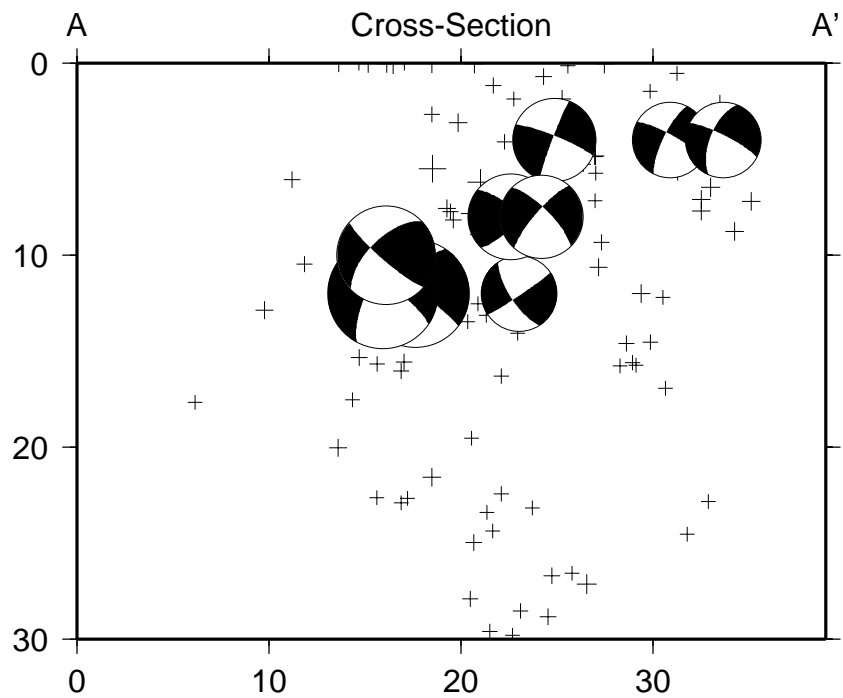
Figure 3.20: Cross-sections for the Klamath Falls earthquake east-west and north-south across the aftershock region. Aftershock locations are from the Northern California Earthquake Data Center. Moment tensors from regional surface waves.

to unambiguously resolve which of the two possible fault planes slipped in the earthquake, although the east-dipping fault was slightly favored. The slip distributions of the two events along the east-dipping fault is shown in figure 3.21. The first mainshock slipped towards the NW, but also had a significant component along dip, while the second mainshock slipped along strike, again towards the NW.

### 3.4.3 Northridge

On 17 January, 1994 at 12:30 UTC (4:30 am Pacific Standard Time) a $M_w$ 6.7 earthquake struck the San Fernando Valley near the town on Northridge. The earthquake was felt very strongly throughout the Los Angeles metropolitan area, and caused 60 deaths and over \$20 billion in damage in the region. Acceleration exceeded 1.0g at several locations in the region, and was recorded as high as 1.8g. It was felt as far away as Turlock, CA; Las Vegas, NV; Richfield, UT; and Ensenada, Mexico. The San Fernando Valley is one of the many west or northwest trending deep sedimentary basins that characterize this part of southern California both onshore (Los Angeles, Soledad, and Ventura basins) and offshore (Santa Monica, Santa Barbara, and Catalina basins). The regional surface wave moment tensor inversion indicates that the earthquake was a thrust event striking at 312°. The earthquake occurred near the region of the 1971 San Fernando earthquake ($M_w$ 6.7). Similar in both location and magnitude, the 1971 and 1994 earthquakes differ in that the San Fernando event had a north-dipping fault plane and the Northridge event had a south-dipping fault plane.

Beyond the great losses in both lives and property caused by an urban earthquake, in many ways the Northridge earthquake was unremarkable. Moment tensor solutions were calculated for 21 earthquakes in the sequence. As illustrated in figure 3.22, the vast majority of earthquakes in the sequence were thrust events with W-NW/E-SE strike orientations. Tests of slip distribution on the north-dipping and south-dipping fault planes show that the south-dipping plane is the causative structure (Dreger, 1994). This has been borne out by the aftershock seismicity (Hauksson, *et al.*, 1995), which further show this to be on a "blind thrust" fault that does not daylight because it appears to terminate at the north-dipping San Fernando and Santa Susana faults. The orientation and type of faulting in both this earthquake and San Fernando is consistent with the massive mountain building of the Santa Susana and Santa Monica
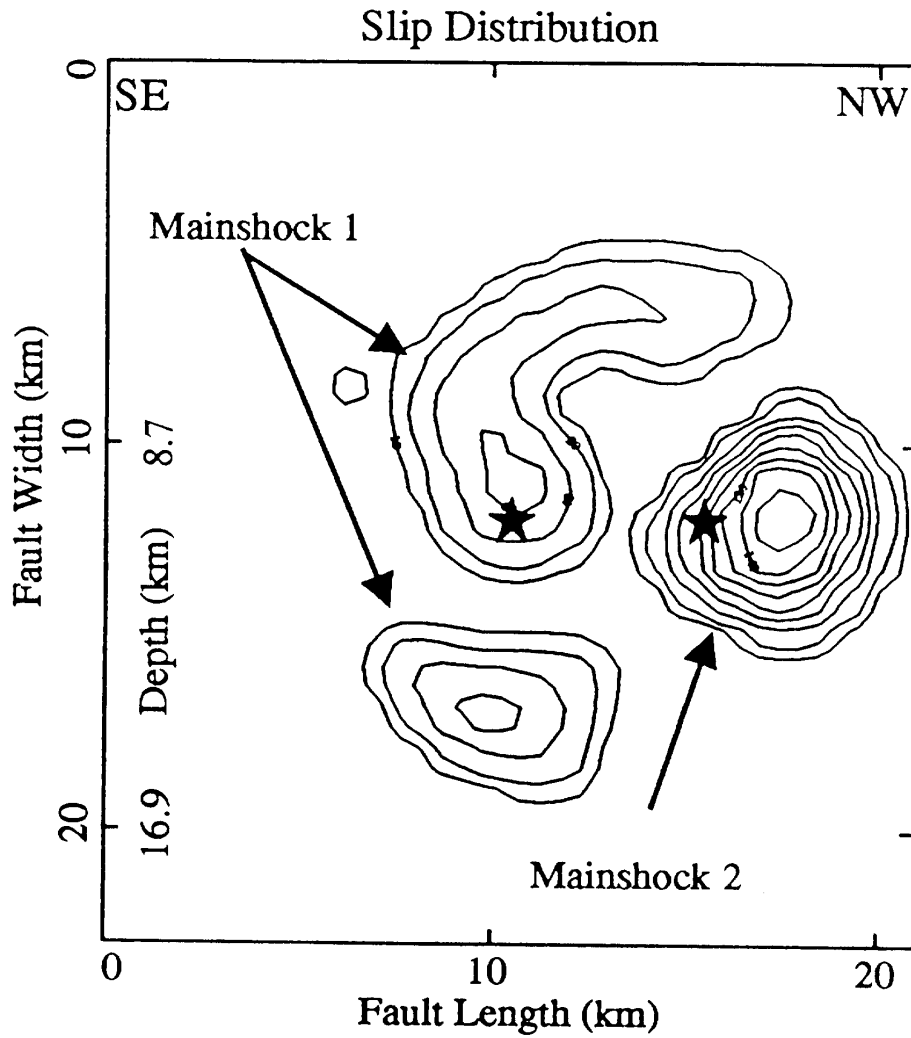
Figure 3.21: Slip distributions for the two Klamath Falls mainshocks (from Dreger,
*et al.*, 1995). The star denotes the hypocentral location. Contours of slip every 20
cm are shown in addition to the 10 cm contour.

Mountains, both east-west trending ranges.

A cross-section of the Northridge region illustrating both aftershock locations and moment tensor solutions is shown in figure 3.23. Events at 6 km are those with depths which are not well constrained, and so are fixed at that depth. The fault plane is indicated by the linear trend in seismicity which extends from the surface near the A' region to about 20 km depth. The dip illustrated from the aftershock distribution is approximately 45°, and is consistent with the 47° dip estimated from the moment tensor solution. The northern end of the seismicity is not as well defined, and represents a combination of events on both the northern end of the south-dipping faults, the north-dipping faults, or diffuse deformation of the anticlinal folds of the Santa Susana Mountains (Hall, *et al.*, 1994). The hypocenter of the mainshock is illustrated by the largest symbol at 18.4 km, but the centroid depth of the event is 14 km, indicating an upward rupture. Other events, including the largest aftershock (23:33 UTC; $M_w5.9$) exhibit this pattern as well.

Slip distributions mapped onto the fault plane both from strong motion, teleseismic, and geodetic measurements (Wald and Heaton, 1994) and from regional broadband data (Dreger, 1994) have determined that the earthquake ruptured updip and to the west from the hypocenter, and had two main subevents. Again, this is consistent with the aftershocks' moment tensors and locations. Furthermore, Dreger [1994] observed that aftershocks clustered at the edges of the rupture area and the largest aftershocks occurred in the unruptured updip regions. This can be seen in figure 3.23 cross-section B. From the hypocenter, there is a sparse patch of aftershock seismicity updip and to the northwest, about 15 km in both directions. The centroid plots roughly in the center of the patch. All of the aftershocks have centroid depths shallower than the mainshock (14 km), and the majority of aftershocks, particularly those that occurred in the first few days after the event, were located to the west of the mainshock hypocenter.

Although the majority of earthquakes have reverse mechanisms, there are quite a number of oblique reverse mechanisms and even a few strike-slip earthquakes in the group. Two of the strike-slip events occur in the center of the mainshock slip region, where there is a plethora of both strike-slip and reverse aftershocks. Thio and Kanamori [1996] group the aftershocks into three regions: the eastern part where aftershocks have thrust mechanisms similar to the mainshock, a central area with
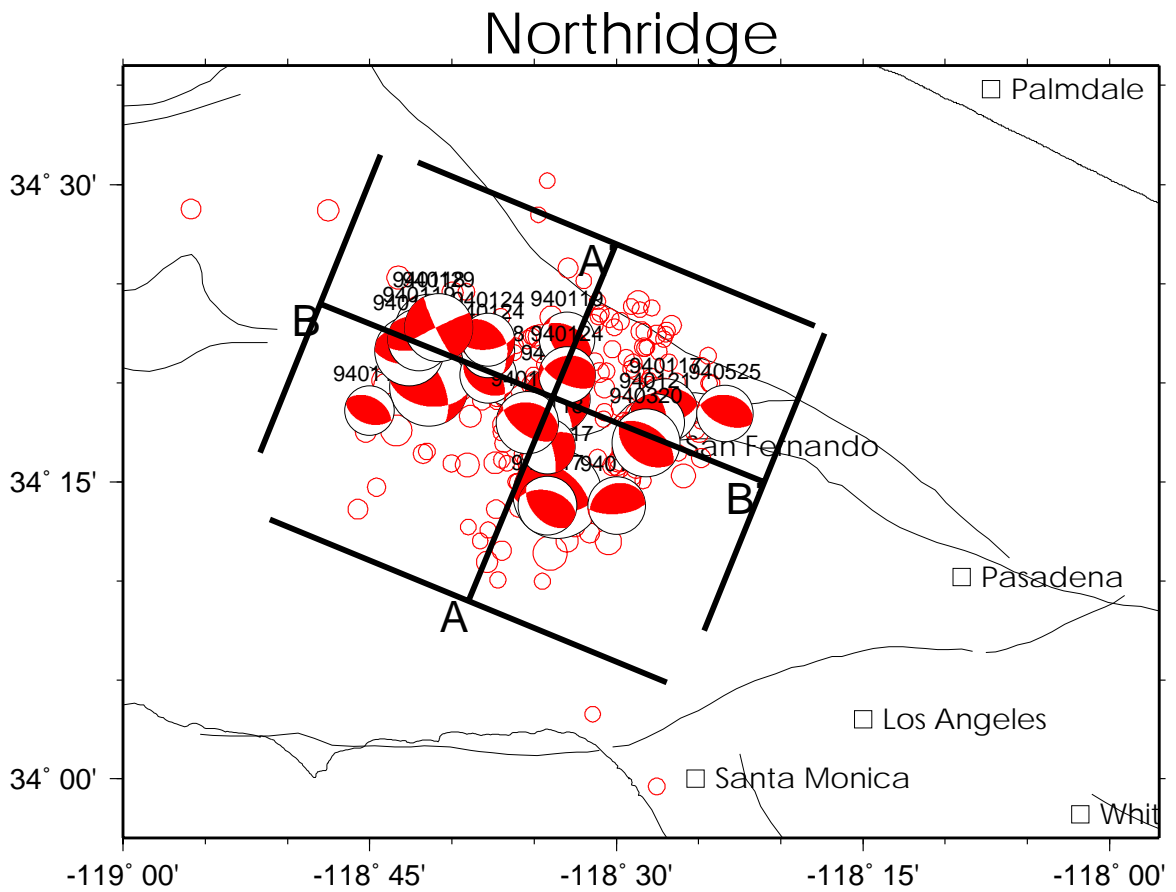
Figure 3.22: Map of Northridge moment tensors with seismicity and moment tensor solutions. Lines show the coastline and major faults. Areas viewed in cross-sections are designated.
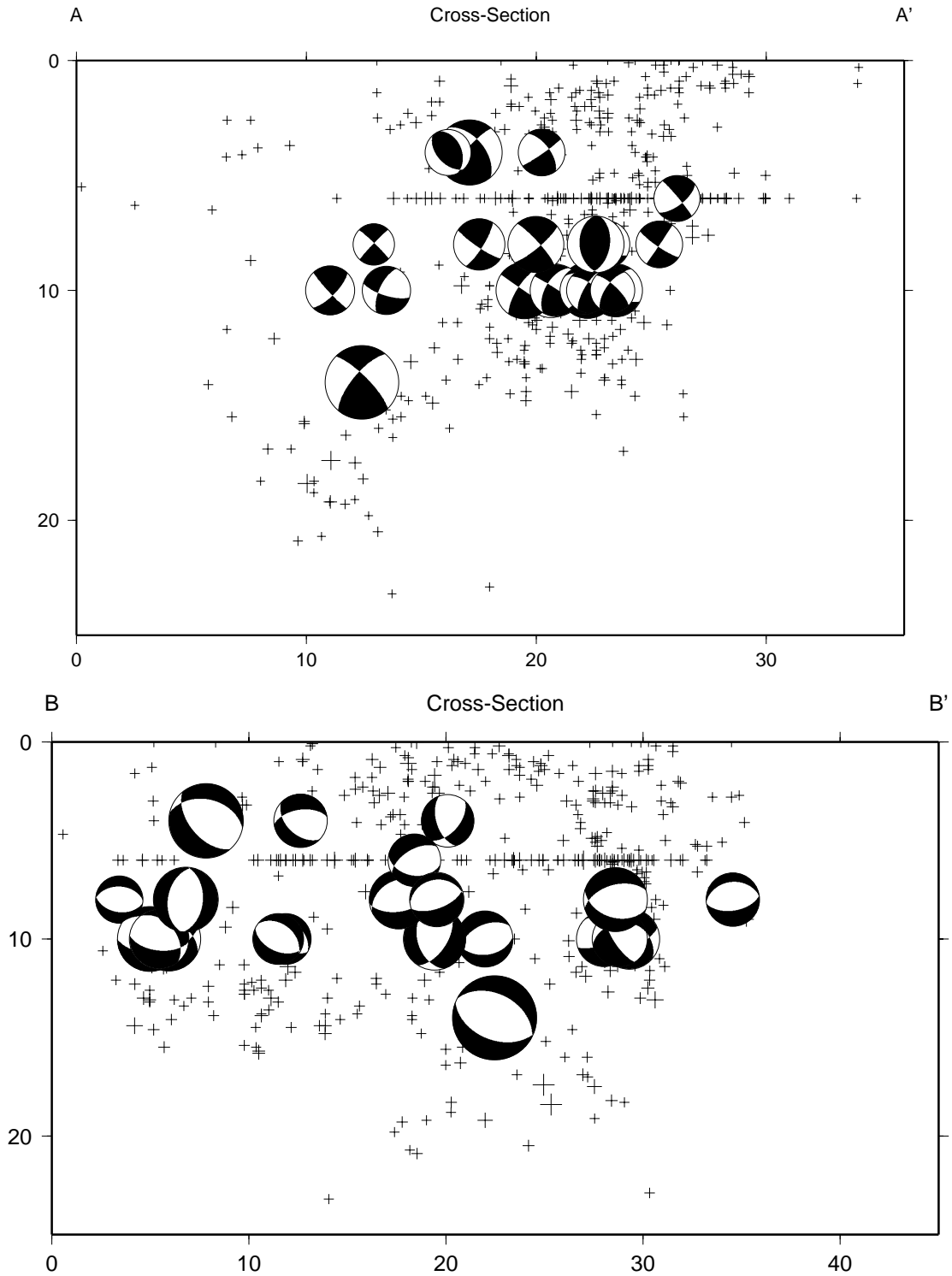
Figure 3.23: Cross-sections for the Northridge earthquake. Aftershock locations are from the Southern California Earthquake Center. Moment tensors from regional surface waves. Some earthquakes shown have depths which are not well constrained and are fixed at 6 km.

predominantly strike-slip events, and an area to the west with oblique thrust events. Using this evidence, they postulate that the fault system of the Northridge earthquake is segmented. This central ridge is also the location of the high slip region of the Dreger [1994] regional inversion, but a low slip region of the Wald and Heaton [1994] strong motion inversion. The slip map from Dreger [1994] is shown in figure 3.24. The rupture starts in the southeast portion of the fault (B′) at depth and propagates in the northwest direction towards the surface. The largest slip (> 3 m) is found in the center portion of this slip region. There is also a band on slip on the northwest edge of the rupture at depth. Aftershocks are generally located away from the main slip ridges, but close to the edges.

### 3.4.4  Mendocino Fault

The Mendocino fault earthquake occurred at 15:15 UTC (8:15 am Pacific Daylight Time) on September 1, 1994. The moment magnitude ($M_w$) was estimated to be 6.9 using the regional surface wave moment tensor inversion. The hypocentral location (40.445 degrees N; 125.897 degrees W) and depth (20 km) placed the earthquake off-shore along the Mendocino fault, about 140 km west of Cape Mendocino (figure 3.25). It was widely felt throughout the area but, due to its location far offshore, only minor damage at Honeydew was reported. It was felt in southern Oregon and in California as far south as Fresno. Offshore earthquakes are more difficult to precisely locate than those onshore because of the poor azimuthal coverage due to the lack of ocean bottom seismographs to constrain the location. While onshore locations in the region are considered accurate within 2 km, the hypocenter location for the Mendocino fault earthquake is only accurate within a range of ~15 km.

The Mendocino fault is a 260 km long east-west structure which forms the transform plate boundary between the older and thicker Pacific plate to the south and the younger and thinner Gorda plate to the north. The Gorda ridge terminates the fault's western edge. To the east, the Mendocino fault joins the Mendocino triple junction (MTJ), a complex region in the vicinity of Cape Mendocino where the Gorda, North American, and Pacific plates meet (see Dengler *et al.*, 1992 and Section 3.2.5 for a more detailed description of the tectonics of this region). The Mendocino fault is nearly vertical and motion is primarily right-lateral strike-slip with the Gorda plate
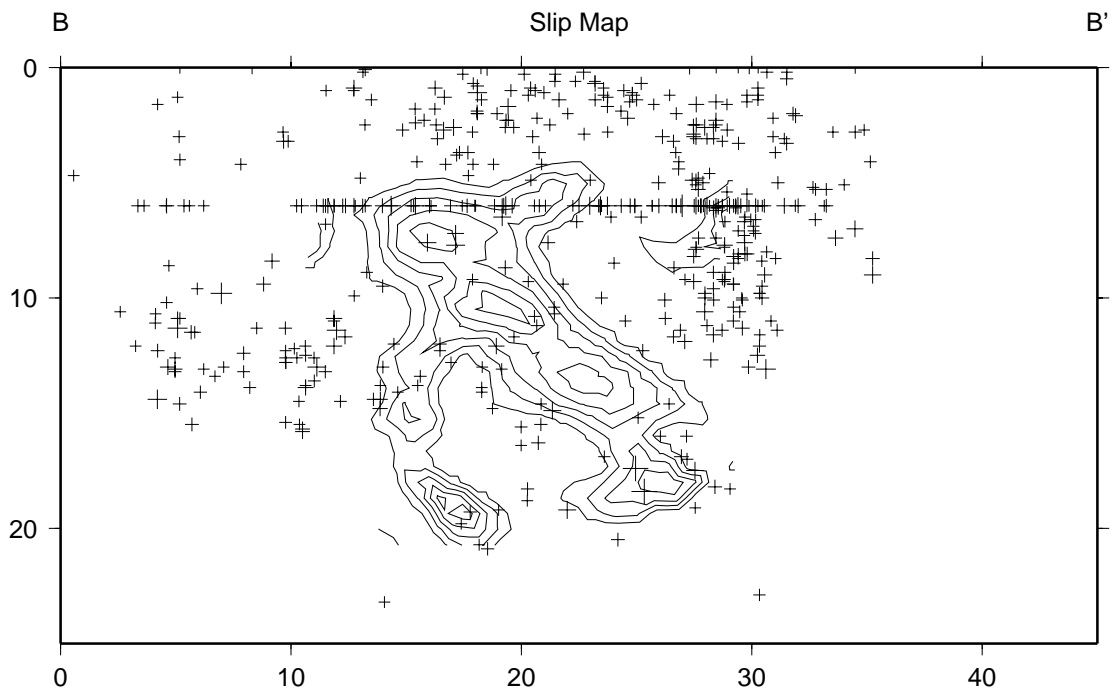
Figure 3.24: Northridge Slip Map plotted on cross-section B-B' of the previous figure. Slip values courtesy of Dreger, personal communication. Results and methods presented in Dreger [1994]. Contours are shown at 50 cm intervals and have a maximum slip of 330 cm.

Figure 3.25: Map of Mendocino Fault earthquake sequence with seismicity (M $\geq$ 3.0) and moment tensors from 09/01/94 – 09/01/95. Lines show coastline and major faults. Areas viewed in cross-section are designated.

moving east relative to the Pacific plate (De Mets, 1990; Jachens and Griscom, 1983). The depth of the fault zone deepens and reverse movement has been recorded in earthquakes near the eastern end of the Mendocino fault close to the MTJ (Nowroozi, 1973; McPherson, 1989).

The North Coast region is one of the most seismically active areas in the contiguous United States. The Mendocino fault is responsible for about 30% the area's seismic activity and has been the single most active structure in the region during historic times. Since 1950, nine magnitude 5.5 or larger earthquakes have been identified with this structure; the largest prior to the 1994 event was a $M_L 6.6$ in 1984. Earlier large earthquakes may have been generated by the Mendocino fault, including the $M_s 7.6$ 1922 earthquake, the largest historic North Coast event. However, because of the difficulties in precisely locating offshore earthquakes, it is difficult to distinguish Mendocino fault earthquakes from those occurring within the southern portion of the Gorda plate. The ability to determine moment tensors for offshore events allows discrimination between these two earthquake source regions. Offshore earthquakes along the Mendocino fault and those within the Gorda plate both exhibit strike-slip faulting along nearly vertical fault planes. The Gorda plate events show northeast and northwest trending fault and auxiliary planes, while Mendocino fault earthquakes are characterized by nearly east-west and north-south planes.

The moment tensor solution of the 9/1/94 $M_w$ 6.9 event (partially hidden under others in figure 3.25) characterizes it as a strike-slip earthquake. The fault plane is oriented 92 degrees, and the alignment of aftershocks parallel to the mapped trend of the fault clearly identifies this as a Mendocino fault sequence. Cross-sections of the region taken perpendicular to the Mendocino Fault and east-west along the fault are shown in figures 3.26a and b, respectively. Most early aftershocks clustered in the area between 126° and 125.3° W, which would suggest a rupture length of about 65 km, consistent with the seismic moment of this earthquake. The mainshock lies near the western edge of the aftershock zone and suggests that rupture proceeded from the mainshock hypocenter to the east. In addition, for the first few months after the event, seismicity clustered at the MTJ. Only after several months did the seismicity east of 125.3° W appear, as well as the sequence which occurred within the Gorda Plate northeast of the mainshock. Cross-section A – A' (figure 3.26a) illustrates the concentration of seismicity along the Mendocino Fault, separating the inactive

Pacific Plate (left) from the seismically active Gorda Plate (right). In cross-section B – B' (figure 3.26b), seismicity associated with the MTJ is shown towards the right. With the exception of the seismicity associated with the 02/19/95 Gorda Plate event, the large region without seismicity on the left is most likely the rupture area of the Mendocino Fault earthquake.

The number of aftershocks following the Mendocino fault earthquake seems anomalously low. The paucity of magnitude 3 aftershocks may be due largely to the difficulty of recording small earthquakes located so far offshore. However, there has also been a lack of aftershocks at higher levels. Excluding the events which were clearly off the Mendocino Fault (such as the 02/19/95 Gorda Plate event), only six events occurred at the magnitude 4 level, and no earthquakes greater than magnitude 4.5 for the year following the mainshock. The November 8, 1980 ($M_S$ 7.1) had one magnitude 5.2 aftershock and twenty greater than magnitude 4 within twenty days following the mainshock. The largest Mendocino fault aftershock in the same time interval was a $M_w$ 4.6 event on September 21, 1994.

Aside from the San Andreas fault, the Mendocino fault was widely considered the only structure in the North Coast area capable of producing magnitude 7 or larger earthquakes. More recently, attention has focused first on the intraplate seismic activity within the Gorda plate (Smith and Knapp, 1980; Wilson, 1989; McPherson, 1989) and the seismic hazards posed by the Cascadia subduction zone (Heaton and Kanamori, 1984; Heaton and Hartzell, 1987; Clarke and Carver, 1992). The September 1 earthquake clearly shows that the Mendocino fault is capable of producing large earthquakes. However, it is still unclear just how large an earthquake this structure is capable of generating. A rupture of the whole fault length would produce an earthquake in the upper magnitude 7 range. Some evidence suggests, however, that the Mendocino fault is more likely to fail by the occurrence of separate earthquakes on different segments of the fault, rather than by a single event encompassing the entire fault. There is no record of past events large enough to involve rupture of the entire fault. The historical record does show earthquake activity over a wide magnitude range along the length of the fault. Although no one has analyzed in detail the total slip produced by historic earthquakes, the present rate of activity may well account for the observed rate of slip between the Pacific and Gorda plates.

The segment of the Mendocino fault east of the 1994 rupture seems to behave
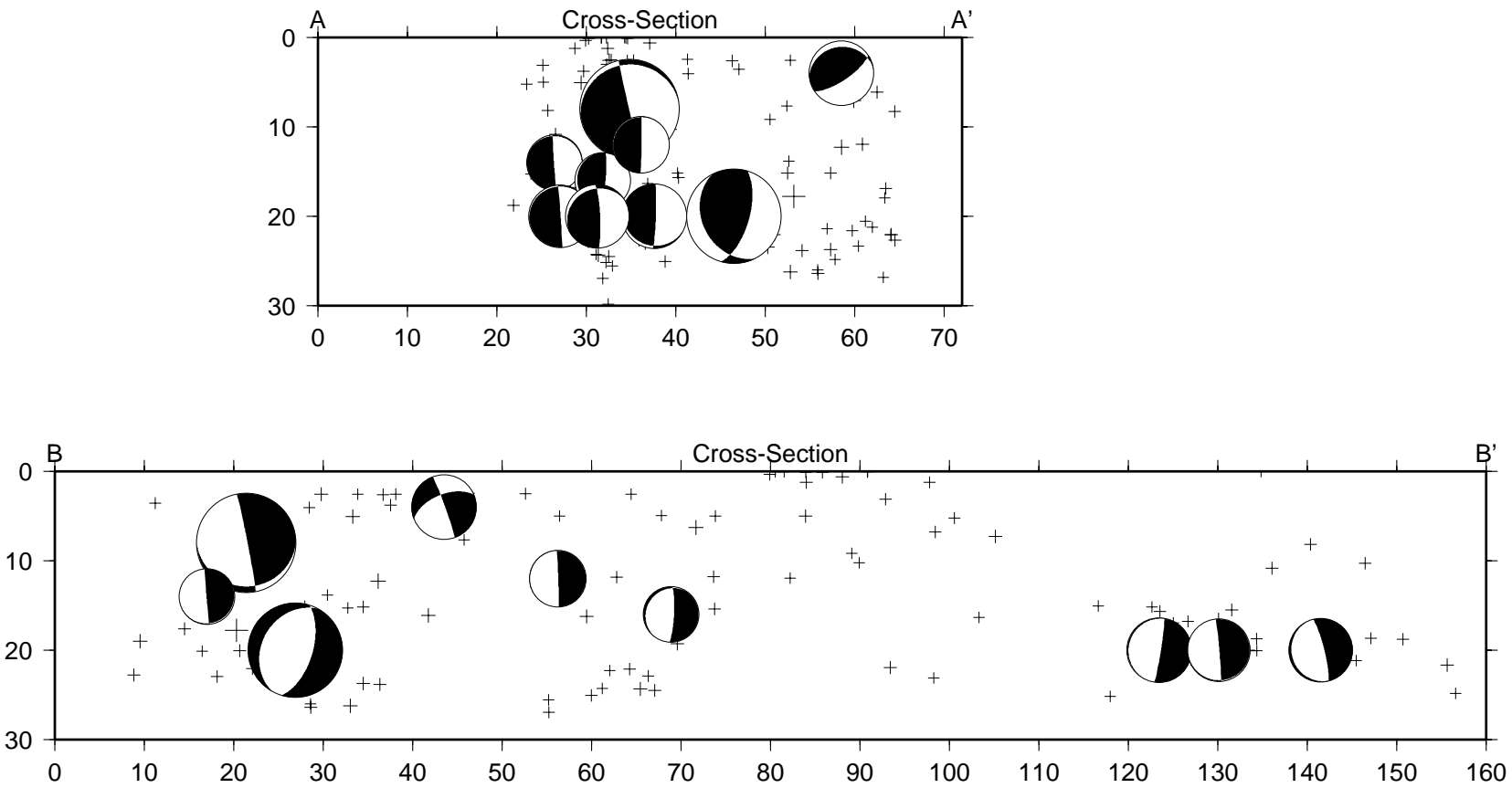
Figure 3.26: Cross-sections for the Mendocino Fault earthquake approximately perpendicular and parallel to the Mendocino Fault. Aftershock locations from the Northern California Earthquake Data Center. Moment tensor solutions from regional surface waves.

144

differently from the rest of the fault. This segment is extremely active, producing numerous small to moderate "sympathetic" aftershocks whenever larger earthquakes occur in the vicinity. The small earthquakes in figure 3.25 located between the coast and 125.1° W are examples of this activity. Similar high activity levels on this segment were observed after the 1980 Trinidad (M7.4), 1991 Honeydew (M6.1), and 1992 Cape Mendocino earthquake sequence (M7.1, M6.5, M6.7), none of which were centered on the Mendocino fault. The relationship between the Mendocino fault earthquake and other recent large North Coast earthquakes is unclear. The 1980 Trinidad earthquake broke along a northeast trending fault extending from just offshore of Trinidad to near the Mendocino fault (Kilbourne and Saucedo, 1981). The intersection of the 1980 rupture with the Mendocino fault lies close to the epicenter of the September 1 earthquake. While the 1994 earthquake relieved strain on the Mendocino fault, it increased the strain of the locked portion of the subduction zone, hastening the arrival of the next megathrust earthquake. Clearly, adjacent plates and structures are affected by the complex interplay of fault movement in the vicinity of the MTJ and the Mendocino fault.

It is generally accepted that very large Cascadia subduction zone earthquakes have occurred in the past and have produced large tsunamis (Clarke and Carver, 1992). The April 1992 Cape Mendocino earthquake produced a small tsunami that arrived at coastal tide gauges within twenty minutes of the earthquake (Oppenheimer, *et al.*, 1993). Locally produced tsunamis would arrive at coastal communities before the seismic waves may even reach the seismographic stations of distant tsunami warning centers. No local tsunami watch was initiated after the lightly felt September 1 earthquake even though some earthquakes of this size have produced devastating tsunamis. A tsunami was generated with a maximum wave height of 14 cm (peak-to-trough) at Crescent City. Not until subsequent processing of the coastal tide data was it clear that no tsunami threat existed. To address this concern, computer codes which estimate the size of a tsunami based on factors such as earthquake size, mechanism, location, and depth could be piggybacked onto the automatic moment tensor codes to produce tsunami warnings.

### 3.4.5  Double Spring Flat

On September 12, 1994 at 12:23 UTC (5:23 am Pacific Daylight Time) a $M_w$

= 6.0 event occurred near Double Spring Flat, an area located 30 km southeast of Lake Tahoe close to the California-Nevada border (38.819° N, 119.652° W, z=12 km). The event was felt over large portions of California and Nevada, including San Francisco, Sacramento, and Reno. Slight damage was reported near the epicenter at Gardnerville and Virginia City, NV and Markleeville, CA. The epicentral area is in the northern portion of the Walker Lane Belt and sits at the transition between the major tectonic provinces of the Sierra Nevada Mountains and the Basin and Range Province. Regional moment tensors indicate that the mainshock had a strike-slip mechanism, either right-lateral on a NE-SW striking plane or left-lateral on a NW-SE striking plane. Many aftershocks in the sequence, including the largest, however, have a normal mechanism on a N-S striking plane. Double Spring Flat is a topographically flat area of Pliocene volcanics situated along the steeper terrain of the Pine Nut Mountains to the northeast and between the recent alluvium of the Carson Valley to the northwest and the Antelope Valley to the southeast. The major faults in the region are the Genoa Fault and Antelope Valley Fault, which are the Basin-Range normal faults occurring at the western edge of the Carson and Antelope Valleys, respectively, and appear to constitute the dominant tectonic activity in the region. Between the two basins, the region is covered with a large number of small, mostly normal, faults of all orientations.

Overall, moment tensors were calculated for 24 events in the sequence M ≥ 3.4 and for one possible foreshock occurring earlier in the year (figure 3.27). The moment tensors are complete at this magnitude level, with the exception of those events occurring right after the mainshock. There is a clustering of seismicity and moment tensors along two distinct planes. One plane, running diagonally from northwest to southeast, is dotted with right-lateral strike-slip earthquakes. The normal earthquakes are located along a second fault, running north-south. There are significant gaps in seismicity towards the southeast along the northwest-southeast fault system and towards the northeast along the northeast-southwest fault system, possibly outlining areas of the fault plane which the mainshock completely relieved of stress, depending which of the two possible fault planes were activated during the mainshock. Smaller clusters were located off the two major fault planes WNW of the mainshock at the southern end of the Carson Valley and NNE of the mainshock. Interestingly enough, earlier in the year (7 March 1994), a $M_w3.7$ normal event occurred in the vicinity

of the north-south striking normal events. It appeared to have a typical aftershock sequence associated with the event, with M 2 events occurring in the region primarily in the first week, but continuing until May.

A relocation technique was used to obtain the best possible locations for the sequence. The method employed was a variation of the master event relocation technique using multiple master events. Five large events in the sequence which had a range of depths were selected and the best possible solutions were obtained with standard location techniques (BDSN stations, NCSN, and University of Nevada at Reno stations). Next, the station adjustments were computed for all available stations for each of the events. All of the station adjustments were averaged to get a master station adjustment file. Finally, all of the earthquakes in the sequence were relocated with the master station adjustment file, including the previously located events.

Cross-sections of the aftershock region taken in both the northwest-southeast and southwest-northeast are shown in figures 3.28a and b, respectively. The seismicity along cross-section A - A′ primarily shows strike-slip earthquakes, while the B - B′ cross-section intersects most of the north-trending normal events. In general, the depths of the strike-slip events (8 − 14 km) were consistently deeper than those for the normal mechanism events (4 − 8 km depth). The possible foreshock occurring earlier in the year also had a shallow depth (6 km) consistent with this observation. Unfortunately, this is not borne out in the cross-sections of the relocated data. While the epicentral locations of the relocated events appear to be very good, the depths of the relocated events were not very well constrained due to the absence of any nearby stations. In this case, the centroid depths determined from the regional moment tensor techniques seem better able to resolve event depth.

In addition, there seems to be several significant spatial and temporal progressions of the sequence (figure 3.29, top). First, the sequence switched back and forth between mechanisms, starting with the strike-slip mechanisms of the mainshock and the first few aftershocks (events 1 and 2). Several events occurring in the coda of the mainshock presumably had this type of mechanism as well. Roughly five hours after the event and continuing for about 17 hours, all of the large events had normal mechanisms (events 3 − 9). Later on, the strike-slip earthquakes continued (events 10 − 12); afterwards, the sequence had mixed mechanisms (events 13 − 20). Secondly, the earliest activity in the sequence, including both strike-slip and normal events,
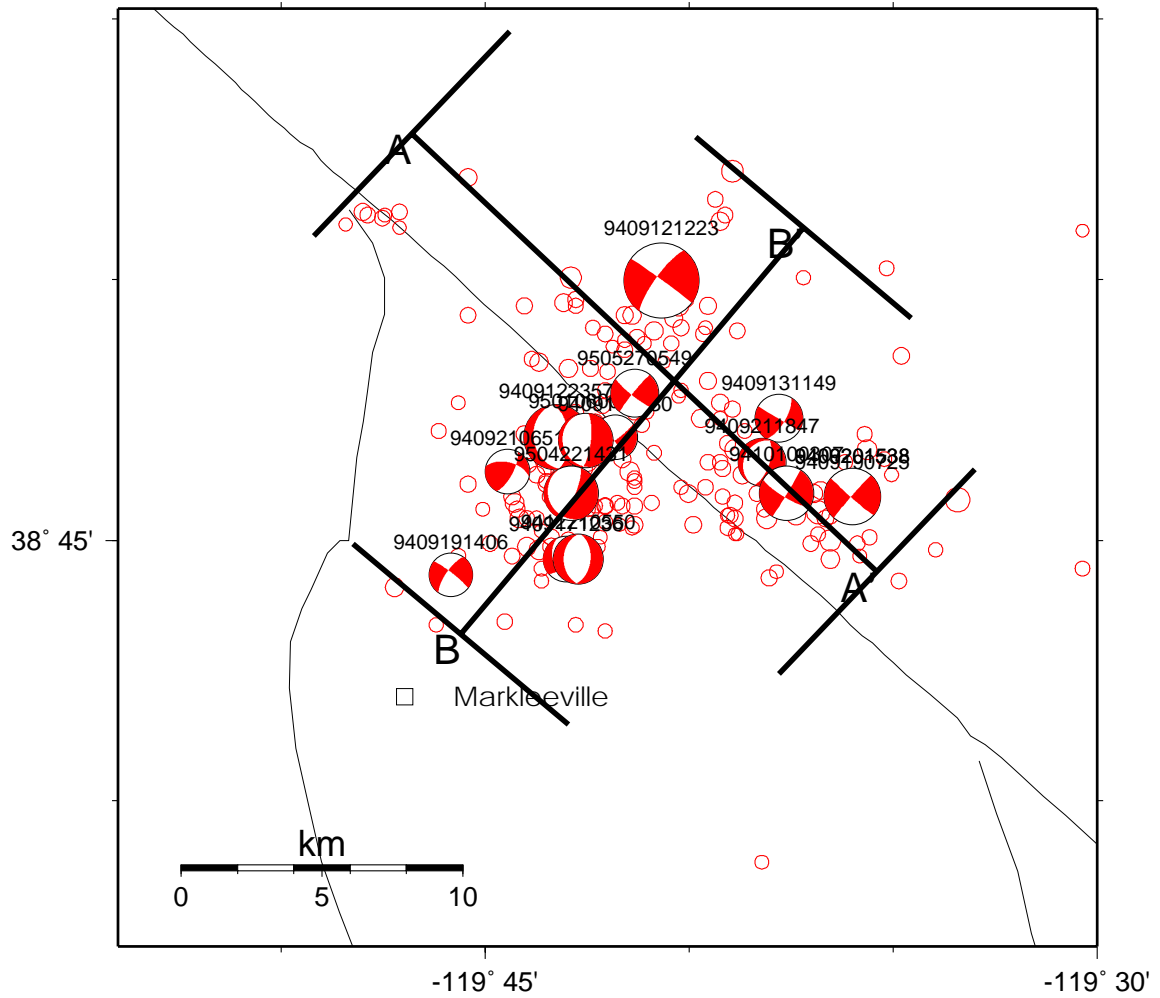
Figure 3.27: Moment tensors for 20 events in Double Spring Flat sequence. Events are plotted at relocated epicenters. Line shown is the California-Nevada border.
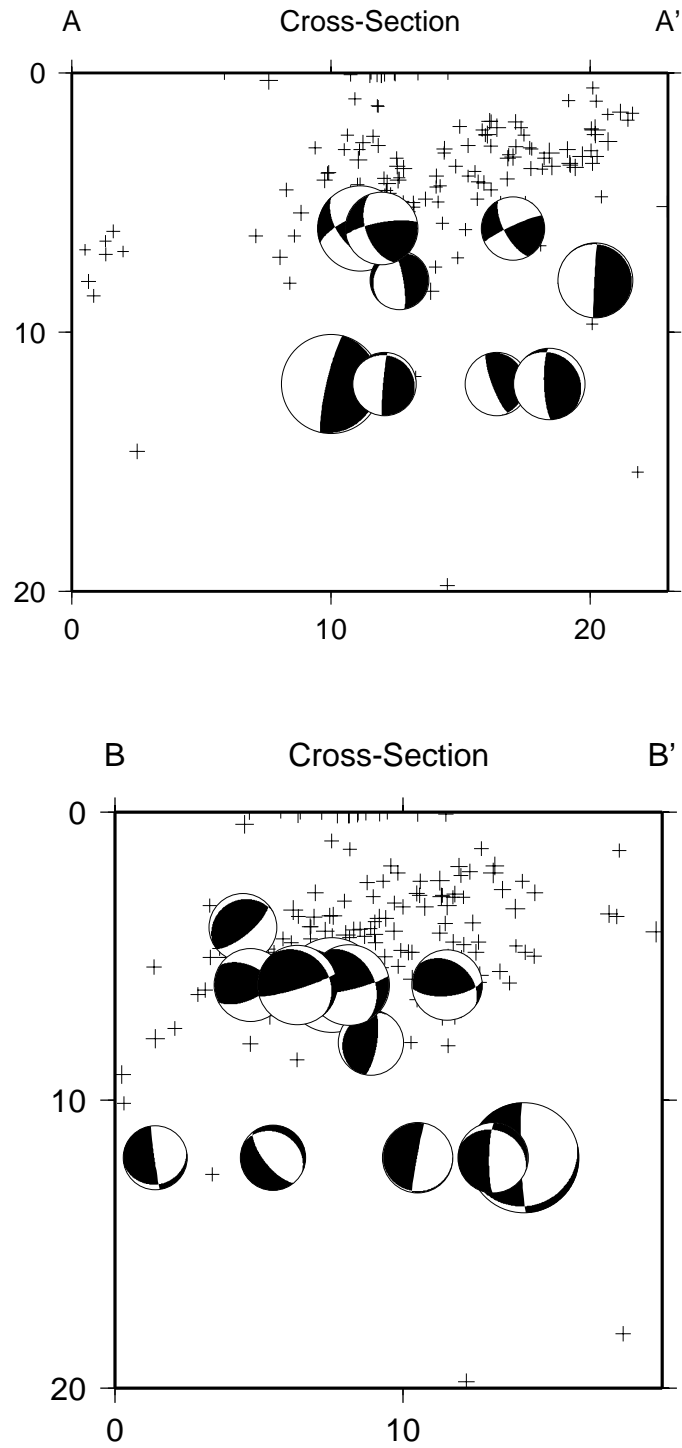
Figure 3.28: Cross-sections for the Double Spring Flat earthquake in the north-south and east-west direction. Aftershock locations generated using relocation technique. Moment tensor solutions from regional surface waves.

took place close to the mainshock. Later events were located at the southeast and south portions of the strike-slip and normal faults, respectively.

Figure 3.29 (bottom) also shows the P and T axes as determined from the moment tensors. The T axis is relatively stable, while the P axis varies from event to event. The changing compressional axis is spatially partitioned. $S_1$ (as indicated by the P or compressional axis) ranges from vertical to due north (or south), $S_2$ (indicated by the B or null axis) ranges from vertical to due north as well, and $S_3$ (indicated by the T or tensional axis) varies from WNW to WSW. This is consistent with the regional stress field given by $S_N \approx S_V \gg S_W$ (see section 3.3.2). The magnitudes of the vertical and greatest principal horizontal stresses are nearly equal and can readily exchange. Local variations in the relative magnitudes of $S_N$ and $S_V$ and local faulting trends may determine whether strike-slip or normal faulting occurs. In the case of shallow earthquakes, we see that $S_V > S_N \gg S_W$, and normal faulting occurs. As the depth increases, the horizontal stress increases until $S_N > S_V \gg S_W$ and strike-slip faulting occurs. Since, in this earthquake sequence, there are two distinct mechanisms and faults, it is interesting to see whether this behaviour can be attributed purely to gravitational loading or whether it is associated with the static stress changes caused by the earthquakes.

The Coulomb criteria for failure was applied to the problem (see section 3.3.6) with the following assumed conditions: no pore pressure, no cohesion, and the regional stress orientation as determined from the earthquake moment tensors. The resulting regional stress field had an azimuth of tension oriented at 85° and a reasonable amplitude of 75 bars. The DLC Dislocation Programs (Bob Simpson, personal communication), which creates dislocation models based on rectangular slip surfaces, was used to calculate the resulting elastic fields in a 3-D halfspace. Faults were chosen based on seismicity and moment tensors, as well as major faults in the region. Every fault was broken into 2 km × 2 km squares for the calculations. The mainshock was represented by a 6 km × 6 km rectangular patch with appropriate slip determined from $M_0$ (0.93 m). The stress drop $\Delta\sigma$ on the fault surface is approximately 25 bars.

In the case of right-lateral failure, there were large increases in the Coulomb Failure Function on the mainshock fault plane and on the strike-slip fault to the north. All of the strike-slip earthquakes on the fault plane occurred at the edge of the patch with high $\Delta CFF$. The two strike-slip events to the north also occurred at a region of very

150
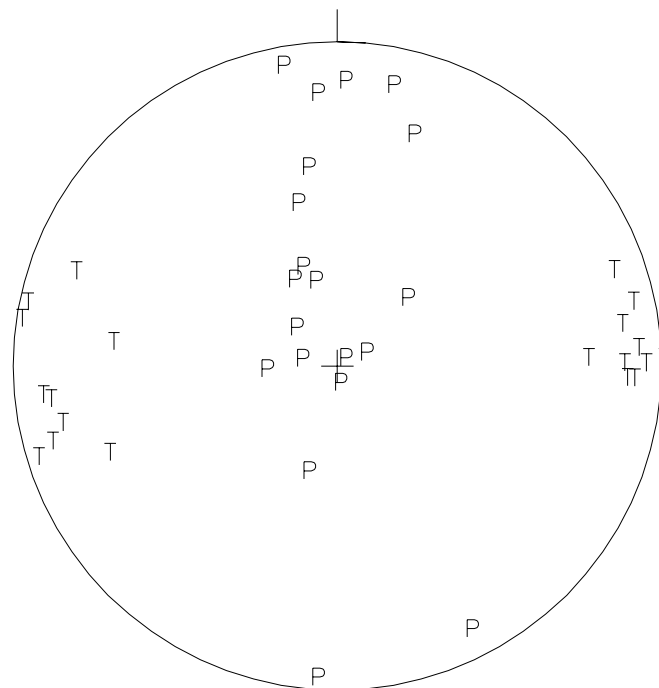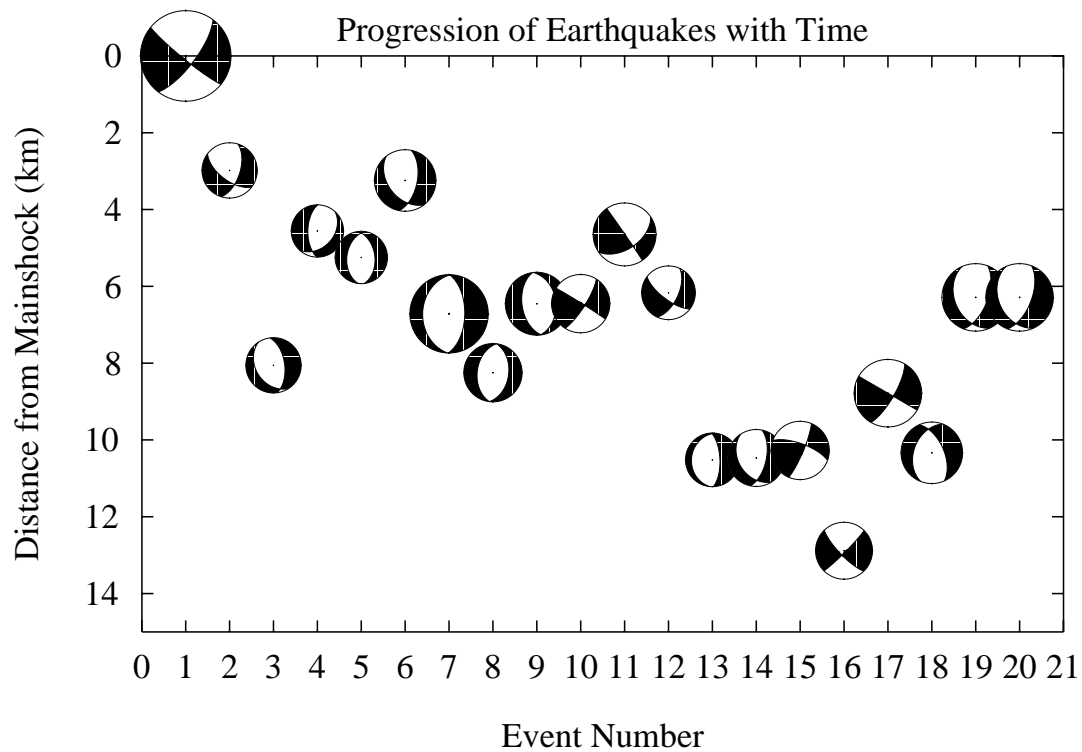
Figure 3.29: Top figure shows the spatial and temporal progression of events in the Double Spring Flat sequence with time. Bottom figure is a plot of the P-axis and T-axis for events in the sequence.

high $\Delta CFF$. For normal failure, the regions of high $\Delta CFF$ occurred along normal faults close to the mainshock, at deep depths in the northern portion of the fault, and at shallow depths in the southern portion of the fault. Most of the normal fault earthquakes, all of which had shallow depths, occurred in the southern portion of this fault. The Genoa and Antelope Valley Faults did not have any significant increases in CFF from the mainshock. There are obvious limitations of this method. Uniform slip of the fault surface may be satisfactory for calculations in the far-field. This is still useful as a first step in looking at the static stress changes. In some of the near-field measurements that are being considered, however, the details of the slip distribution become more important. The next step will be to consider the stress changes from the slip distribution calculated from regional broadband stations.

Using the method of Mori and Hartzell [1990] modified for regional distances, the variation in the source time function shape can be mapped into the spatial and temporal distribution of slip on the fault plane and constitutes a perturbation to the point-source assumption implied by the deconvolution process (see Dreger, 1994 for a detailed description of this technique). Although both rupture velocity and dislocation rise time are fixed for each inversion, velocity values range from 2.0 to 3.4 km/s. There is no clear minimum in the variance with respect to rupture velocity although a value of 2.8 km/s represents the location of the flattening of the curve. This value is consistent with other studies in that it is approximately 78% of the shear wave velocity at hypocentral depth. The slip distribution indicates that the mainshock had components of both east and updip directivity. The former is required to fit the relatively long durations at stations to the west and the short duration to the east. On a northwest-striking fault plane, this would indicate that the earthquake ruptured to the southeast. The peak slip in the model is 125 cm with an average value of 25 cm. The stress drop determined from this model ranges from 17 to approximately 50 bars, depending upon whether the entire slip model or just the most robust features are used to compute fault area. Replacing the uniform slip of the mainshock with this slip distribution does not change the CFF results much, although some large changes in CFF are very localized.

In summary, it appears that in the Double Spring Flat earthquake sequence a large portion of the data can be explained simply by stress loading and fault geometry. It also appears that the Coulomb Failure Function is certainly not inconsistent with

aftershock locations and, perhaps, can explain the concentration of stress in particular areas. There are also some interesting spatial and temporal patterns in the aftershock sequence, which need to be addressed. However, in this particular region and with the current geometry, it is hard to assess the relative importance of the various factors. In an area where the earthquake locations (or relocations) are better and the fault geometry is well known, then the significance of each factor may be resolved.

# Chapter 4

# Phase Velocity and Layered Velocity Inversions

This chapter will focus on the detailed estimation of structure using surface waves, which is accomplished in two steps. In the first step, the measured dispersions along source-receiver paths are used in a phase velocity tomography of the western United States. Sections will describe the data set, the inversion method, and discuss the inversion results. The second step of the procedure concerns the inversion of the phase velocity tomography results maps for layered velocity models in the region. The reward for performing this additional inversion is a more intuitive parameterization of the velocity model from phase velocities as a function of frequency to seismic velocity (either P or S wave) as a function of depth. The dividends of the reparameterization include such useful constructions as maps of crustal thickness, average crustal velocity, mantle velocity, and cross sections.

## 4.1  Phase Velocity Tomography

Regional dispersion data have been inverted in order to provide estimates of the S-wave velocity structure in California and the western United States. Previously, most surface wave investigations have been limited by several factors (Cara, 1983): (1) only vertical component Rayleigh waves have been used because of the lower signal-to-noise ratio on the horizontal components, (2) the necessity of rotating photographic records in order to separate horizontal Love and Rayleigh waves, and (3) because the dispersion analysis must not be performed over periods where the amplitude

spectrum drops off quickly, one is limited by the frequency response of the instrument. A problem with using only Rayleigh waves is that, even for periods as short as 30 seconds, they are primarily sensitive to mantle velocities and are therefore limited in determining crustal structure. With the installation and accessibility of digital broadband instrumentation, these problems are eliminated and surface wave analysis can be performed easily and reliably.

Earlier work in this field has applied these tomographic techniques to Tibet (Bourjot and Romanowicz, 1992), the Pacific (Suetsugu and Nakanishi, 1985), the Indian and Pacific Oceans (Montagner, 1985) and the world (Knopoff, 1972). Smaller scale studies have inverted the dispersion curves for only single or a few paths. Although single dispersion curves can be inverted for the structure, the result would represent an average of the structure along the path. In order to isolate features occurring in different regions, it is necessary to use a method known as seismic tomography. By subdividing the area of interest into blocks or other spatial functions, the data measured along many paths can be inverted for the perturbations in the medium. The method employed here will be to find the surface wave dispersion for many source-receiver paths. This will be fairly simple because of the large number of moment tensor solutions and large number of broadband stations. A tomographic inversion will then be performed at discrete frequencies for each surface wave type. A complete surface wave tomography using both Love and Rayleigh waves on this scale is a relatively untested subject matter.

### 4.1.1 Motivation for Inversion

There are a number of reasons why surface waves are both suitable and desirable for regional velocity inversions. First, surface wave techniques are relatively simple because there is horizontal propagation only and, therefore, a two-dimensional problem at individual frequencies. Secondly, long period surface waves, which are very well recorded for large earthquakes, sample deeply into the earth and can be used to study the structure of the upper mantle. Unlike other techniques, using surface wave dispersion will also allow the imaging of low velocity zones. In addition, surface waves dominate the seismograms for distant events and can be utilized to study areas, such as the western United States, which do not have many very large earthquakes by

using distant stations. Finally, a tomographic type inversion of surface waves from these recordings gives insight in the study of geophysical and tectonic problems. Furthermore, this technique can be implemented with current algorithms and computing power.

Surface waves basically sample the integrated effects of shear wave velocity with depth. Hence, another advantage of using phase velocities is their effectiveness at measuring average crustal properties. Because of its integral nature, however, a phase velocity inversion is perhaps not the best method to estimate the strength and location of discontinuities in the crust and upper mantle, which are much more effectively measured by body wave methods. The point is that the phase velocity measurements are able to provide complementary information to other methods towards determining crust and upper mantle structure.

### 4.1.2   Data Set and Inversion Method

As discussed in section 2.1.1, the signal recorded at any particular station will be a function of the source, propagation, and instrument operators, which are multiplications in the frequency-domain.

$$U(r, \theta, \omega) = U_s(\theta, \omega) \, U_p(r, \theta, \omega) \, U_i(\omega) \tag{4.1}$$

where $U_s$, $U_p$, and $U_i$ are the source, propagation, and instrument terms. In this particular case one is interested in isolating the wave propagation term, so the data already being used in the surface-wave moment tensor inversion can be utilized. Because the data have already been corrected for instrument response, geometrical spreading, and attenuation, one can isolate the wave propagation simply by removing the source term.

An example of spectrum with the source term removed for a Mammoth Lakes event is shown in figure 4.1. As the magnitude of the event is only 3.7, the data above about 60 seconds have a low signal-to-noise ratio and should be ignored. Under perfect conditions, the amplitude should be equal to one, because this data have been corrected for the effects described above. Modulations in the amplitude are due to complications such as the focussing and defocussing of the raypaths, the incorrect estimation of source parameters and source depth, or large changes in attenuation with frequency.
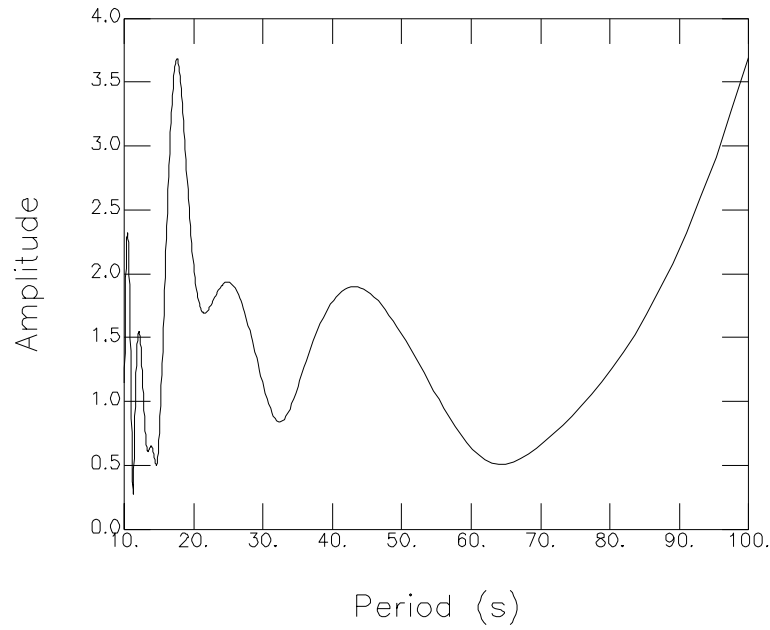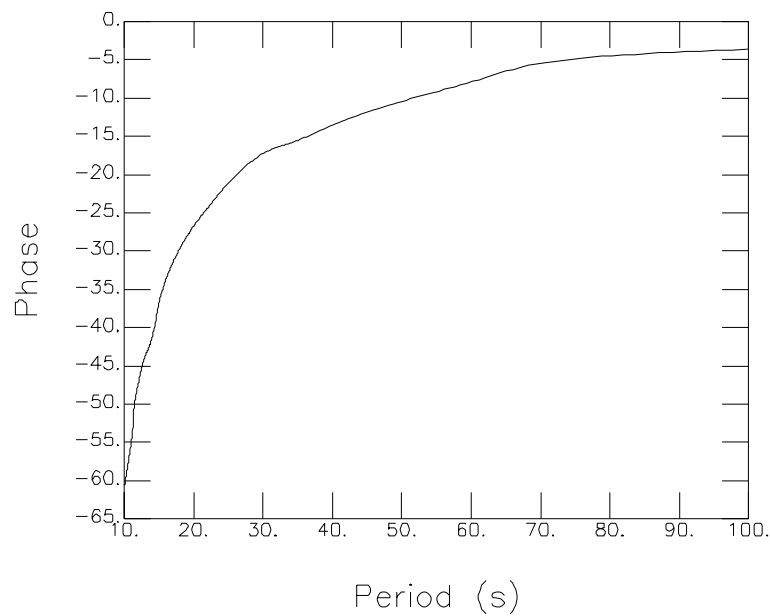
Figure 4.1: Example of spectrum with source term removed for a M 3.7 Mammoth Lakes event recorded at station JRSC. Amplitude as a function of period is shown on top. Phase as a function of period is shown below.

Presumably there can be some errors in the estimated source parameters; therefore, it is useful to consider what errors in phase velocity could be produced by removing from the spectra changes in the source term. In general, changing the angles of the focal mechanism do not result in any large scale changes in the estimated phase velocity. Changes in the strike, rake, and dip of up to 20 degrees were tried without causing serious problems except perhaps at nodal points. Completely changing the mechanism (i.e. from a strike-slip fault to a normal fault) causes quite serious problems. Because nodal stations are routinely removed and larger uncertainties in the focal mechanism are not expected (see section 2.3), this is not considered to be a major problem. Other parameters, such as focal depth and source duration, are much more sensitive. Source duration, in particular, can have the effect of changing the long period phase velocities by a constant offset. This can be particularly problematic since, as mentioned earlier, source time estimations can depend on shifts in the origin time.

Once the source and instrument terms have been removed, the remaining propagation term can be written as:

$$U_p(r,\omega) = \frac{1}{\sqrt{\sin \Delta}} \exp[\frac{i\omega r}{c(\omega)}] \exp[-\eta(\omega)r] \tag{4.2}$$

where the first term is the geometrical spreading term, r and $\Delta$ are the source-receiver distance (in km and degrees), and $c(\omega)$ and $\eta(\omega)$ represent the average phase velocity and attenuation coefficient, respectively. Thus, by removing the source estimated from regional moment tensors, a large data set of source-receiver paths suitable for the inversion were generated. Sparsely covered areas were supplemented with older events for which data and moment tensor solutions were readily available.

The original data set used consisted of 1272 paths from 80 events ranging in magnitude from 3 to 7. When possible, several measurements along the same path (from a mainshock and an aftershock recorded at the same station, for example) were taken because discrepancies between the two readings provide an accurate estimate of the uncertainties of the measurements. At this point, paths were eliminated for one or more of the following reasons: the signal-to-noise ratio was too low, the path was nodal for the particular wave type, errors in source mechanism or large source complexity did not adequately remove the source term from the propagation term, and contamination from higher modes. In addition, paths that were shorter than 100

km were removed. What remained after this inspection was a data set consisting of 1179 paths from 80 events. The paths range in length from about 100 km to 1875 km.

An example of the coverage of the region by the dispersion curves is given in figure 4.2, which shows the propagation paths for Love waves at 40 seconds. The path coverage indicates where the resolution is best and worst. Most of onshore California is well covered by many crossing paths. Exceptions include the westernmost portions of central California, as well as the northeast corner and southernmost portion of the state. Offshore regions north of the Mendocino Triple Junction are pretty well covered by earthquakes along the Mendocino and Gorda ridges and within the Gorda Plate. Coverage in the offshore Borderlands regions of southern California is assisted by a broadband station located on one of the Channel Islands which, unfortunately, is often noisy. Coverage to the north and east have been aided by the recent availability of NSN data for stations in the western United States. In general, however, coverage in the offshore Borderlands, with both sparse earthquake and station coverage, is poorer than in California. The phase velocities are computed at a number of different frequencies. The range of measured phase velocities is shown by figure 4.3, which shows a histogram of Love wave phase velocities at 30 seconds. The path velocities form a skewed bell curve with a maximum between 3.975 and 4.000 km/s and a longer tail at the low velocity end.

The tomographic method of Montagner [1985] has been used in order to invert the phase velocity data without an *a priori* parameterization of the model space. This is the application of the generalized non-linear inverse algorithm of Tarantola and Valette [1982] in its continuous form to the case of surface waves. This method assumes that geometrical optics are valid, and that the apparent phase slowness between an epicenter and a station is the average of phase slowness along the great circle path connecting the two points. The data are described using the observed values and their standard deviations. Since this is a highly underdetermined problem because the model can be anything away from the exact travel path, some constraints are put on the inversion. First, there is an initial model (or models) with some uncertainty. Specifically, two initial models are used in this inversion, an offshore (or oceanic) model and an onshore (or continental) model. Secondly, the model is assumed to be smooth in order to avoid a highly oscillatory model.
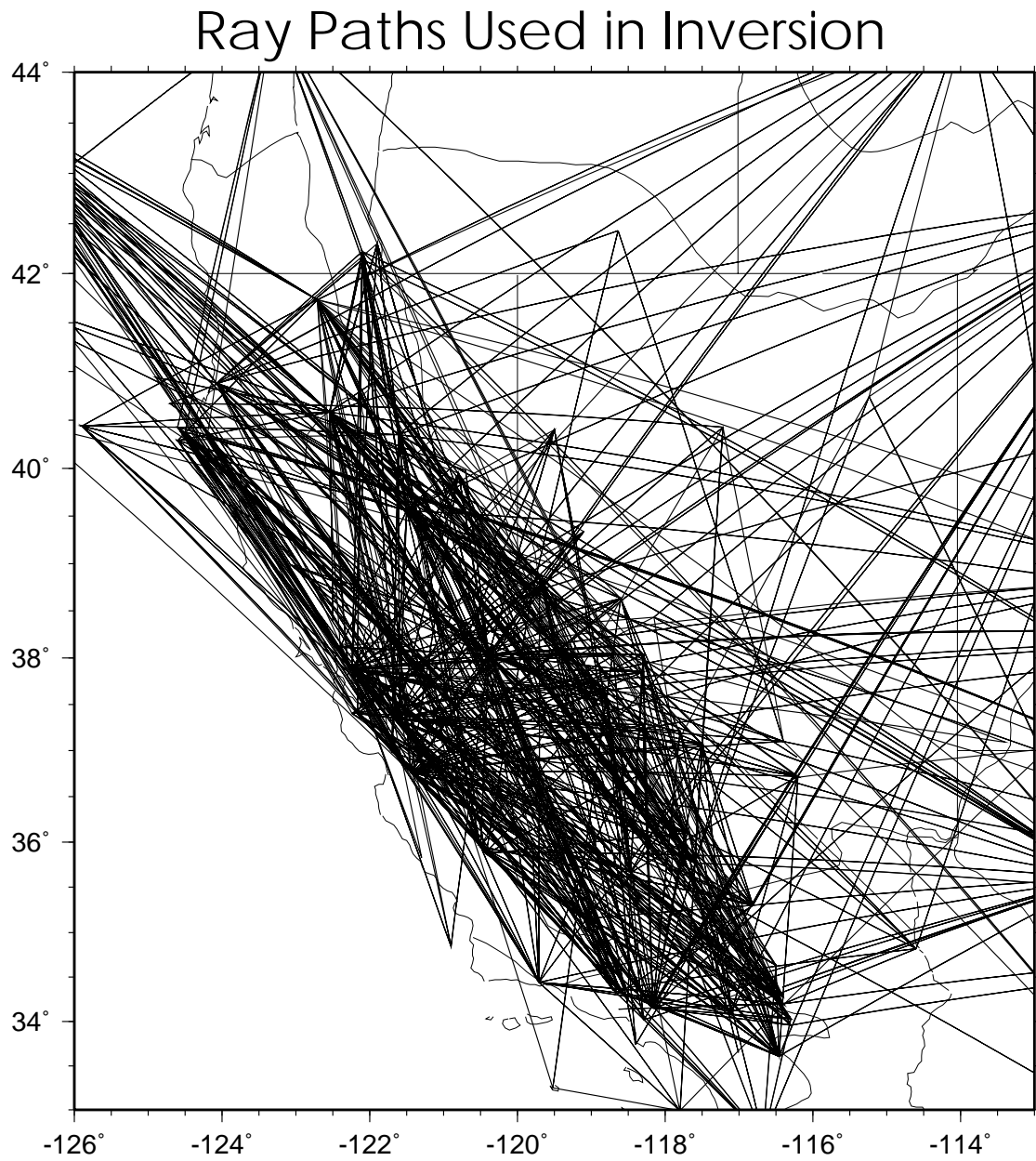
Figure 4.2: Coverage of region from source-receiver paths used in phase velocity tomography.
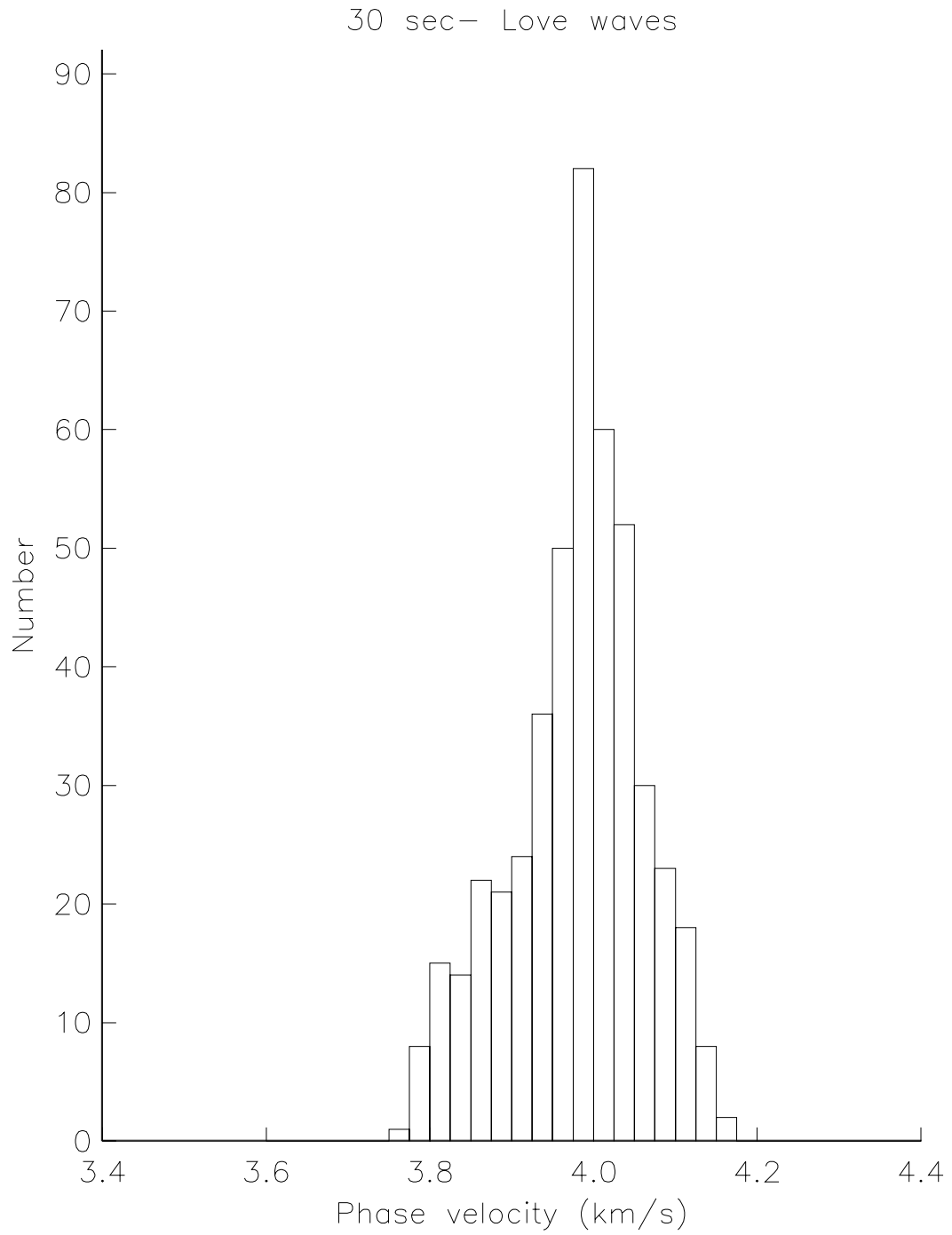
Figure 4.3: Histogram of Love wave phase velocities at 30 seconds.

The constraints of smoothness and the initial model in Montagner's method are applied through the use of the covariance function on parameters at any two points. It is simplest to utilize the Gaussian (or normal) form of the covariance matrix $C_{p_o}$, which is defined as:

$$C_{p_o}(M_1, M_2) = \sigma_0(M_1) \cdot \sigma_0(M_2) \cdot \exp((\cos(\Delta_{M_1 M_2} - 1)/L^2) \qquad (4.3)$$

where $\Delta_{M_1 M_2}$ is the angular distance between two points $M_1$ and $M_2$, $\sigma_0(M)$ is the amount that the velocity can vary between at a given point, $p_o$ is the starting model, and $L$ is the correlation length. High uncertainties, short source-receiver distances, and long correlation lengths produce a large covariance. At any given point, the parameter $p(r)$ can vary between $p_o(r) - \sigma$ and $p_o(r) + \sigma$. The correlation length $L$ acts as a smoothing parameter by specifying that the variation of $p$ at point $r'$ within a distance $L$ from $r$ will be the same as that at $r$. See Montagner [1985] for a detailed description of this method. Figure 4.4 illustrates the way the inversion method would work for a 1-D phase velocity model at a particular frequency. Where there is coverage, the model is appropriately drawn away from the starting model to satisfy the data. Away from the data points, smoothness contraints drive models towards those of neighboring regions. In regions of no data coverage, however, the model will not change significantly away from the starting model. As with any tomographic method, the results are non-unique and can be strongly affected by the damping parameters used in the inversion. The final model depends on the distribution of variance over the paths, which is controlled by the damping.

Figure 4.5 illustrates the behavior of the inversion method and covariance matrix for two representative examples. In the first case, the two source-receiver paths are quite distinct, crossing once and within a correlation length L of each other for only a small portion of the individual paths. Because the paths are so dissimilar, self-consistent data will have little effect on the *a posteriori* model near the intersection because the velocity information will be distributed along the raypath. By the same measure, however, inconsistent data will not have a large effect on the new velocity model. In the second case, the two paths are very similar and a large percentage of one individual path will be within a correlation length of the other. Here, as a consequence of the first set of data, the resulting model will change significantly from the starting model and the variance will decrease as well to reflect the consistent
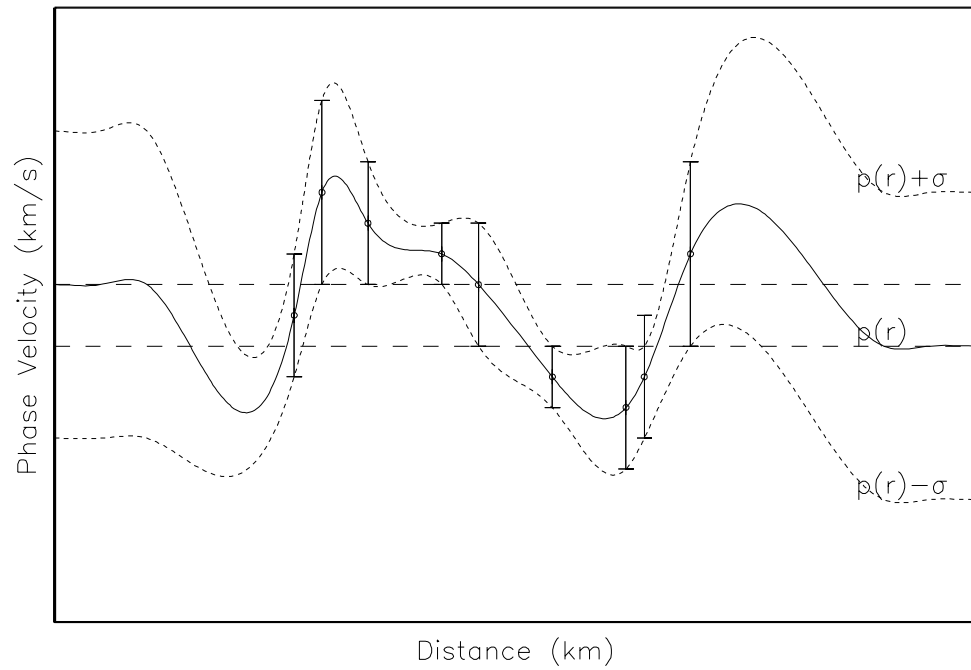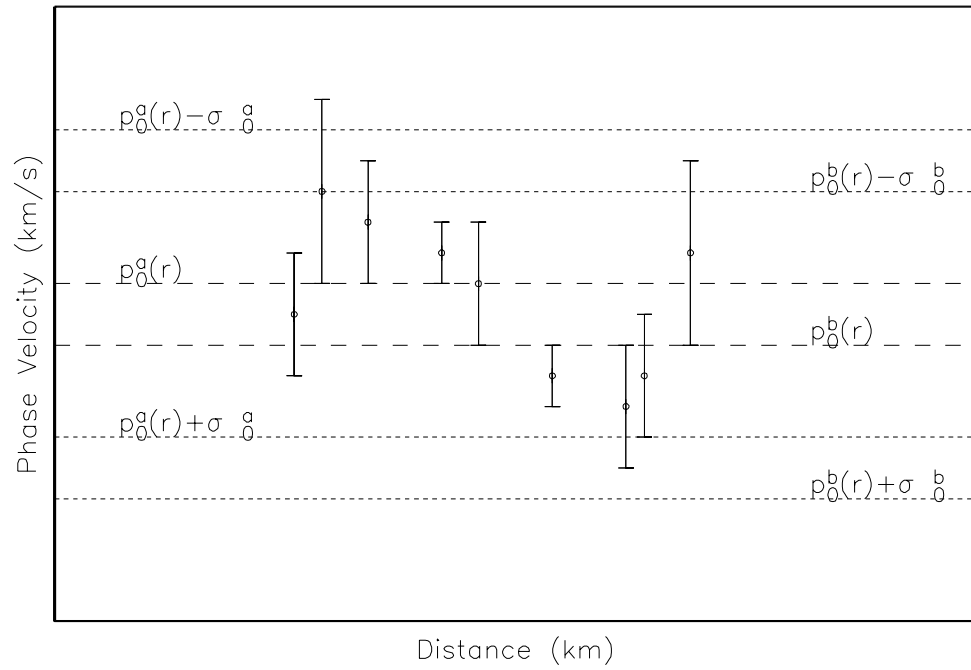
Figure 4.4: Illustration of inversion method for a 1-D model. The x-axis is distance, and the y-axis is phase velocity. The top figure shows the initial velocity models ($p_o^a$ and $p_o^b$) and uncertainties ($\sigma_o^a$ and $\sigma_o^b$), along with the data and its uncertainties (symbol and bar). The bottom figure shows the resulting model (p and $\sigma$).

164

observed velocities. Where the data are not consistent, however, the velocity model will change as well, since there is only a small remaining area to contain the variations. Hence, the data will change from the *a priori* model, although the uncertainties in the area will probably remain high.

The result is a smooth model that satisfies the data within the allowable tolerances. This statistical method was chosen specifically because there can exist some spurious measurements in the data. It permits some data variation by not necessarily mapping measurements directly into the data, but by allowing some increased uncertainties in the model and allowing only large scale changes that are consistent and robust. Another advantage of this method is that using the covariance function allows one to go from a discrete parameterization to a continuous one. The particular method of parameterization is important in characterizing an inversion problem. Even in the basic case of partitioning the model region into simple blocks, the final model will be significantly influenced by the choice of block size. By having a continuous model, one can avoid the problems associated with choosing an inappropriate parameterization for the problem. While free of any *a priori* parameterization of the model space, a number of variables (such the starting model, correlation length, or *a priori* error of the parameters) can be changed to alter the scope of the inversion and to provide constraints on smoothness and variability of the resulting solution. For example, increasing the correlation length in the problem relaxes the constraints on the data, allowing for spurious measurements, but also smooths out some of the finer details of the inversion. Montagner recommends the following strategies to avoid spurious anomalies and to have a well posed problem: take as a starting model the average velocity of the data, take an *a priori* error of the parameters slightly higher than the residuals corresponding to the starting model, and use a very long correlation length. Each of these parameters was tried for a number of different values and the residuals were compared for each trial run. The final values were those which minimized the variance of the source-receiver residuals.

In the inversion, the correlation length acts as a smoothing parameter on the dataset, and can be changed. The problem then becomes how to choose a suitable correlation length. In the limits, a correlation length of zero will cause the method to reproduce the exact velocities along the source-receiver path, but it will yield absolutely no information about the velocities just off the path. This is unsatisfactory
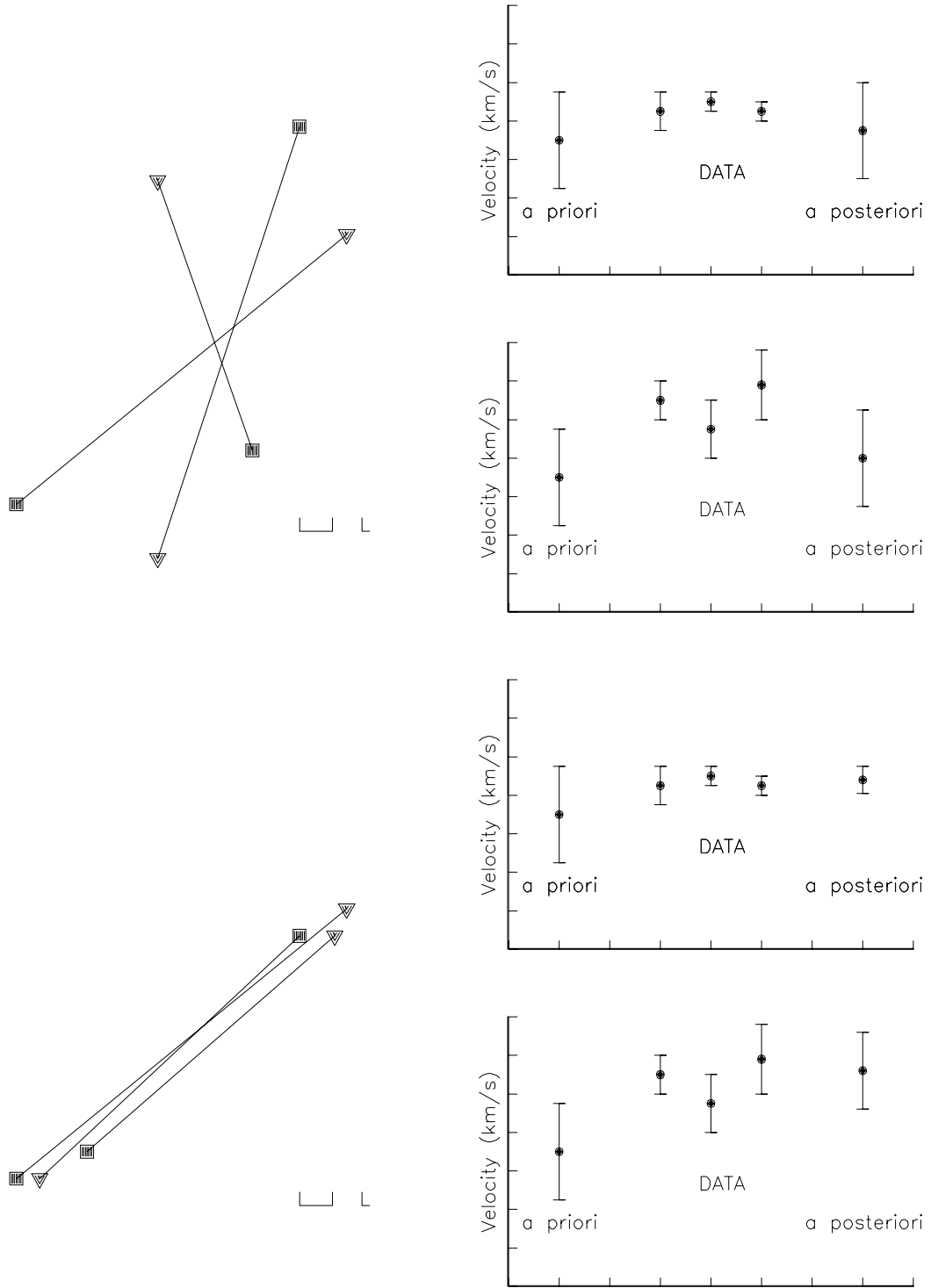
Figure 4.5: Cartoon of covariance and inversion behavior. In the top example, source-receiver paths are dissimilar and in the bottom example, source-receiver paths are similar. The correlation length is shown by L. The figures to the right show the *a priori* velocity, the data, and the *a posteriori* velocity resulting from consistent and inconsistent data in both cases.

from the point of view of an inversion, since one can never hope to retrieve any information which isn't specifically measured. On the other hand, an infinite correlation length will produce a single velocity model with no spatial variation. Using more realistic values for this parameter, if L is too high, then the model is too smooth, and if L is too low, then spurious anomalies can be produced. Since one of the goals of the study is to image crustal and upper mantle structure with enough resolution to show lateral variation between the principal tectonic blocks, the procedure is to try and get the shortest correlation length as possible without increasing the variance.

Other studies (Roult and Rouland, 1994; Roult, *et al.*, 1994) using this technique have indicated that short correlation lengths allow the refinement of detailed structure and that the location of the velocity anomalies are still stable. Therefore, some effort was made to determine the optimal correlation lengths. Tests were performed of model variance as a function of correlation length that indicate a correlation length of 75 − 100 km is optimal in most cases, with a shorter correlation length being more appropriate for shorter periods (figure 4.6). For Love waves between 15 and 60 seconds, the variance is minimized for correlation lengths around 75 km. At longer periods, correlation lengths on the order of 125 km are more appropriate. However, in an effort to more finely examine the structure of the earth, a slightly shorter correlation length of 50 km (the shortest length before there is a significant increase in the model variance) was chosen. The result is a finer resolution inversion, which may contain occasional spurious measurements at a particular location or for a particular period.

Similar tests were performed for other variables such as the variance of the phase velocity measurements, the starting models, and the starting variance of the models. For the most part, other variables were less sensitive and did not make as great a difference in the model variance as correlation length. Also, the size and location of anomalies did not change very much. One notable effect, however, was on the average phase velocity measurements. The average velocity of the data replaced a western United States starting model because it resulted in a significant improvement in the residuals. In the end, a correlation length of 50 km and *a priori* errors of 0.20 km/s were selected for the inversion. Both of these values were consistent with recommendations for slightly higher starting uncertainties and long correlation lengths.
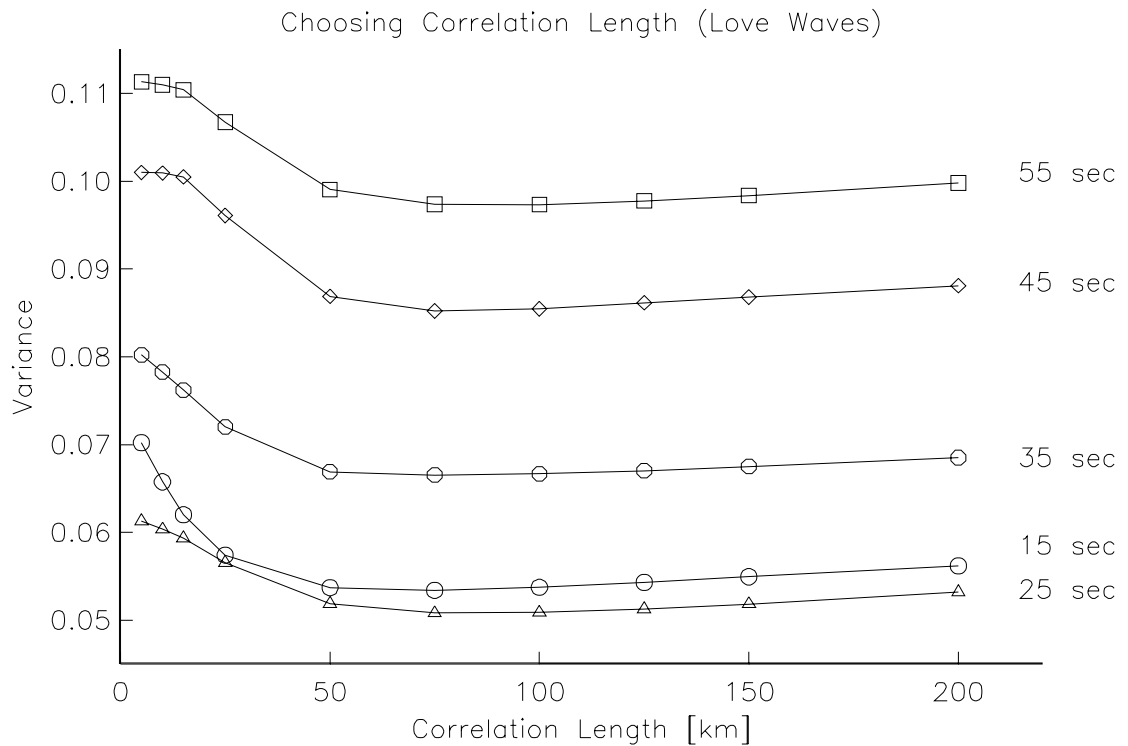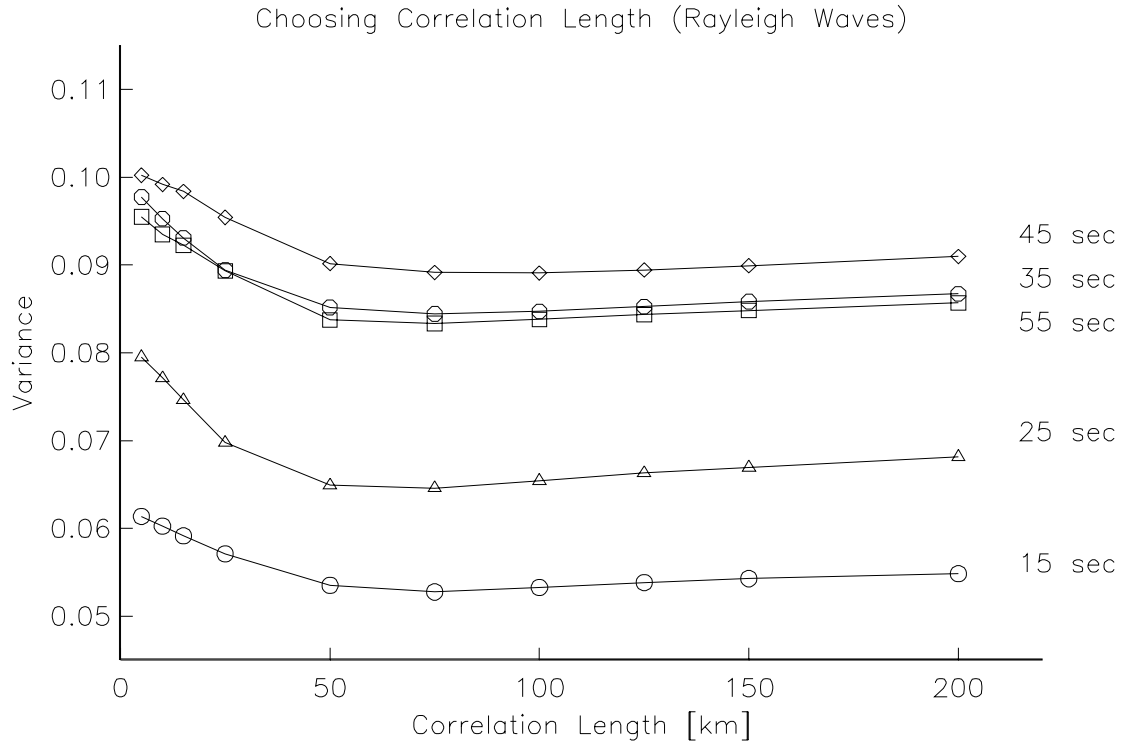
Figure 4.6: Chart showing the relation between model variance and correlation length for Rayleigh wave and Love wave data of different periods from 15 to 55 seconds. Lengths of 5, 10, 15, 25, 50, 75, 100, 125, 150, 200 km were sampled.

## 4.1.3   Assumptions, Smoothing, and Continuity

By inverting phase velocity data in this manner, several major assumptions have been made. First of all, there is the assumption of straight line source-receiver propagation. Any deviations from the straight line path will affect the total distance travelled and therefore the phase velocity. One way to avoid this problem would be to iterate on a solution in order to account for large deviations from the straight line assumption, if it turns out that they are significant enough to matter.

Another assumption that has gone into this inversion is that there will be no significant mode conversion at the boundaries of the different velocity regions. Finite element calculations modelling surface wave transmission across continental boundaries and subduction zones (Drake and Bolt, 1980; Bolt and Drake, 1986; Drake and Bolt, 1989) has shown that for long period waves ($> 13$ seconds), there will be a minimal mixing of modes, particularly for Rayleigh waves. Even more significant is the fact that the calculated phase velocities of the fundamental-mode surface waves were within 1% of the mean of the phase velocities of fundamental-mode surface waves.

One might reasonably question the validity of using one-dimensional surface wave analysis in order to infer the three dimensional structure of the crust and upper mantle. Mooney [1989] discusses the reasonability of this assumption and its effects on the analysis. He argues that since this assumption reduces the number of degrees of freedom in the solution, it allows for a well-constrained estimate of the average velocity structure. This premise was also successfully applied to account for the average velocity along paths in the moment tensor inversion. In addition, a number of studies (Helmberger, 1983; Dreger and Helmberger, 1990) have shown excellent agreement of one-dimensional synthetic seismograms to the data over wide distance ranges. So, although the particular details of a model may not be valid, as demonstrated by the range of models that fit a given surface wave data set, the gross shear-wave velocity structure should be well estimated. Furthermore, the uncertainties of the model will be significantly reduced if seismic refraction data are available to constrain the crustal thickness and compressional-wave velocity structure.

At this point, each frequency is then inverted independently. In practice, however, the phase velocities will vary smoothly with frequency, and some sort of smoothness with frequency can be imposed. Due to the similar nature of the problems, many of

the techniques used in digital image processing can be utilized for the purposes of this inversion. Multi-dimensional FFTs are particularly important in the field of image processing. One commonly desires to filter high or low frequency spatial components from an image; or to convolve or deconvolve the image with some instrumental point spread function (Press, *et al.*, 1992). Lowpass filtering results in blurring or smoothing the image by removing the high-frequency portion of the image. Highpass filtering results in image sharpening by removing the low-frequency portion of the image. This has the effect of emphasizing edges and other abrupt changes. In the future, this type of filtering might be useful for defining both broad features or sharp ones such as boundaries, when finer sampling will yield more points both spatially and with respect to frequency. However, in the current configuration ($0.5°$ by $0.5°$ spatial sampling and $5 - 10$ second period sampling or $49 \times 29 \times 14$), these are not particularly feasible options.

## 4.1.4   Dispersion Curve Behavior

In order to recognize what one can see in the phase velocity inversions, it is useful to try and understand the behavior of the phase velocity dispersion curves. Consequently, before looking at the inversion results, significant changes in the crustal structure such as sediment thickness, average crustal velocity, crustal thickness, and mantle velocity are explored in order to gain an intuitive feel as to what effect typical variations in these parameters will have on the dispersion curves.

For instance, can one hope to resolve the thickness of unconsolidated sediments in the uppermost portion of the crust? Figure 4.7a and 4.7b compare the Rayleigh and Love wave dispersion curves, respectively, for three different crustal models. Each model is composed of four layers (sediment, upper crust, mid crust, and lower crust) and a half-space. The thickness and velocity of each of the layers, including the half-space, are the same for each model, except for the sediment layer, which varies from 0 to 4 km. At periods shorter than about 50 seconds for Rayleigh waves and shorter than about 40 seconds for Love waves, the models with large sediment thicknesses start to have significantly lower phase velocities than the initial model. The deviation becomes especially large for short periods (i.e. 0.4 km/s difference in both Rayleigh and Love waves at 20 seconds for 4 kilometers of sediments). More typical sediment loads of less than about 1 km thickness, however, will probably not be seen except at

higher frequencies, so this particular parameter might not be resolved for all but the largest sediment loads.

Another useful parameter to explore is average crustal velocity. Results are shown in figure 4.8a and 4.8b. In this case, a single lower crustal layer of fixed thickness is sandwiched between an upper crust layer which does not change in velocity and thickness, and a half-space of constant velocity. The variable is the velocity of the lower crustal layer which produces average crustal velocities of 6.25, 6.50, and 6.75 km/s for the test. As in the previous example, most of the differences from the crustal changes can be seen at shorter periods. Also, the effect is larger for Love waves than Rayleigh waves, especially at intermediate periods (~30 seconds), by which point Rayleigh waves are primarily sampling upper mantle. Consequently, changes broadly observed over intermediate periods, particularly for Love waves, are indicative of average crustal velocities.

Crustal thickness is one of the most significant features determining phase velocity in the periods being considered. It is therefore extremely important to see if it can be resolved. Figure 4.9a and 4.9b compare the Love and Rayleigh wave dispersion curves, respectively, for three crustal models. Each model is composed of three layers and a half-space. The parameters of each of the layers, including the half-space, are the same for each model. The only difference is that, in the second and third models, the third layer is 10 and 20 kilometers thicker than the initial model. At every period, the model with the 25 kilometer crust is faster than the model for the 45 kilometer crust, although the differences are less significant at very long and very short periods. The change is most significant for Rayleigh waves around 20 seconds, where there is over a 0.3 km/s difference in the phase velocities, and for Love waves at 35 seconds, where there is about a 0.2 km/s difference. Also, note the more significant change in the slope of the Rayleigh wave dispersion curve for thinner crusts. Noting the break and its sharpness is an essential means for determining crustal thickness.

Finally, tests are performed for typical upper mantles in California and the western United States. In this case, the crustal structure (both layer thickness and velocity) does not vary, but the velocity in the half-space is perturbed. As figure 4.10a and 4.10b illustrate, at short periods the dispersion curves do not vary at all for changes in mantle velocity ranging from 7.8 to 8.0 km/s. The largest variations occur by about 50 seconds for Rayleigh waves and about 70 seconds for Love waves. At even
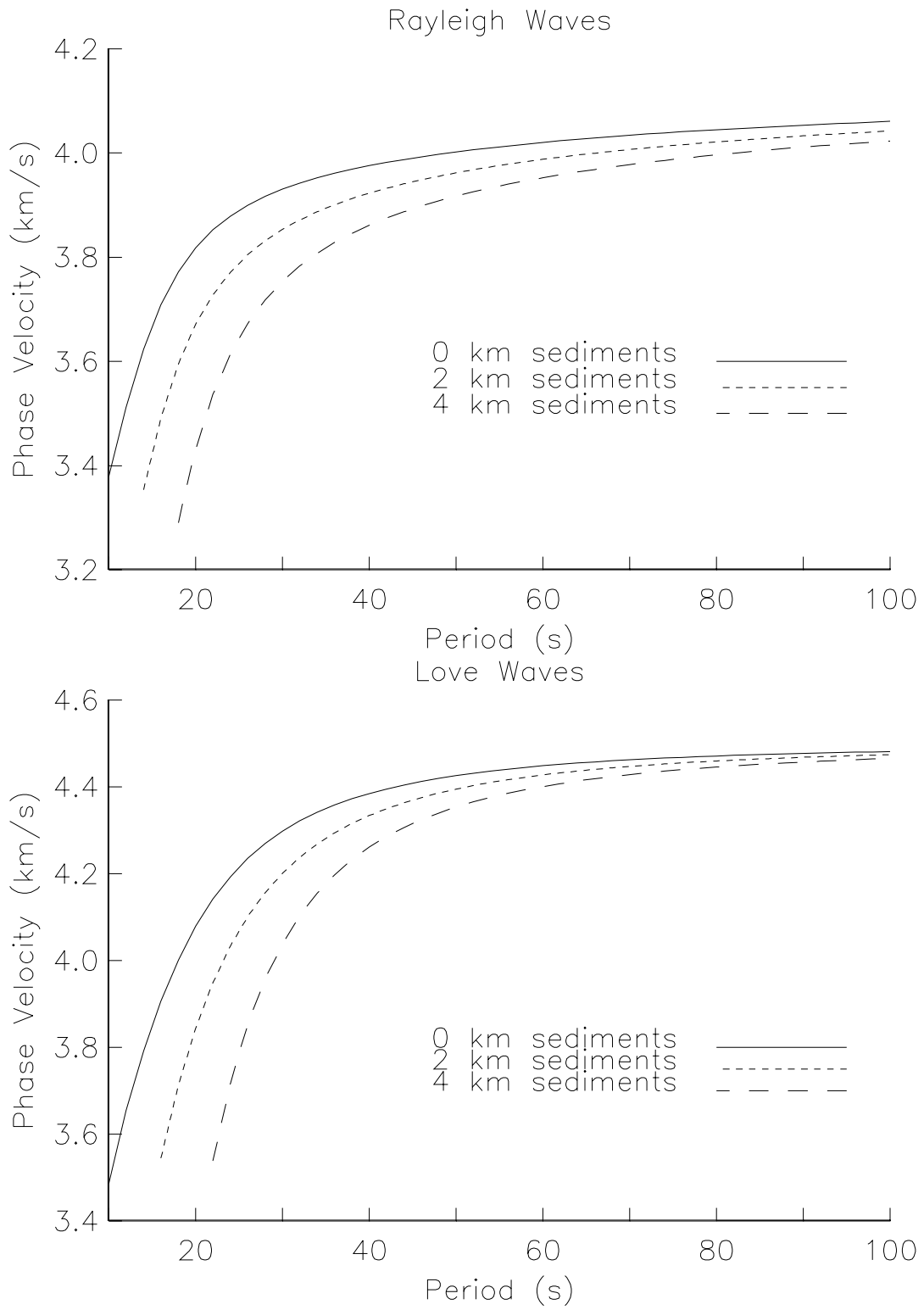
Figure 4.7: Sediment thickness comparison for Love and Rayleigh waves.
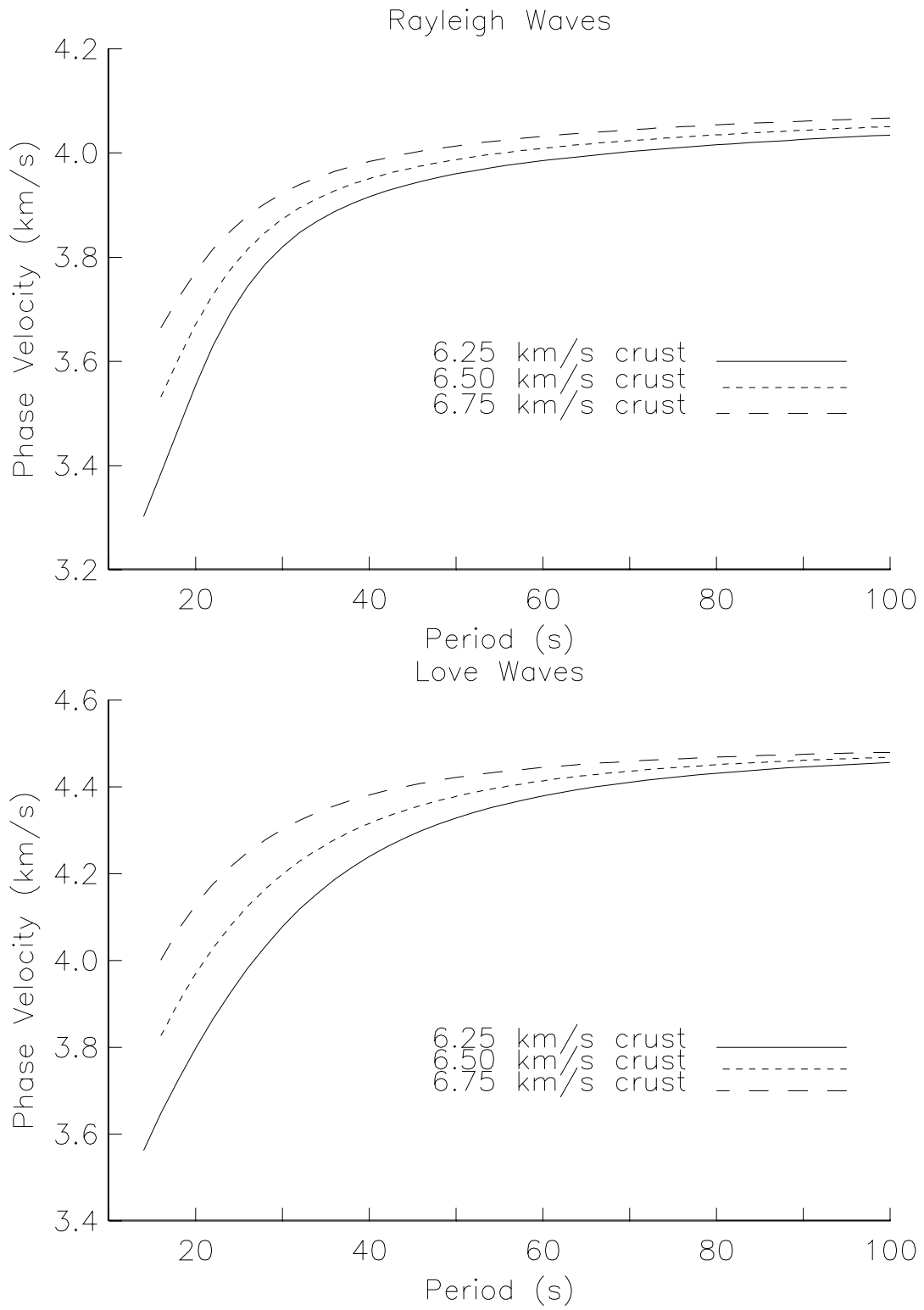
Figure 4.8: Crustal velocity comparison for Love and Rayleigh waves.
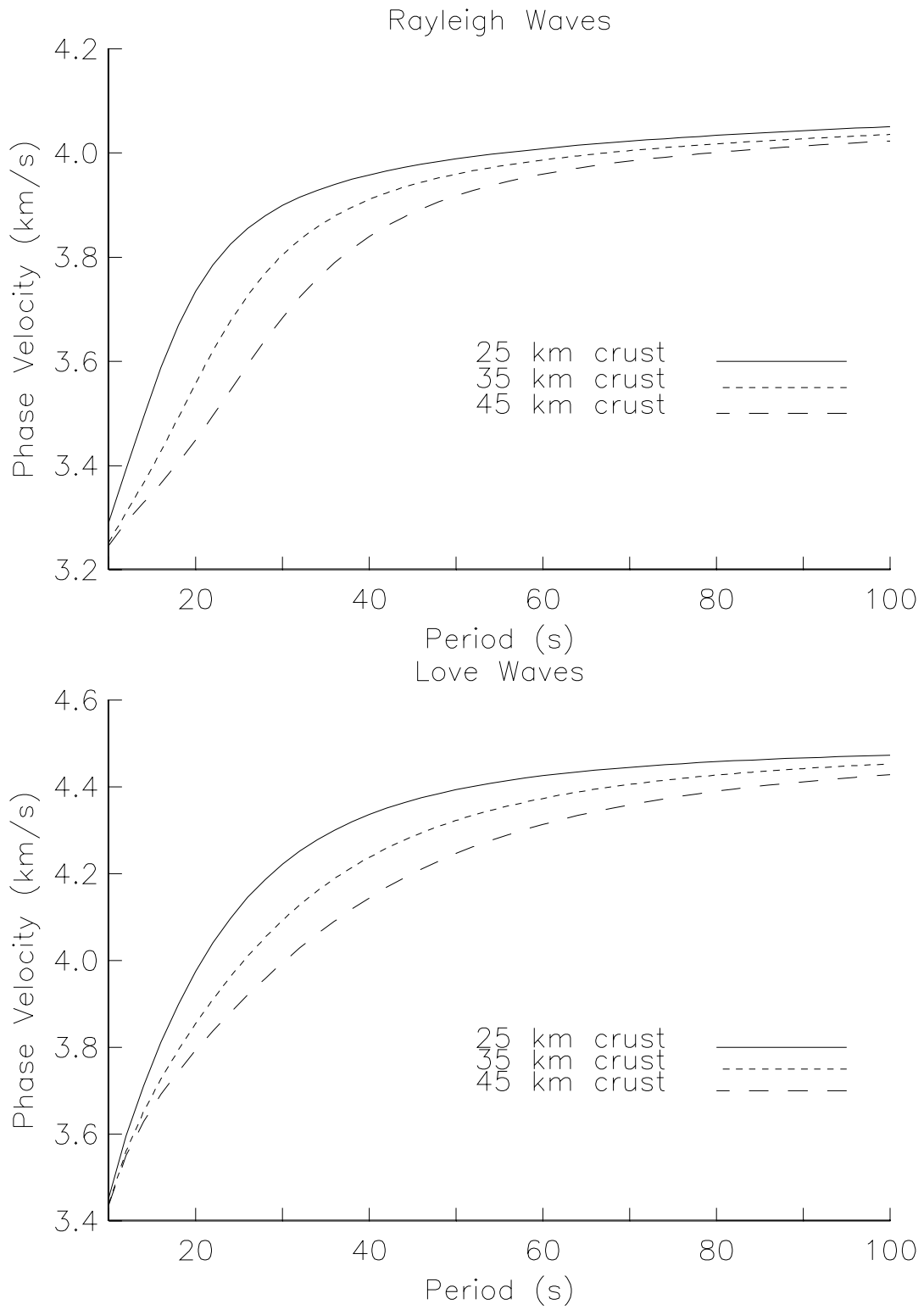
Figure 4.9: Moho comparison for Love and Rayleigh waves.

174

longer periods, the variations (on the order of 0.05 km/s for each 0.1 km/s change in mantle velocity) are constant over period. Only if there are small fluctuations in the long period phase velocities, can one hope to resolve these typical variations in upper mantle velocity.

### 4.1.5    Inversion Results

The tomographic-type inversions of phase velocity, depicted as phase velocity maps, represent the results of the first step in the two-step procedure for recovering depth-dependent earth structure. The mean phase velocity and standard deviation of the western United States from the tomography is shown in table 4.1. As this measurement is a path-length weighted average of all path velocities, it primarily emphasizes the average phase velocity of the best-sampled regions (i.e. Central California). Figures 4.11 and 4.12 show the mean results for both Love and Rayleigh waves compared to a reference model for a typical 30 km crust. Results for both surface waves have slower phase velocities, which would indicate either a thicker crust or a slower mantle velocity. The standard variations in velocity are between about 2.0 to 2.5% of the average velocity indicating that about 68% of the velocities are within that range, about 90% are within 4 to 5%, and about 95% are within about 6 to 7.5% of the mean. One unusual observation is the fact that the estimated uncertainties do not decrease with increasing period, which might be expected from the large heterogeneities observed near the earth's surface.

Figures 4.13–4.15 show the inversion results for Love waves between 15 and 90 seconds. Similarly, figures 4.16–4.18 show the inversion results for Rayleigh waves for the same frequencies. In each figure, the color indicates the velocity (blue and violet being fast and red and orange being slow) and the shading indicates the resolution at that area, as measured by the uncertainties. Areas in full color represent regions with good resolution. With decreasing resolution, the colors start fading into white. Areas shown in white are the areas with poorest resolution. In most of the figures, the center of the plot (northern and central California) is at the highest resolution and has many crossing paths. Resolution falls slowly to the north (Oregon), east (Nevada), and southeast (southern California) due to few or no crossing paths. The data is unresolved to the southwest because of the absence of paths. In addition, the
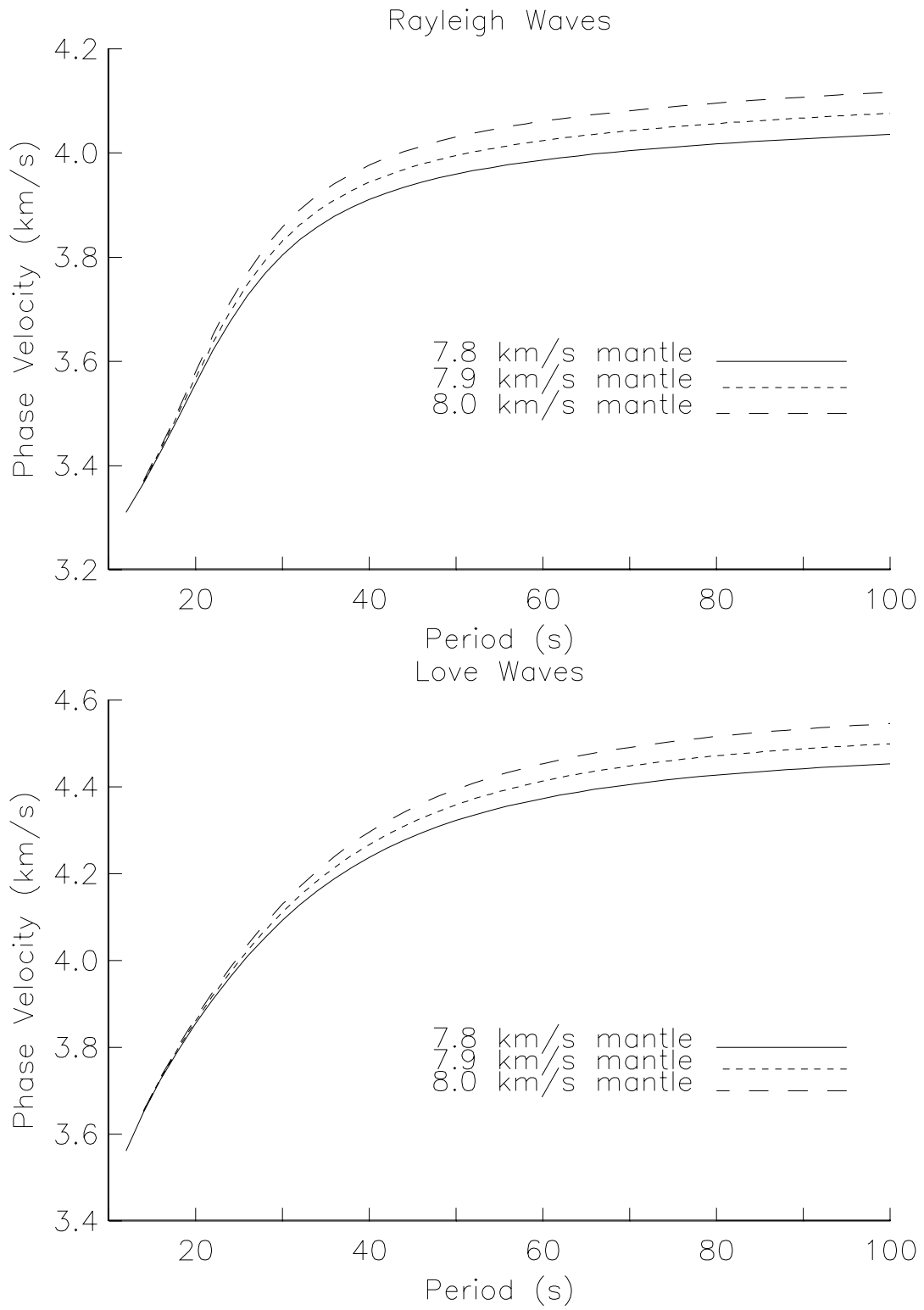
Figure 4.10: Mantle comparison for Love and Rayleigh waves.
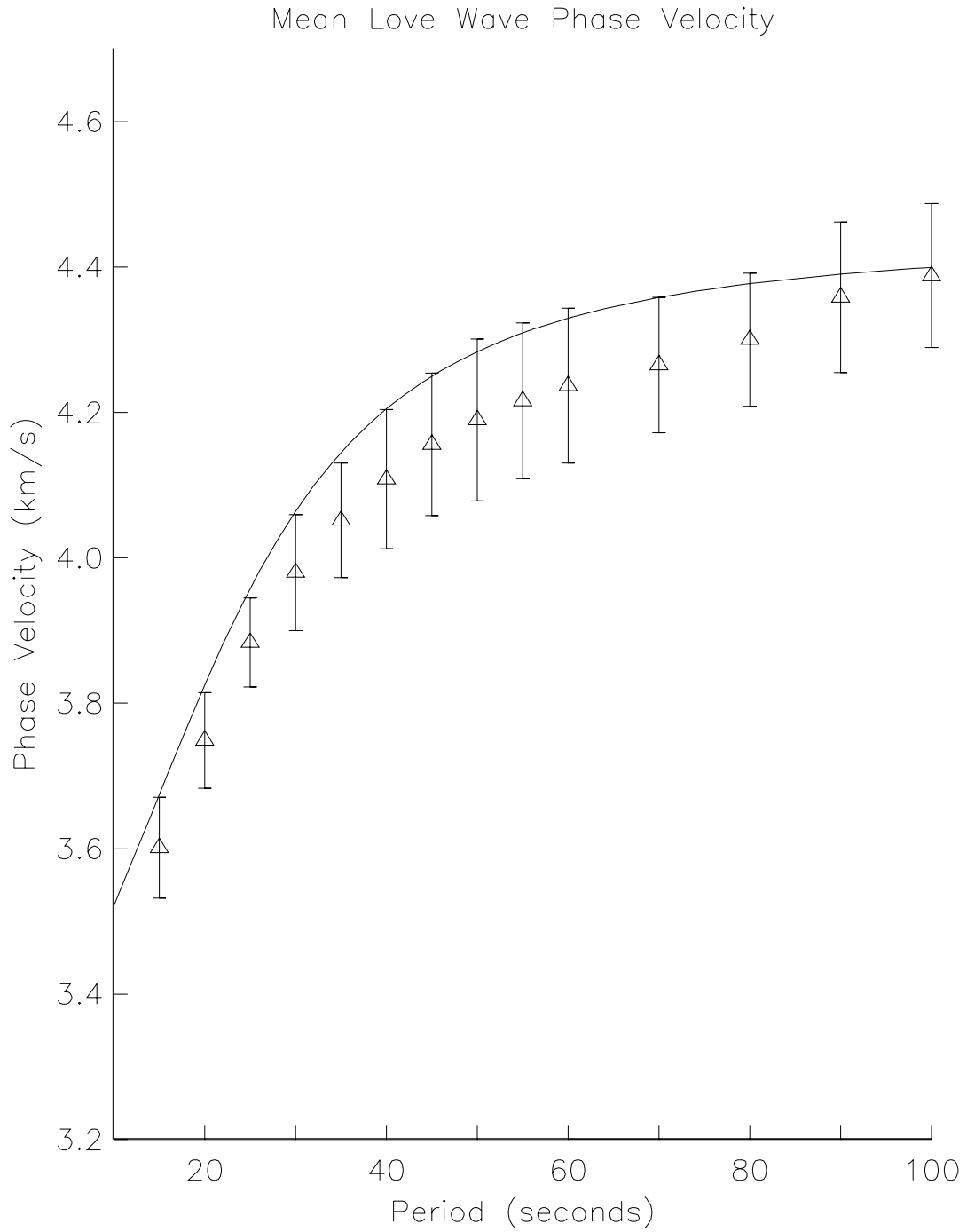
Figure 4.11: Mean Love wave dispersion curve with standard deviation (shown by symbols). Reference curve for model with 30 km crust is shown by the solid line.
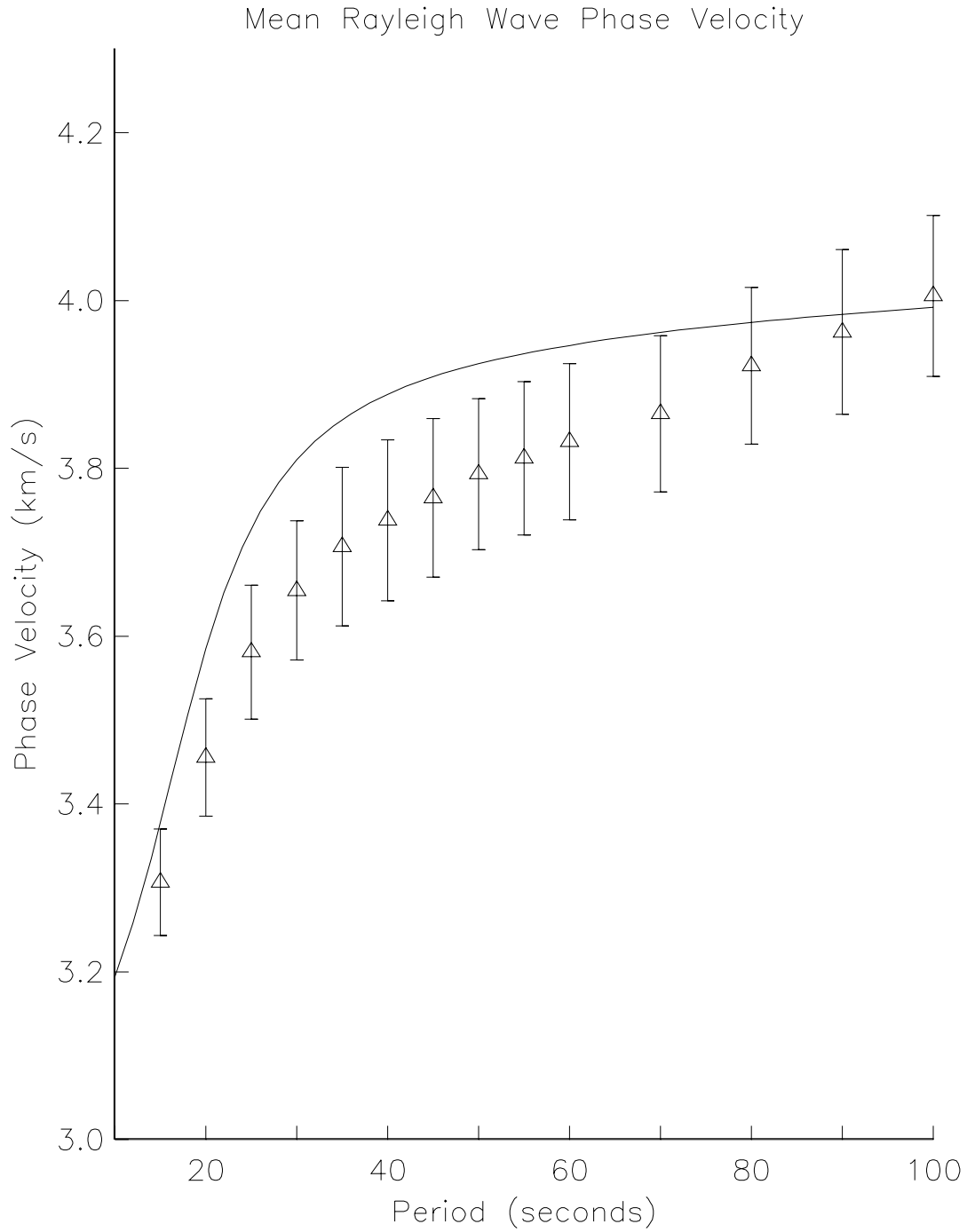
Figure 4.12: Mean Rayleigh wave dispersion curve with standard deviation (shown by symbols). Reference curve for model with 30 km crust is shown by the solid line.

Table 4.1: Mean Western United States Model.

| Period (s) | Love Wave Velocity (km/s) | Rayleigh Wave Velocity (km/s) |
|---|---|---|
| 15.0 | 3.60 ± 0.07 | 3.31 ± 0.06 |
| 20.0 | 3.75 ± 0.07 | 3.46 ± 0.07 |
| 25.0 | 3.88 ± 0.06 | 3.58 ± 0.08 |
| 30.0 | 3.98 ± 0.08 | 3.65 ± 0.08 |
| 35.0 | 4.05 ± 0.08 | 3.71 ± 0.09 |
| 40.0 | 4.11 ± 0.10 | 3.74 ± 0.10 |
| 45.0 | 4.16 ± 0.10 | 3.77 ± 0.09 |
| 50.0 | 4.19 ± 0.11 | 3.79 ± 0.09 |
| 55.0 | 4.22 ± 0.11 | 3.81 ± 0.09 |
| 60.0 | 4.24 ± 0.11 | 3.83 ± 0.09 |
| 70.0 | 4.27 ± 0.09 | 3.87 ± 0.09 |
| 80.0 | 4.30 ± 0.09 | 3.92 ± 0.09 |
| 90.0 | 4.36 ± 0.10 | 3.97 ± 0.10 |
| 100.0 | 4.39 ± 0.10 | 4.01 ± 0.10 |

Mean phase velocity model for the Western United States from the inversion along with the standard deviation of all measurements.

data at longer periods generally have poorer resolution than for the same region at shorter periods. This is due to fewer paths and more inconsistent data.

A word of caution in viewing the phase velocity maps at individual frequencies: not every single anomaly at every frequency is necessarily real, and hence interpretable. Because of oscillations that exist in the noisier dispersion measurements, as well as changing path coverage at different frequencies, any isolated measurements may be spurious. Anomalies that persist over a broader frequency range should be robust and indicative of earth structure. Due to the nature of the sensitivity functions, the Love wave phase velocities tend to be much smoother over period than the Rayleigh waves. This is due to the larger overlap of depth sampling with the Love waves (see figures 2.18 and 2.19). Therefore, in general, Rayleigh waves sample depth slices of velocity which increase in depth with increasing period. In comparison, the Love

waves sample the average radial velocity which spans from the surface to a depth that increases with increasing period.

Figure 4.13 shows the results for Love waves at 15 seconds, which samples the upper part of the crust (0 − 12 km; refer to figure 2.18). The most obvious feature are the very slow velocities in the Central Valley. This slow phase velocity persists in the Love wave data at 20 seconds but dies out by 25 seconds, indicating that it is a shallow crustal feature. The anomaly is also strongest on the western side of the Central Valley, where the thickness of the sediments is greatest. At 25 seconds, the slow velocities are confined to geothermal areas, such as the Cascades, Mammoth Lakes, and the Geysers. These features are also in the data at 15 to 20 seconds, but are obscured by the stronger shallow structures.

The fast areas become much more localized at 30 − 35 seconds (figure 4.14), and fast phase velocities start to intrude upon the continent, first in Central California, then at the Mendocino Triple Junction (MTJ) and Southern California. These features continue in the phase velocity data, which changes slowly between 30 and 40 seconds, until about 50 seconds. At 50 seconds, at the eastern edge of the Sierra Nevada Mountains from the Cascades down to the Mojave Desert, there is the emergence of a band which has slow Love wave phase velocities relative to the east and west (shown in green). Since Love waves at this frequency are just starting to sample depths of 80 − 100 km, perhaps these anomalies are related to lithospheric thicknesses. The slow region in the Mojave Desert, unexplained, stays strong at longer periods. By 80 seconds (figure 4.15), the velocity character of the region has changed completely and a large velocity contrast exists between the fast northern and slow southern portions with the big change occurring in the northern portion of the Coast Ranges. The depth at which the anomaly appears (starting at about 80 km) and the location of the velocity contrast suggests that this feature might be associated with the subducting slab.

Although Nevada is not as well resolved as California, there are still some persistent features which can be seen. For example, most of the areas in Nevada have higher phase velocities than those to the west, most notably in the eastern portion of the state. This is probably due to the anomalously shallow crust throughout the state, which is particularly shallow in eastern Nevada and western Utah near the Wasatch Front. The Gorda Plate, another poorly resolved region, also shows relatively con-

sistent features over a wide range of periods. In general, the northern portion of the Gorda Plate is much faster relative to the continental Klamath Mountains region to the east. The southern portion of the plate, close to the MTJ, has comparable velocities to the nearby continental region at short periods, but also becomes faster at long periods.

Figure 4.16 shows the results for Rayleigh waves at 15 seconds. The phase velocities at this period are complicated (fast in the Sierran Foothills and slow in the Coast Ranges, particularly in the north); perhaps more surprisingly, the phase velocities are very different and even more complicated at 20 seconds. Here one observes a very large area of high velocities in the central Coast Ranges and the slowest velocities in the Cascades and around the MTJ. At these periods, the Rayleigh waves are essentially a weighted average of the crustal velocity with the greatest weight at about 15 km (or mid crustal depths) for 15 second waves and about 25 km (or lower crustal depths) for 20 second waves. There are great differences between the measurements at 15 and 20 seconds, indicating a large velocity contrast between the upper and lower crust. A mid-crustal velocity discontinuity may correspond to the Conrad discontinuity, at least in the San Francisco Bay Area and south.

By 25 seconds, the Rayleigh waves are sampling deep structure (20 − 40 km), and should be very sensitive to Moho depth. In general, there are slower phase velocities from west to east, due to the changing crustal thickness. In addition, however, there is a superposition of slower velocities in volcanic areas, such as the Cascades and Mammoth Lakes, and also at the MTJ. Southern California, which is thought to have a close to uniform thickness of the crust, has a fairly constant phase velocity at this period. Thirty second Rayleigh waves are similarly sensitive to crustal thickness, and one sees much of the same patterns. The very slow phase velocity in the Cascades disappears, indicating it is a shallower crustal feature.

Between 35 − 50 seconds (figure 4.17), over which there are only slowly changing features in the phase velocities, the MTJ remains slow, while the Mammoth Lakes and Cascade areas become fast. Faster velocities start to appear along the coast and the northern and southern interior of California. At 60 − 70 seconds (figure 4.18), the slow phase velocity in the region below central California starts to become prominent. At even longer periods, the northern negative phase velocity anomaly near the MTJ starts to wane, while the one in Central California is still very strong and widens to

a 650 km long and 150 km wide band of low velocity at 80 seconds. This is sampling a very deep but wide portion of the mantle (about 60 – 140 km). At these periods and these sampling depths, the largest velocity contrast that we see in the region is on the order of 4%. For comparison, the contrasts found at shorter periods can be as high as 10%.

There are also a few cases where the Rayleigh and Love wave phase velocities are somewhat similar. For example, some likenesses can be seen between the phase velocities of 25 second Rayleigh waves and both 20 and 25 second Love waves, although the peaked nature of the Rayleigh wave partial derivatives sample a much narrower depth range than the broad sampling of the Love waves. The Rayleigh waves also show some of the same features as the Love waves in areas outside of the central region. Eastern Nevada and the Gorda Plate generally have faster Rayleigh phase velocities than the central regions of the study area. As in the case of the Love waves, the area right around the MTJ is an exception at the shorter periods.

### 4.1.6 Reapplication to Moment Tensor Inversions

One immediate application of the phase velocity inversion results are to substitute the average phase velocity calculated for each source-receiver path for the regionalized phase velocities used in the initial moment tensor inversion. An obvious advantage is that each path will be individually computed. For example, an event in the Sierra Nevada recorded at stations in the Coast Ranges could use a path that represents an average of the contribution of the Coast Ranges, Great Valley, and Sierra Nevada, instead of using an approximation of the path, by using the Great Valley region, which represents the longest segment. One disadvantage, however, is that these paths cannot be calculated ahead of time, and must be computed "on the fly", which means that the inversion takes longer to complete. As a result, this is generally not used for quick, automated moment tensors, but can be applied in the refinement stage of the solution.

An example of a comparison of the two methods is illustrated in figure 4.19. Moment tensor solutions for a M 4.8 Double Spring Flat aftershock (12/22/95) are shown using the regionalized models and the path-specific models. The corrected phase measurements are very similar between the two inversions, indicating that there are no big differences in the phase velocity calculated by the two approaches,
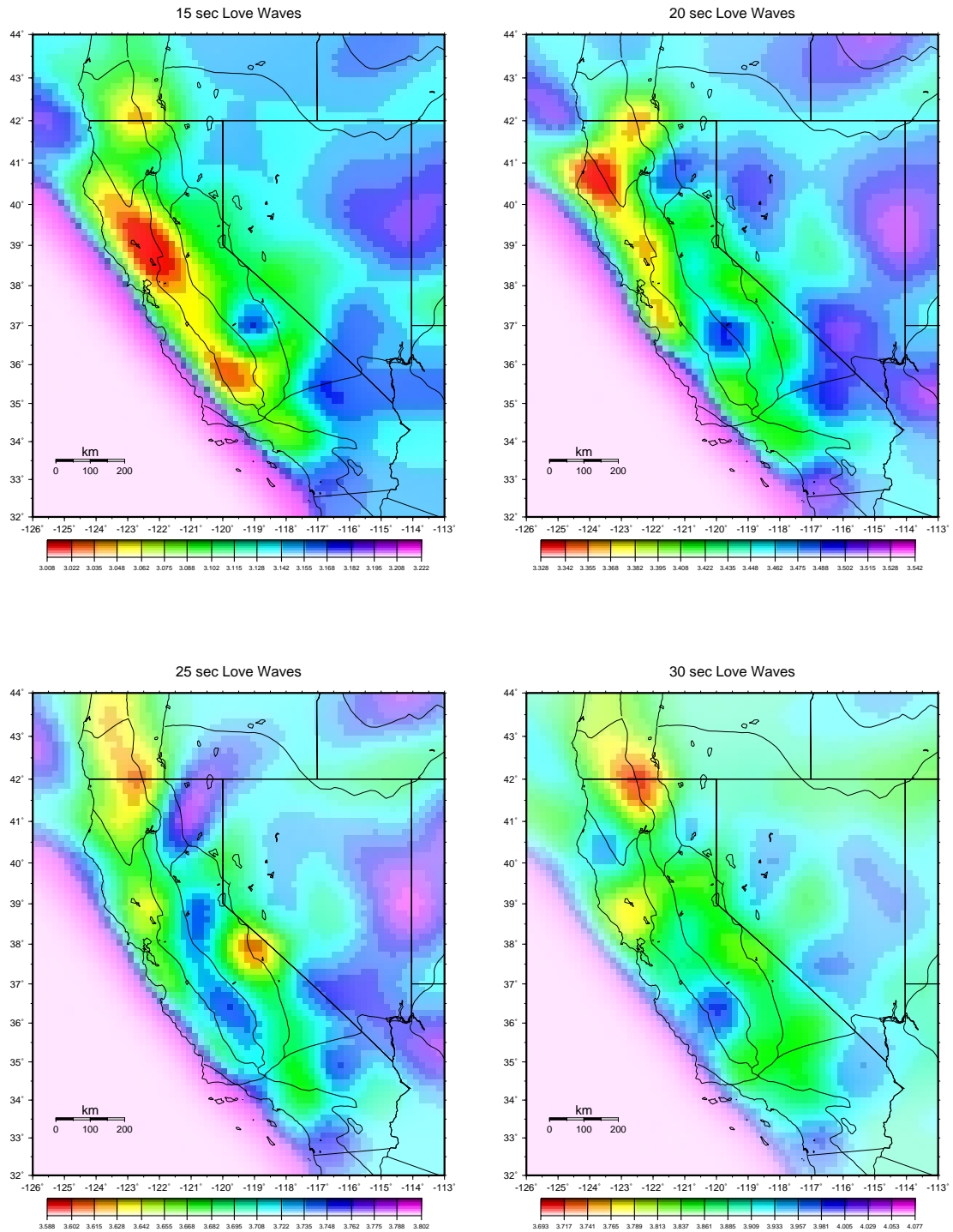
Figure 4.13: Love wave phase velocity inversion at 15, 20, 25 and 30 seconds for the region of California, Nevada, and portions of Oregon, Idaho, Utah, Arizona, and Mexico. Lines represent coastlines, state boundaries, and boundaries of tectonic regimes.
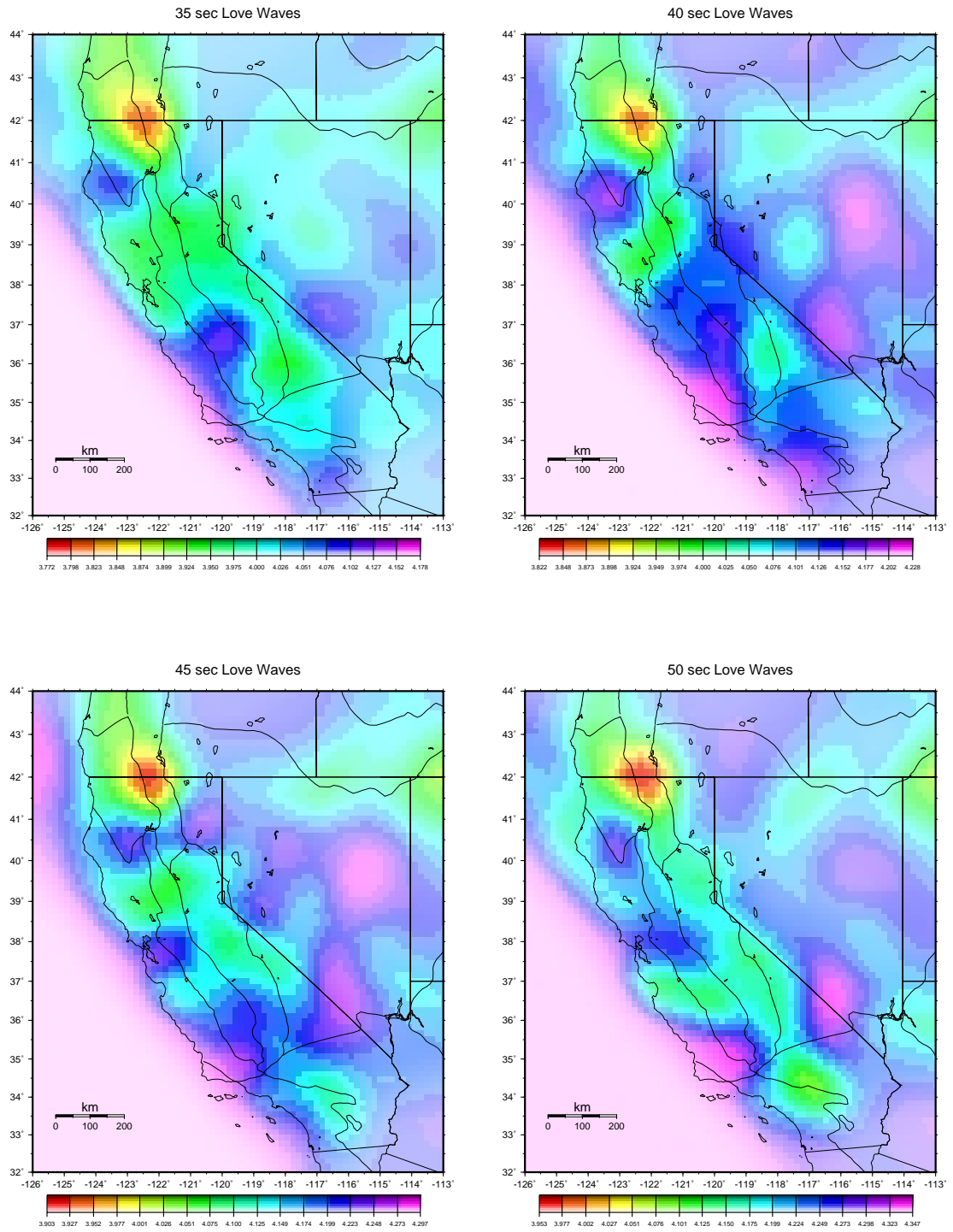
Figure 4.14: Love wave phase velocity inversion at 35, 40, 45, and 50 seconds. Otherwise, same as previous figure.
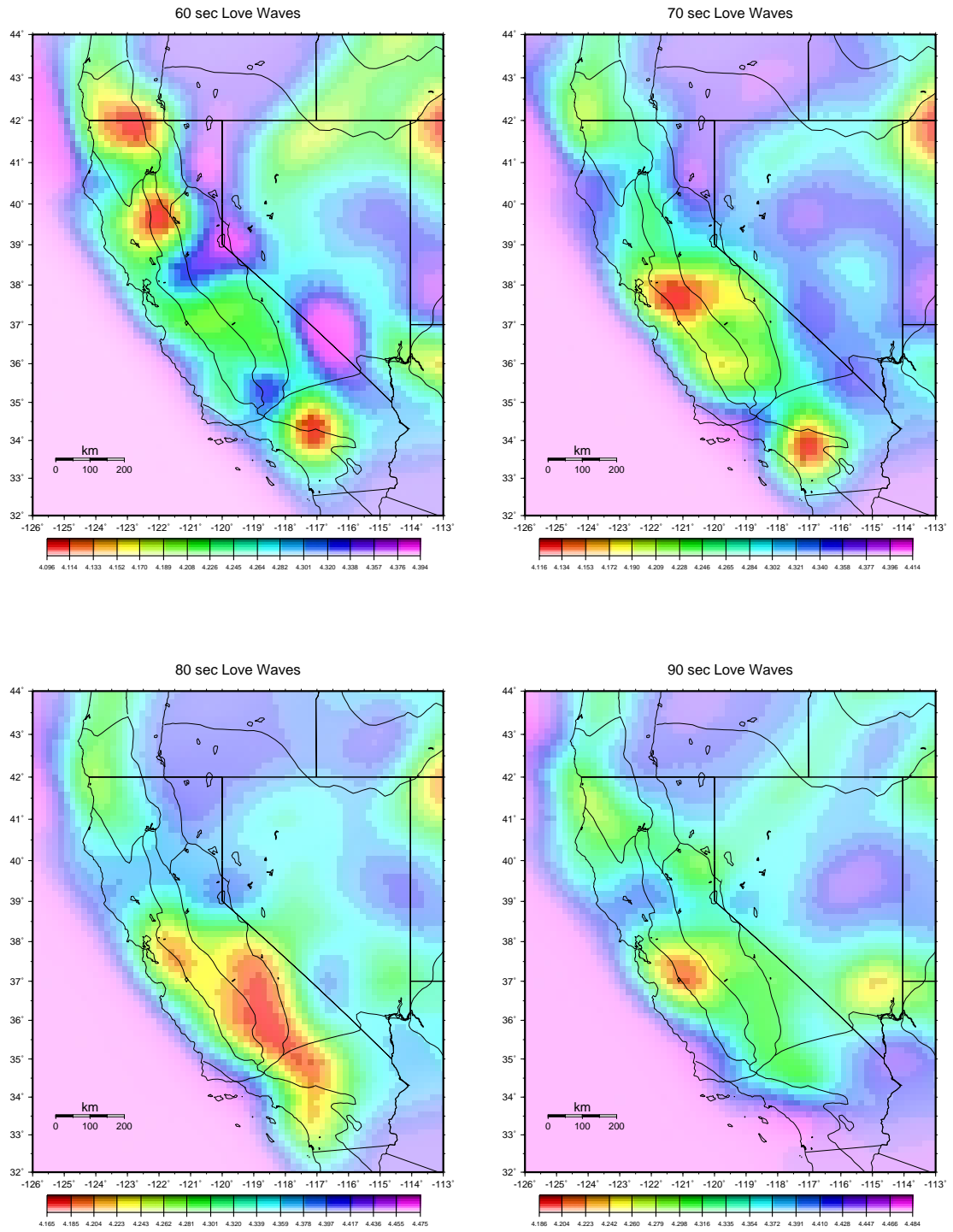
Figure 4.15: Love wave phase velocity inversion at 60, 70, 80, and 90 seconds. Otherwise, same as previous figure.
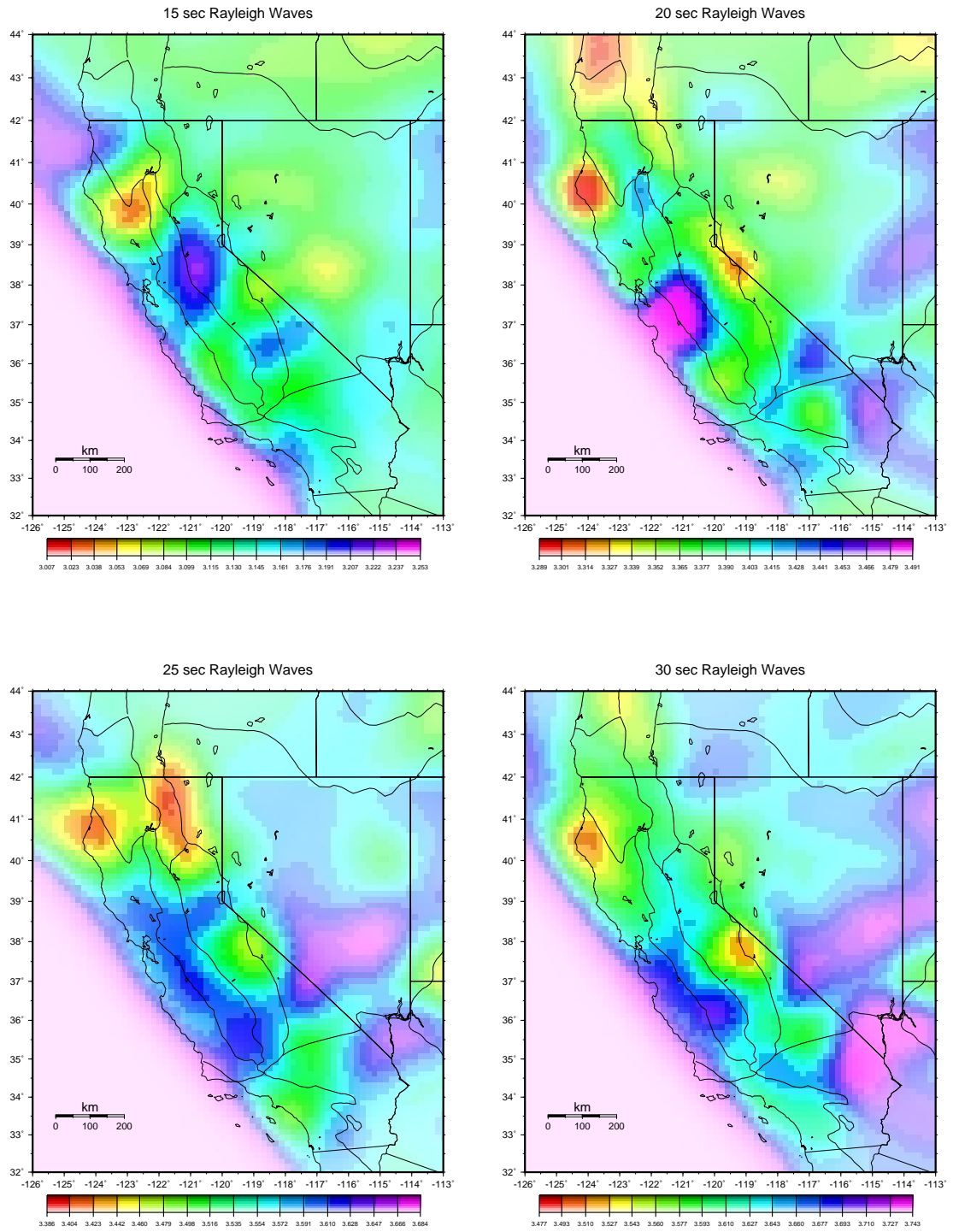
Figure 4.16: Rayleigh wave phase velocity inversion at 15, 20, 25, and 30 seconds. Otherwise, same as previous figure.
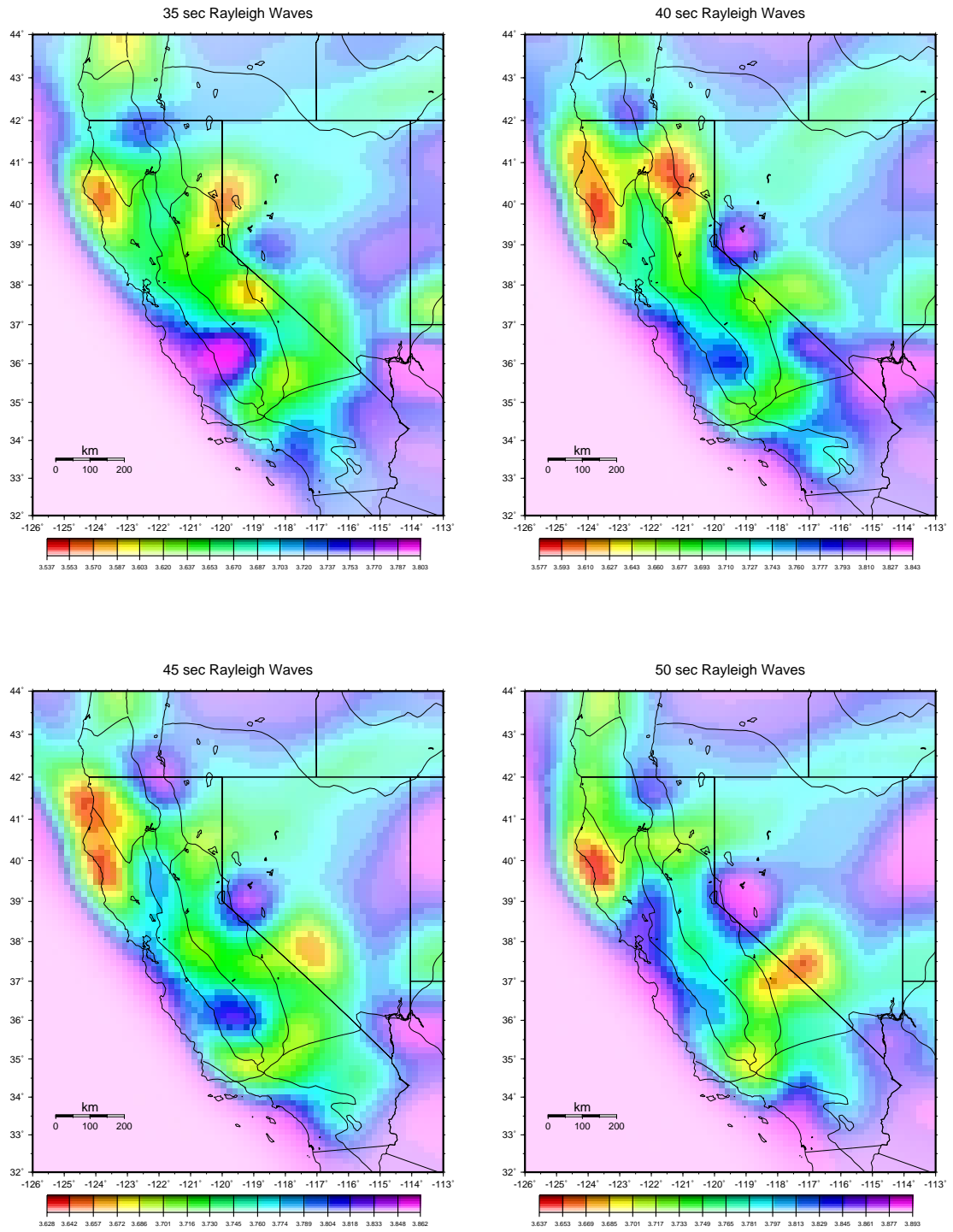
Figure 4.17: Rayleigh wave phase velocity inversion at 35, 40, 45, and 50 seconds. Otherwise, same as previous figure.
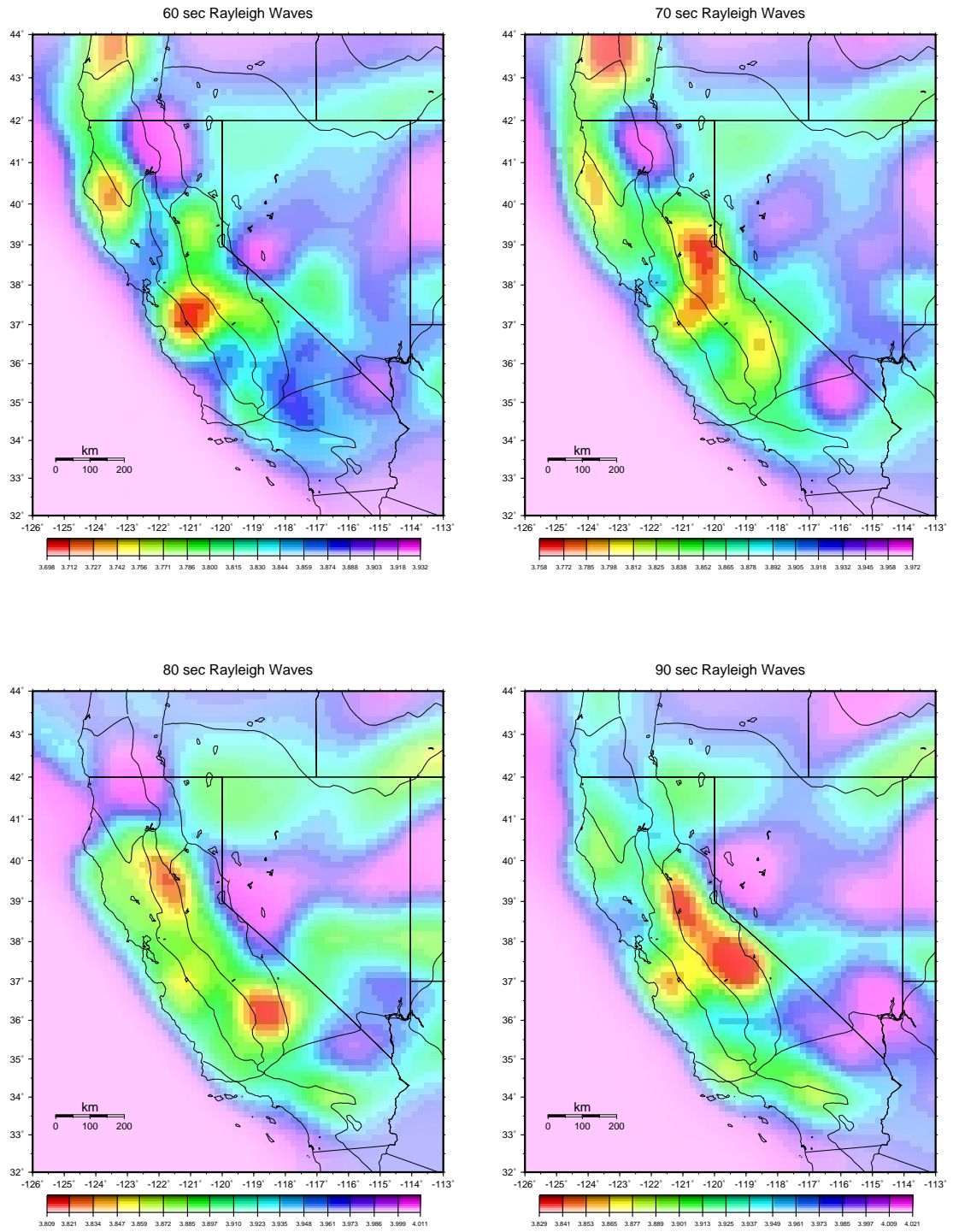
Figure 4.18: Rayleigh wave phase velocity inversion at 60, 70, 80, and 90 seconds. Otherwise, same as previous figure.

at least not for this wave type and frequency. The estimated source depth changes from 16 to 12 km and is mainly the result of the broad residual minimum seen in the regionalization approach. Still, this difference has only a minimal effect on the mechanism and seismic moment, which increases slightly from 1.9e23 dyne-cm to 2.1e23 dyne-cm. The remarkable similarity between the two solutions indicates that there are also no large systematic differences between the two approaches for these source-receiver paths over the period range of the inversion.
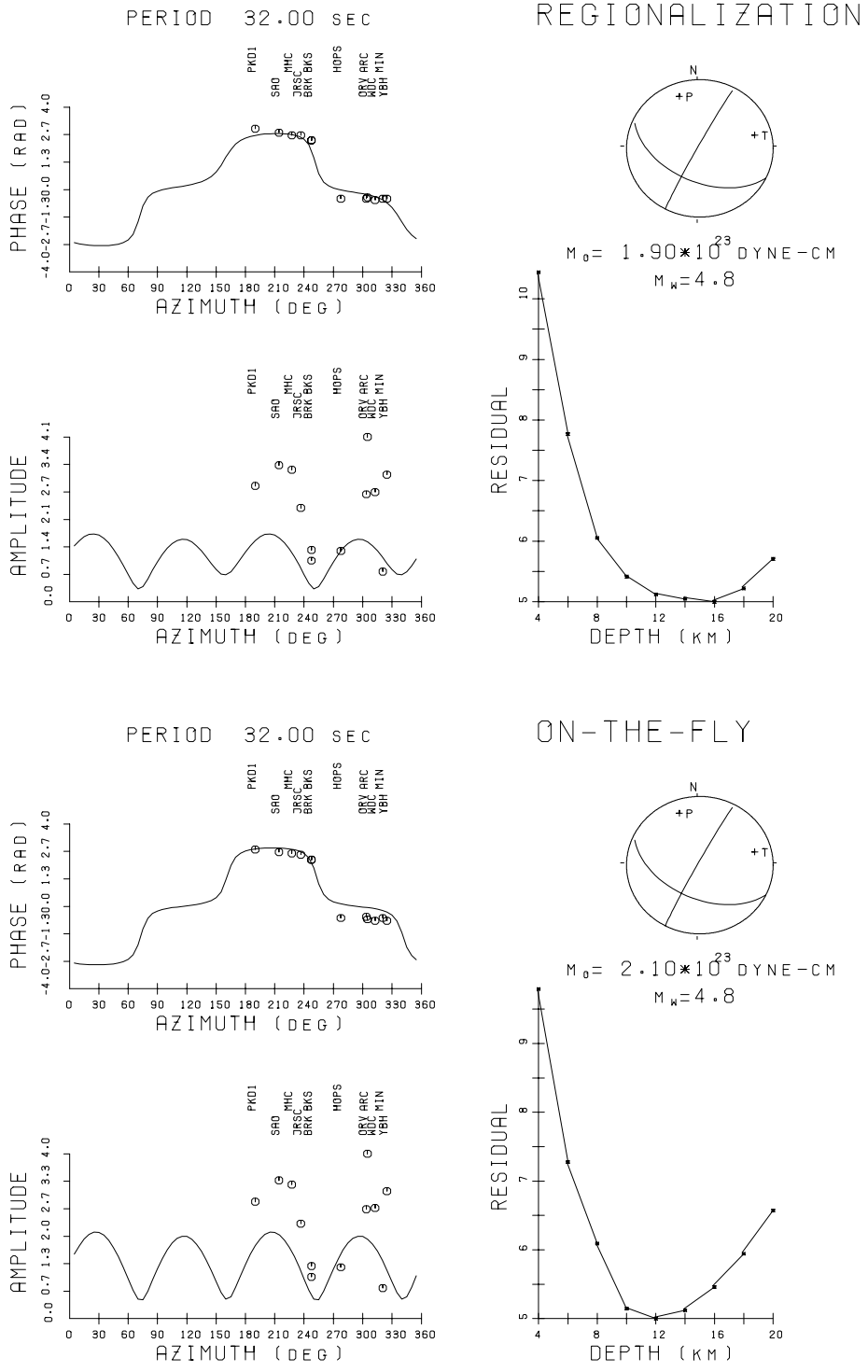
Figure 4.19: An example of the reapplication of phase velocity measurements for the regional moment tensor for a 12/22/1995 Double Spring Flat event. The first inversion is performed using the regionalized models, while the second inversion is performed using path-specific models. The amplitude and phase of 25 second Love waves are shown.

## 4.2 Layered Velocity Inversion and Interpretation

Although phase velocity is a fundamental parameter when dealing directly with surface waves (simply the velocity of a particular phase), it is not an intuitively easy quantity to understand. The results of the phase velocity tomography can be used to correct for the effects of the regional structure on the moment tensor inversion, but for some other purposes, the phase velocities are limited. Since one of the stated goals is to determine the structure of the earth, in this section the phase velocities are themselves inverted with depth to obtain regional earth structure.

### 4.2.1 Layered Velocity Inversion

At this point, the inversion has yielded phase velocities at a number of discrete frequencies. Once again, using the SURF programs of Herrmann and Russell, structural interpretations can be made from the phase velocity dispersion curves for several of the significant regional features in the velocity inversion. The first step in this process involves interpolating the phase velocities to produce complete dispersion curves from 15 to 100 seconds from the velocities at discrete frequencies that were determined from the tomographic surface wave inversion. The data was experimentally fit with several different functions in order to obtain a smooth fit and to take the uncertainty of the measurements into account. A number of methods were tested for the interpolation, including several different cubic splines and various polynomials. The preferred method was a cubic function ($y = ax^3 + bx^2 + cx + d$) with a least squares fit that was weighted by the variance of the point, and where the slope was constrained to be positive. This resulted in the most "natural" looking dispersion curve without a negative slope in phase velocities which would only result in a very large low-velocity zone. Because of the limited coverage in some areas, the inversion area for this step was reduced to a latitude range of 32 to 44°N and a longitude range of 126 to 113°W. The inversion was then performed at every half degree in latitude and longitude over the area where there was enough data coverage.

Next, each of these dispersion curves were inverted for structure using the SURF programs (Herrmann, 1991). At specific locations, the Love and Rayleigh wave phase velocities at the inversion periods are assembled to form two dispersion curves for the region. At each node, the dispersion curves are then inverted for a 1-D velocity of the

crust and upper mantle using the same procedures described earlier in Section 2.2.3 for the inversion of the regional phase velocity curves. Since only isotropic models are allowed, any Love and Rayleigh wave inconsistencies are effectively treated as a source of noise. Using equation 2.23 and the partial derivatives of the previously determined model, a series of linear inversions of both layer thickness and layer velocity are performed with increasing damping parameter.

The starting model in each case was an "average" crustal model for California, which consisted of four crustal layers (sediment, upper crust, mid crust, and lower crust), an upper mantle layer, and a half-space representing the rest of the mantle. This model is illustrated in figure 4.20. The sediment layer (P-wave velocity = 2.25 km/s) actually starts with no thickness, so as to not allow the layer unless it is required by the inversion. The upper crust has a velocity of 5.30 km/s and is 3 km thick, the mid crust has a velocity of 6.10 km/s and is 15 km thick, and the lower crust has a velocity of 6.70 km/s and is 10 km thick. The upper mantle layer (20 km thick) and mantle half-space start with the same initial mantle velocity (7.85 km/s), but are allowed to vary away from each other. Afterwards, where layer thickness became small, a layer was "pinched out", and where the velocity difference between two layers became small, the layers were combined into a single layer. The resulting velocity structures could have anywhere up to four crustal layers, and up to two mantle velocities.

This setup was found to be a very robust way to prevent low velocity zones, which may develop in the first few steps of the inversion and become difficult to remove. This was also used to figure out if the model requires a high velocity lithospheric "lid" in the mantle overlying a lower velocity asthenosphere. In this case, the depth to the bottom of the lid would provide an estimate of the lithosphere thickness. Reasonable values for Poisson's ratio were selected for each layer type and these values were fixed in the inversion. As discussed in section 2.2.3, either this constraint or, alternatively, having the density $\rho$ fixed is required to obtain both P and S velocities using waves which is primarily sensitive to S velocity. Although the surface waves and, therefore, the model results are largely reflective of S velocity, it is generally easier to compare P models to the majority of other studies that are available in the literature. Consequently, P-wave velocities will be presented here.

Because of the huge tradeoff between mantle velocity and crustal thickness, the
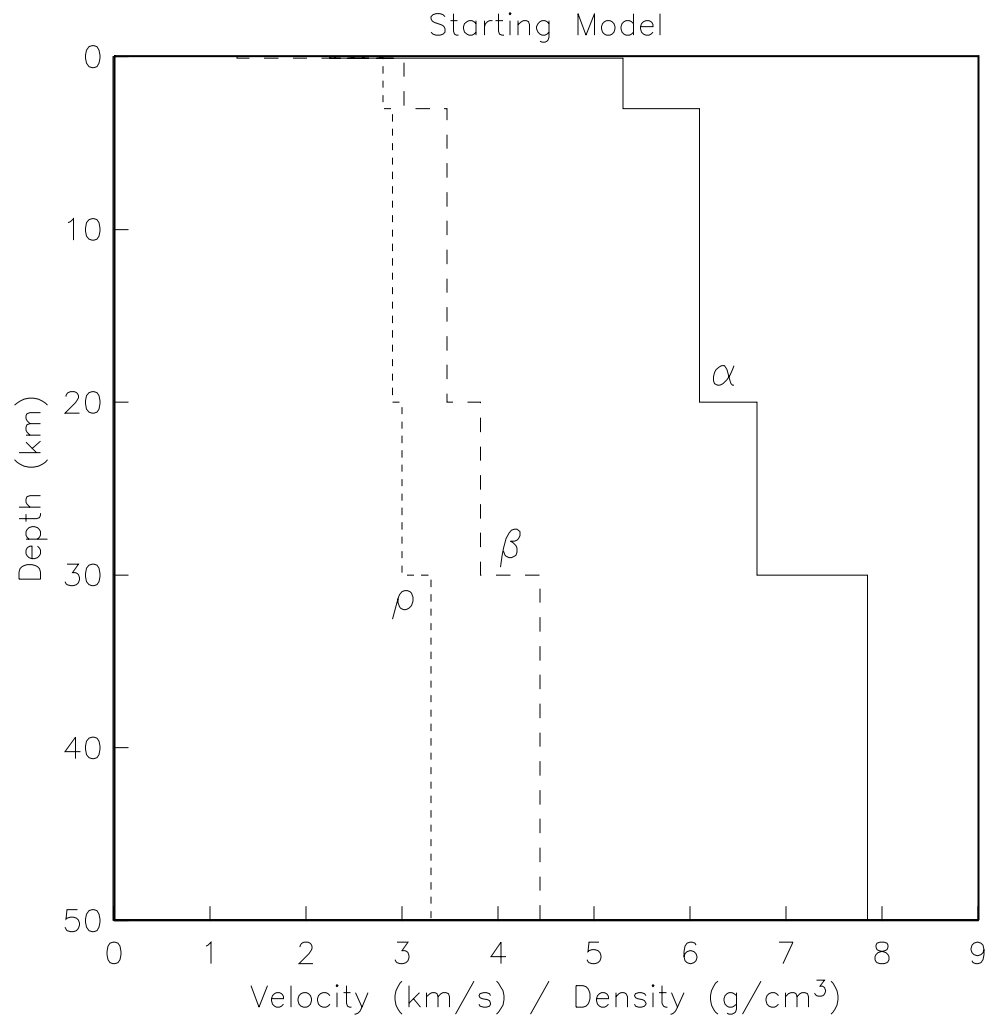
Figure 4.20: Starting model for inversion of phase velocity dispersion curves into layered velocity models. $\alpha$, $\beta$, and $\rho$ refer to P-wave velocity, S-wave velocity, and density, respectively.

inversion is highly sensitive to the initial mantle velocity used in the starting model. To illustrate this point, figure 4.21 shows the same phase velocity dispersion curves fit using starting models with mantle velocities of 7.8, 7.9, 8.0, and 8.1 km/s. The final models share the same characteristics in both the crust and upper mantle. The crustal thickness, mainly driven by an increase in the thickness of the third layer, varies dramatically. The Moho discontinuity is located at 34, 38, 42, and 46 km, respectively. $P_n$ measurements from other studies, which might provide an independent estimate of this value, vary widely, across the region ranging from 7.6 – 8.1 km/s in California, and from 7.7 – 8.0 km/s in central California alone (Hearn, *et al.*, 1991). For several reasons, including the thinner crusts and the smaller contrasts across the pseudo-boundary in the mantle, the slower starting mantle velocities are preferred and 7.85 km/s is used.

### 4.2.2   Layered Velocity Models

Figures 4.22 and 4.23 show the result of the layered velocity inversion in a number of tectonic regions. Each figure is a plot of P-wave velocity as a function of depth, and represents a depth slice through the crust in a particular region. In each case, the layered velocity inversion is shown by the solid lines. For comparison, the USGS layered velocity models for this region are also shown (in dotted lines). The first example is shown for the San Francisco Bay Area (figure 4.22a). The model has a 32 km crust, which is thicker than the USGS Hayward Model. In addition, the uppermost layer is significantly slower but has about the same thickness as the comparison model. This is probably due to the wide spatial sampling of the phase velocity inversion. Because of imposed smoothing, the phase velocities actually represent the average phase velocity of a finite region, which has an area on the order of the square of the correlation length. As a result, the inversion probably includes more of the sediment-rich regions such as the Santa Clara Valley. Otherwise the models are quite similar to one another.

The second case was taken from the vicinity of Parkfield (figure 4.22b). In this particular case, the models are very similar. This is a typical velocity model for the Coast Ranges. In both cases, the crust is a little under 30 km thick and divided into four regions. The uppermost sedimentary layer (2.27 km/s) is 3 – 4 km thick, the
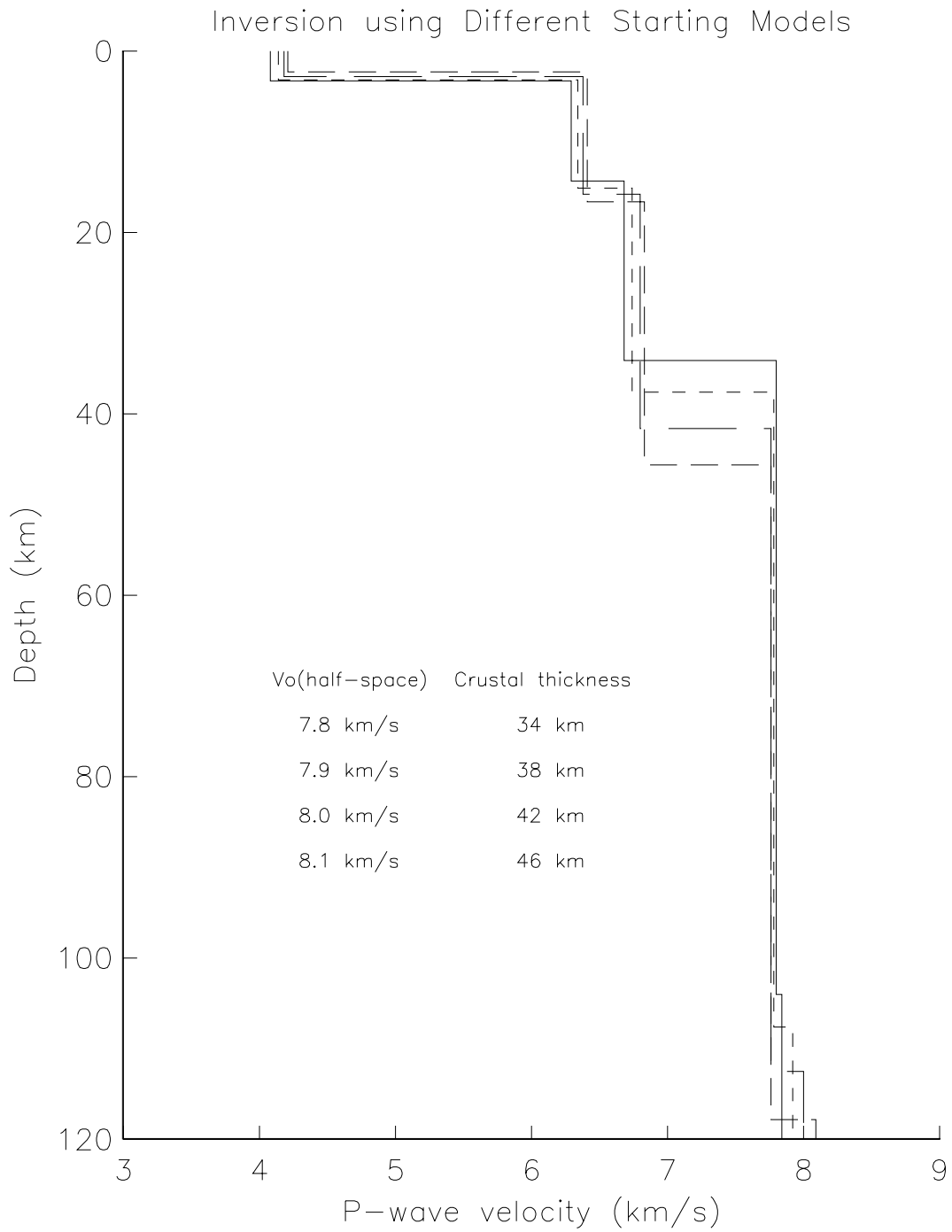
Figure 4.21: Layered velocity inversion using four different starting models each with different mantle velocities. The resulting profiles are shown for the four models, each ending up with a different crustal thickness.

upper crust (5.22 km/s) extends down to about 10 km, and the discontinuity between the upper and mid crust is not very significant. The velocity and thickness of the mid and lower crust (velocities of 6.05 and 6.69 km/s, respectively) are also very similar between the two models. Finally, the velocity of the mantle from the profile is 7.94 km/s.

The next cases move inland from the Coast Ranges first across the Great Valley (figure 4.22c), and then into the Sierra Nevada Mountains (figure 4.22d). The layered velocity model for the Great Valley has an uppermost layer which is unusually slow (P-wave velocity of 1.79 km/s) representing the unconsolidated sediments of the region. There is also a large mid-crustal contrast at about 12 km. Finally, the Moho occurs at a depth of about 32 km. Many of these same features are seen the USGS Coalinga model. The mid-crustal discontinuity is deeper and larger than for the layered inversion, and the crust is slightly thinner. The Sierra Nevada profile is, unfortunately, in many ways similar to the Great Valley, and is seen in profiles taken from other points along the Sierra Nevada. Again, this is probably due to the large correlation length and wide spatial sampling of the inversion method. The USGS Auburn model, which is used to locate earthquakes over much of the Sierra Region, has a very thin layer of slower material overlying a large granitic block (6.20 km/s) which extends down to 34 km depth, and an overall crustal thickness of 36 km.

The layered velocity model further up the coast, in the vicinity of the Mendocino Triple Junction, is illustrated in figure 4.23a. One thing to note are significant changes in this model from the starting model. Several of the layers (upper crust and lower crust) have become very small and are close to pinching out completely. The mid-crustal layer becomes dominant and the crust is relatively thin, which is similar to the USGS model for the region. This model has a 4 km uppermost layer, and the upper crust with relatively slow seismic velocities (5.05 km/s) extends almost 18 km, until a 2 km layer of intermediate material, overlying a 7.9 km/s upper mantle.

The profile near the Cascade Range is illustrated in figure 4.23b. Similar to the previous case, the profile has changed significantly from the starting model. In this case, the crust has become significantly thicker (close to 39 km), although not as thick as the 42.5 thick crust of the USGS Shasta model (which is used to locate earthquakes in Oregon and the northernmost portion of California). The uppermost sedimentary layer has all but pinched out, placing high velocity material (about 5.0 km/s) very

close to the surface. This is in contrast to the USGS model which has a 5 km thick layer of 3.10 km/s. In both cases, the mid-crust layer is a significant layer in the profile.

Figure 4.23c is the profile for the Southern California region taken from near the Los Angeles basin. Perhaps this can explain the large uppermost velocity layer seen in the profile. The USGS model is characterized by little variation in the velocity of the crustal layers (6.2 – 6.8 km/s) from the base of the uppermost layer to the top of the crust. The Moho depth of 30 km seen from the profile is consistent with the 28 – 32 thickness of the crust throughout Southern California, which is slightly lower than the thickness from the USGS model.

The profile in the Walker Lane Belt is shown in figure 4.23d and is compared to the USGS Basin and Range model. The layered velocity profile yields a crustal thickness of about 32 km. This is indicative of an extended crust in this region, since this is quite thin considering the high topography of the region. Another significant of this profile and over much of the Basin and Range is that, in general, the mid and lower crust have some relatively high velocities (> 6.0 km/s). Compare this to some of the other profiles on the page which have much slower velocities in these layers.

A test of using *a priori* information is performed with the Sierra Nevada dispersion data. Other studies indicate that the near-surface velocity in the Sierra Nevada Mts. is fast. Consequently, in the inversion the weight of the top layer is modified to discourage a change in its thickness. The resulting velocity model (shown by the smaller dashed line in figure 4.22c) has a single upper crustal layer 12 km thick and a P-wave velocity of about 5.0 km/s, slightly higher than the previous upper crustal layer. Otherwise, though, the rest of the resulting layered model is similar to the previous model, with subsequent layer boundaries at 27 and 33 km. This is encouraging from the standpoint of using other information in the inversion because using some *a priori* information did not totally change the rest of the results, rendering them meaningless. Nor did this completely ignore the slower phase velocities needed for the shorter periods because of smearing. One can, however, use information from other studies to make some directed change. Similar directed change could be made using information on basin thickness from seismic profiles, upper mantle velocity from $P_n$ studies, etc.
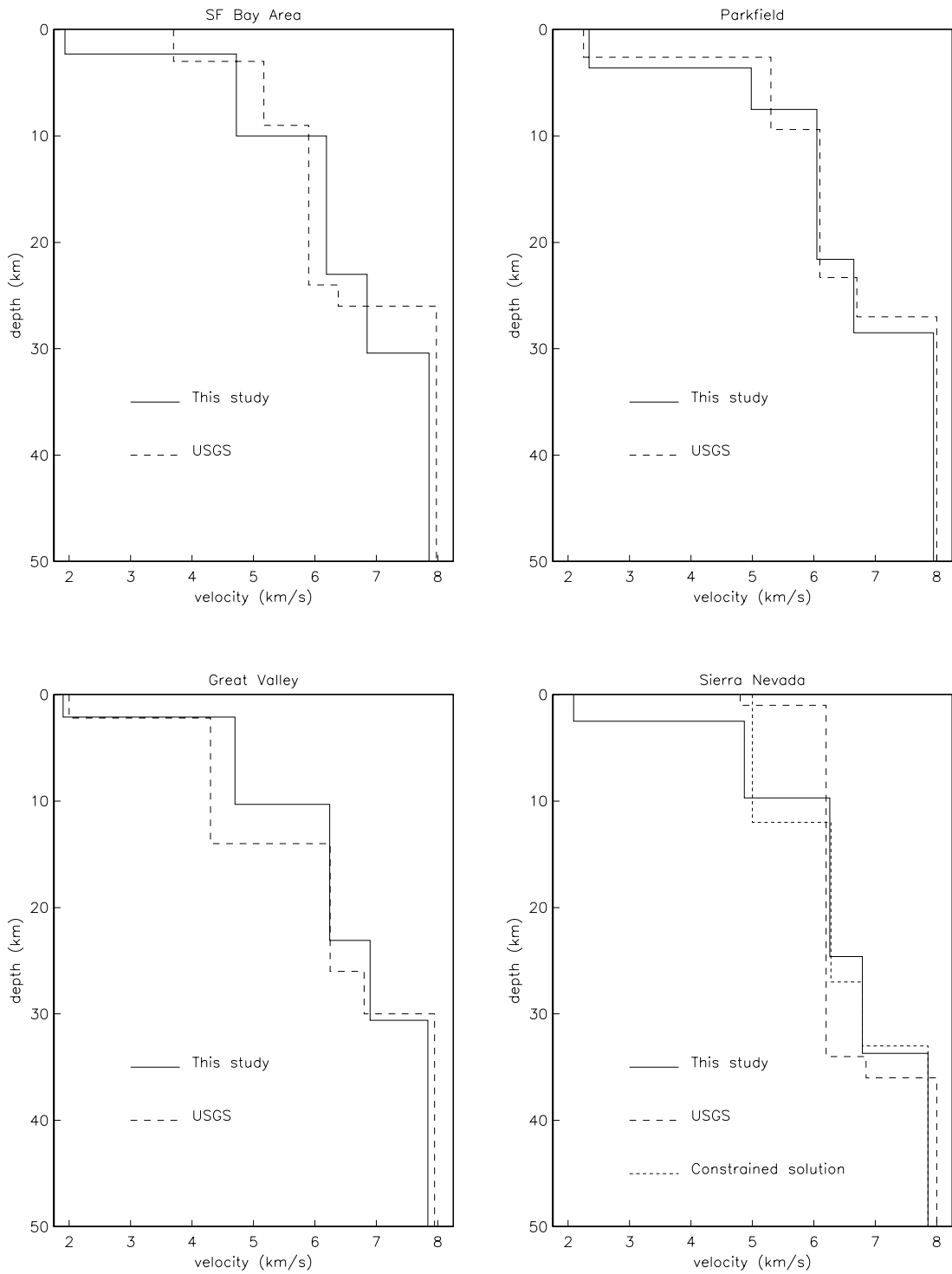
Figure 4.22: Layered velocity model in the vicinity of the San Francisco Bay Area, Parkfield, Great Valley, and Sierra Nevada regions. Solid line is the layered P-wave velocity determined from inverting phase velocities. Dashed line is the USGS model for the region. Additional constrained model shown for the Sierra Nevada region.
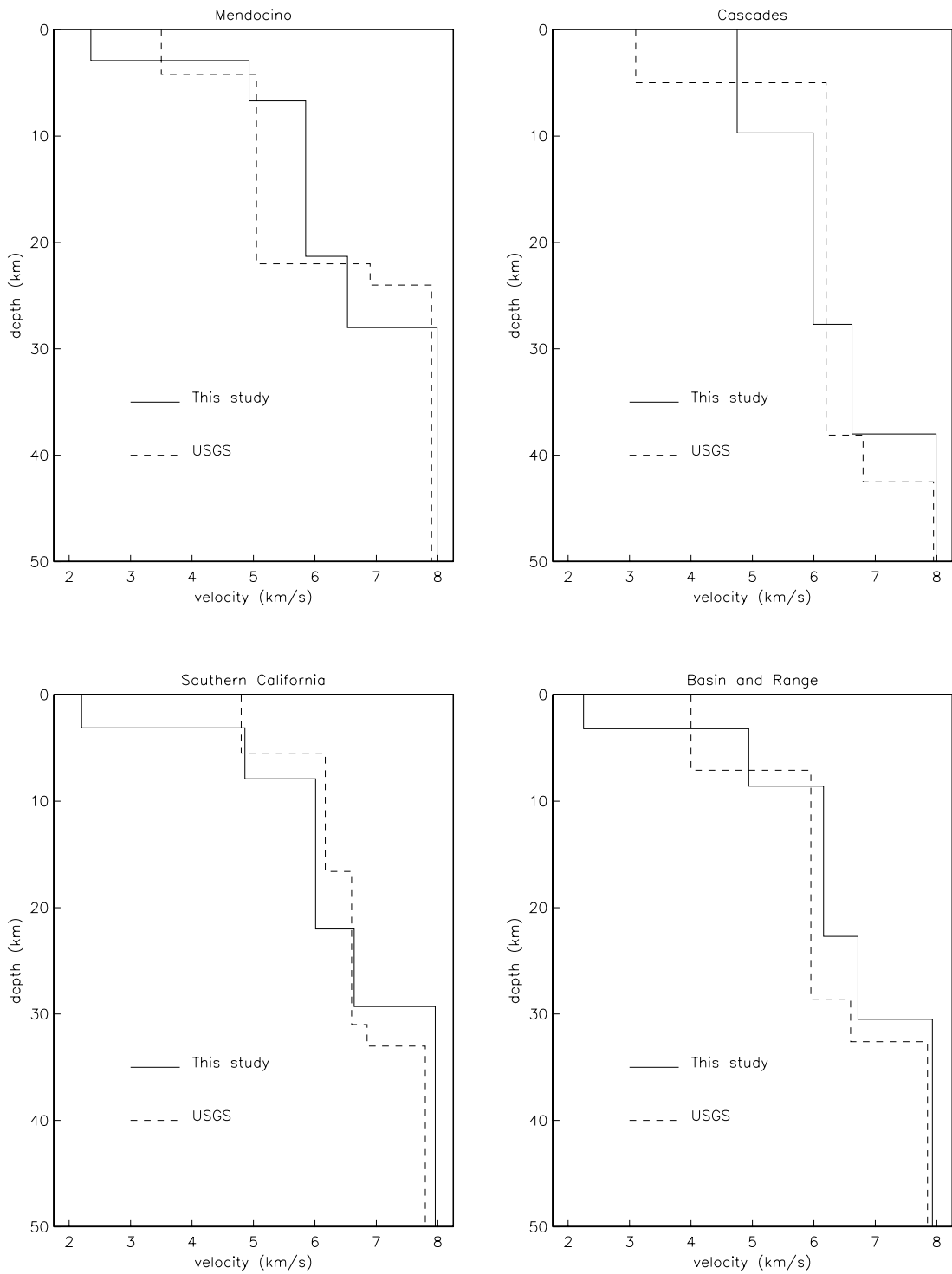
Figure 4.23: Layered velocity model in the vicinity of Mendocino, Cascades, Southern California, and the Basin and Range. Otherwise same as previous figure.

### 4.2.3 Results from Other Studies

Before discussing the results of the layered velocity inversion over the whole region, it is important to review some of the results from other studies in the region. The results of Taylor and Patton [1986], Fuis and Mooney [1990] and Benz, *et al.,* [1992] are outlined here. Taylor and Patton [1986] utilized observations of Rayleigh and Love wave phase velocity dispersion in the 6 − 60 second period range to look at lateral variation of shear-velocity structure in the Basin and Range, using a simple 300 × 300 km block-province grid for most of the inversion area. Their results indicate that there is a well-developed, upper mantle low velocity zone in the central Basin and Range. Also, crustal thicknesses were found to be thicker (∼35 km) in the central part of the Basin and Range and thinner (∼25 km) on the outer edges. An upper-mantle lid was found which varied in thickness from 10 − 30 km and indicated a lithospheric thickness of 45 km.

Fuis and Mooney [1990] examine the lithospheric structure and tectonics from seismic-refraction and gravity data. In particular, they compile a contour map of crustal thicknesses in California which provides a useful comparison for the velocity inversion (figure 4.24). The results indicate that crustal thickness along the San Andreas increases from 16 − 24 km in northern California to 28 − 32 km in southern California. North of Cape Mendocino, the crust thickens eastward from about 16 km at the coast to about 38 km in the southern Cascade Range. In central California, the crust thickens eastward from about 25 km near the coast to as much as 55 km in the Sierra Nevada, but this general landward thickening is interrupted by a thin crust (25 km) beneath the Great Valley. In southern California, the crust thickens eastward from about 20 km at the western margin of the California Continental Borderland to about 32 km in the eastern Transverse Ranges. Mooney and Braile [1989], who examine the crustal thickness of North America, indicate that for the rest of the study area, crustal thicknesses generally remain high between 35 and 45 km. Exceptions are a thinning along the Northwest coast similar to that of the Coast Ranges, and anomalously thin crusts (< 30 km) within the Basin and Range. Additionally, in limited areas direct comparisons can be made to studies from reflection profiles, such as COCORP (Brown, *et al.,* 1986).

Benz, *et al.,* [1992] used teleseismic P-wave travel-time residuals recorded across
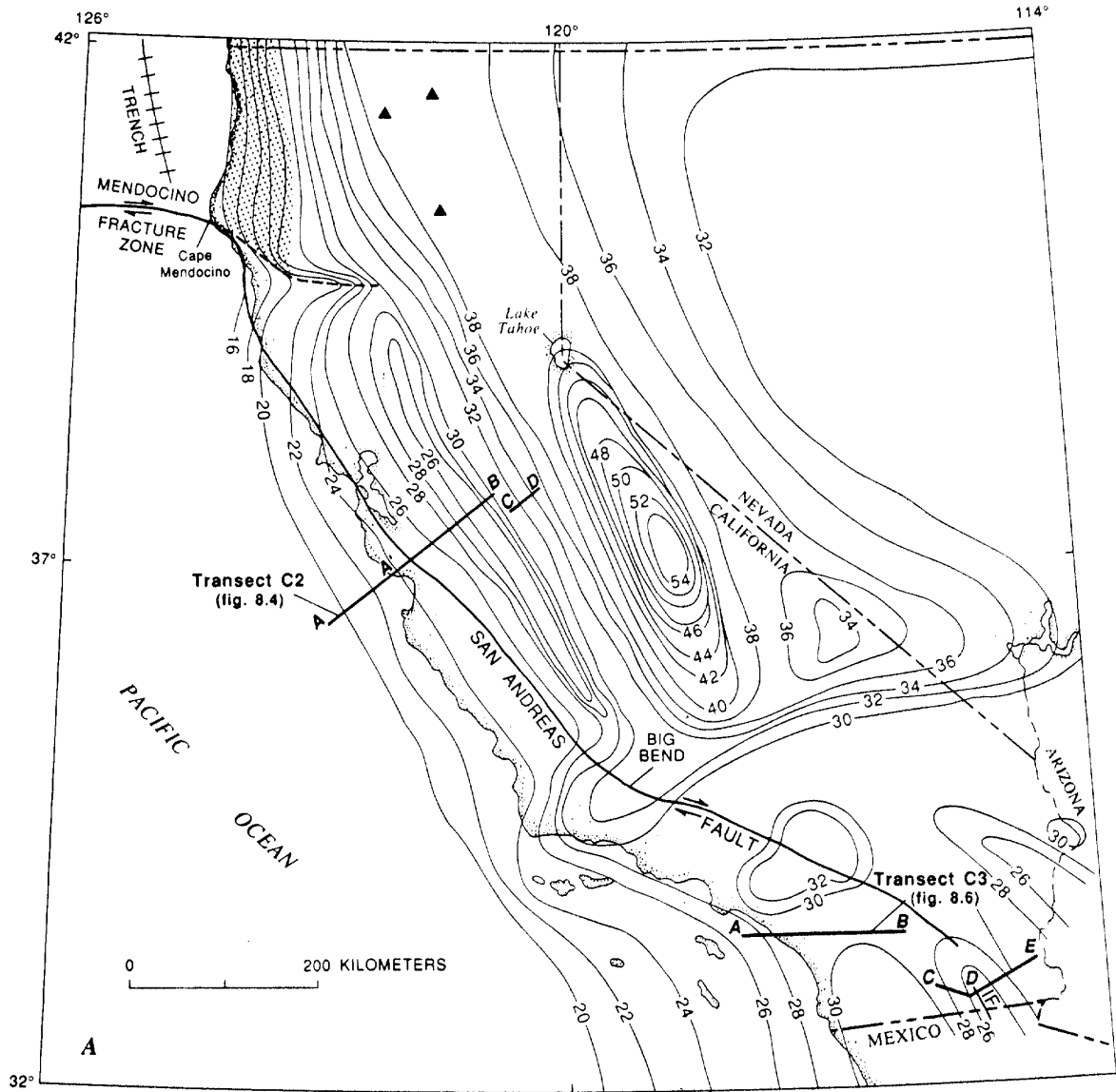
Figure 4.24: Crustal thickness for California and adjacent regions (Fuis and Mooney, 1990).

201

the short-period NCSN to determine the lithospheric P-wave velocity structure beneath Northern California. They found localized regions of slow velocity in the crust beneath Mt. Shasta, Mt. Lassen, and Clear Lake, which were attributed to the presence of active magmatic bodies. They also saw slow velocities beneath Cape Mendocino, in the northern Coast Ranges, and west of San Francisco Bay which have no correlation with surface geology, and which are attributed to a variety of subsurface processes. Localized fast velocities were also observed beneath Sutter Butte and the northern end of the Sacramento Valley, which were associated with cooled magmatic bodies. Other non-volcanic fast regions were found beneath the Foothills Metamorphic Belt and in the eastern Klamath Mts. , and were attributed to ophiolite suites.

Similarly, there are a number of studies which have looked at the upper mantle velocity structure of the western United States (Romanowicz, 1979; Romanowicz, 1980; Aki, 1982; Hearn, *et al.* 1991; Benz, *et al.*, 1992). Iyer and Hitchcock [1989] provide a useful synopsis of the studies of the upper mantle in this region. They note that the three-dimensional studies show the existence of long-wavelength heterogeneous structure extending throughout the upper mantle. In summary, most regional investigations have revealed heterogeneous velocity structures associated with: (1) the ongoing subduction of the Juan de Fuca plate beneath Washington and Oregon, (2) the cessation of subduction of the Farallon plate beneath California during early Tertiary time, (3) rifting in Imperial Valley, (4) hot-spot magmatism in the Yellowstone Plateau, (5) large-scale asthenospheric upwelling in the region of the Rio Grande Rift, and (6) the orogenic belts in the northeastern United States.

For example, in a three-dimension study of the continental United States using P-wave residuals, Romanowicz [1979] found that Layer 1 (0–250 km) had features that showed a high correlation with tectonic features: low velocities in the Basin and Range Province and high velocities in the Columbia Plateau. Layer 2 (250–450 km) and Layer 3 (450–700 km) showed broad distinct spatial patterns that corresponded to the western, central, and eastern United States. Furthermore, the evidence for a high velocity near-surface layer in the northwestern United States and for a strong north-south band of high velocity material deeper down and further to the east is compatible with the presence of the subducted Farallon Plate (Romanowicz, 1980).

Other studies of seismic velocities in the upper mantle derived from teleseismic

delay-time data were focussed on California. Aki [1982] summarized the results of Cockerham and Ellsworth [1979] and Raikes [1980] in a seismic velocity map for the upper mantle (figure 4.25). Low velocities are seen in central California (due to the slabless window), beneath Long Valley, Salton Trough, and the eastern Mojave Desert (interpretated to be asthenospheric upwelling). High velocities occur in Southern California (attributed to sinking lithospheric mantle beneath the Transverse Ranges), at the MTJ, and in the southern portion of the Great Valley. Although the details of this figure are not important, it shows that features within the upper mantle (in this case primarily the asthenosphere) are not necessarily related to crustal tectonic regimes or to crustal features such as the San Andreas Fault.

Hearn, *et al.* [1991] conducted a tomography study of the Western United States from regional arrival times to estimate $P_n$ velocities in the upper mantle. Simultaneously, they also solved for crustal station delays. Negative station delays indicate thin or fast crust. Positive delays primarily represent the effect of thick crust, but may also be caused by a slower crust. They find that uppermost mantle velocity variations range from 7.6 km/s in the Sierra Nevada to 8.1 km/s along the Pacific Northwest coast. The Great Basin and the Snake River Plain were also found to have low velocities, while the Colorado Plateau, the Mojave and the Rockies had high velocities.

In the top layer of the upper mantle (30 − 70 km), Benz, *et al.* [1992], using teleseismic P-wave travel time residuals, found that the velocities are arranged in parallel bands of alternating high and low velocities. To the west, a band of slightly higher velocity runs beneath the coastal region from Cape Mendocino to the San Francisco Bay, and is bounded by very low velocities beneath the Klamath Mts. and the Northern Coast Ranges. Moving northeastward, the highest velocities are found beneath Mt. Shasta, Mt. Lassen, between Mt. Lassen and Sutter Buttes, and east of Sutter Buttes. Finally, lower velocities are observed under the Cascade Range and the northern portion of the Sierra Nevada Mts. These bands of high and low velocity migrate eastward with greater depth.

The largest upper mantle velocity variations occur between 30 and 110 km depth, where there is a variation in velocity from -5.5% to +9.5%, and are attributed to the thickness and geometry of the Pacific, North American, and Gorda plates. The high-velocity region which extends below the northern portion of California is interpreted
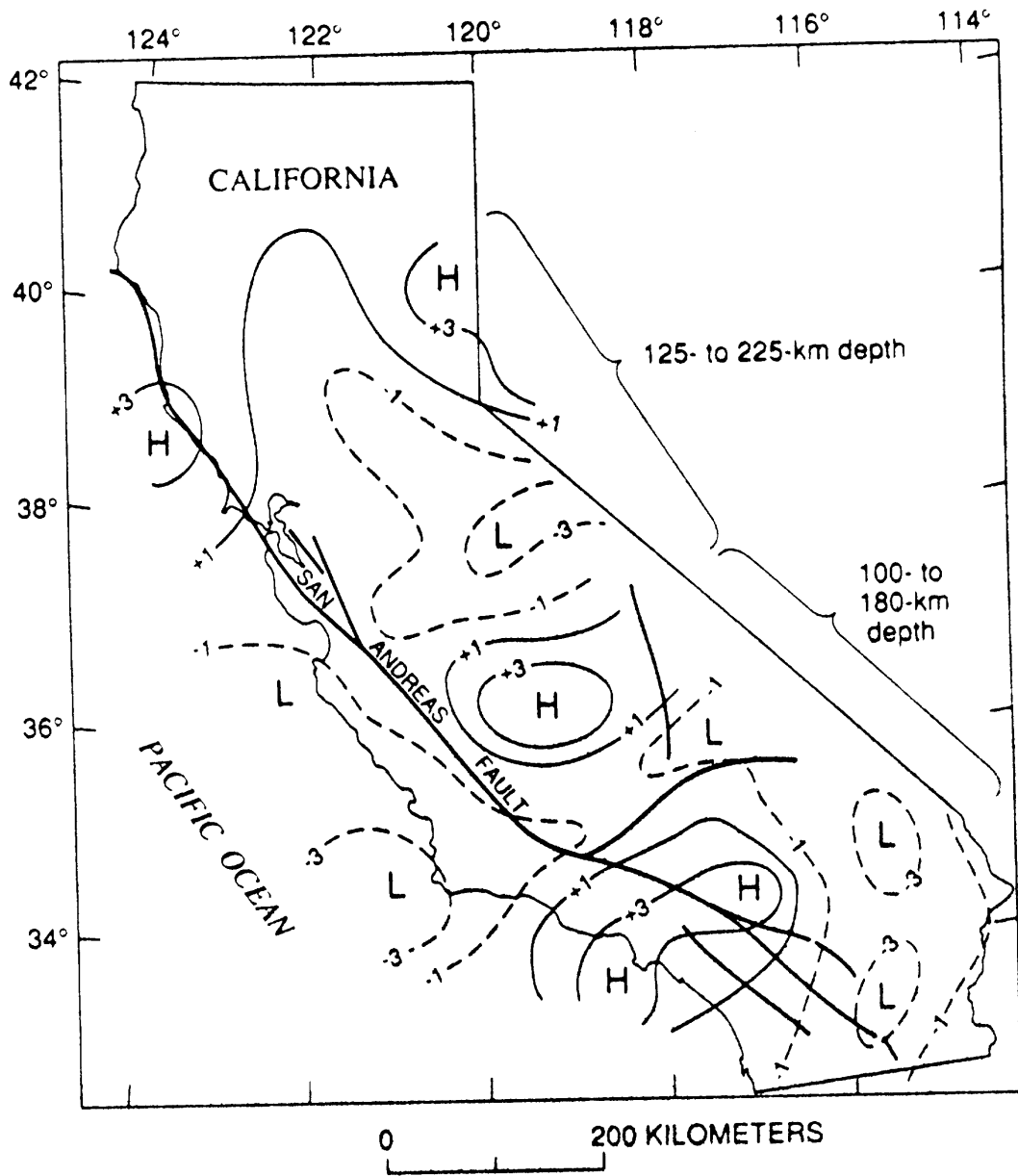
Figure 4.25: Upper mantle velocity anomalies from teleseismic delay-time data (Aki, 1982). Contours are percent deviations in velocity.

204

as the Gorda Plate dipping steeply into the upper mantle. A possible explanation for the low velocity beneath the Modoc Plateau is an asthenospheric wedge between the base of the North American lithosphere and the top of the dipping Gorda Plate, which is the source area for volcanism in the southern Cascade Range. The low-velocity beneath the Coast Ranges is probably due to the effects of the slab window (Dickinson and Snyder, 1979).

## 4.2.4 Regional Models

By calculating the velocity profiles at regular spatial intervals (in this case, every half of a degree in latitude and longitude) and compiling the results, a number of parameters that are indicative of the regional tectonics can be found. For example, low crustal and upper mantle velocities are very good indicators of high heat flow in a region (Mooney and Braile, 1979). Similarly, a shallow Moho discontinuity found under a topographically high area can indicate that the crust in the region is not in isostatic compensation and, as a result, is probably still experiencing active elevation changes. A summary of some of the results are shown in figure 4.26.

Figure 4.26a shows the near-surface velocity for the region. The color indicates the velocity (red being slow and purple being fast), which ranges from about 1.8 to 2.3 km/s. On the map, full color indicates good resolution, and faded to white indicates poor resolution. Areas that require either no uppermost layer or a relatively fast one are the large regions indicated in purple. Because this is not a well resolved parameter, it is difficult to correlate many of the features to the geology, although there are some indications that slow surface velocities are required in the center of the inversion area, most likely due to the Great Valley. In order to resolve this parameter better, higher frequency surface waves are needed. As alluded to earlier, however, there is also significant smearing of the low velocity region.

The average velocity of the crust ($\bar{V}_p$), excluding the surface sedimentary layers, is shown in figure 4.26b. The color scheme is similar to the previous one, except the velocities now range from about 5.9 km/s to 6.3 km/s. There are large variations in this parameter, particularly in the northern part of the state. Even though the phase velocity measurements in this region are well-resolved, the strong variations in this parameter may simply be an effect of a poor estimation in the layered velocity

inversion, and may not be real. In central California, there appears to be a more general progression from slow $\bar{V}_p$ at the coast to higher velocities inland. In areas of active magmatism (Cascades, Mammoth Lakes, and Ridgecrest), the average crustal velocity is slower than the surrounding regions. It has been recognized that the high heat flow from these regions can significantly lower the velocities of the lower crust (Christensen, 1979). In contrast, the southern portion of the state has little variation in this parameter, although there seems to be a curious linear feature possibly associated with the Garlock fault.

Figure 4.26c shows contours of the depth of the Mohorovičić discontinuity, which is defined as the crust-mantle boundary. In this case, the color indicates the thickness of the crust (red being shallow and purple being deep), which varies from 28 to 38 km. Again, there is a general progression from shallow (< 30 km) to deep across the tectonic structure from west to east. In the Coast Ranges, however, there is a fairly systematic bias to a thicker crust than what was found by other methods. This could be due to the tradeoff between upper mantle velocity and Moho depth, or it could be due to the long correlation length and one-sided data coverage of the region.

In addition, the slower velocities of the volcanic regions (i.e. Cascades) map into the crustal thickness. A finer sampling of phase velocities with period, instead of using a smoothed version of the dispersion curves, would go far towards separating these effects. Compared to the Fuis and Mooney [1990] estimates (> 54 km in the central Sierra Nevada), crustal thicknesses in the Sierra Nevada are too low. There is, however, mounting evidence for lack of a crustal root in the Sierra Nevada Mountains. Using regional $P_n$ and teleseismic arrival times, Jones, *et al.* [1994b] find no evidence of a large crustal root and infer a depth of 33 ± 5 km for the Moho beneath the southern High Sierra. Other interesting features in the crustal thickness map include some very thin crusts to the east, over portions of the Northern Basin and Range, and also throughout much of the Southern Basin and Range. In addition, thinner crust is observed on the coast of southern California than in northern California.

Finally, figure 4.26d shows the compressional velocity in the top portion of the upper mantle, otherwise known as $P_n$. The scale ranges from a mantle velocity of 7.82 km/s to over 8.02 km/s. Curiously, it appears that features in the mantle are still generally north-northwest striking like the surface tectonic features. Once again, however, it appears that the properties of the volcanic features are superimposed on

the other features. In this case, the Cascades, Clear Lake, and Long Valley regions all have high mantle velocities associated with them. Most other features, however, seem to be associated with the subduction of the Farallon / Juan de Fuca plate. North of the MTJ, there is a clear low velocity that starts from the Cascadia subduction zone and increases towards the Cascades. The volcanic arc generally has low mantle velocities due to partial melt in the ascending magma. This is also reflected in slow crust velocities, which are observed. The high-velocity beneath the Cascade Range is attributed to the cold slab sinking beneath the arc. The low-velocity anomaly in Central California is a relatively broad feature and may be somehow related to the remnant slab, as well. Finally, the high velocity anomaly of the Transverse Range has been interpreted as the descending lithosphere that has been postulated for the region.

The Conrad discontinuity is thought to represent either a boundary between mafic and granitic rocks in the midcrust, a rheological boundary, or a thermodynamically controlled interface (Lay and Wallace, 1995). Due to the nature of the layered velocity inversion that is performed, there will always be some mid-crustal discontinuity between the mid and lower crust, unless these layers have combined. If, however, the inversion finds either a significantly slower mid crust or a significantly faster lower crust (usually the former), then a sharper discontinuity may be required. The starting model has a 0.6 km/s velocity contrast across this boundary, but in the inversion, contrasts of up to 35% greater than this are seen. The discontinuity is defined where there is a jump in the P-wave velocity to lower crustal velocities ($> 6.50$ km/s) in the mid-crust (between about 10 and 25 km). This is not defined where there is only a single crustal layer.

Figure 4.27 shows contours of the strength of the Conrad discontinuity in the Greater Bay Area, where a large contrast is observed. The Conrad runs from northwest to southeast under the Central Coast Ranges and the western portion of the Great Valley from just north of the bay down past the Salinas Valley. The discontinuity is strongest under the South Santa Cruz Mountains, stays strong to the southwest but disappears beneath the Central Valley. The depth to the discontinuity increases from about 15 km near the coast to around 25 km under the Central Valley. Since even the existence of this discontinuity is in question, it will be interesting to see how these results compare to other studies which also find this feature. The map-
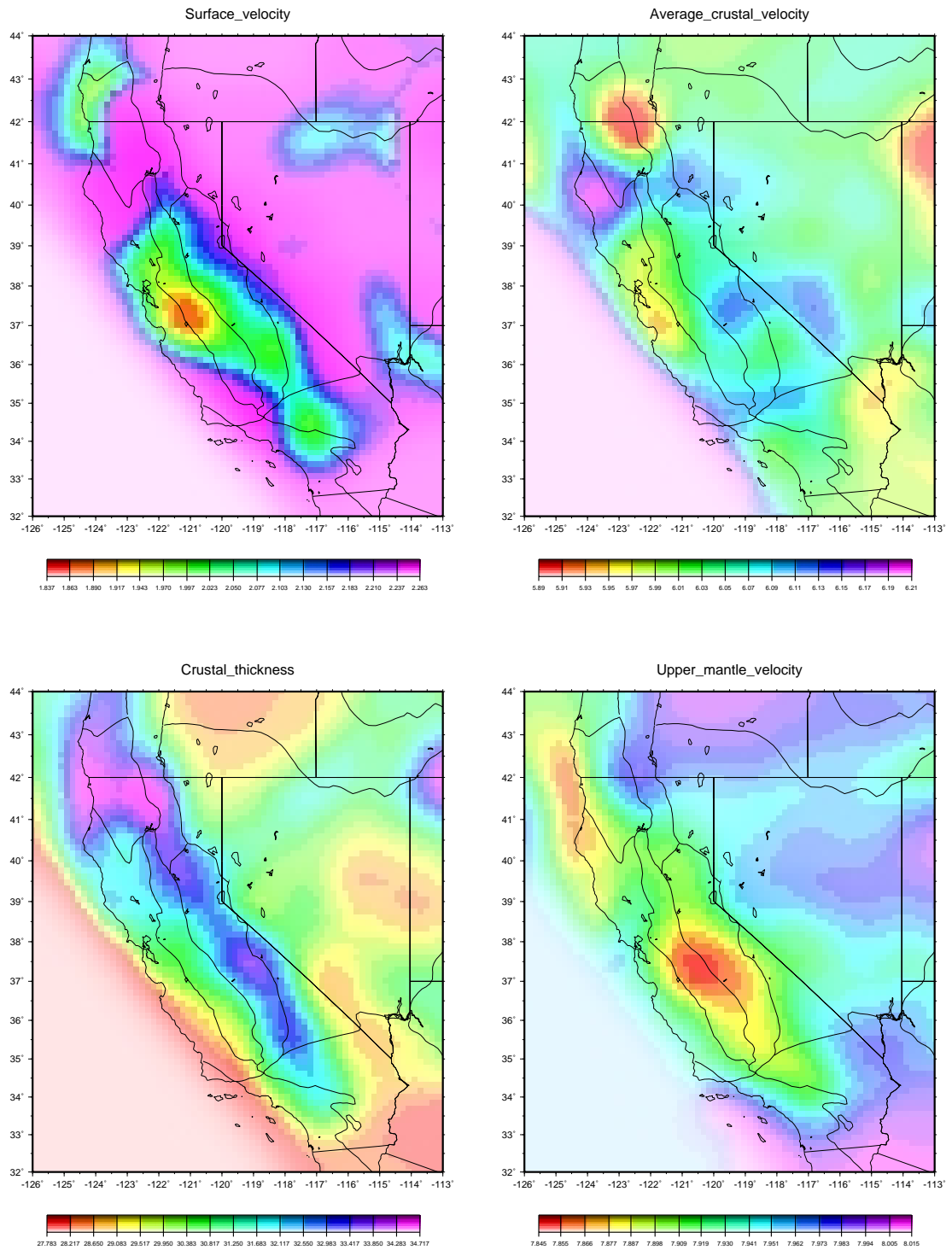
Figure 4.26: Surface velocity, average crustal velocity, depth to Mohorovičić disconti-
nuity, and upper mantle velocity, as determined from the inversion of phase velocities.
Velocities are in units of km/s, depth to Moho given in km.

ping of this boundary in the Bay Area from body-wave studies is currently underway (Dreger, personal communication).

## 4.2.5 Cross Sections

Cross-sections have been compiled for lines across several portions of California. The location of each is shown in figure 4.28. Notice that the cross-sections were taken perpendicular to the structural boundaries. Figure 4.29a shows a nearly east-west cross-section across Northern California at a latitude between 40 and 41°. This profile spans from Gorda Plate off the coast, past Cape Mendocino and the Northern Coast Range, through the southern portion of the Klamath Mountains and Cascade Range, and across the Modoc Plateau. Topography is shown in black above the profile. Cape Mendocino and Mt. Lassen are also labelled for reference. The color scale ranges from P-wave velocities of 3.6 km/s in red to 8.0 km/s in purple. Velocities greater than 8.0 km/s are marked by an additional contour line.

To first order, the depth of the crust in the profile (represented by the transition from blue to purple) reflects the average topography of the overlying crust. For example, the crust beneath the Klamath Mountains and Cascade Range is thicker than in the region off the coast or the region in the center of the profile which skirts by the northernmost portion of the Central Valley (about 240 km along profile). The Modoc Plateau, however, even with its rather high topography, still has a relatively thin crust. One significant change seems to occur about 50 km west of Cape Mendocino. In this region, one can see a large velocity contrast in the mid-crust, going from slower velocities to faster velocities moving eastward.

The Central California cross-section is shown in figure 4.29b. This cross-section runs from the Pacific Ocean, onshore into the southern Coast Ranges, across the San Andreas Fault System, through the Central Valley, across the Sierra Nevada Mountains, and into the Walker Lane Belt of the Basin and Range. Parkfield, the Great Valley, and Mt. Whitney are shown for reference. The most striking feature about this cross-section is the steady progression in the depth to the Moho from less than 20 km offshore to over 35 km under the Sierra Nevada Mountains. The thickness of the crust under the Coast Ranges is, in general, higher than other estimates, but this is probably due to the smearing caused by the one-sided nature of the data in this area. Also, the Sierran root is not a sharp feature, but is a rather broad feature

209
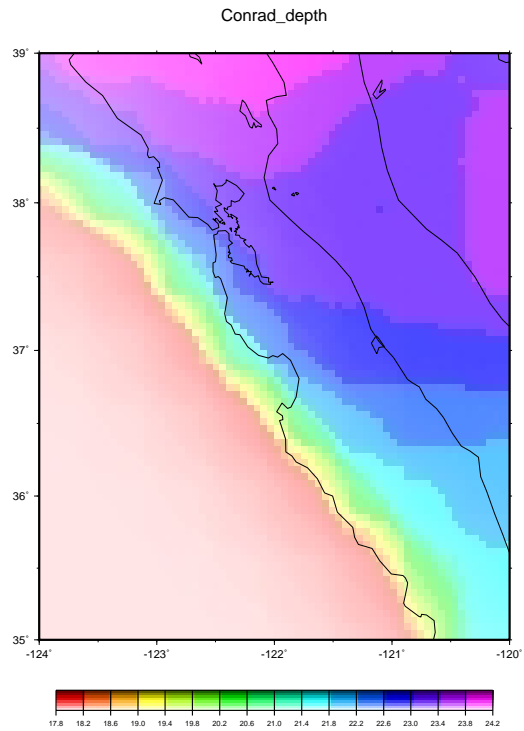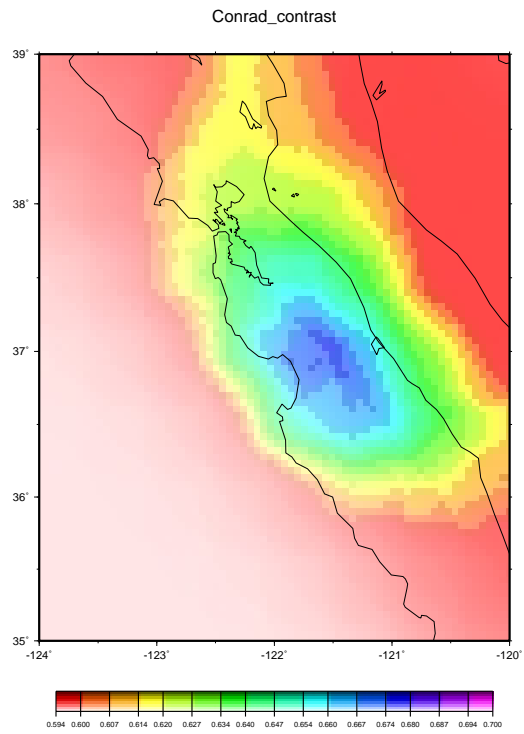
Figure 4.27: Strength and depth of the Conrad discontinuity in the Greater Bay Area, as determined from the inversion of phase velocities.

which extends over a wide area. One thing that is not seen is any large velocity contrasts at depth across the San Andreas Fault. This may either be due to the poor resolution of small-scale features, or to the inadequate coverage of the area west of the San Andreas in central California.

Finally, figure 4.29c illustrates the Southern California cross-section. This cross-section runs from the Pacific Ocean, across the California Borderlands, onshore through the Peninsular Ranges, across the Salton Trough, and into the southern Basin and Range. San Clemente Island and the Salton Trough and marked for reference. In this case, the thickest crust is seen under the western portion of the Peninsular Ranges. For a large portion of the cross-section, however, crustal thickness does not change very much. The transition from oceanic to continental crust does not occur at the coastline, but rather over a hundred kilometers west of it. Also, there are some rather complicated variations in the mid-crustal velocities along this profile. Notice the high-velocity mantle underneath the California Borderlands and the eastern portion of the cross-section.

## 4.2.6   Comparison with Other Studies

In this section, the results were compared to other velocity and crustal models of California and the Western United States, which were discussed in section 4.2.3. For simplification, some of the principal studies have been abbreviated: the compilation of Fuis and Mooney [1990] as FM, the $P_n$ study of Hearn *et al.* [1991] simply as the Hearn study, and the teleseismic study of Benz *et al.* [1992] as the Benz study. The results from this study are referred to by the phase velocity or PV study. Also, studies such as Mooney and Braile [1989] and Braile, *et al.* [1989], henceforth M&B, are compilations of numerous published studies. These studies represent more of a comprehensive and somewhat consensus view of tectonics in North America than any particular individual study, and hence are useful for comparisons. In particular, they produce maps and histograms of crustal thickness, average crustal velocity $\bar{V}_p$, and upper mantle velocity $P_n$. In an effort to relate the two data sets, similar compilations and figures were made for this study. Compare figure 4.31 to figure 4.32.

In comparison to the crustal thicknesses of the continent, California and Nevada crusts are significantly thinner than the continental average ($36.1 \pm 8.97$ km) (fig-
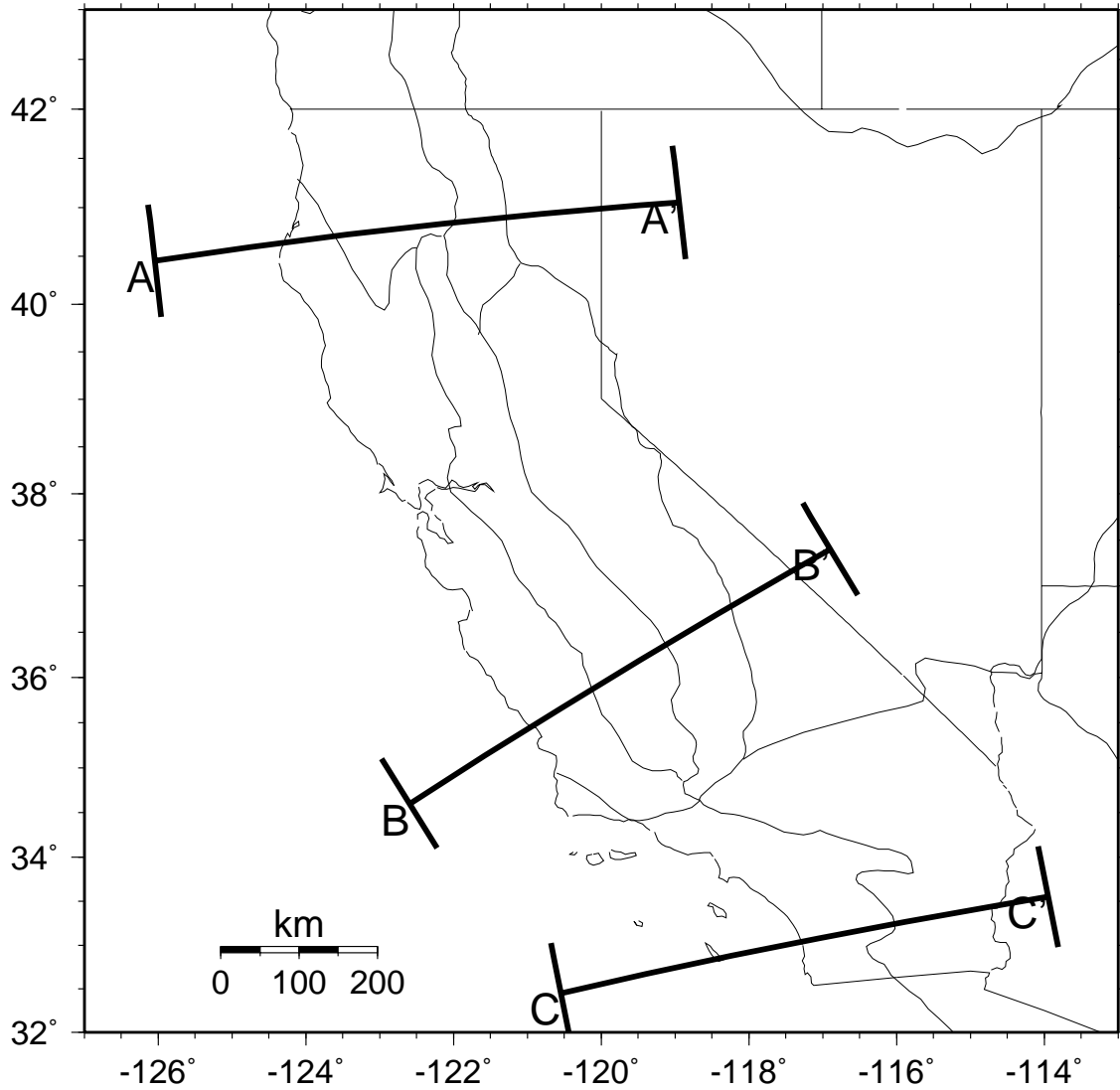
Figure 4.28: Map showing location of cross-sections across Northern, Central, and Southern California. Lines other than the coastlines and state boundaries represent tectonic boundaries.
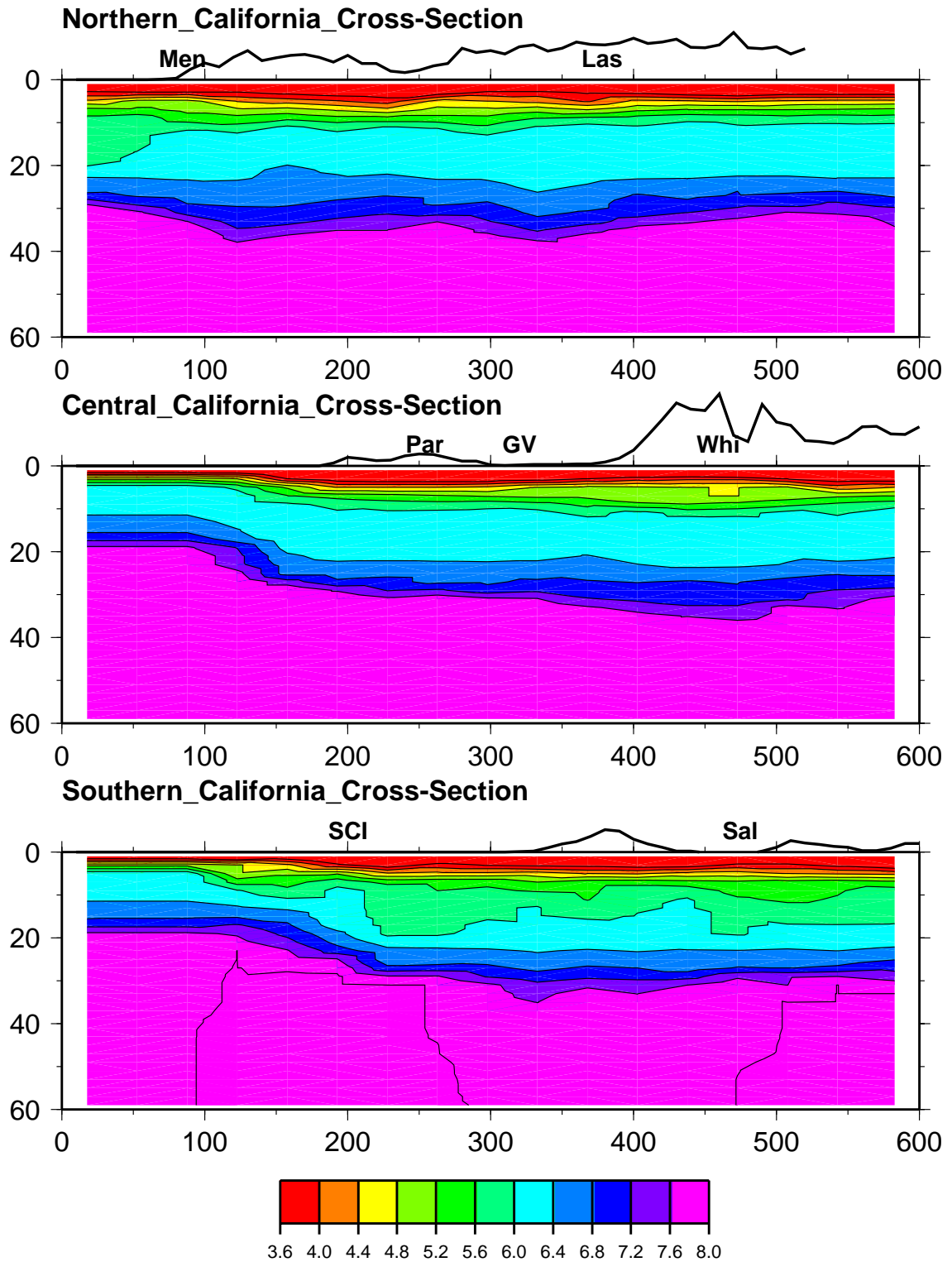
Figure 4.29: Three cross-sections across Northern, Central, and Southern California (locations are shown on previous map). The color scale ranges from velocities of unconsolidated sediments (less than 3.6 km/s) to ultramafic mantle rocks (greater than 8.0 km/s). Depth profile is exaggerated 2 times; topography 10 times.

213

ure 4.32 and 4.33). This is indicative of the recently accreted crust of the western margin region (M&B). The thickest crustal measurement in North America is outside of the area of resolution (58 km in eastern Montana), but the regions with the thickest crust determined from this study – the southern portion of the Cascade Range in California (42 km) and in the southern Idaho / northern Utah region (42 km) – are also regions of thick crust determined by M&B. The Moho depth of the Cascades is representative of the 40 – 44 km thickness of the volcanic range along its length. The thickness of southern Idaho and northern Utah is probably due to the increasing thickness of the crust approaching the Rocky Mountains. However, this region does not have many crossing paths and is not well resolved, so the data is probably smeared over a large area. The thinnest onshore crusts in this study occur along the central California coast (22 – 25 km), eastern California near Death Valley (28 km), and eastern Nevada (28 km). Seismic profiles from M&B classify all of the aforementioned regions as thin crust, although one region in coastal Oregon (north of the study area) has the distinction of the profile with the thinnest crust (18 km).

A closer comparison of the crust in California, as illustrated in figure 4.24, shows that this study and F&M share many of the same features. Both indicate the progression from thin crusts along the coast to thick crusts inland. The largest difference in this regard are that the phase velocity study indicates thinner crust in the Sierra (36 km instead of 54 km), but thicker crusts in the Cascade Range (up to 44 km instead of 38 km). Also, the thickness of the crust along the California coast is not as given by F&M, which are generally around 25 km thick. The results with respect to crustal thickness were also compared to the Hearn study. The two studies are very similar: thick but uncompensated crust in the Sierra Nevada (40 – 43 km), thin crust under the California coast (30 – 33 km), thicker crust (40 – 50 km) underlying the Rocky Mountains and Colorado Plateau, and Moho depths throughout the Basin and Range that do not depart significantly from 30 km.

Before examining average crustal velocities, it is useful to review the relationship between seismic velocity and rock types. Figure 4.30, taken from Christensen [1965] illustrates the general association between these two parameters for crystalline rocks at 5 km or greater depths. Below about 6.4 km/s, the crystalline rocks are classified as felsic, meaning that they are poor in iron and magnesium and typically contain abundant felspars (the "fels" in felsic) and quartz. An example of felsic rock is

granite. Greater than about 7.0 km/s, rocks are considered mafic. These rocks are rich in magnesium and iron (the "ma" and "f" in mafic) and contain pyroxene, amphibole, and olivine. A typical mafic rock is gabbro. Rocks falling between the felsic and mafic classifications are generally referred to as intermediate rocks. Beyond about 7.6 km/s, rocks are usually classified as ultramafic and represent rocks typical of mantle materials. Peridotite is an example of ultramafic material.

An examination of the compiled results for the crust shows that most of the region has average crustal velocities which are lower than the mean continental values (6.44 ± 0.24 km/s) (figure 4.32 and 4.33). In general, the eastern United States has faster crustal velocities ($V_p > 6.5$ km/s) than the western United States. Since, as indicated above, low $V_p$ values suggest a dominantly felsic crust and high $V_p$ values suggest a dominantly mafic crust, the results denote that the crust of the western United States is primarily felsic in character, which is consistent with the accreted and extended nature of the western crust. Average crustal velocity values from this study, however, are even lower than the western United States values from M&B ($V_p$ between 6.2 and 6.6 km/s). Since average crustal values are generally taken by stripping away surface sediments, a discrepancy might arise from different definitions of what constitutes hard rock. In any case, the relative values for average crustal velocity in each individual model is consistent.

In addition to rock composition, average crustal velocities can also be significantly affected by temperature. High heat flow can lower the average velocity of the crust by 0.05 - 0.2 km/s (Christensen, 1979). Extreme values of average crustal velocity occur in eastern Nevada / western Utah (5.85 km/s), and in the Cascades (5.83 km/s). In both of these regions, high heat flow is probably the significant contributor. On the other hand, the highest average crustal velocities that are observed occur near Cape Mendocino (6.39 km/s). Since this area is generally considered to have high heat flow (at least south of the MTJ), this anomaly cannot be explained by temperature effects. This might indicate that a significant portion of the crust in this region is mafic.

Using information from crustal delays, the Hearn $P_n$ study has data which could provide measurements of the average velocity of the crust. However, much in the same way that the layered velocity inversion has a tradeoff between crustal thickness and upper mantle velocity, the $P_n$ tomography has a tradeoff in the crustal delays between

215
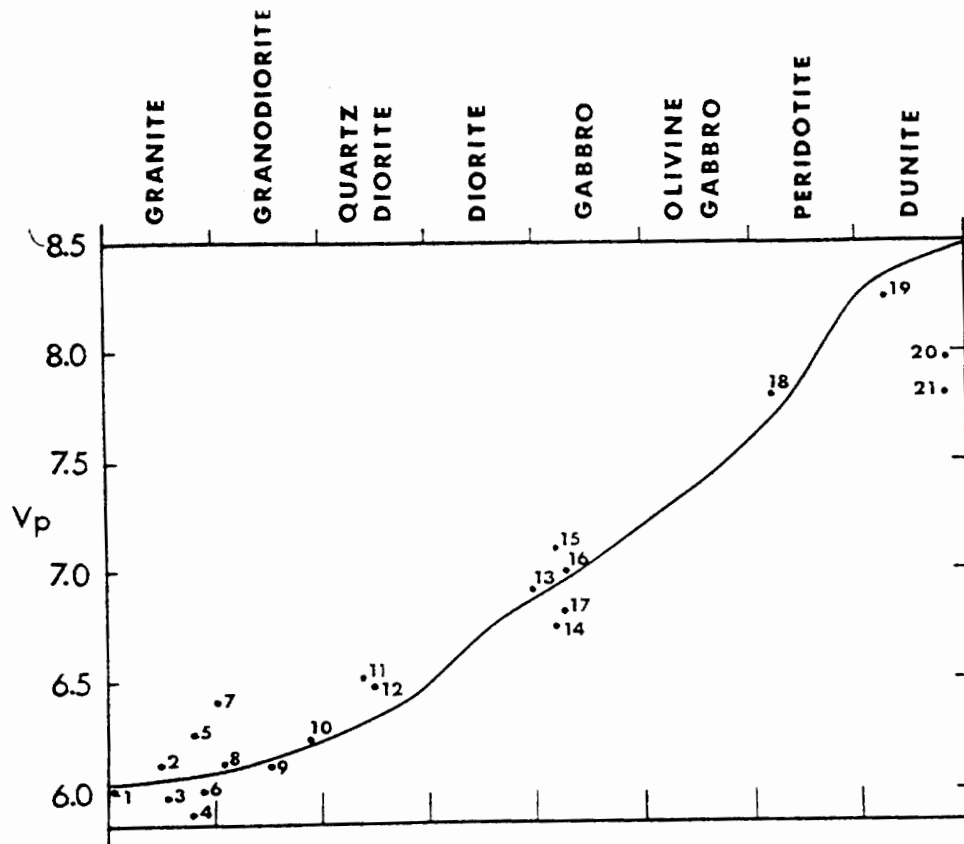
Figure 4.30: Relationship between compressional wave seismic velocity and crustal and upper mantle rock types (ranging from granite to dunite) at 5 km or greater depths (from Christensen, 1965).

crustal thickness and average crustal velocity. Positive crustal delays could be caused by either a thicker crust or a slower average velocity, while negative crustal delays could be caused by either a thinner crust or faster average velocity. A simplification is made that all variation is due to changes in the Moho depth, and an average crustal velocity of 6.3 km/s is assumed.

Average crustal velocities derived from the phase velocity study had many features in common with those from the Benz study obtained using teleseismic P-wave travel time residuals. Unfortunately, this study was limited to only northern California, running from the Bay Area to Lake Tahoe in the south to the California border in the north. In comparing the results, it is also important to note the huge difference in scale between the two studies. The average model block size is about 6 km and many of the strong velocity perturbations are less than 20 km. They find anomalies on the order of $\pm$ 10% in P-wave velocity, as compared to anomalies of only about half of that from the PV study. However, even with many of the differences in the parameterization of the model in the two studies, there are a still a few aspects in common. Similar to the phase velocity study, they found localized regions of slow velocity in the crust that were attributable to active magmatism, usually associated with high heat flow. Beneath Cape Mendocino, where there is a large positive velocity anomaly in the phase velocity study, they find both slow velocity north of the MTJ and fast velocity south of the MTJ.

Finally, upper mantle velocity is compared. Keep in mind that this parameter may not be very well resolved by the tomography. M&B find mean continental values of $8.02 \pm 0.21$ km/s (figure 4.32 and 4.33), making this parameter very robust over large geographic areas. Large deviations can be due to mantle composition, temperature, and seismic anisotropy of olivine (M&B). The main feature shown in this compilation is a very broad change across most of the study area from fast mantle velocities to the west and off-shore ($> 8.0$ km/s) to very slow mantle velocities ($< 7.8$ km/s), with the the slowest mantle velocity in the United States occurring under the eastern Basin and Range.

This general progression from the Pacific Coast to the Basin and Range is not seen in the phase velocity inversion. The fastest upper mantle velocity occurs in northern Mexico and the southernmost portion of California (8.13 km/s), and the slowest velocities occur along the coast near the Oregon-California border (7.77 km/s) and

in the central portion of the Great Valley (7.81 km/s). Fast mantle velocities to the south are probably due to the extension of the spreading ridge in Baja California and the Salton Sea. It is unclear, however, why slow velocities are found in the aforementioned regions. Perhaps it is more easily explained by a north-south trending band of slow velocities, which is broken in the central portion by the faster mantle velocities near the Clear Lake / Geysers volcanism. The band may be related to flow in the upper mantle. Zandt and Carrigan [1993] have suggested that the slab window may produce instabilities in the mantle. Small-scale convection consisting of the sinking of cool (and fast) mantle and an upward counterflow of warm (and slow) mantle would develop. Sinking would be limited to a few unstable regions, but counterflow should exist over a large area.

These features share a remarkable resemblance to the upper mantle velocity from the Hearn study, at least in the well-resolved portion of the study area. Although the Great Basin mantle velocities estimated from this study generally have slightly higher velocities than those determined by Hearn, the low $P_n$ velocities under the Sierra Nevada and the Central Valley are consistent with the slow upper mantle velocities that are determined for central California in this inversion. If the mountain root for the Sierra Nevada exists, then the upper mantle velocity determined from the Hearn study ($P_n = 7.6$ km/s) is thought to be an underestimate because of regional $P_n$ waves tunneling through the root. Unfortunately, regions like the Snake River Plain (low $P_n$ velocity), the Rockies (high $P_n$ velocity), and the Colorado Plateau (also high $P_n$ velocity) are not well covered by the surface wave measurements.

However, only a few of the features are consistent between the Aki [1982] compilation and this study. For example, both studies found slow velocities in Central California east of the Bay Area and near Long Valley Caldera, and fast velocities in the southern portion of the Great Valley. But, while the teleseismic study found generally lower velocities along the coast and in the northern portion of the Central Valley, the phase velocity tomography produced high velocities in these regions. One likely explanation for the large discrepancy in velocities is the depth of the mantle that is being sampled in each case. Both $P_n$ and the phase velocity studies are primarily sampling the uppermost region of the mantle, just below the crust, which for much of the study area is around 30 km. In contrast, the teleseismic delay-time data that is summarized by Aki is sampling around $100 - 200$ km depth mantle. If

there is no radial variation in these velocity anomalies, then this differential sampling should not matter. However, in the case of dipping mantle structure, which might be expected in the vicinity of active and recent subduction, it is easy to envision how discrepancies could arise. The result would be a lateral shift in the location of the velocity anomalies that are associated with the subducting slab.

In general, the phase velocity study seemed to have more in common with the mantle features from the Benz teleseismic study for northern California. The most prominent features that they found in the mantle were NNW-SSE striking bands of high, low, and high velocity from the coast landward. As in the scale differences between the two studies mentioned for the crust, the anomalies in the PV study are only about half of the amplitude of anomalies found in the Benz study. The anomalies are particularly strongest in the uppermost portion of the mantle (30 − 70 km depth). These bands continue across the MTJ and the across the edge of the subducting Gorda Plate. This is similar to some of the mantle features observed from the phase velocity measurements. Not only is there the similar high, low, high velocity feature, but these bands also continue across the boundary of the subduction zone. There is, however, a slight shift westward of these bands in the phase velocities, as compared to the teleseismic results. In addition, in the PV study, the bands are interrupted by high mantle velocity in the vicinity of Clear Lake.

### 4.2.7   Interpretation and Discussion of Results

In this section, the results are summarized by tectonic provinces and are extensively compared to other results to note the similarities and major differences between them. North of Cape Mendocino, the tectonic framework of the Pacific Coastal States changes from the strike-slip regime of the San Andreas fault system to subduction of the Juan de Fuca plate beneath North America (Mooney and Weaver, 1989). It is convenient to group the geologic provinces in this area into three general areas: fore arc, volcanic arc, and back arc. The fore arc consists of the Klamath Mountains, the Coast Ranges of Oregon and Washington, the Olympic Mountains, and the Williamette Lowland- Puget Sound Basin. The volcanic arc includes the North Cascades of Washington, where little late Cenozoic volcanism has occurred, and the long, linear portion of the Cascade Range to the south, where late Cenozoic volcanism is more extensive. The back arc consists of diverse geologic terrains, to the south,
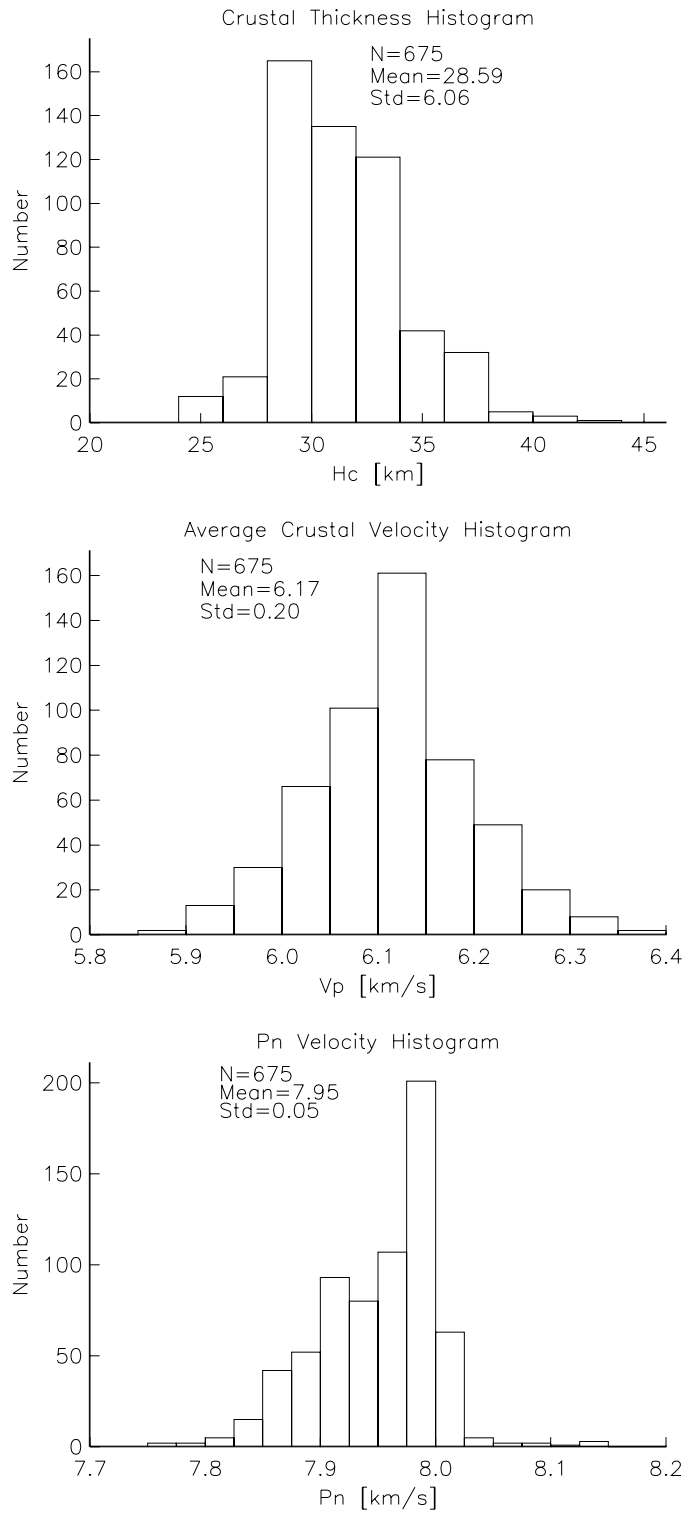
Figure 4.31: Crustal thickness (top), average crustal velocity (center), and $P_n$ velocity (bottom) histograms from this study.

**A**

**CRUSTAL THICKNESS HISTOGRAM**

N=337
MEAN=36.1
STD=8.97

NUMBER

Hc (km)

**B**  **AVERAGE CRUSTAL VELOCITY HISTOGRAM**

N=255
MEAN=6.44
STD=0.24

NUMBER

$\overline{V}p$ (km/s)

**C**  **Pn VELOCITY HISTOGRAM**

N=320
MEAN=8.02
STD=0.21

NUMBER

Pn (km/s)
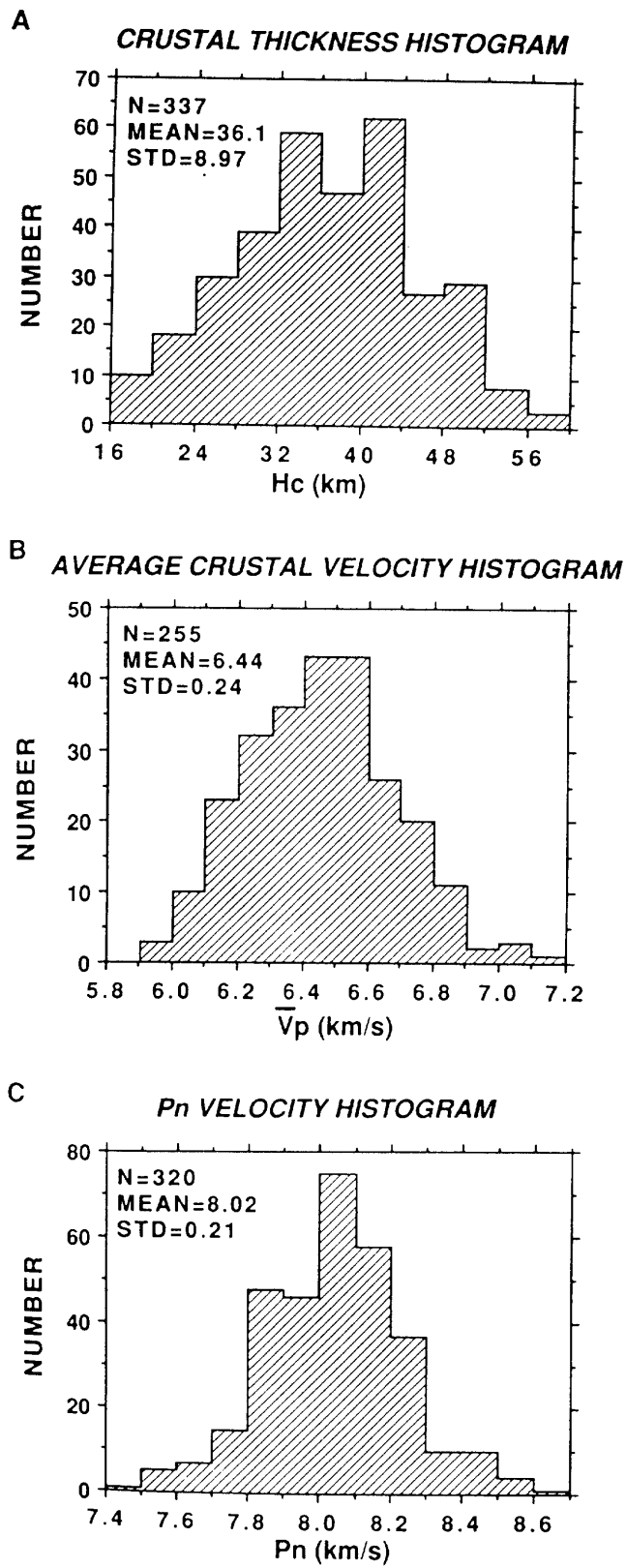
Figure 4.32: Crustal thickness (top), average crustal velocity (center), and $P_n$ velocity (bottom) histograms from Mooney and Braile.

221
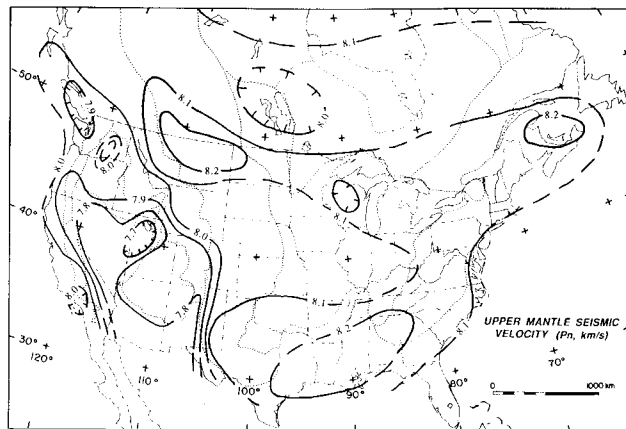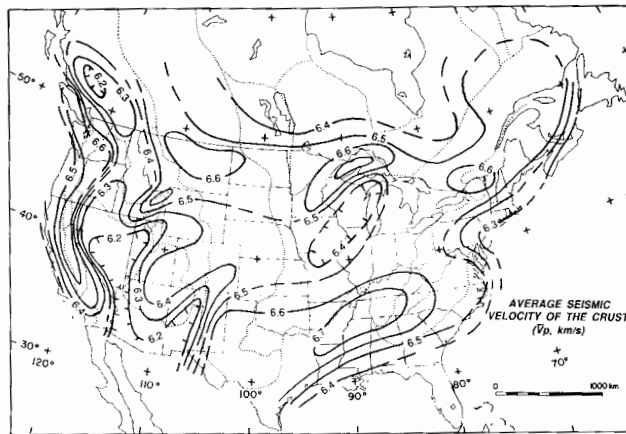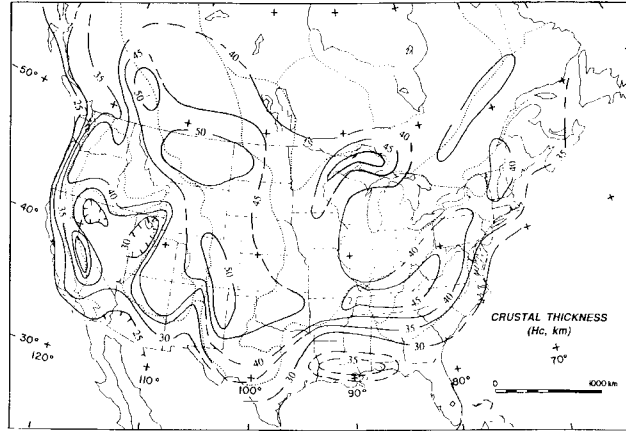
Figure 4.33: Crustal thickness (top), average crustal velocity (center) and upper mantle velocity (bottom) maps from Mooney and Braile.

the Modoc Plateau and the High Lava Plains, and to the north the Blue Mountains, Columbia Plateau, and the Okanogan Highlands.

In Northern California, the Klamath Mts. fore arc is characterized by a varied surface velocity. The generally fast crustal velocities are consistent with the mafic accretionary oceanic material which comprises much of the fore arc. Some slower crustal velocities are observed in the southeast portion of this region. Crustal thicknesses typically increase from the coast to the inland regions, as shown in the Northern California cross-section (figure 4.29a), and the maximum thickness can be rather large (up to 38 km). Although there is the common trait of eastward thickening crust, the crust estimated from F&M is found to be significantly thinner, ranging from 16 – 35 km. Mantle velocities in the region are quite slow, a characteristic that has been attributed to the mantle wedge above the sinking slab.

In the Cascade volcanic arc, surface velocities are faster than in the fore arc and the uppermost layer in the layered inversions is often pinched out. The velocity of the crust, particularly at the southern end, is very slow. The Moho discontinuity is as deep or deeper than to the west, but the mantle velocities are generally faster. At the suture between the Klamath Mts. and the Modoc Plateau, the Cascades have been interpreted as an opportunistic location for the ascent of magma. Moving eastward into the back arc, the Modoc Plateau is characterized by a fast surface velocity and average crustal velocity. Flood basalts at the surface have seismic velocities of 4.5 – 5.2 km/s and an average thickness of 4.5 km (Fuis, *et al.*, 1986). Crustal thicknesses run about 35 km or so under the flood basalts of the plateau, but thin to around 30 km east into the northern portion of the Great Basin. This general progression of velocity anomalies in the upper mantle across the whole subduction arc is also persistent in the Benz study, although the crustal velocities, not well resolved in either study, are rather different.

Because of its unique geometry, the tectonics near the Mendocino Triple Junction can be dramatically different than the surrounding regions. The migrating triple junction produces what is known as the slab window (Dickinson and Snyder, 1979). South of the MTJ, the North American plate no longer abuts the Gorda plate, but instead, is in direct contact with upwelling asthenosphere. One curious observation in the inversion is the striking difference in average crustal velocity seen between the MTJ and its vicinity. However, this anomaly seems to be a unique feature of the

phase velocity inversion. This would also seem to be in stark contrast with the high heat flow, which would tend to lower the average velocity of the crust. In comparison, Benz, *et al.* [1992] see rather small (20 km radius), but high (± 10%) negative and positive velocity contrasts just north and south of Cape Mendocino.

Perhaps this observation can be explained by the unusually thin lithosphere (< 30 km and as thin as 20 km) created by the slab window, probably the thinnest lithosphere in California and North America (Zandt and Furlong, 1982). Since the crustal thicknesses determined from the layered inversions in this region are around 32 km, mantle material is obviously being included in the calculations of the average crustal velocity. If the high velocity lower layer is excluded from the calculation (see figure 4.23a for a reference example), then the average crustal velocity will obviously drop. In any case, it will be interesting to see if this situation persists in future inversions, when coverage in the area will be improved. Otherwise, the MTJ shares the same features (fast surface velocities, moderate crustal thicknesses, and fast upper mantle velocities) as the neighboring areas.

South of Cape Mendocino, central and northern California consists of four basic geologic provinces: the Coast Ranges, Great Valley, Sierra Nevada, and westernmost Basin and Range (Mooney and Weaver, 1989). The Coast Ranges consist of broad belts of marine metasedimentary rocks (the Franciscan assemblage and Great Valley sequence), a large plutonic terrain of dominantly granitic composition (Salinian block), and Tertiary sedimentary and volcanic rocks. The Great Valley of California is a 700-km-long by 100-km-wide sedimentary basin situated between the granitic and metamorphic terrane of the Sierra Nevada and the Coast Ranges. The Sierra Nevada is a 600-km-long by 100-km-wide batholith that was emplaced over a period of nearly 100 m.y., from approximately 180 to 80 Ma. The western Basin and Range province of southeastern California occupies the triangular region east of the Sierra Nevada escarpment and north of the Mojave Desert block, as marked by the easterly extension of the Garlock fault.

The California Coast Ranges are characterized by large variations in many of the estimated model parameters. The surface velocity varies from fast velocities in the north to slower velocities in the center and back to faster velocities in the south. The slow velocities around the San Francisco Bay are likely due to the concentration of sedimentary basins (Santa Clara, Santa Rosa, Livermore, and Salinas) around the

224

bay, as well as from the bay itself. Average crustal velocities also follow the same fast/slow/fast progression with the northernmost portion of the Coast Ranges having the higher average velocity in the inversion. Crustal thicknesses increase from thin crusts along the coast to thicker crusts west towards the Central Valley (also seen in F&M). Another progression exists from thicker crusts in the north to thinner crusts in the south. In this case, F&M see the opposite trend. There is also considerable variation in mantle velocity. Slow mantle velocities are found in the north and east Coast Ranges, while faster mantle is observed in the west and in the central Coast Ranges. In both the PV and Benz studies, this feature persists across both the subduction and transform regimes.

There has been an ongoing debate over the evolution and current state of the Franciscan assemblage, the Salinian block, and subducted Farallon plate. Using data from the Bay Area Seismic Imaging eXperiment (BASIX), Brocher, *et al.* [1994] present seismic evidence for a lower-crustal detachment beneath San Francisco Bay and propose that this reflector marks the base of the Franciscan assemblage. Interpretations of the detachment include the belief that the high-velocity lower crustal rocks that underlie the bay represent magmatic underplating associated with the passage of the triple junction. There is also the hypothesis that the mafic layer is a slab of oceanic crust, either Pacific plate or captured Farallon plate. Jones, *et al.* [1994a] suggest that the reflector is a decollement surface that is effectively the plate boundary. The major faults in the area, such as the San Andreas, Hayward, and Calaveras Faults, are wedge boundaries that splay from the decollement. In these scenarios, one might expect to find a velocity contrast across the fault in the upper crust, but no such contrast should exist at depth.

More recently, Holbrook, *et al.* [1996] offer interpretations of the crustal structure of the San Francisco Bay Area block and the offshore continental margin. In their preferred interpretation, the Pacific Plate oceanic crust underlies the margin only as far as the Farallon Ridge and does not extend beneath the Salinian block. However, they cannot completely rule out a model where the Pacific / Farallon oceanic crust forms the lower crust beneath the entire margin. In this case, the velocity contrast across the San Andreas should continue at depth. One of the major benefits of the PV study is the ability to find and map the depth extent of this discontinuity. The cross-section from Central California (figure 4.29b), which is taken from south of the Bay

Area, illustrates that at least as seen from the inversion, the San Andreas Fault does not represent a significant discontinuity in the crust or the mantle. These findings would tend to support the first theory, although this argument would be stronger if the inversion produced a larger velocity contrast in the shallow crust. Of course, the correlation length used in the inversion is large relative to the features that one might expect to find, so this result may not be too significant.

Surface velocities in the Great Valley are slower relative to the Coast Ranges, which is what is expected from the large sediment load of the region. Overall, the crust has average velocity properties, indicating a relatively uniform structure of the crust along most of its length. Although there are clearly some indications from the surface wave dispersion that slow near-surface velocities are required in the Central Valley, the specifics of this feature is not well resolved from this study. F&M found that the seismic velocities in the sedimentary section of the area range from 1.6 to 4.1 km/s, with the slowest velocities ($< 2.0$ km/s) near the surface. The PV study found that the slowest near-surface velocities in the inversion ($\sim 1.8$ km/s) are in the Central Valley, and fall within this range. These are somewhat encouraging findings in the recovery of the broad features in the region.

Although it is well known that rocks of the Great Valley Sequence underlie the valley in the upper crust, much of the crust below this sequence is not well determined. Results from the inversion indicate that there are no significant velocity contrasts in the lower crust of the tectonic province. Generally, the crustal thicknesses are similar to the thickness in the eastern portion of the Coast Ranges. Upper mantle velocities determined from the inversion vary considerably along the axis of the valley, although this is currently not explained. Velocities in the central portion of the valley, east of the Delta, are some of the slowest in the inversion.

The Sierra Nevada Mountains rise from the Great Valley to the east. In the north, at the base of the range lies the Foothills Belt, a region of highly metamorphosed sedimentary and volcanic rocks. To the south, the transition from the Great Valley to the Sierra Nevadas is much more abrupt. The inversion suggests that surface velocities in this region remain rather low, but as this is not observed, it probably represents smearing from the Central Valley. Although the granitic rocks near the surface and in the upper crust are relatively fast, in the mid and lower crust, the same rocks from the batholith are generally slower than surrounding rocks. In any case, the

overall crustal velocity is about average to slightly higher than average. As previously mentioned, the crustal thicknesses in the Sierra Nevada Mountains determined from the inversion (maximum of 36 km) are much lower than some previous estimates, but are more in line with recent studies of the crustal root (Jones, *et al.*, 1994b). F&M suggest that the crustal root in the region is substantial ($> 54$ km), but the Hearn study also found a shallow root ($\sim 40$ km). For the most part, slow upper mantle velocities are observed under the Sierra Nevada. This is consistent with $P_n$ observations from the Hearn study, but inconsistent with M&B summary figures.

Moving inland to the Walker Lane Belt of the Basin and Range Province, and beginning with the Owens Valley, the topography starts to take on the typical horst-and-graben trait of extended continental crust. Crustal thicknesses vary from high near the Sierra Nevada to lower inland, especially under Death Valley and southern Nevada. Surface velocities in this region mainly run high, and average crustal velocities somewhat mimic the crustal thickness. The velocities are highest where the crust is thinnest. Mantle velocities from the inversion are generally average to high, which is in stark contrast to other studies which predict low mantle velocities in this region. Taylor and Patton [1986] found the thinnest crusts ($\sim 25$ km) at the outer edges of the Basin and Range. F&M, in particular, also share the rapid thinning of the crust from the Sierra high to the eastern California low in this area. Moving across the same area, the Hearn study found an increase in the $P_n$ velocity from 7.6 km/s in the Sierra Nevada to greater than 7.8 km/s in the province interior.

Southern California is divided into four geological provinces (Mooney and Weaver, 1989). West of the San Andreas fault, the California Borderland and coastal province form a composite province consisting of the continental margin, Peninsular Range batholith, Los Angeles and Ventura basins, and Western Transverse Ranges. The Mojave Desert east of the San Andreas fault is the interior province. Separating the coastal and interior provinces are the Central and Eastern Transverse Ranges, which obliquely cross the generally northwest-southeast-trending tectonic features of southern California. The fourth province is the Salton Trough, a modern crustal pull-apart associated with the opening of the Gulf of California.

The Coastal Province, which encompasses a wide range of faulting and tectonic styles, mainly has fast surface velocities. The western portion of the province near the Los Angeles Basin is an exception, but not the Ventura Basin which has poorer

coverage. Crustal velocities run from slightly higher than average near the continental shelf to slightly lower than average further east. Moho depth starts to increase near the western edge of the province, a point illustrated in the Southern California cross-section (figure 4.29c). Finally, the velocity in the upper mantle also varies across the province, from very fast to the south and west to more average velocities to the north and east. $P_n$ measurements indicate the same trend of decreasing northeast velocities (Hearn study).

The Central and Eastern Transverse Ranges are located to the northeast. The velocity at the surface is high in the western portion of the province, but decreases heading to the east. Crust measurements made throughout the Transverse Ranges show average seismic velocities. The crustal thickness does not change from the gradual thickening of the crust that is observed to the north and south. It appears that the Transverse Ranges have little or no crustal root. The upper mantle has a fast velocity which is fairly constant throughout the region, with slightly slower velocities to the northeast. The Hearn study also records this continuing trend of decreasing upper mantle velocities. Humphreys, et al., [1994] infer that there is subducting lithosphere below the Transverse Ranges that extends downward as far as 250 km, and which causes a 3% velocity increase in the mantle.

The Salton Trough, lying very far to the south, is not well covered by the inversion, although this can be remedied in the future by the addition of a few earthquakes from the Gulf of California. In general, however, the region has a fast surface velocity, slow overall crustal velocity, a thinned crust and high mantle velocity, particularly in the south. Lastly, to the east lies the Mojave Desert. The crustal parameters in the Mojave block vary from its eastern boundary to its western boundary with the Transverse Ranges and Tehachapi Mountains. The western portion is characterized by a slow surface velocity, fast crustal velocity, thick crust, and slow mantle. The eastern portion, in contrast, has a fast surface velocity, slow overall crust, thin extended crust, and faster than average mantle velocities.

The Basin and Range province, a unique region of broad continental rifting, is characterized by extension fault-block mountains and deep, sediment-filled basins (Thompson, et al., 1989). In Nevada and Utah, the province lies between the uplifted, comparatively unbroken blocks of the Sierra Nevada on the west and the Colorado Plateau on the east. To the south, in Arizona and New Mexico, the province sweeps

around the Colorado Plateau to join the Rio Grande rift. The high elevations of the bounding regions (the Sierras and Colorado Plateau) are characteristic of rift margins worldwide.

As vast as the Basin and Range province is, there are many features which extend throughout the region. Except for the easternmost portion of the area, velocities in the crust are typically average and vary only over long distances. Surface velocities are high everywhere in the Great Basin. Crustal thicknesses do fluctuate, but mainly are quite thin, especially in the west from the Modoc Plateau down to the southern portion of the Walker Lane Belt, and also in central-eastern Nevada and central-western Utah. Most of the general results summarized above for the Walker Lane Belt apply here. Taylor and Patton [1986] found thicker crusts in the center of the province than on the edges. The Hearn $P_n$ study generally finds a contrast between the crusts in the northern and southern portions of the Basin and Range and estimated that the delay trends indicated a crustal thickening by almost 5 km from northern to southern Nevada. As in the Walker Lane Belt, mantle velocities predicted from the inversion disagree with some estimates from other studies. $P_n$ velocities from other studies generally range from $7.7 - 7.8$ km/s.

In summary, although there can be rather large differences about many of the details of the crust and upper mantle structure of the western United States, overall there is generally a consensus among studies which used vastly different techniques. For example, in different studies, crustal thickness has been variously determined by the two-way travel time to a crustal reflector, crustal station delays from $P_n$, and changes in phase velocity with period, yet all the studies remarkably lead to nearly the same answer. Most of these same gross features are derived in this study using phase velocity tomography, although there can be dissimilarities in the details of the various models. In addition, by applying this technique and using the full capabilities of the data, a broad and detailed model is developed which can start to answer some questions that can only be addressed with a comprehensive three-dimensional model (such as mid-crustal discontinuities or structure of volcanic regions).

# Chapter 5

# Summary

This chapter provides a synopsis of the methodologies and the results, and discusses future work that could be done to improve and expand the results demonstrated in this dissertation.

## 5.1 Conclusions

It is clear that the regional surface wave moment tensor method is an effective way to quickly and reliably determine moment tensors for moderate to large regional events. As outlined, it is a relatively straightforward procedure which is easy to implement. In fact, once the velocity model has been accurately calibrated, the method easily lends itself to automation. Moment tensor solutions determined using the method have been compiled. The large number of moment tensors calculated in active regions or in aftershock sequences provides a powerful tool for seismotectonic and earthquake studies.

Many of the results are not new findings, but merely confirmations of an increasing body of knowledge of the state of stress in the crust of California and vicinity. Movement along the major transform segments in the regions (San Andreas Fault System, Mendocino Fault, etc.) are primarily right-lateral strike-slip. North of the Mendocino Triple Junction, the divergent margin near the Gorda Ridge produces normal earthquakes, while the compressed Gorda Plate near the convergent margin produces both thrust and strike-slip earthquakes. South of the Triple Junction, in addition to the transform motion, there is also a transpressive component to motion along the San Andreas System, exemplified by Coalinga thrust and Loma Prieta

231

oblique-thrust earthquakes. In Southern California, large scale compression occurs in a north-south direction producing mountain-building in the Transverse Ranges. Inland, the Basin and Range province produces primarily normal earthquakes, which are responsible for the horst and graben topography. Within the Walker Lane Belt, however, the divergent motion is accompanied by a change in reverse direction, as well as a significant portion of strike-slip motion.

The phase velocity tomography and subsequent dispersion curve inversion allow a thorough study of the present state of the crust and upper mantle in California and vicinity. From the inversion of the phase velocity tomography results, one can ascertain such fundamental parameters as average crustal velocity, crustal thickness, and upper mantle velocity. Although there are a few discrepant observations between this and other studies (i.e. mantle velocity in the Basin and Range), for the most part the findings obtained using this technique are consistent with other studies, and can add distinctly different constraints on the overall problem. Some major results include the possibility of the subducting slab at depth beneath Northern California. There is also evidence of a slab window near the Mendocino Triple Junction. Other interesting features seen in this study which have been supported by others include no velocity contrast across the San Andreas Fault at depth, and the lack of a crustal root under the Sierra Nevada Mountains. In addition, there is some indication of a crustal detachment in the Coast Ranges, but stronger evidence for this will have to come from methods more sensitive to layer boundaries.

In its current incarnation, this technique will simply improve with the inclusion of data both from new broadband stations (which continue to be installed), as well as from earthquakes occurring in new and favorable locations. For example, an earthquake occurring either on the coast or offshore from the southern portion of the Coast Ranges would vastly improve the resolution of that area. Even the resolution of moderately well covered areas will be incrementally improved by the addition of more crossing paths. As more accurate models are developed from these inversions, the results can be used to address and contribute to specific regional problems, such as velocity contrasts associated with structural features along major faults, mid-crustal discontinuities, the existence of mountain roots, and velocity variations in the upper mantle. Furthermore, the phase velocities can be used to produce an accurate estimation of the velocity structure along source-receiver paths for use in the regional

moment tensor inversions.

## 5.2   Future Work

Clearly, one would like to improve the results of the methodology by expanding the phase velocity measurements to a wider range of periods. Moving to short periods is particularly important, as it will allow a significant increase in resolution of the uppermost part of the crust, which is particularly important for modelling small earthquake sources. Similarly, expanding to longer periods will increase resolution of the upper mantle velocity over the western United States. In both cases, however, one must proceed with caution in obtaining data. Short period data should only be used from robust measurements uncontaminated by multipathing, and long period data should only be used from long paths from large regional events, limiting the data available.

There still might be some problems applying the technique to short periods, such as conversion of modes at boundaries. Additionally, moving to periods shorter than 15 seconds, one approaches high levels of microseismic noise (which has its peak at around 6 seconds) on the seismograms. One must further limit the events to those large enough to have a good signal-to-noise ratio, but small enough to still be well approximated by a point source. For instance, it would not be prudent to extract 10 second period surface wave data from a source that has a complex source duration greater than 10 seconds, or even half of that.

Another possibility is using information that is contained in off-path propagation to look at sharper lateral structural boundaries. In many ways, this is similar to the problem of locating earthquakes. Instead of just using the timing of a phase at stations to triangulate the location, one can use the angle of incidence of the phase to back-project the location. Of course, information about earth structure along the way is contained in the phase. In the case of surface wave tomography, this would entail looking for evidence of Love waves found on the radial component or Rayleigh waves found on the transverse component to measure propagation of the wave off the great circle path. This information can be incorporated in the inversion for structure instead of using only the phase velocities. Laske, *et al.* [1994] and Laske [1995] have observed off great circle propagation of long period surface waves. Since polarization

data depend on the lateral gradient of phase velocity, they are more sensitive to shorter-wavelength structure than phase data. These studies have found that the off great circle propagation of the surface-wave packets is easy to interpret within a ray-theoretical framework.

A potential extension to the direct phase velocity inversion problem is the inversion for phase velocity as a function of direction of propagation. This approach might be particularly appropriate for California, given the tectonics and structural geology of the region. Using the shear-wave splitting in teleseismic shear waves, Savage and Silver [1993] investigated anisotropy in the western United States. For most of the stations, they found anisotropy with a consistent fast polarization azimuth, generally in the E-W direction throughout the Basin and Range, but in the N-S direction in the Colorado Plateau. Close to the San Andreas, however, the data could only be fit by two anisotropic layers with different symmetry axes. The fast direction of the upper layer was parallel to the fault and that of the lower layer was oriented E-W. The depth and thickness of each of these layers, however, was not well resolved.

Because of the way surface waves sample the velocity at depth in an integral manner, they can be a powerful method of determining the vertical extent of anisotropy. If the anisotropy is weak, then the phase velocity $c$ of the surface waves has a dependence on the azimuthal direction of propagation $\phi$, as given by Smith and Dahlen [1973]:

$$c(\omega, \phi) = A(\omega) + B(\omega)\cos(2\phi) + C(\omega)\sin(2\phi) + E(\omega)\cos(4\phi) + F(\omega)\sin(4\phi) \quad (5.1)$$

When Forsyth [1975] applied this procedure to surface wave data in the Pacific, he did not include the $4\phi$ terms because they have only a minor effect.

A simple inversion of the phase velocity data for anisotropy can be made by just inverting for the velocity A and the azimuthal coefficients (B–E) given above (and not for a laterally varying velocity and anisotropy). These "back-of-the-envelope" calculations indicate that anisotropy on the order of 1–2% would be appropriate for the region. Furthermore, it appears as though the direction of anisotropy is oriented with the fast direction at about 60° and the slow direction at about 160°, although there is substantial variation in the data with frequency. For comparison, the San Andreas fault strikes at 140-145° (normal at 50-55°) along most of its length, while the Cascade Range strikes at about 180° (normal at 90°). Where the ray paths are

well distributed with azimuth these variations should not affect the phase velocities, since the measured velocity should represent the azimuthally averaged velocity. In particular regions, like most of California, however, much of the data is oriented along certain azimuths and could bias the results because only data of particular azimuths are being sampled.

This study used only fundamental mode surface waves. In order to study the mantle area in a more thorough manner, higher mode surface waves could be used. Excitation curves show that higher modes preferentially sample deeper earth structure (figures 5.1 and 5.2). Since all of the modes except the fundamental mode have a low-frequency cutoff, one is forced to move to higher frequencies. In the figures, for example, only the fundamental and first-higher mode exist at the relatively short period of 10 seconds. Of course, the benefit is having another set of independent measurements to constrain earth structure. So, difficulties of using higher modes include separating the modes from one another and all of the problems of moving to higher frequencies discussed above. Some effort must be taken in separating higher modes by carefully selecting group velocity windows and not using short source-receiver distances where the modes have not had a chance to separate. One could start by using large earthquakes at long distances where the modes would be easier to separate in the time domain. Other techniques include looking at energy diagrams to choose appropriate windows.

One fruitful extension of this technique would be to investigate the phenomena of multipathing and focussing. Since the method described in the dissertation has produced detailed models of California and vicinity, it would be interesting to see whether numerical methods, such as finite difference (Frankel and Clayton, 1986), run through the model would be able to produce many of the observations that are seen in the data, particularly at high frequency. The very low near-surface velocities in the Central Valley and the velocity contrasts both between tectonic regimes and across faults should be able to produce some of these features.

Another interesting extension of the problem would be to investigate the properties of resolution and uniqueness. The inversion methods chosen (i.e. phase velocity tomography, layered velocity inversion) were selected for their ease, applicability, and robustness; however, they are not exact and unique. Many inversion techniques have recently come into favor as quick and efficient ways of completely sampling the
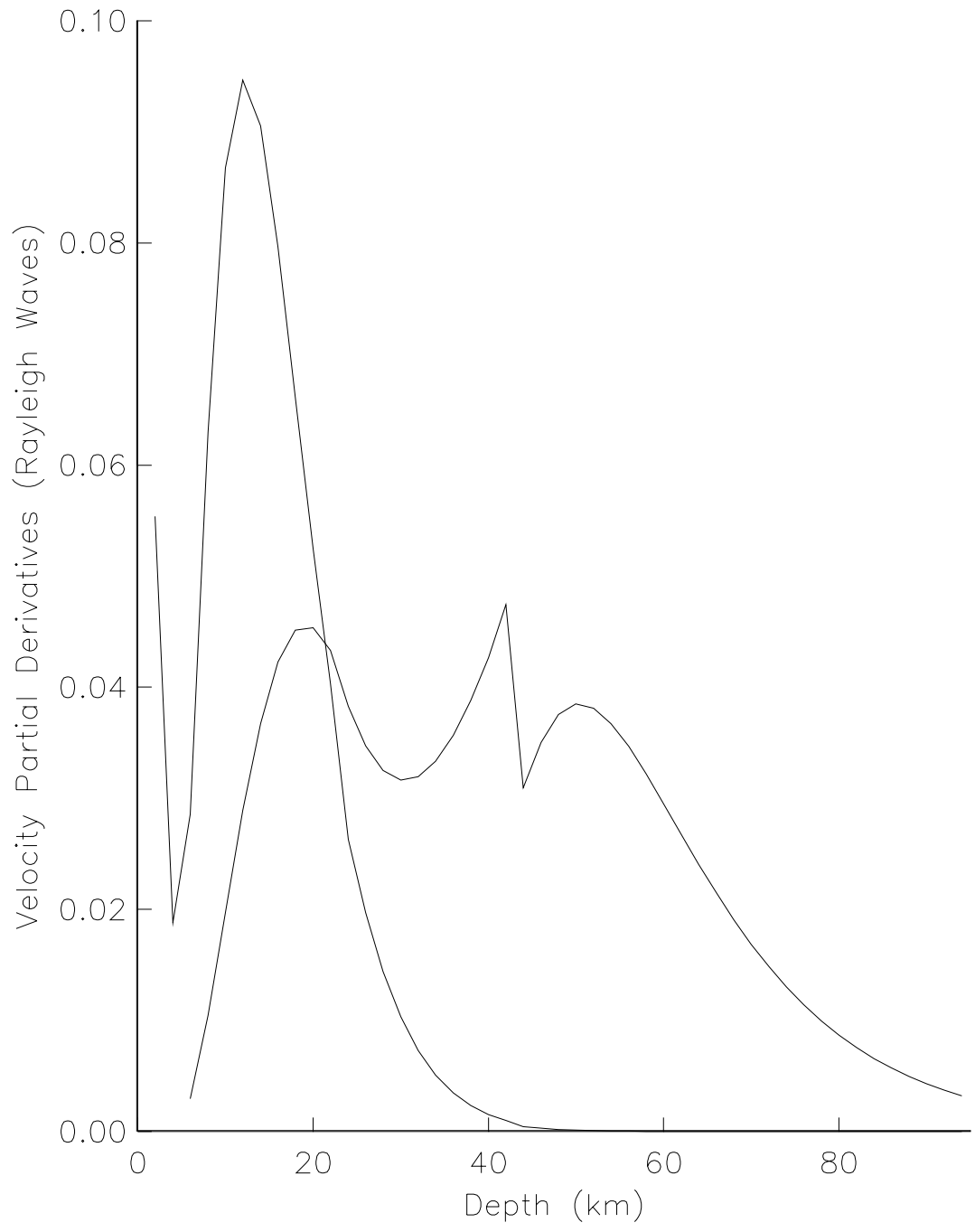
Figure 5.1: Velocity partial derivatives for 10 second Rayleigh waves shown for fundamental (peak at about 15 seconds) and first-higher mode.
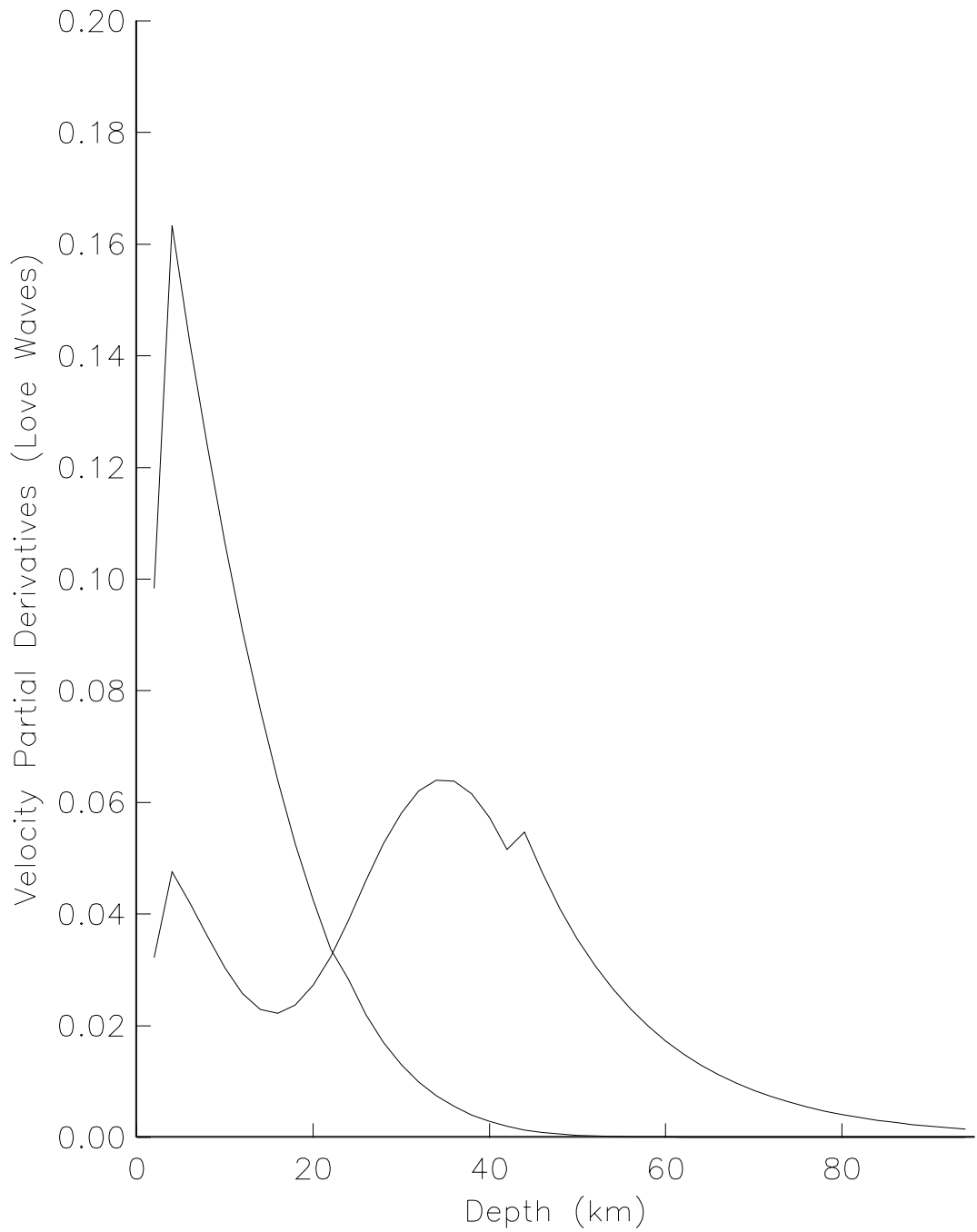
Figure 5.2: Velocity partial derivatives for 10 second Love waves shown for fundamental (peak at about 7 seconds) and first-higher mode.

model space. These include Monte Carlo techniques, Genetic Algorithms, Simulated Annealing, Random Walk techniques, Importance Sampling, etc. It would be interesting to apply some of these methods to fully test the resolution and uniqueness of the problem.

In the future, this technique could be applied to other areas of the world. Broadband networks that already exist or are planned (GEOSCOPE, MEDNET, POSEIDON, IRIS/IDA, USNSN) could supply the necessary data to study specific areas, such as Europe and North Africa, Japan and East Asia. In the case of the global networks, stations may be concentrated in some areas to allow one to proceed in the same way as this study of California and the Western United States. Figure 5.3 is an example of a European earthquake inverted with the regional surface wave method. The data used include both GEOSCOPE and IRIS stations. The solution is comparible with the Harvard CMT solution for the event. Compare the phase and amplitude fits of the data to those in a well-calibrated region (figure 2.7 – 2.9). Large discrepancies in the phase are due to unmodelled structure along the source-receiver paths.

Finally, it is hoped that the information on the earth's structure that has been gathered from surface waves can be combined with the corresponding information from body waves and other geophysical methods in order to develop a comprehensive three-dimensional model for California and the vicinity. The philosophy here was to provide, as best as possible, an unbiased estimation of earth structure from surface wave information. The positive aspect of this reasoning was providing a truly independent data set which must be satisfied by a comprehensive model. The downside of this independence, however, was a difficulty in isolating some model parameters. For example, in the inversion from phase velocities to layered structure, there was a tradeoff between Moho depth and upper mantle velocity. If one of these parameters could be pinned down by other techniques (seismic refraction or deep reflection profiles to obtain crustal thickness or $P_n$ studies to estimate the upper mantle velocity), then the problem of the tradeoff is resolved. This was demonstrated in theory in section 4.2.

One problem, of course, is deciding which outside parameters to use. As was shown in section 4.2.3, there is often no consensus among various studies on many of even the most basic model features. Clearly, by adding independent estimates of these parameters, one is biasing the solution. This bias can be helpful or harmful,
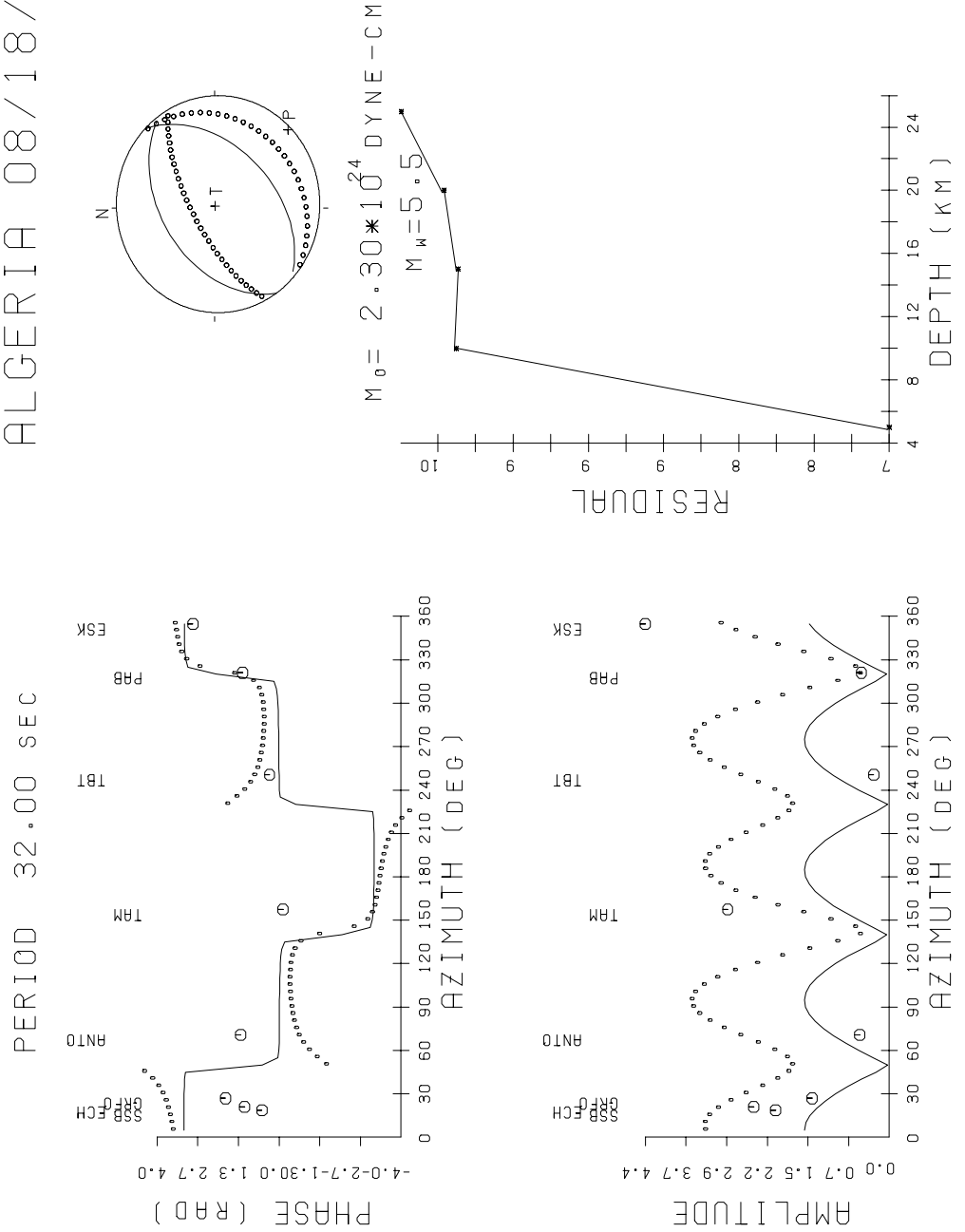
Figure 5.3: Example of the regional moment tensor for a European earthquake. The event occurred on 08/18/94 and was located in Northern Algeria. Comparison solution (shown in small circles) is the Harvard CMT solution for this event.

depending on the correctness of the independent data. In the example of the tradeoff between Moho depth and upper mantle velocity, a correct independent estimate of the Moho depth will not only render a better estimate of upper mantle velocity, but also of other parameters such as the average crustal velocity. If, however, this estimate was incorrect, then the estimates of the other parameters will actually be made worse. Hence, only outside information with the most certitude should be used.

With the possible exception of seismology using controlled sources (i.e. exploration seismology), the science of seismology has been troubled with the dual efforts of learning about both seismic sources and earth structure. This work represents an effort to improve in both areas using broadband data and surface waves, and to apply this knowledge to other applications, such as earthquake sequence studies, stress studies, and tectonic problems. I hope to have illustrated that one can start to fully employ a broadband network by applying the methodologies of the regional surface wave moment tensor inversion and phase velocity tomography to a region.

It should be relatively easy to transport these techniques to other areas, as well. The most critical aspect of the problem is to properly calibrate the region by studying the regionally recorded broadband data for large events for which the source mechanism is well known from global inversions. This might be particularly applicable to regions that are monitored in the interest of the Comprehensive Test Ban Treaty (CTBT), in which the discrimination between nuclear explosions, earthquakes, and mining-induced collapses is critical.

# References

Aki, K., Three-dimensional Seismic Inhomogeneities in the Lithosphere and Astheno-
  sphere: Evidence for Decoupling in the Lithosphere and Flow in the Asthenosphere,
  *Rev. Geophys. Spac. Phys., 20,* 161-170, 1982.

Aki, K. and P.G. Richards, *Quantative Seismology, Theory and Methods, Volume I,*
  W.H. Freeman and Company, New York, NY, 557 pp., 1980a.

Aki, K. and P.G. Richards, *Quantative Seismology, Theory and Methods, Volume II,*
  W.H. Freeman and Company, New York, NY, 932 pp., 1980b.

Anderson, E.M., *The Dynamics of Faulting,* 2nd edition, Oliver and Boyd, Edinburgh,
  206 pp., 1951.

Atwater, T., Implications of Plate Tectonics for the Cenozoic Tectonic Evolution of
  Western North America, *Geol. Soc. Am. Bull., 81,* 3513-3536, 1970.

Bailey, R.A., G.B. Dalrymple, and M.A. Lanphere, Volcanism, Structure, and Geochronol-
  ogy of Long Valley Caldera, Mono County, California, *J. Geophys. Res., 81,* 725-
  744, 1976.

Bakun, W.H. and A.G. Lindh, Local Magnitudes, Seismic Moments, and Coda Du-
  rations for Earthquakes near Oroville, California, *Bull. Seism. Soc. Am., 67,*

615-629, 1977.

Bakun, W.H. and A.G. Lindh, The Parkfield, California Earthquake Prediction Experiment, *Science, 229,* 619-623, 1985.

Bakun, W.H. and T.V. McEvilly, Recurrence Models and Parkfield, California earthquakes, *J. Geophys. Res., 89,* 3051-3058, 1984.

Baldwin, E.M., *Geology of Oregon,* Kendall/Hunt Publishing Company, Dubuque, IA, 170 pp., 1981.

Benz, H.M., G. Zandt, and D.H. Oppenheimer, Lithospheric Structure of Northern California from Teleseismic Images of the Upper Mantle, *J. Geophys. Res., 97,* 4791-4807, 1992.

Bolt, B.A. and L.A. Drake, Love Mode Dispersion Across Subduction Zones by Finite Element Modelling, *Geophys. J. R. astr. Soc., 84,* 515-528, 1986.

Bolt, B.A. and M. Herraiz, Simplified Estimation of Seismic Moment from Seismograms, *Bull. Seism. Soc. Am., 73,* 735-748, 1983.

Bolt, B.A., J.E. Friday and R.A. Uhrhammer, A PC-based Broadband Digital Seismograph Network, *Geophys. J. R. astr. Soc., 93,* 565-573, 1988.

Bourjot, L. and B. Romanowicz, Crust and Upper Mantle Tomography in Tibet Using Surface Waves, *Geophys. Res. Lett., 19,* 881-884, 1992.

Braile, L.W., W.J. Hinze, R.B. von Frese, G.R. Keller, Seismic Properties of the Crust and Uppermost Mantle of the Conterminous United States and Adjacent Canada, in L.C. Pakiser and W.D. Mooney, *Geophysical Framework of the Continental United States,* Geological Society of America Memoir 172, Boulder, CO, 655-680, 1989.

Braunmiller, J., J. Nábělek, and B. Leitner, The 1993 Klamath Falls, Oregon Earth-

quake Sequence: Source Mechanisms from Regional Data, *Geophys. Res. Lett., 22,* 105-108, 1995.

Brocher, T.M., J. McCarthy, P.E. Hart, W.S. Holbrook, K.P. Furlong, T.V. McEvilly, J.A. Hole, S.L. Klemperer, Seismic Evidence for a Lower-Crustal Detachment Beneath San Francisco Bay, California, *Science, 265,* 1436-1439, 1994.

Brown, L., M. Barazangi, S. Kaufman, and J. Oliver, The First Decade of COCORP, *Reflection Seismology - A Global Perspective: AGU Geodynamics Series 13,* 107-120, 1986.

Cara, M., Lateral Variations of S Velocity in the Upper Mantle from Higher Rayleigh Modes, *Geophys. J. R. astr. Soc., 57,* 649-670, 1979.

Cara, M., Crust-Mantle Structure Inferred from Surface Waves, in H. Kanamori and E. Boschi, *Earthquakes: Observation, Theory and Interpretation,* North-Holland Publishing, Amsterdam, 319-329, 1983.

Christensen, N.I., Compressional Wave Velocities in Metamorphic Rocks at Pressures to 10 Kilobars, *J. Geophys. Res., 70,* 6147-6164, 1965.

Christensen, N.I., Compressional Wave Velocities in Rocks at High Temperatures and Pressures, Critical Thermal Gradients, and Crustal Low-Velocity Zones, *J. Geophys. Res., 84,* 6849-6857, 1979.

Clarke, S.H., Jr. and G.A. Carver, Late Holocene Tectonics and Paleoseismicity of the Southern Cascadia Subduction Zone, Northwestern California, *Science, 255,* 188-192, 1992.

Cockerham, R.S. and W.L. Ellsworth, Three-dimensional Large-scale Mantle Structure in Central California, *EOS, Trans., AGU, 60,* 875, 1979.

DeMets, C., R.G. Gordon, D.F. Argus, and S. Stein, Current Plate Motions: *Geophys.*

*J. Int., 101,* 415-478, 1990.

Dengler, L., G. Carver, and R. McPherson, Sources of North Coast Seismicity, *California Geology, 45,* 40-53, 1992.

Dengler, L., K. Moley, R. McPherson, M. Pasyanos, J. Dewey, M. Murray, The September 1, 1994 Mendocino Fault Earthquake, *California Geology, 48,* 43-53, 1995.

Dickinson, W.R. and W.S. Snyder, Geometry of Subducted Slabs Related to San Andreas Transform, *Journal of Geology, 87,* 609-627, 1979.

Drake, L.A. and B.A. Bolt, Love Waves Normally Incident at a Continental Boundary, *Bull. Seism. Soc. Am., 70,* 1103-1123, 1980.

Drake, L.A. and B.A. Bolt, Finite Element Modelling of Surface Wave Transmission Across Regions of Subduction, *Geophys. J. Int., 98,* 271-279, 1989.

Dreger, D., Empirical Green's Function Study of the January 17, 1994 Northridge, California Earthquake, *Geophys. Res. Lett., 21,* 2633-2636. 1994.

Dreger, D.S. and D.V. Helmberger, Broadband Modeling of Local Earthquakes, *Bull. Seism. Soc. Am., 80,* 1162-1179, 1990.

Dreger, D.S. and D.V. Helmberger, Complex Faulting Deduced from Broadband Modeling of the 28 February 1990 Upland Earthquake ($M_L = 5.2$), *Bull. Seism. Soc. Am., 81,* 1129-1144, 1991.

Dreger, D.S. and D.V. Helmberger, Determination of Source Parameters at Regional Distances with Single Station or Sparse Network Data, *J. Geophys. Res., 98,* 8107-8125, 1993.

Dreger, D. and B. Romanowicz, Source Characteristics of Events in the San Francisco

Bay Region, *USGS Open File Rep. 94-176,* 301-309, 1994.

Dreger, D.S., L.S. Gee, S. Loper, M.R. McKenzie, and R.A. Uhrhammer, *Bulletin of the Seismographic Stations, 60-61,* University of California Press, Berkeley, CA, 79 pp., 1993.

Dreger, D., J. Ritsema, and M. Pasyanos, Broadband Analysis of the 21 September, 1993 Klamath Falls Earthquake Sequence, *Geophys. Res. Lett., 22,* 997-1000, 1995.

Dziewonski, A. and D. Anderson, Preliminary Reference Earth Model, *Phys. Earth Planet. Inter., 25,* 297-356, 1981.

Dziewonski, A.M., T.A. Chou, and J.H. Woodhouse, Determination of Earthquake Source Parameters from Waveform Data for Studies of Global and Regional Seismicity, *J. Geophys. Res., 86,* 2825-2852, 1981.

Eaton, J., Dense Microearthquake Network Study of Northern California, in J. J. Litehiser ed., *Observatory Seismology: An Anniversary Symposium on the Occasion of the Centennial of the University of California at Berkeley Seismographic Stations,* University of California Press, Berkeley, CA, 199-224, 1989.

Eaton, J.P., Determination of Amplitude and Duration Magnitudes and Site Residuals from Short-Period Seismographs in Northern California, *Bull. Seism. Soc. Am., 82,* 533-579, 1992.

Eberhart-Phillips, D. and D.H. Oppenheimer, Induced Seimsmicity in The Geysers geothermal area, California, *J. Geophys. Res., 89,* 1191-1207, 1984.

Ekström, G., A System for Automatic Earthquake Analysis, *EOS, Trans., AGU, 73,* 70, 1992.

Forsyth, D.W., The Early Structural Evolution and Anisotropy of the Oceanic Upper Mantle, *Geophys. J. R. astr. Soc., 43,* 103-162, 1975.

Frankel, A. and R.W. Clayton, Finite Difference Simulations of Seismic Scattering: Implications for the Propagation of Short-period Seismic Waves in the Crust and Models of Crustal Heterogeneity, *J. Geophys. Res., 91*, 6465-6489, 1986.

Fuis, G.S. and W.D. Mooney, Lithospheric Structure and Tectonics from Seismic-Refraction and Other Data, in *The San Andreas Fault System, California: USGS Professional Paper 1515,* 207-236, 1990.

Fuis, G.S., J.J. Zucca, W.D. Mooney, and B. Milkereit, A Geological Interpretation of Seismic-Refraction Results in Northeastern California, *Geol. Soc. Amer. Bull., 98,* 53-65, 1986.

Gee, L.S., D. Neuhauser, D. Dreger, M. Pasyanos, B. Romanowicz, and R. Uhrhammer, The Rapid Earthquake Data Integration System, *Seism. Res. Lett., 66,* 32, 1995.

Gee, L.S, D.S. Neuhauser, D. Dreger, M. Pasyanos, R.A. Uhrhammer, and B. Romanowicz, Real-Time Seismology at UC Berkeley: The Rapid Earthquake Data Integration Project, *Bull. Seism. Soc. Amer., in press,* 1996.

Gephart, J.W. and D. Forsyth, An Improved Method for Determining the Regional Stress Tensor using Earthquake Focal Plane Mechanism Data: Application to the San Fernando Earthquake Sequence, *J. Geophys. Res., 89,* 9305-9320, 1984.

Giardini, D., Moment Tensor Inversion from Mednet Data, *Geophys. Res. Lett., 19,* 713-716, 1992.

Gonzalez, R.C. and R.E. Woods, *Digital Image Processing,* Addison-Wesley Publishing Group, Reading, MA, 716 pp., 1992.

Hall, J.F., editor, *Northridge Earthquake - January 17, 1994, Preliminary Reconnaissance Report,* EERI Publication Number 94-01, 96 pp., 1994.

Hanks, T.C. and H. Kanamori, A Moment Magnitude Scale, *J. Geophys. Res., 84,* 2348-2350, 1979.

Hauksson, E., L.M. Jones, and K. Hutton, The 1994 Northridge Earthquake Sequence in California: Seismological and Tectonic Aspects, *J. Geophys. Res., 100,* 12335-12355, 1995.

Heaton, T.H. and S.H. Hartzell, Earthquake Hazards on the Cascadia Subduction Zone, *Science, 236,* 162-168, 1987.

Heaton, T.H. and H. Kanamori, Seismic Potential Associated with Subduction in the Northwestern United States, *Bull. Seism. Soc. Am., 75,* 933-942, 1984.

Hearn, T., N. Beghoul, and M. Barazangi, Tomography of the Western United States from Regional Arrival Times, *J. Geophys. Res., 96,* 16369-16381, 1991.

Helmberger, D.V., Theory and Application of Synthetic Seismograms, in H. Kanamori and E. Boschi, *Earthquakes: Observation, Theory and Interpretation,* North-Holland Publishing, Amsterdam, 174-222, 1983.

Herrmann, R.B., The Use of Duration as a Measure of Seismic Moment and Magnitude, *Bull. Seism. Soc. Am., 65,* 899-913, 1975.

Herrmann, R., *Computer Programs in Seismology,* Computer Program, 1991.

Hill, D.P., J.P. Eaton, and L.M. Jones, Seismicity, 1980-1986, in *The San Andreas Fault System, California: USGS Professional Paper 1515,* 115-151, 1990.

Holbrook, W.S., T.M. Brocher, U.S. ten Brink, and J.A. Hole, Crustal Structure Beneath the San Francisco Bay Block and the Central California Continental Margin, *submitted to J. Geophys. Res.,* 1995.

Humphreys, E.D., R.W. Clayton, and B.H. Hager, A Tomographic Image of Mantle

Structure Beneath Southern California, *Geophys. Res. Lett., 11,* 625-627, 1984.

Iyer, H.M. and T. Hitchcock, Upper-mantle Velocity Structure in the Continental U.S. and Canada, in L.C. Pakiser and W.D. Mooney, *Geophysical Framework of the Continental United States,* Geological Society of America Memoir 172, Boulder, CO, 681-710, 1989.

Jachens, R.C. and A. Griscom, Three-dimensional Geometry of the Gorda Plate beneath Northern California, *J. Geophys. Res., 88,* 9375-9392, 1983.

Jones, D.L., R. Graymer, C. Wang, T.V. McEvilly, and A. Lomax, Neogene Transpressive Evolution of the California Coast Ranges, *Tectonics, 13,* 561-574, 1994a.

Jones, C.H., H. Kanamori, and S.W. Roecker, Missing Roots and Mantle "Drips": Regional $P_n$ and Teleseismic Arrival Times in the Southern Sierra Nevada and Vicinity, California, *J. Geophys. Res., 99,* 4567-4601, 1994b.

Jost, M.L. and R.B. Herrmann, A Student's Guide to and Review of Moment Tensors, *Seism. Res. Letters, 60,* 37-57, 1989.

Kanamori, H. and D.L. Anderson, Theoretical Basis of Some Empirical Relations in Seismology, *Bull. Seism. Soc. Am., 65,* 1073-1095, 1975.

Kanamori, H. and J.J. Cipar, Focal Process of the Great Chilean Earthquake May 22, 1960, *Phys. Earth Plant. Inter., 9,* 128-136, 1974.

Kanamori, H. and J. Given, Use of Long-period Surface Waves for Rapid Determination of Earthquake Source Parameters, *Phys. Earth Planet. Inter., 27,* 8-31, 1981.

Kanamori, H. and E. Hauksson, TERRAscope, *IRIS Newsletter, Vol. X,* 1-3, 1991.

Kanamori, H., E. Hauksson, and T. Heaton, TERRAscope and CUBE project at

Caltech, *EOS, Trans., AGU, 72,* 564-565, 1991.

Kilbourne, R.T. and G.J. Saucedo, Gorda Basin Earthquake, Northwestern California, *California Geology, 34,* 53-57, 1981.

King, G. and J. Nábělek, Role of Fault Bends in the Initiation and Termination of Earthquake Rupture, *Science, 228,* 984-987, 1985.

King, G., R.S. Stein, and J. Lin, Static Stress Changes and the Triggering of Earthquakes, *Bull. Seism. Soc. Amer., 84,* 935-953, 1994.

Klein, F.W., User's Guide to HYPOINVERSE, *USGS Open File Rep. 89-314,* 58 pp., 1989.

Knopoff, L., Observation and Inversion of Surface-wave Dispersion, *Tectonophysics, 13,* 497-519, 1972.

Laske, G., Global Observations of Off-great-circle Propagation of Long-Period Surface Waves, *Geophys. J. Int., 123,* 245-259, 1995.

Laske, G., G. Masters, and W. Zürn, Frequency-dependent Polarization Measurements of Long-Period Surface Waves and their Implications for Global Phase-velocity Maps, *Phys. Earth Planet. Inter., 84,* 111-137, 1994.

Lawson, C.L. and R.J. Hanson, *Solving Least Squares Problems,* Prentice-Hall, Inc., Englewood Cliffs, NJ, 340 pp., 1974.

Lay, T. and T.C. Wallace, *Modern Global Seismology,* Academic Press, San Diego, CA, 531 pp., 1995.

Lee, W.H.K., R. Bennet, and K. Meagher, A Method of Estimating Magnitude of Local Earthquakes from Signal Duration, *USGS Open File Rep.* 28 pp., 1972.

Lister, G.S., M.A. Etheridge, and P.A. Symonds, Detachment Faulting and the Evolution of Passive Continental Margins, *Geology, 14,* 246-250, 1980.

Loper, S., M. Pasyanos, D. Dreger, B. Romanowicz, Broadband Source Study of the 1993 Eureka Valley, California, Earthquake Sequence, *EOS, Trans., AGU, 74,* 69, 1993.

McPherson, R.C., Seismicity and Focal Mechanisms near Cape Mendocino, Northern California: 1974-1984, *Masters Thesis,* Humboldt State University, Arcata, CA, 75 pp., 1989.

Mendiguren, J.A., Inversion of Surface Wave Data in Source Mechanism Studies, *J. Geophys. Res., 82,* 889-894, 1977.

Miller, E.L., P.B. Gans, and J. Garing, The Snake Range Decollment: An Exhumed mid-Tertiary Brittle-Ductile Transition, *Tectonics, 2,* 239-263, 1983.

Moehle, J.P., editor, *Preliminary Report on the Seismological and Engineering Aspects of the January 17, 1994 Northridge Earthquake,* Earthquake Engineering Research Center, UCB/EERC 94-001, 523 pp., 1994.

Montagner, J.P., Regional Three-dimensional Structures using Long-period Surface Waves, *Ann. Geophys., 4,* 283-294, 1986.

Mooney, W.D., Seismic Methods for the Determination of Earthquake Source Parameters and Lithospheric Structure, in L.C. Pakiser and W.D. Mooney, *Geophysical Framework of the Continental United States,* Geological Society of America Memoir 172, Boulder, CO, 11-34, 1989.

Mooney, W.D. and L.W. Braile, The Seismic Structure of the Continental Crust and Upper Mantle of North America, *The Geology of North America, Vol A,* 39-52, 1989.

Mooney, W.D. and C.S. Weaver, Regional Crustal Structure and Tectonics of the Pacific Coastal States; California, Oregon, and Washington, in L.C. Pakiser and W.D. Mooney, *Geophysical Framework of the Continental United States,* Geological Society of America Memoir 172, Boulder, CO, 129-162, 1989.

Moos, D. and M.D. Zoback, State of Stress in the Long Valley Caldera, California, *Geology, 21,* 837-840, 1993.

Mori, J. and S. Hartzell, Source Inversion of the 1988 Upland Earthquake: Determination of a Fault Plane for a Small Event, *Bull. Seism. Soc. Amer., 80,* 507-518, 1990.

Mount, V.S. and J. Suppe, State of Stress near the San Andreas Fault: Implications for Wrench Tectonics, *Geology, 15,* 1143-1146, 1987.

Norris, R.M. and R.W. Webb, *Geology of California,* John Wiley and Sons, Inc., New York, NY, 541 pp., 1990.

Nowroozi, A., Seismicity of the Mendocino Escarpment and the Aftershock Sequence of June 26, 1968, Ocean Bottom Seismic Measurements, *Bull. Seism. Soc. Amer., 63,* 441-456, 1973.

O'Connell, D.R.H. and L.R. Johnson, Progressive Inversion for Hypocenters and P Wave and S Wave Velocity Structure: Application to the Geysers, California, Geothermal Field, *J. Geophys. Res., 96,* 6223-6236, 1991.

Oppenheimer, D.H., Extensional Tectonics at The Geysers Geothermal Area, California, *J. Geophys. Res., 91,* 11463-11476, 1986.

Oppenheimer, D., G. Beroza, G. Carver, L. Dengler, J. Eaton, L. Gee, F. Gonzalez, A. Jayko, W. H. Li, M. Lisowski, M. Magee, G. Marshall, M. Murray, R. McPherson, B. Romanowicz, K. Satake, R. Simpson, P. Sommerville, R. Stein, D. Valentine, The Cape Mendocino, California, Earthquakes of April 1992: Subduction at the

Triple Junction, *Science, 261,* 433-438, 1993.

Pasyanos, M., D. Dreger, S. Fulton, B. Romanowicz, 12 September, 1994 Double Spring Flat Earthquake Sequence, *Seism. Res. Lett., SSA, 66,* 41, 1995.

Pasyanos, M.E., D.S. Dreger, and B. Romanowicz, Towards Real Time Estimation of Regional Moment Tensors, *Bull. Seism. Soc. Amer., in press,* 1996.

Patton, H., Reference Point Equilization Method for Determining the Source and Path Effects of Surface Waves, *J. Geophys. Res., 85,* 821-848, 1980.

Patton, H. and G. Zandt, Seismic Moment Tensors of Western U.S. Earthquakes and Implications for the Tectonic Stress Field, *J. Geophys. Res., 96,* 18245-18259, 1991.

Press, W.H., S.A. Teukolsky, W.T. Vetterling, and B.P. Flannery, *Numerical Recipes in C,* 2nd edition, Cambridge University Press, Cambridge, U.K., 994 pp., 1992.

Raikes, S.A., Regional Variations in Upper Mantle Structure beneath Southern California, *Geophys. J. R. astr. Soc., 63,* 187-216, 1980.

Real, C.R. and T. Teng, Local Richter Magnitude and Total Signal Duration in Southern California, *Bull. Seism. Soc. Am., 63,* 1809-1827, 1973.

Reasenberg, P.A. and D. Oppenheimer, FPFIT, FPPLOT, and FPPAGE: Fortran Computer Programs for Calculating and Displaying Earthquake Fault-plane Solutions, *USGS Open File Rep. 85-739,* 109 pp., 1985.

Reasenberg, P.A. and R.W. Simpson, Response of Regional Seismicity to the Static Stress Changes Produced by the Loma Prieta Earthquake, *Science, 255,* 1687-1690, 1992.

Richter, C.F., An Instrumental Earthquake Scale, *Bull. Seism. Soc. Am., 25,* 1-35, 1935.

Richter, C.F., *Elementary Seismology,* W.H. Freeman and Company, San Francisco, CA, 768 pp., 1958.

Ritsema, J. and T. Lay, Rapid Source Mechanism Determination of Large ($M_w \geq 5$) Earthquakes in the Western United States, *Geophys. Res. Lett., 20,* 1611-1614, 1993.

Ritsema, J., T. Lay, D. Dreger, M. Pasyanos, B. Romanowicz, Moment Tensor Inversion for Western United States Earthquakes: Calibration of Methods, *Seism. Res. Lett., SSA, 65,* 33, 1994.

Romanowicz, B., Seismic Structure of the Upper Mantle Beneath the United States by Three-Dimensional Inversion of Body Wave Arrival Times, *Geophys. J. R. astr. Soc., 57,* 479-506, 1979.

Romanowicz, B.A., Large scale three-dimensional P-velocity Structure beneath the Western U.S. and the Lost Farallon Plate, *Geophys. Res. Lett., 7,* 345-348, 1980.

Romanowicz, B., Moment Tensor Inversion of Long Period Rayleigh Waves: a New Approach, *J. Geophys. Res., 87,* 5395-5407, 1982.

Romanowicz, B., D. Dreger, M. Pasyanos, and R. Uhrhammer, Monitoring of Strain Release in Central and Northern California Using Broadband Data, *Geophys. Res. Lett., 20,* 1643-1646, 1993.

Romanowicz, B., L. Gee, and R. Uhrhammer, Berkeley Digital Seismic Network: A Broadband Network for Northern and Central California, *IRIS Newsletter, Vol. XI,* 1-5, 1992.

Romanowicz, B. and P. Guillemant, An Experiment in the Retrieval of Depth and Source Parameters of Large Earthquakes using Very Long-period Rayleigh Wave Data, *Bull. Seism. Soc. Am., 74,* 417-437, 1984.

Romanowicz, B. and T. Monfret, Source Process Times and Depths of Large Earthquakes by Moment Tensor Inversion of Mantle Wave Data and the Effect of Lateral Heterogeneity, *Ann. Geophys., 74,* 271-283, 1986.

Romanowicz, B., D. Neuhauser, B. Bogaert, and D. Oppenheimer, Accessing Northern California Earthquake Data Via Internet, *EOS, Trans., AGU, 75,* 257-260, 1994.

Roult, G. and D. Rouland, Antartica I: Deep Structure Investigations Inferred from Seismology; A Review, *Phys. Earth Planet. Inter., 84,* 15-32, 1994.

Roult, G., D. Rouland, and J.P. Montagner, Antartica II: Upper-mantle Structure from Velocities and Anisotropy, *Phys. Earth Planet. Inter., 84,* 33-57, 1994.

Russell, D.R., Multichannel Processing of Dispersed Surface Waves, *Ph.D. Dissertation,* St. Louis University, St. Louis, MO, 162 pp., 1986.

Savage, M.K. and P.G. Silver, Mantle Deformation and Tectonics: Constraints from Seismic Anisotropy in the Western United States, *Phys. Earth Planet. Inter., 78,* 207-227, 1993.

Scholz, C.H., *The Mechanics of Earthquakes and Faulting,* Cambridge University Press, Cambridge, U.K., 439 pp., 1990.

SEED (Standard for the Exchange of Earthquake Data) Reference Manual, SEED Format Version 2.3, *IRIS,* 203 pp., 1993.

Smith, M.L. and F.A. Dahlen, The Azimuthal Dependence of Love and Rayleigh Wave Propagation in a Slightly Anisotropic Medium, *J. Geophys. Res., 78,* 3321-3333, 1973.

Smith, S.W. and J.S. Knapp, The Northern Termination of the San Andreas fault, in R. Streitz and R. Sherburne, *Studies of the San Andreas Fault Zone in Northern*

*California: Calif. Div. Mines Geol., 140,* 153-164, 1980.

Smith, S.W., J.S. Knapp, and R. McPherson, Seismicity of the Gorda plate, Structure of the Continental Margin, and an Eastward Jump of the Mendocino Triple Junction, *J. Geophys. Res., 98,* 8153-8171, 1993.

Strand, R.G., Geologic Map of California, Mariposa Sheet, *Calif. Div. Mines Geol., map,* 1967.

Suetsugu, D. and I. Nakanishi, Tomographic Inversion and Resolution for Rayleigh Wave Phase Velocities in the Pacific Ocean, *Journal of Physics of the Earth, 33,* 345-368, 1985.

Suppe, J., *Principles of Structural Geology,* Prentice-Hall, Inc., Englewood Cliffs, NJ, 537 pp., 1985.

Tarantola, A. and B. Valette, Generalized Nonlinear Inversion Problems Solved using the Least Squares Criterion, *Rev. Geophys. Spac. Phys., 20,* 219-232, 1982.

Taylor, S.R. and H.J. Patton, Shear-velocity Structure from Regionalized Surface-wave Dispersion in the Basin and Range, *Geophys. Res. Lett., 13,* 30-33, 1986.

Thatcher, W. and T. Hanks, Source Parameters of Southern California Earthquakes, *J. Geoph. Res., 78,* 8547-8576, 1973.

Thio, H.K. and H. Kanamori, A Surface Wave Study on the Structure of the Crust and Upper Mantle under Southern California, *EOS, Trans., AGU, 72,* 324, 1991.

Thio, H.K. and H. Kanamori, Moment Tensor Inversions for Local Earthquakes using Surface Waves Recorded at TERRAscope, *Bull. Seism. Soc. Amer., 85,* 1021-1038, 1995.

Thio, H.K. and H. Kanamori, Source Complexity of the 1994 Northridge Earthquake

and Its Relation to Aftershock Mechanisms, *Bull. Seism. Soc. Amer., 86,* S84-S92, 1996.

Thompson, G.A., R. Catchings, E. Goodwin, S. Holbrook, C. Jarchow, C. Mann, J. McCarthy, and D. Okaya, Geophysics of the Western Basin and Range Province, in L.C. Pakiser and W.D. Mooney, *Geophysical Framework of the Continental United States,* Geological Society of America Memoir 172, Boulder, CO, 177-204, 1989.

Tsai, Y.B. and K. Aki, Amplitude Spectra of Surface Waves from Small Earthquakes and Underground Nuclear Explosions, *J. Geophys. Res., 76,* 3440-3452, 1971.

Tsumara, K., Determination of Earthquake Magnitude from Total Duration of Oscillation, *Bull. Earth. Res. Inst., 15,* 7-18, 1967.

Uhrhammer, R.A., Characteristics of Northern and Central California Seismicity, *Bull. Seism. Soc. Amer., 57,* 21, 1986.

Wald, D.J. and T.H. Heaton, Spatial and Temporal Distribution of Slip for the 1994 Northridge Earthquake, *USGS Open File Report 94-278,* 16 pp., 1994.

Wernicke, B., Low-angle Normal Faults in the Basin and Range Province: Nappe Tectonics in an Extending Orogen, *Nature, 291,* 645-648, 1981.

Wernicke, B. and B.C. Burchfiel, Modes of Extensional Tectonics, *Journal of Structural Geology, 4,* 105-115, 1982.

Wiley, T.J., D.R. Sherrod, D.K. Keefer, A. Qamar, R.L. Shuster, J.W. Dewey, M.A. Mabey, G.L. Black, and R.E. Wells, Klamath Falls Earthquakes, September 20, 1983 - Including the Strongest Quake ever Measured in Oregon, *Oregon Geology, 55,* 127-134, 1993.

Wilson, D.S., Deformation of the so-called Gorda plate, *J. Geophys. Res., 94,* 3065-3075, 1989.

Zandt, G. and C.R. Carrigan, Small-scale Convective Instability and Upper Mantle Viscosity under California, *Science, 261,*, 460-463, 1993.

Zandt, G. and K.P. Furlong, Evolution and Thickness of the Lithosphere beneath Coastal California, *Geology, 10,* 376-381, 1982.

Zoback, M.L. and M.D. Zoback, State of Stress in the Conterminous United States, *J. Geophys. Res., 85,* 6113-6156, 1980.

Zoback, M.D., M.L. Zoback, V.S. Mount, J. Suppe, J.P. Eaton, J.H. Healy, D.H. Oppenheimer, P.A. Reasenberg, L.M. Jones, C.B. Raleigh, I.G. Wong, O. Scotti, and C.M. Wentworth, New Evidence on the State of Stress of the San Andreas Fault System, *Science, 238,* 1105-1111, 1987.

# Appendix A

# Berkeley Digital Seismic Network

Table A.1: Location and Instrumentation of Stations in the Berkeley Digital Seismic Network

| # | Station | Latitude | Longitude | Instruments | Date of Operation |
|---|---------|----------|-----------|-------------|-------------------|
| 1 | BKS | 37.877 | -122.235 | STS-1; FBA-23 | 05/91 - Present |
| 2 | STAN | 37.404 | -122.174 | STS-2; FBA-23 | 06/91 - 07/94 |
| 3 | PKD1 | 35.873 | -120.425 | STS-2; FBA-23 | 10/91 - Present |
| 4 | MHC | 37.342 | -121.642 | STS-1; FBA-23 | 04/92 - Present |
| 5 | ARC | 40.877 | -124.074 | STS-2; FBA-23 | 05/92 - Present |
| 6 | SAO | 36.765 | -121.445 | STS-1; FBA-23 | 06/92 - Present |
| 7 | CMB | 38.035 | -120.385 | STS-1; FBA-23 | 06/92 - Present |
| 8 | WDC | 40.580 | -122.540 | STS-2; FBA-23 | 07/92 - Present |
| 9 | ORV | 39.556 | -121.500 | STS-1; FBA-23 | 07/92 - Present |
| 10 | MIN | 40.345 | -121.605 | STS-1; FBA-23 | 03/93 - Present |
| 11 | YBH | 41.732 | -122.711 | STS-1; FBA-23 | 07/93 - Present |
| 12 | JRSC | 37.404 | -122.238 | STS-2; FBA-23 | 07/94 - Present |
| 13 | HOPS | 38.994 | -123.072 | STS-1; FBA-23 | 10/94 - Present |
| 14 | BRIB | 37.919 | -122.151 | CMG-T30; FBA-23 | 07/95 - Present |
| 15 | KCC | 37.324 | -119.318 | STS-1; FBA-23 | 11/95 - Present |

# Appendix B

# Moment Tensor Distribution Mail

Figure B.1 is an illustrates a typical moment tensor email message that is send out after an event.

```
          This is a preliminary UCB moment tensor solution for
          the 950618 22:23 UTC event located 21 km ESE of Quincy, CA
          (39.84N; 120.72W; BDSN).  The ML averaged across the BDSN
          network was 4.4.  A Mw 4.1 was obtained from long-period
          three-component waves and surface wave amplitude and phase
          spectra.

           Best Fitting Double-Couple

                  Three-Component waves    Surface waves
              Mo = 1.52E+22 Dyne-cm        1.70e+22
              Mw = 4.1                      4.1
              Z  = 11km                     8 km
              NP1 = 212/-22/85             204/-32/68
              NP2 = 304/-175/68            07/-154/61


          Regards,
          Doug Dreger
          Mike Pasyanos
          UCB Seismographic Station

                  Three-component waves solution
                           -------
                       ------------------
                    ---------------------##
                   ----------------------######
                 ------------------------#########
            ####-------------------##########
           ###########----------###############
          ################------###############
          ####################--################
         ######################---###############
         ######################------#############
         ####################----------###########
         #    ###############------------##########
         # T ###############-------------#########
             ###########----------------######
          #############------------------#####
           ###########---------------------###
            ##########----------------------#
             ########------------------------
               ####-----------   ---------
                ##------------ P -------
                  -----------   ----
                     -------

          Lower Hemisphere Equiangle Projection
```

Figure B.1: A typical moment tensor email. Shown for a M4.1 earthquake near Quincy, CA that occurred on 18 May, 1995.

262

# Appendix C

# Moment Tensor Programs

Figures C.1–C.3 are the online manual pages for programs used in generating the regional surface wave moment tensors: SAPLING, SMTINV, and MT_PROGRAMS.

**NAME**

       sapling – SEED Analysis Program 'LlowIng Nifty Geophysics

**SYNOPSIS**

       **sapling**

**DESCRIPTION**

       *Sapling* is a miniSEED processing program. It can either be interactively driven by simply typing "sapling" or can be command line driven by typing all of the options on the command line. The list of commands can be accessed by typing "sapling help end".

```
**********************************
*                                *
*          SAPLING               *
*   miniSEED Processing Program   *
*        Michael Pasyanos         *
*                                *
**********************************
```

       command line driven
```
GENERAL          h help man clear cont
GENERAL           quit stop exit end
INPUT          input reload instr event trace make
OUTPUT         ah ascii seed
INFORMATION     list header minmax
SELECTING        sele dese orient stat stream
PROCESSING      filter resample rotate demean detrend
PROCESSING      integ diff hilbert
SPECTRA         spectra sratio
PLOTTING        plot ps record time xlim ylim xunits
PLOTTING        dist azi alpha ramp ot vel ttimes
PLOTTING        part partps tf tfps label comment title
```

       Currently, the processed data can be written out in miniSEED, AH or ASCII. Hopefully, there might be some more to come in the future.

**DOCUMENTATION**

       **On-line help is available.**

       **Complete documentaton is located in /home/u1/mike/latex/sapling.tex.**

**FILES**

       **/data/06/mike/libraries/libmike** - location of some of my personal library functions

       **/usr/contrib/lib/libahio.a** - AH input/output archive

       **/usr/local/src/quanterra/libqlib.a** - miniSEED input/output archive

**SEE ALSO**

       **smtinv**(1) -- Surface wave moment tensor program

**BUGS**

       I'm sure there are a few still floating around. Please send suggestions/problem descriptions/questions to *mike@seismo.berkeley.edu*.

**AUTHOR**

       Michael Pasyanos, UC Berkeley Seismographic Station

Sun Release 4.1                    Last change: 1 September 1995                    1

Figure C.1: Manual page for SAPLING program.

**NAME**

smtinv – Surface-wave Moment Tensor Inversion

**SYNOPSIS**

**smtinv** [**-h**|**-d**|**-m**|**-p**|**-r**|**-nd**|**-gmt**|**-pager**|**-message**|**-noise**|**-summary**] [**-qlp**|**-qvbb**|**-qvlp**|**-qlg**|**-terra**|**-terra_i**|**-seed**] [**-iris[n]**|**-geoscope**|**-nsn[n]**|**-cnsdc**|**-sac**|**-uw**|**-uw2**|**-wash**|**-uofo**] [**-lp**|**-vlp**|**-vbb**|**-brb**|**-ubb**|**-lg**]/[**-ppick**|**-alarm**|**-redi**] <*eventfile*>

**DESCRIPTION**

*Smtinv* is a program which, with a minimum of effort, will calculate the moment tensor inversion of regional earthquakes with surface waves. The major options include extracting the data [–d], calculating the moment tensor [–m], generating summaries [–summary], sending out pages [–pager], and generating nice maps [–gmt].

In extracting the data, smtinv either extracts data in miniSEED format or processes the data to get miniSEED. Sapling is used to process the data by reading the files, getting instrument and event information, resampling the data if necessary, rotating the data, and writing it out in AH data, which is used by the moment tensor codes.

The moment tensor is calculated using the regional surface wave moment tensor procedure.

**OPTIONS**

The following main options are recognized by smtinv:

–**h**      Displays a help screen summary of this manual page.

–**d**      Acquires data necessary for the inversion.

–**m**      Calculates the moment tensor inversion.

–**p**      Calculates path phase velocities.

–**gmt**    Plots the solution using GMT.

–**pager**  Sends out a pager message.

–**message**

        Sends out an email message.

–**summary**

        Generates event summary messages.

Other options recognized by smtinv:

–**nd**     No display option produces no window displays.

–**r**      Reruns while removing stations located in file 'station'.

–**noise**  Run with filter based on signal-to-noise ratio.

–**qlp**    Uses quanterra lp data on mass store (seed format).

–**qvbb**  Uses quanterra vbb data on mass store (seed format).

–**qvlp**  Uses quanterra vlp data on mass store (seed format).

–**qlg**   Uses quanterra lg data on mass store (seed format).

–**terra**  ftps to get TERRAscope data in RTP directory (seed format).

–**terra_i**

        ftps to get TERRAscope data in IRIS directory (seed format).

–**seed**  Uses seed data files in "seed" file (seed format).

–**iris**   Uses data extracted from IRIS (SEED volume)

Figure C.2: Manual page for SMTINV program.

**–geoscope**

   Uses data extracted from GEOSCOPE (SEED volume)

**–nsn[i]**   Uses data from U.S. National Seismic Network (GSE)

**–cnsdc**   Uses data from Canadian National Seismological Data Centre (GSE)

**–sac**      Uses sac data files in "sac" file (sac format)

**–uw**       Uses data from University of Washington (AH format)

**–uofo**    Uses data from University of Oregon (seed format)

**–lp**        Uses lp data.

**–vlp**      Uses vlp data.

**–brb**      Uses brb data.

**–vbb**      Uses vbb data.

**–ubb**      Uses ubb data.

**–lg**        Uses lg data.

**–ppick** *file*

   The input file is a ppicker file *file*.

**–alarm** *file.el*

   The input file is .el file *file.el*.

**–redi** *file*

   The input file is a REDI file *file*.

**DOCUMENTATION**

   **Complete documentaton is located in /home/u1/mike/latex/mtinv.tex.**

**FILES**

   **/home/u1/mike/progs/mtinv/smtinv_config - configuration file that contains various parameters used by the smtinv programs. Must be sourced by typing "source /home/u1/mike/progs/mtinv/smtinv_config"**

   **/home/u1/mike/dat -- location of files containing shell script routines**

**SEE  ALSO**

   **qdata**(1) -- quanterra data retrieval

   **rdseed**(1) -- read an FDSN SEED format volume

   **sapling**(1) -- miniSEED processing program

   **gmt**(1) -- The Generic Mapping Tools data processing and display software package

**BUGS**

   I'm sure there are a few still floating around.  Please send suggestions/problem descriptions/questions to *mike@seismo.berkeley.edu*.

**AUTHOR**

   Michael Pasyanos, UC Berkeley Seismographic Station

Figure C.2: Manual page for SMTINV program (continued).

**NAME**
　　　　dist_ah, gsnspec, gsnprop_ext, gsninv, smech_flex – Moment tensor programs

**SYNOPSIS**
　　　　dist_ah < cx_dist

　　　　gsnspec < c_spec

　　　　gsnprop_ext < cx_prop_ext

　　　　gsninv < cx_inv

　　　　smech_flex < cx_input1 smech_flex < cx_input2

**DESCRIPTION**
　　　　*Dist_ah* is a program which generates the distances and azimuths.

　　　　*Gsnspec* calculates the spectra of the surface waves given the group velocity window.

　　　　*Gsnprop_ext* corrects the spectra for the propagation through various media.

　　　　*Gsninv* inverts the spectra at the given periods for the moment tensor, centroid depth, and source duration.

　　　　*Smech_flex* plots the moment tensor solution and data.

**FILES**
　　　　**/data/07/mike/modes** -- location of mode files

**SEE  ALSO**
　　　　**smtinv**(1) -- surface wave moment tensor inversion

**BUGS**
　　　　I'm sure there are a few still floating around.  Please send suggestions/problem descriptions/questions to *mike@seismo.berkeley.edu*.

**AUTHOR**
　　　　Michael Pasyanos, UC Berkeley Seismographic Station

Figure C.3: Manual page for MT_PROGRAMS.